THE EFFECT OF IRRADIANCE ON ALGAL BIOMARKERS: TOWARDS THE INTERPRETATION OF STABLE ISOTOPIC SIGNATURES AND IMPLICATION FOR SEA ICE RECONSTRUCTIONS

A thesis submitted to the

School of Environmental Sciences

of the

University of East Anglia

in partial fulfilment of the requirements for the degree of

Doctor of Philosophy

By

Simin Gao

September 2022

Abstract

Source-specific highly branched isoprenoids (HBIs) have recently served as a binary or semi-quantitative biomarker to indicate the sea ice extent in the past. The type, thickness and overlying snow cover of the sea ice determine the light intensity underneath and can further have a significant impact on the productivity of photoautotrophic organisms. Since environmental water is the sole source of hydrogen for the biosynthesis of the biomarkers from these organisms, the hydrogen isotope ratio ($^{2}H/^{1}H$) of HBIs holds the potential to reveal more characteristics of sea ice. Based on the *in situ* irradiance underneath sea ice in polar regions, marine diatom *Navicula salinicola*, *Pleurosigma intermedium* and *Rhizosolenia setigera* were grown at varying light levels in laboratory conditions and harvested from exponential phase and stationary phase respectively to investigate the effect of light and growth phase on hydrogen and carbon isotope fractionation in HBIs and other algal lipids.

Gas chromatography-mass spectrometry (GC-MS) screening showed that *P. intermedium* produced C25 triene (C25:3) and tetraene (C25:4) HBIs, while pentaene (C25:5) was the only HBI detected in *R. setigera*. Minor diene (C25:2) and a triene with a new structure were found in samples from *N. salinicola*. Besides HBIs, fatty acids C14:0, C16:1, C16:0, and isoprenoid lipids phytol and squalene were detected in most samples. A remarkable decline in the ratio of C25:3 versus C25:4 was observed as irradiance increased. Hydrogen isotopic compositions of fatty acids, HBIs, phytol and squalene showed different directions in response to the increase of light. The relative proportion of NADPH and pyruvate originated from photosynthesis and the metabolic pathway for different lipid classes might account for this discrepancy. More than 20 per mil differences in $\delta^{13}C$ of algal lipids in lowest and highest irradiance and a linear correlation between $\delta^{13}C$ value and growth rate were observed. This is likely because of the limitation of environmental carbon transport into cells at high growth rate and of carboxylation by RuBisCO during photosynthesis at low growth rate.

The characterisation of hydrogen and carbon isotopic signatures of different algal lipid classes under varied light conditions will lead to a better understanding of the effect of light on diatom metabolism and biochemistry. This knowledge will be instrumental to a more robust interpretation of stable isotope data from environmental samples and thus will contribute to further developing HBI biomarkers as a tool for estimating not only the absence/presence of sea ice but also the ice type, thickness, and snow cover.

Key words: *Pleurosigma intermedium*, *Rhizosolenia setigera*, HBIs, variable irradiance, stable hydrogen isotope, stable carbon isotope, MEP, MVA

Acknowledgements

First and foremost, I am extremely grateful to my supervisors, Dr. Nikolai Pedentchouk (University of East Anglia) and Prof. Thomas Mock (University of East Anglia) for their invaluable advice, continuous support, and patience during my Ph.D. study. Their immense knowledge and plentiful experience have encouraged me all the time in my academic research and daily life.

Second, I would like to thank Prof. Youping Zhou (Southern University of Science and Technology) and his team for kindly offering the GC-MS analysis and the introduction of collaboration with Nanjing University for further GC-IRMS analysis. Honestly, the project could not be done in time without his help. I particularly appreciated Prof. Zhou for his time in the first-hand data processing and reviewing of my Ph.D. thesis.

I would also like to thank Mr. Robert Utting and the technician teams in Science Faulty, University of East Anglia for their technical support in my study. Thank all the members of Mock's lab. It is their kind help and support that have made my study and life in the UK a wonderful time.

Thank Prof. Simon T. Belt and Dr. Lukas Smik from University of Plymouth for demonstrating the lipid extraction methods and NMR analysis. Thanks for their effort in deliberating the fabulous data for my first publication.

I also want to express my appreciation to Prof. Thomas Wagner and Dr. Mark Chapman as my external and internal examiners for my VIVA. I fully understand how much effort has been made for the three of us to get through my thesis.

Finally, I would like to express my gratitude to my dearest parents, my cat, and my friends. Without their tremendous understanding and encouragement over the past few years, it would be impossible for me to complete my study.

Back to the beginning of my Ph.D., I have never imagined that doing a Ph.D. can be such a tough thing. Covid-19 pandemic (2019-2022) took 3 years of my whole Ph.D., which made things extremely depressing and difficult. I am very proud of myself for completing such a big thing and I would like to continue doing what I have been doing during the past four years.

Thank you and cheers!

Content

List of Figures

List of Tables

Abbreviation

Abbreviation	Description
3-PGA	3-PhosphoGlyceric Acid
ACT	Acetogenic
ADP	Adenosine DiPhosphate
ATP	Adenosine TriPhosphate
Chl *a*	Chlorophyll *a*
CoA	Coenzyme A
DMAPP	DiMethylAllyl PyroPhosphate
DMSP	DiMethylSulfonioPropionate
DOXP	1-deoxy-D-xylulose-5-phosphate
FAs	Fatty Acids
FNR	Ferredoxin – NADP reductase
G3P	Glycerol-3-Phosphate
GC	Gas Chromatography
HBIs	Highly Branched Isoprenoids
IP_{25}	Ice proxy with 25 carbon atoms
IPP	Isopentenyl PyroPhosphate
$IPSO_{25}$	Ice proxy for the Southern Ocean with 25 carbon atoms
IRD	Ice Rafted Debris
IRMS	Isotope Ratio Mass Spectrometry
KIE	Kinetic Isotope Effect
LGM	the last glacial maximum
MEP	2-C-Methyl-D-Erythritol 4-Phosphate
MIZ	Marginal Ice Zone
MS	Mass Spectrometry
MSA	MethaneSulphonic Acid
MSD	Mass Selective Detector
MVA	Mevalonate
$NADP^+$	Nicotinamide Adenine Dinucleotide Phosphate
NADPH	Reduced Nicotinamide Adenine Dinucleotide Phosphate
NMR	Nuclear Magnetic Resonance
PAR	Photosynthetically Active Radiation
PC	PlastoCyanin
Pi	inorganic Phosphate
PQ	PlastoQuinone
PS-I	PhotoSystem I
PS-II	PhotoSystem II
PUFA	PolyUnsaturated Fatty Acids
PUFAs	PolyUnsaturated Fatty Acids
RT	Retention Time
RuBisCO	Ribulose-1,5-Bisphosphate Carboxylase-Oxygenase
RuBP	Ribulose 1,5-BisphosPhate
SST	Sea Surface Temperature

1 Introduction

1.1 Background

Sea ice plays a critical role in Earth's system with regard to energy budget, climate change, physical oceanography and biosphere. In the climate system, sea ice acts as an amplifier. Owing to its high albedo, it reflects a significant proportion of the incoming solar radiation and limits the heat and gas exchange between the ocean and atmosphere in the polar regions. Not only influences the polar regions themselves, pack ice also drives global ocean thermohaline circulation patterns through the formation of cold, dense deep water masses (Thomas & Dieckmann, 2003). Sea ice is the dominant feature governing the ecology of polar regions and also an ephemeral feature of the Baltic, Caspian and Okhotsk seas. With a maximum extent area comprising 13% of the earth's surface, sea ice hosts a diverse community of primary producers (Arrigo, 2017), zooplankton (Caron et al., 2017) and polar marine mammals and birds (Tynan et al., 2010), and provides key habitat for one of the most unique ecosystems on Earth. Actually, the primary production associated with sea ice can be even greater than that of the open ocean. Since it directly controls light penetration, supplies nutrients and microorganisms to the pelagic community, sea ice has a profound effect on the distribution of phototrophic organisms (Arrigo et al., 2010).

Despite over 200 years of scientific endeavour in the Arctic and Antarctic, polar marine research is still a rather young research area. In the past decade, there has been increasing interest in the effects of global climate warming on sea-ice dynamics, and the consequences for global ocean circulation and the ecology of polar regions. Reconstruction of sea ice conditions in polar regions is a key objective in palaeoceanography and palaeoclimatology (de Vernal et al., 2013a).

Arctic sea ice extent and thickness are declining at an accelerating rate due to unprecedented, anthropogenic-induced, and warming over the last century. (Kwok & Untersteiner, 2011; Serreze et al., 2009; Stroeve et al., 2007). The impacts of this decline are not well constrained and considerable scientific attention has been paid to Arctic warming over the past few decades. (Francis et al., 2005; Johannessen et al., 1995; Vinnikov et al., 1999). For example, the thinner sea ice significantly increases the transmission of photosynthetically

available radiation (PAR), further influencing the onset of the spring ice algal bloom and the transformation of the nutrients to higher trophic levels for secondary production (Leu et al., 2011).

The changes in sea ice thickness are closely linked with the insulation effect which strengthens with thinner ice, increasing vertical heat flux and warming overlying air columns. This will lead to the subsequent melting of sea ice (Serreze & Barry, 2011).

In the context of this study, ice thickness only started to be monitored closely since the development of NASA's Ice, Cloud, and land Elevation Satellite (ICESat) in 2003 via passive microwave satellite imagery (Comiso, 2006). Before that, sea ice thicknesses were determined using qualitative, often patchy, maritime sealing and whaling records which produced large uncertainties in coupled atmosphere-ocean general circulation models (AOGCM) (de la Mare, 1997; Divine & Dick, 2006) and provided a limited basis for millennial-scale reconstructions.

If paleo sea ice thickness can be better constrained by a definitive proxy, then it can offer an improved understanding of the complex Arctic ocean-atmosphere-ice system and its role in past and present global climate variability. Further, data from this study and others could be used in AOGCM's to improve the accuracy of future climate predictions, vital for understanding the extent to which anthropogenic activities have altered climatic parameters and whether that alteration is enough to reach a turning point in the climate system (Briner et al., 2016; Kaufman et al., 2016; Sundqvist et al., 2014).

1.2 Sea ice dynamics

1.2.1 Seasonal variations of sea ice extent

Due to the action of winds, currents and temperature fluctuations, sea ice becomes the most seasonal and expansive geophysical parameter on the Earth's surface. The dynamics of polar seas and oceans are dominated by the development of the first-year ice and the accumulation of multi-year ice which regulate the extent, thickness, volume and the drift pattern of the sea ice. Sea ice dynamics are distinct in Northern and Southern Hemispheres owing to the very different polar configurations of the land and ocean.

In the Arctic, atmospheric and ocean circulations are characterised by variable patterns. The relative strengths of the Beaufort Gyre and Trans Polar Drift play an important role on variations in the residence time of sea-ice in the Arctic Ocean and in the freshwater budget of the Arctic and Nordic Seas, resulting in asymmetrical distributions of seasonal sea-ice cover.

Through the seasonal cycle, from the latest summer of September 2021 (Figure 1-1 (a)) to the winter of February 2022 (Figure 1-1 (b)), the extent of sea ice cover in the Arctic expands almost threefold ranging from a minimum of 4.9×10^6 km^2 to a maximum of 14.6×10^6 km^2 (Fetterer et al., 2017, updated daily).

(a)

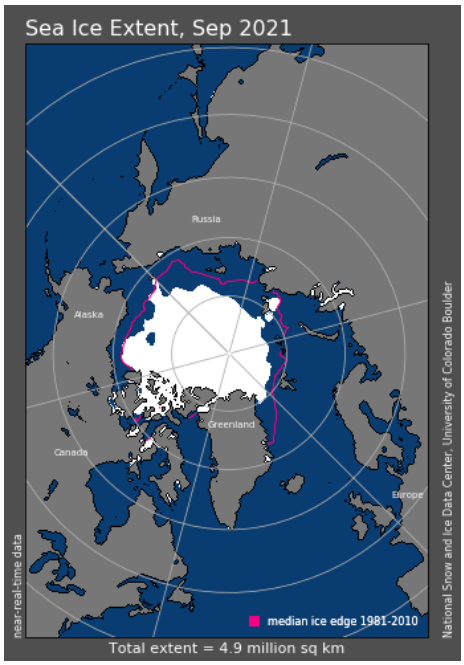

(b)

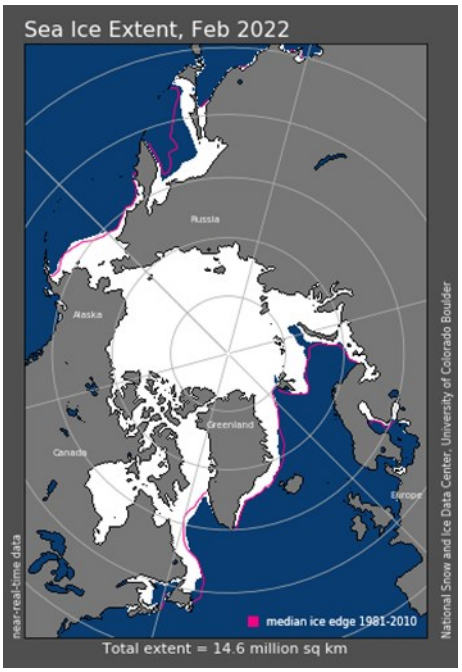

(c)

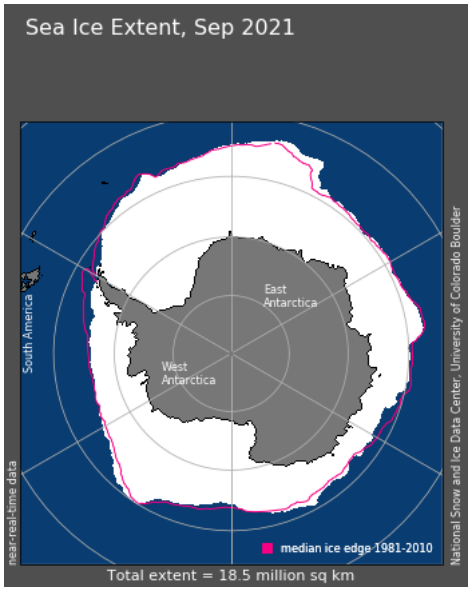

(d)

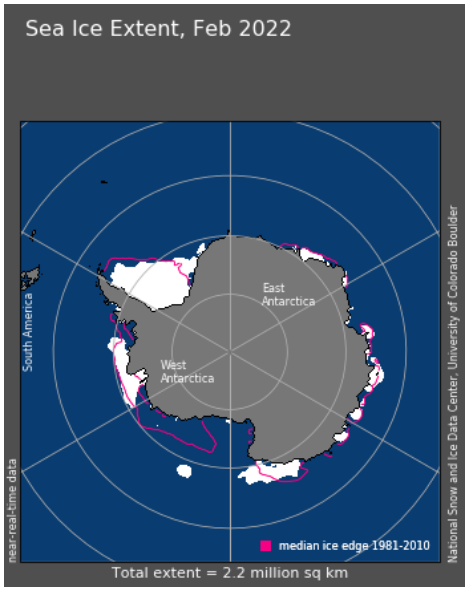

Figure 1-1. Maps showing seasonal sea-ice variations in September 2021 (a), February 2022 (b) in Arctic and September 2021 (c) and February 2022 (d) in Antarctic. The pink line shows a typical ice extent for that month, based on a 30-year climatology from 1981 to 2010. Images courtesy of the National Snow and Ice Data Centre, University of Colorado, Boulder (Fetterer et al., 2017, updated daily).

Compared to the Arctic, the distribution of the sea ice in the Antarctic wintertime is relatively symmetric from a circumpolar perspective. In the Southern Ocean, the magnitude of the seasonal change is even more remarkable with a maximum of 14.6×10^6 km in the winter of September 2021 (Figure 1-1 (c)). The ice margin mainly depends on the interplay between the northward advection of the newly formed ice by winds and the melting of the ice edge in warmer waters. While in summer, sea ice retreats from its maximum extent (ca. 55°S in the Atlantic and Indian Oceans, ca. 60°S in the Pacific Ocean) to the coast of Antarctica, with little or no perennial ice being present around the continent, giving a minimum of 2.2×10^6 km^2 in the summer February 2022 (Figure 1-1 (d)).

1.2.2 Sea ice changes in past few decades

Owing to the development of satellite observation in the late 1970s, satellite passive-microwave imagery made monitoring sea ice conditions possible. These satellite observations show a significant decrease in sea ice concentration over the past few decades with an accelerating retreat of sea ice in the Beaufort Sea, Chuckchi Sea and East Siberian Sea of ca. 20% per decade (Figure 1-2 (a)). The sea ice extent fell to the record of 4.9×10^6 km^2 in 2021. Compared to 7.1×10^6 km^2 in 1979, almost 30% of the sea ice in the Arctic has melted (Figure 1-2 (b)). The decline in sea ice cover has resulted in ca. 30% increase in net primary production by

phytoplankton within the Arctic Ocean between 1998 and 2012 and is likely to have a significant impact on the marine ecosystem in the future.

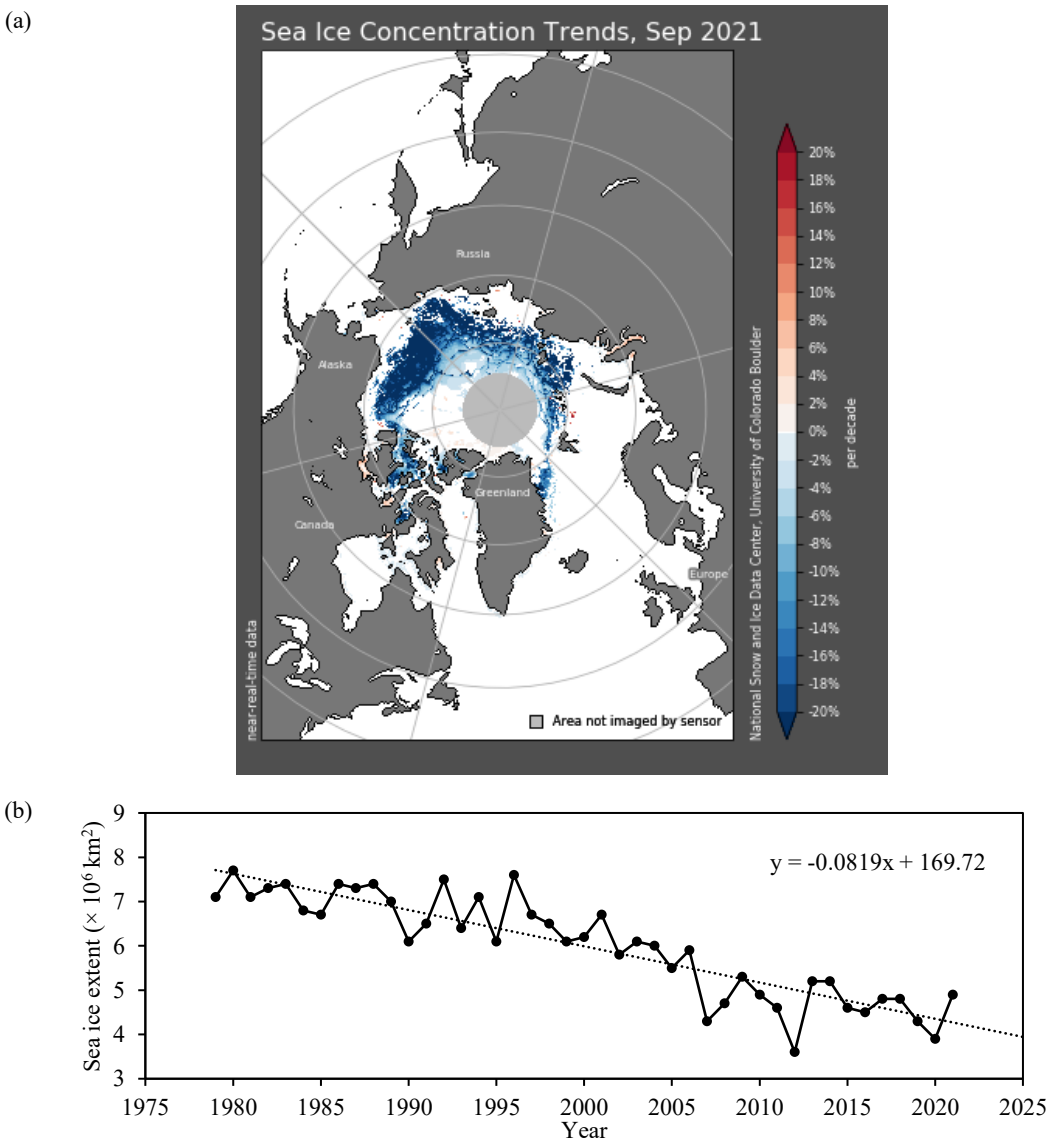

Figure 1-2. Sea ice concentration trends in September 2021 (a) and extent changes during the period of 1979 – 2021 in Northern Hemisphere (b). Data courtesy of National Snow and Ice Data Centre (Fetterer et al., 2017, updated daily).

In the Antarctic, overall sea ice extent slightly decreased (ca. 1.2%) while with relatively higher fluctuation over the past 30 years. The regional variability is particularly large between East and West Antarctic with a remarkable sea ice expansion in the Weddell Sea by ca. 18% per decade while a significant of sea ice retreat of 20% per decade in the Bellingshausen Sea and Amundsen Sea (Figure 1-3).

(a)

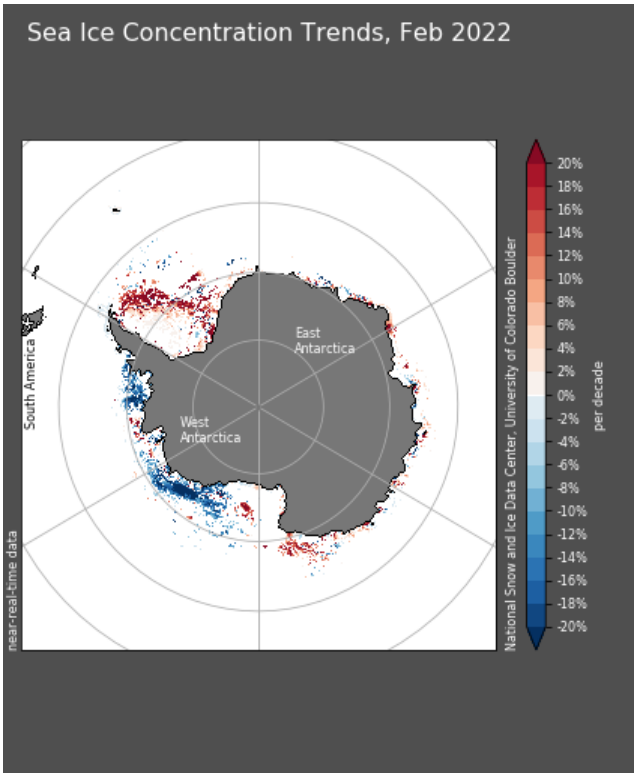

(b)

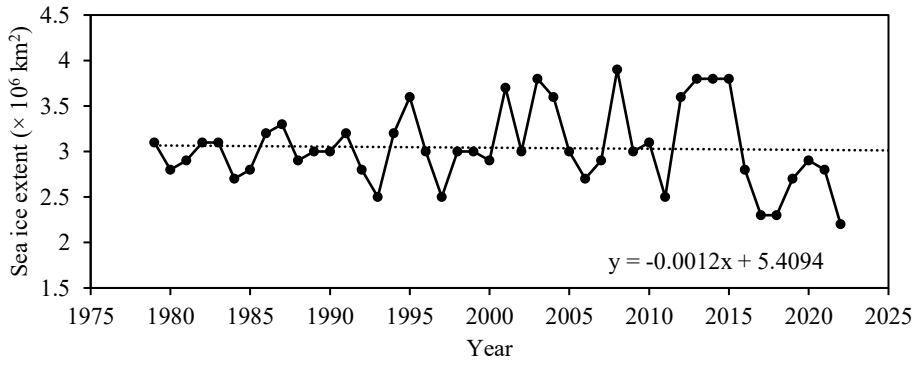

Figure 1-3. Sea ice concentration trends in February 2022 (a) and sea ice extent during the period of 1979 – 2022 in Southern Hemisphere (b). Data courtesy of National Snow and Ice Data Centre (Fetterer et al., 2017, updated daily).

Even recent changes in sea-ice extent and thickness are well documented (Stroeve et al., 2012; Walsh et al., 2017). Major changes in climate in the Arctic and Antarctic during the second part of the 20th century have led to the proliferation of research activity about the mechanisms and consequences of these changes.

1.3 Sea ice and sunlight

Sunlight provides light, heat and energy for the inhabitants on Earth. There are three relevant bands along the solar radiation spectrum, ultraviolet, visible light, and infrared. Of the light that reaches Earth's surface, infrared radiation makes up 49.4% while visible light provides 42.3%. Ultraviolet radiation makes up just over 8% of the total solar radiation (Figure 1-4).

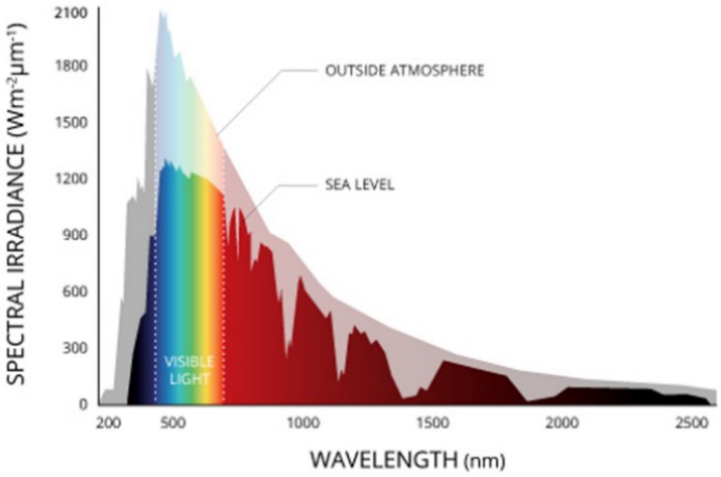

Figure 1-4. Most of the solar radiation that reaches Earth is made up of visible and infrared light. Only a small amount of ultraviolet radiation reaches the surface.

Each of these spectra range has a different impact on the environment. Here, we mainly discussed the visible light, also known as Photosynthetically Active Radiation (PAR), the short-wave radiation of the spectral range from 400 to 700 nanometres. This spectral region is the best fit wavelength for photosynthesis to occur. Hence, the amount of spectral composition of PAR can strongly impact primary productivity and biological activity in and under the sea ice cover. Much of the radiation emitted from the sun has been absorbed, reflected or scattered in the atmosphere. Latitude, season, time of day, cloud cover and altitude will influent the amount and intensity of solar radiation. Ice and snow cover will greatly affect the amount of light absorbed in a body of water. Clean ice has the same percentage of light transmission as liquid water, which is about 72%. However, if the ice is stained or cloudy, the percentage can drop dramatically. Opaque ice and heavy snow can drop the percentage of light transmission to nearly zero.

Not just a product of frozen seawater, sea ice has an intricate structure with ice, brine channel, air bubbles and particulates. The optical properties of sea ice can

be directly affected by its physical structure and further effects the shifting balance between reflected and transmitted light to the underlying seas/oceans. Figure 1-5 demonstrates the interactions between incoming sunlight and sea ice. The incident solar radiation can directly come from the sun or diffuse from the sky then be reflected/absorbed from the sea ice and transmitted through the ice to the ocean. Besides the physical conditions of the sea ice itself, the sun angle, sky conditions, surface state and wavelength of the light will impact the irradiance underlying sea ice as well.

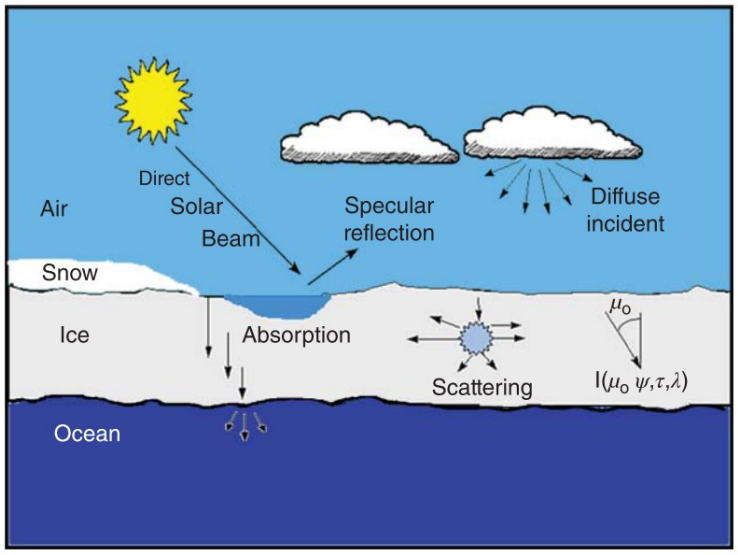

Figure 1-5. Schematic of the interaction of sunlight with sea ice. The three primary sea ice surface types of snow-covered ice, bare ice and ponded ice are shown. From (Perovich, 2017).

Nicolaus et al. (2012) presented the very first large-scale light measurements under Arctic sea ice by a spectral radiometer on a remotely operated vehicle. Their results showed that with a larger melt-pond coverage (42%) in first-year ice, the transmittance through first-year ice (0.11) was almost threefold of through multi-year ice (0.04) which only has 23% melt-pond coverage. The energy absorption was also 50% larger in first-year ice than that in multi-year ice (Figure 1-6).

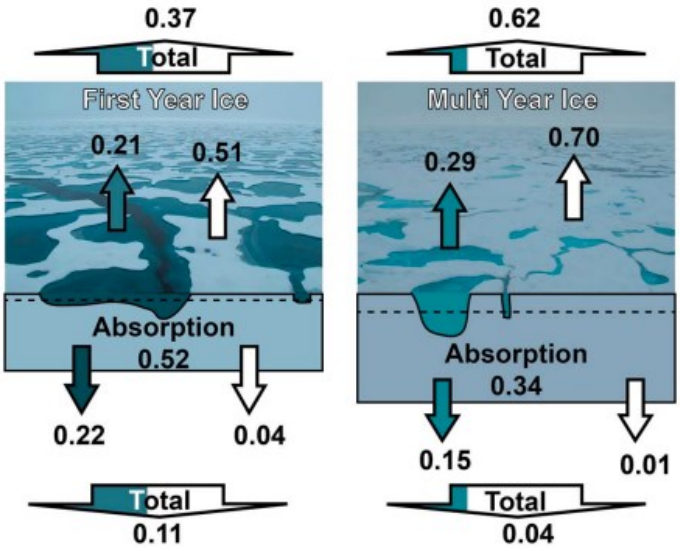

Figure 1-6. Short-wave albedo, transmittance, and absorption of Arctic first- and multi-year sea ice during summer. Coloured arrows refer to melt ponds while white arrows refer to white ice. The pictures show representative photographs of first- and multi-year sea ice. The dashed lines in the sea ice indicate the water level. The "Total" arrows average transmittance and albedo over each sea-ice type, considering 23 and 42% ponded surface fractions of multi- and first-year ice, respectively. This fraction is indicated through the colours in the arrows. Albedo for different ice types is taken from (Perovich, 1996). Absorption is given in the ice as the sum of white ice and ponds. From (Nicolaus et al., 2012).

Leu et al. (2010) reported irradiances and transmittance underneath the ice covered by snow in 3 spots (SH, RIB, BS, Figure 1-7) in Svalbard. In April, the incident PAR irradiances can be as high as 800 µmol m^{-2} s^{-1} around noon under cloudless conditions while the irradiance underneath the sea ice was ca. 20 µmol m^{-2} s^{-1}. When the ice was covered with snow, the light intensity can be even less than 3 µmol m^{-2} s^{-1} with transmittance values less than 0.5%. They also reported substantial differences in sea ice irradiances with similar ice thickness but different snow conditions. The light intensity penetrated through the Low Light (LL) site with approx. 20 cm snow cover and hard ice was only 4 to 5 µmol m^{-2} s^{-1}. Whereas almost 100 m^{-2} s^{-1} at the High Light (HL) site with virtually snow-free area or much softer ice due to melting and snowdrift.

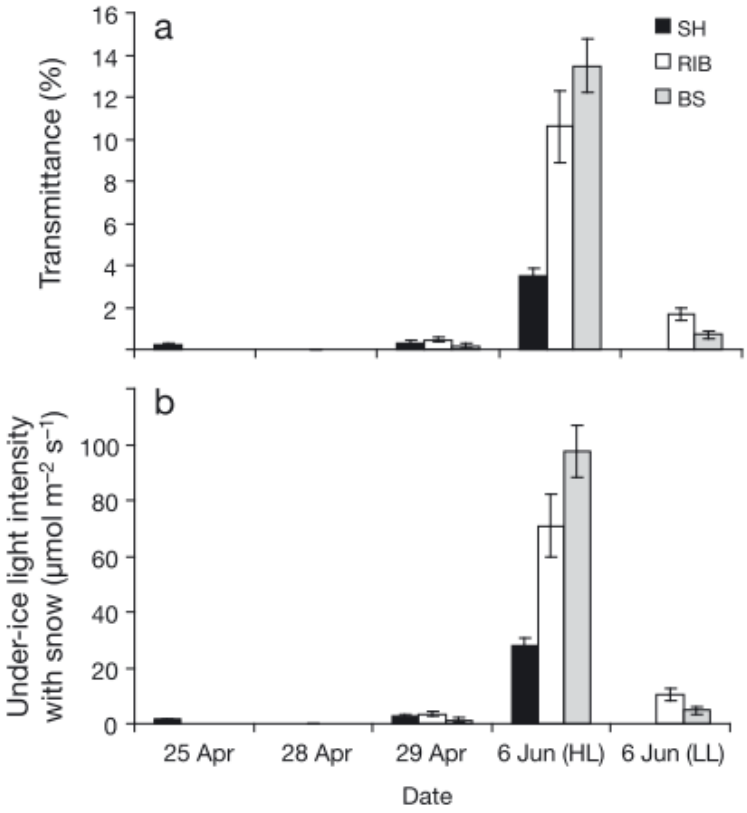

Figure 1-7. Changes in (a) transmittance of ice and snow (% of incident irradiance) and (b) *in situ* PAR irradiances were measured around noon under the ice with a cosine-corrected LiCor Sensor. Presented are average values and standard deviations from measurements of 3 spots at 1 m from a drilled hole. SH, RIB, BS: sampling sites, HL = High Light; LL = Low Light; from (Leu et al., 2010).

1.4 Sea ice as a habitat for primary producers

Sea ice in the Arctic and Antarctic comprises one of the largest ecosystems on Earth. When sea ice melts, vast volumes of freshwater are released into the surrounding sea, often forming a stabilized, low-salinity surface water layer where algal blooms take place. The marginal ice zone (MIZ) can extend up to 100 to 200 km in width. Not only in MIZ, there are also thriving microbial assemblages including viruses, bacteria, algae and small crustaceans underneath the extensive pack and fast ice. The semi-solid matrix of sea ice provides a unique habitat for these polar planktonic organisms that can remain suspended in the upper ocean where light and nutrients are sufficient for net growth (e.g. Figure 1-8).

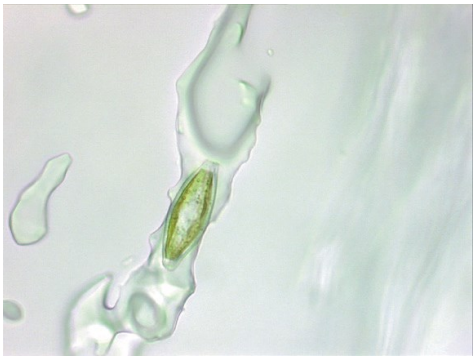

Figure 1-8. A sea-ice diatom in a sea-ice brine channel (photograph: Christopher Krembs) (Kaiser et al., 2011).

The most conspicuous organisms in the sea ice are diatoms, which make up over 90% of the photosynthetic organism diversity with more than 500 species. Flagellate species of algae also have been reported for sea ice, especially in surface ice and ponds of trapped seawater or meltwater.

The concentrations of the algae cell in sea ice can vary from less than 10^4 to more than 10^9 cells per litre, ranging from some newly formed ice or extreme conditions with the lowest abundance to ice-seawater interfaces and surface ponds with high cell concentrations. The chlorophyll *a* (Chl *a*) biomass in sea ice is also different from geographic location, sea ice type and seasons. It has been measured that the volumetric Chl *a* concentrations range from 3 to 800 μg per litre in the Arctic and 3 to a stunning 10100 μg per litre in the Antarctic. It is almost 2000 times of the typical values of Chl *a* per litre in the surface waters in Southern Ocean (0 to 5 μg chlorophyll per litre, (Horner et al., 1992; Lizotte, 2001).

The primary production in the Antarctic sea ice is estimated as 63 to 70 Tg C per year, consisting of ca. 5% of the total annual primary production (1300 Tg C per year) in the sea ice-influenced zone of the Southern Ocean. It may sound minor contribution compared to their phytoplankton counterparts, while is in fact highly significant as the sea ice organisms are the major carbon source for the higher trophic levels, especially during the winner time when other sources of food are lacking.

To tackle the extreme growth conditions, sea ice algae have developed a unique phase in their sensational cycle and some regulation mechanisms such as photo acclimation and adaptation. In low light conditions, the Chl *a* : C ratio can be significantly greater than that at higher light conditions to increase the efficiency of light-harvesting. While when nitrogen, phosphorus, and trace metal are limited, or the growth temperature is relatively low, the Chl *a* : C ratio of a particular photosynthetic organism tends to decrease (Kirst & Wiencke, 1995; MacIntyre & Kana, 2002; Raven & Geider, 2003).

Another example is the production of polyunsaturated fatty acids (PUFAs) which are essential for marine organisms while mostly produced by bacteria and microalgae. Enhanced production of PUFAs within sea ice algae and bacteria in winter was observed by Nichols (2003). This provided a rich PUFAs pool for the grazing organisms.

1.5 Proxies for sea ice reconstructions in Arctic and Antarctic

Changes in sea ice extent and thickness during the last half century are well documented, however, this is a relatively short timescale and during this period, anthropogenically induces warming makes it even more difficult to understand the natural changes in the sea ice. Hence, scientists turn to use sea ice proxies that can provide longer time scales and valuable perspective on climate change, and paleo sea ice reconstruction.

The main methods for reconstructing past sea ice distribution and its seasonal variability are based on the microfossil assemblage distribution including diatoms (e.g. Armand & Leventer, 2010; Crosta et al., 2004; Gersonde et al., 2005; Justwan & Koç, 2008), dinoflagellate cysts (e.g. de Vernal et al., 2001, 2005), ostracods (Cronin et al., 2010) and foraminifera (e.g. Scott et al., 2008), geochemical and sedimentological tracers, organic biomarkers. In both northern and southern high latitudes, the primary method is via the microscopic remains of marine organisms in marine sediments, with new techniques targeting biomarkers linked to microorganisms (Brown et al., 2014b; Massé et al., 2011).

There are large differences in the utility of various types of paleo sea ice proxies in the northern and southern hemispheres though. In the Arctic, quantitative analysis of dinocyst assemblages has been shown to be a relatively powerful tool, while in the Antarctic, diatom assemblages have been the most useful method (Armand et al., 2017).

1.5.1 Microfossil assemblage distribution

1.5.1.1 Dinoflagellates

The dinoflagellates are single-celled eukaryotes that occur in most aquatic environments. Many dinoflagellates are photosynthetic, but a large fraction of these are in fact mixotrophic and some dinoflagellates can produce dinocysts that are highly resistant to dissolution. The mixotrophic nature, and ability to encyst make them survive even under very harsh environmental conditions.

As they are very sensitive to the growth conditions including sea surface temperature (SST), salinity, depth and ice cover, the variation of assemblage composition of dinocysts can be seen as a function of surface water conditions.

Reconstruction of surface ocean conditions through analysis of dinocysts has been done mainly through the application of modern analogue techniques and transfer functions (de Vernal et al., 2001, 2013b). To date, dinoflagellate cysts have become the most powerful proxy recorder of paleo sea ice in the high northern latitudes owning to their diverse and widespread population in the Arctic.

The main limitations with the Arctic dinocyst-based proxy for sea ice reconstruction are the difficulties in estimating perennial and multi-year ice and the mismatch between the time period recorded and surface sediment samples (de Vernal et al., 2013a, 2013b).

1.5.1.2 Diatoms

Diatoms are unicellular microalgae found in the oceans, waterways and sometimes soils. The unique feature of diatom anatomy is that they are surrounded by a hydrated silicon dioxide cell wall called frustule.

Pioneered by Hart (1942), diatoms have been used as paleo sea ice proxies interpreting the chemical, physical and biological conditions of the Southern Ocean owning to their high abundance throughout the Southern Ocean (e.g. Grigorov et al., 2014; Riaux-Gobin et al., 2011; Saba et al., 2014). Certain diatom groups can be associated with the sea ice or the open ocean environment, for example, in the Southern Ocean, diatom species such as *Fragilariopsis curta* were confined to regions south of the Polar Front (Armand et al., 2005). While in the north of the Polar Front, the open ocean zone was dominated by open ocean diatom species such as *Fragilariopsis kerguelensis* (Crosta et al., 2005).

While in the Arctic regions, the application of diatoms as paleo sea ice proxies was highly limited as some frustules were prone to dissolve in the water. The poor preservation of the frustules within the sediment made the identification of the individual diatoms difficult and might result in inaccurate reconstructions, especially the central and marginal Arctic Ocean.

1.5.1.3 Calcareous microfossils - coccolithophorids, ostracods and foraminifera

Calcareous microfossils including coccolithophorids, ostracods and foraminifera have been used to track the sea ice cover over time mainly in the high northern

latitudes as a greater dissolution of $CaCO_3$ in lower water temperature and less species diversity in high latitude.

Emiliania huxleyi and *Coccolithus pelagicus* are the donmiance species in high northern latitudes and the presence of them in marine sediments has been used to indicate seasonally ice-free conditions (Braarud, 1979)Samtleben & Schroder, 1992). The presence of them in marine sediments has been used to trace seasonally ice-free conditions in the Labrador sea (Rahman & de Vernal, 1994); Fram Strait (Hebbeln & Wefer, 1997); North Atlantic (Hebbeln et al., 1998).

Ostracods are small bivalve crustaceans with a low magnesium calcite carapace. They occur throughout the Arctic Ocean and are common in Quaternary Arctic Sediments (Cronin et al., 1994; Taldenkova et al., 2005). Cronin et al. (2010) presented modern distribution data on a sea ice dwelling species *Acetabulastoma arcticum* which parasite with amphipods that live exclusively in perennial sea ice.

1.5.2 Biological products for elucidating past sea-ice extent

Besides satellite records, biological products such as photosynthetic biomarkers also provided certain indirect evidence elucidating the shrinking of the sea ice. As biological products are associated with living creatures, consequently, the presence of these biological products suggests an absence of permanent ice cover.

Early work of the measurement of chlorins and porphyrins concentrations (the diagenetic products of chlorophyll) by Rosell-Melé & Koç (1997) suggested the sedimentary occurrence of vanadyl porphyrins in Nordic sea cores can be used as a biomarker of ice-rafted debris from the Barents ice sheet.

Curran et al., (2003) reported a significant correlation between methanesulphonic acid (MSA, a breakdown product of dimethylsulfoniopropionate (DMSP), produced by algae in the brines with high salinity and low temperature) concentrations from ice cores on the east Antarctic coast and 22 years of satellite-derived sea ice extent for the 80°E to 140°E sector. Their results suggested that the sea ice extent was relatively constant between 1841 to 1950 while then declined by ca. 20% decline thereafter.

Recently, a C_{25} monounsaturated hydrocarbon was detected in sea ice samples from three locations in the Canadian Arctic (Belt et al., 2007). They suggested this

biomarker, namely IP_{25}, may serve as a specific, sensitive and stable proxy for paleo sea ice reconstruction on timescales ranging from less than the past 100 years to over 2 million years. The IP_{25}, IP_{25}-related and its analogues have been used as a sea ice indicator afterward (e.g. Brown, 2011; Köseoğlu et al., 2018; Rontani et al., 2018). A detailed introduction of IP_{25} can be seen in the following section.

1.6 Geochemical tracers: Highly Branched Isoprenoids (HBIs)

As most sea ice proxies are biologically based, the biodegradation typically underrepresents the sedimentary archives of the organisms that live within and/or underneath sea ice. A promising proxy for paleo sea ice reconstruction requires highly stable source-specific compounds biosynthesized by these microalgae.

Fatty acids and sterols are the most common and well-studied algal lipid classes. However, they do not sufficiently satisfy the criterion of source-specific to distinguish sea ice cover from open water conditions. In contrast, a lipid group referred to as Highly Branched Isoprenoids (HBIs) has been found to be biosynthesized by a relatively small number of marine and freshwater diatoms belonging to the *Haslea*, *Navicula*, *Pleurosigma*, *Rhizosolenia* and *Berkeleya* genera (Belt et al., 1996, 2000, 2001; Brown et al., 2014a; Grossi et al., 2004; Kaiser et al., 2016; Sinninghe Damsté et al., 1999; Volkman et al., 1994). This makes them serve as suitable biomarker proxies for discrete oceanographic settings.

As it is named, HBIs differ in terms of biosynthesis from most common acyclic and cyclic isoprenoid natural products because their skeletons are characterized by a distinctive T branch. HBIs occur with C_{20}, C_{25} and C_{30} carbon skeletons, among which C25 alkenes are the most commonly reported ones (Figure 1-9). In the C_{25} HBI alkenes, the T branch is formed by the attachment of a C_{10} isoprenoid unit to a C_{15} isoprenoid at C-7, most likely requiring an unusual set of enzymes. While in the C_{30} HBI alkenes, a C_{15} instead of a C_{10} isoprenoid unit is used.

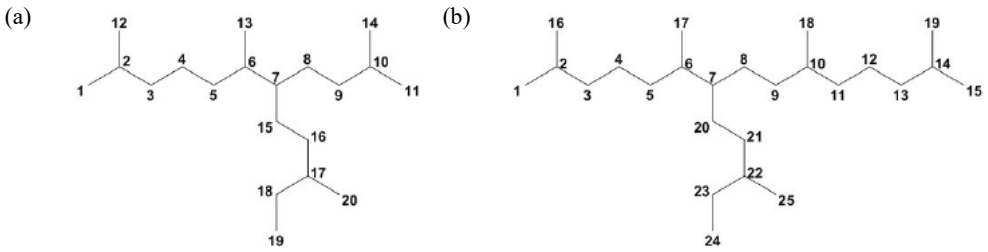

(c)

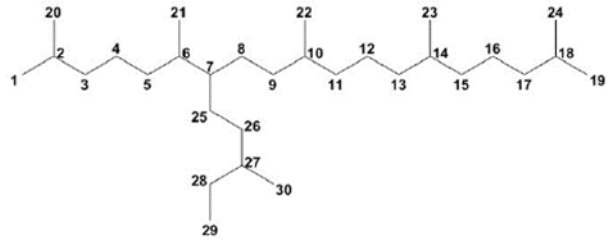

Figure 1-9. Carbon skeleton of C20 (a), C25 (b), C30 (c) HBIs.

Sinninghe Damsté et al. (2004) examined over 120 marine diatom species representing all major orders for lipid composition and 18S rDNA phylogeny (Figure 1-10). Their study showed that only members of the four diatom genera are capable of HBI alkene biosynthesis and phylogenetically these genera fell into two different clusters: the group of centric diatoms comprises Rhizosolenia species (HBI-1) which can produce C_{25} and/or C_{30} and the group of pennate diatoms comprises the genera *Haslea*, *Navicula*, and *Pleurosigma* (HBI-2) which can only produce C_{25}. It has been demonstrated that the changes in the life cycle and environmental conditions can lead to a switch from C_{30} to C_{25} HBI biosynthesis in Rhizosolenia. Both phylogenetic clusters contain some species that apparently do not biosynthesis HBIs.

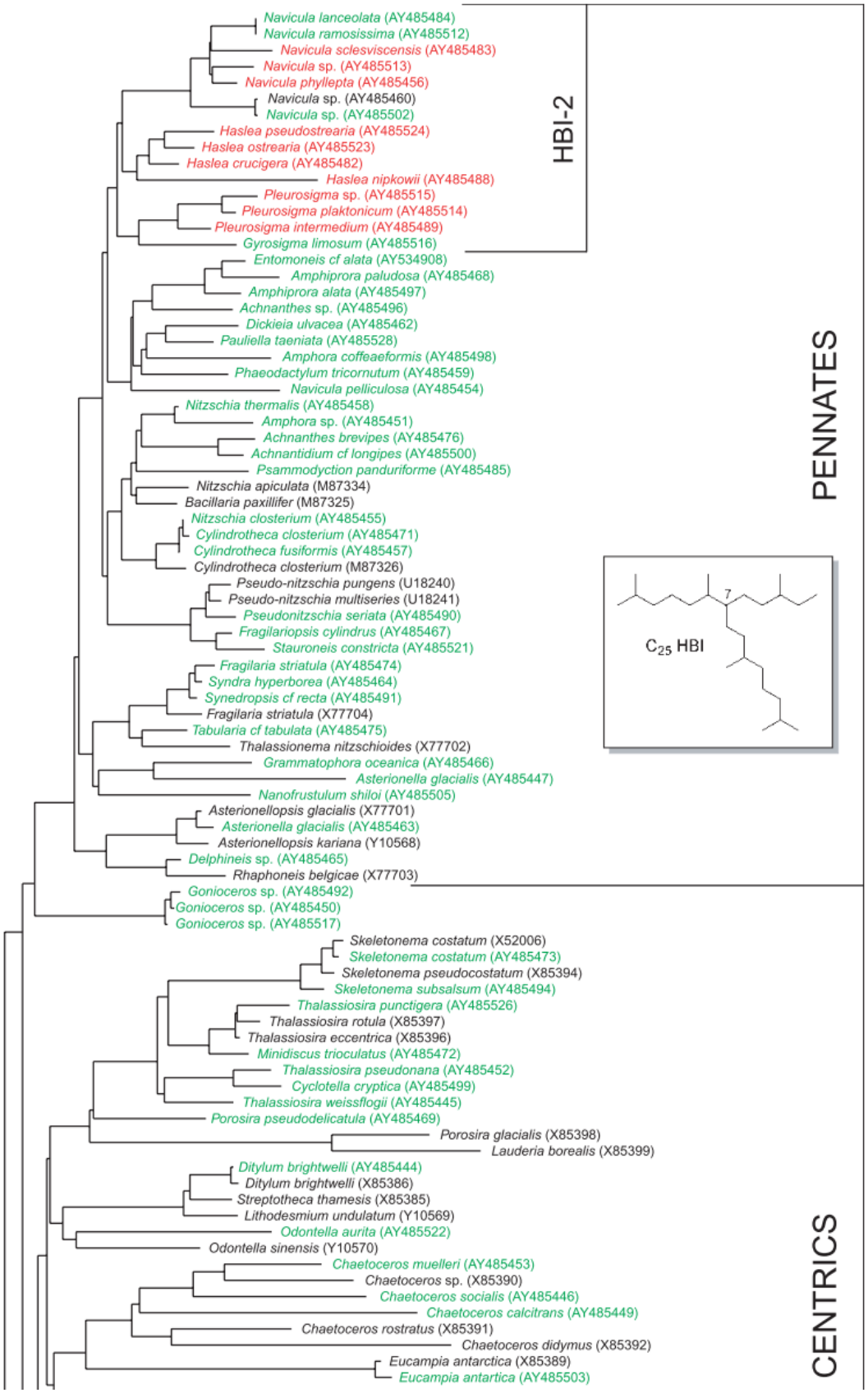

(Continued on next page)

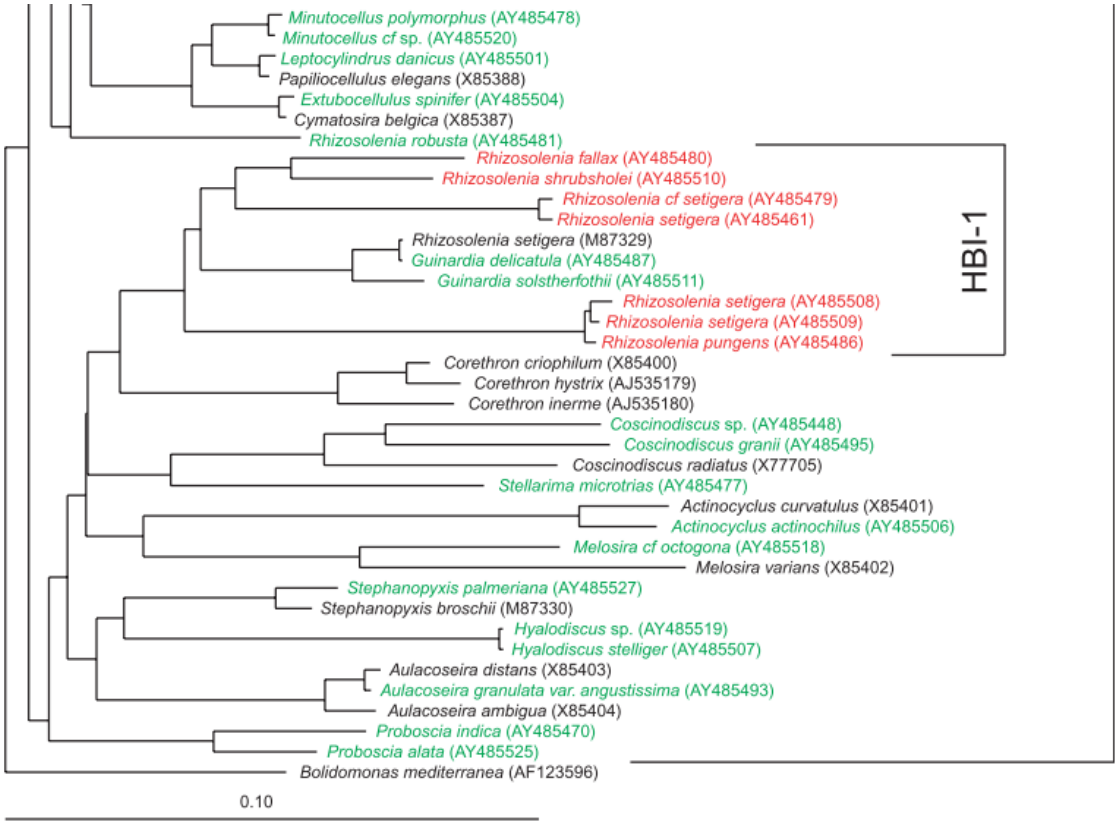

Figure 1-10. Phylogenetic tree based on nearly complete 18S rRNA sequences of diatoms. HBI-biosynthesizing strains are indicated in red. Diatoms in green were tested but did not contain HBI alkenes; diatoms in black were not tested for the presence of HBI alkenes. The scale bar indicates 10% sequence variation (Sinninghe Damsté et al., 2004).

Over the past two decades, the sources and structures of ca. 20 individual HBI lipid biomarkers have been reported, mainly following large-scale cultivation of individual diatom taxa and subsequent analysis of purified extracts using a combination of mass spectrometric (MS) and nuclear magnetic resonance (NMR) spectrometric methods. In particular, these investigations have enabled the number, position and stereochemistry of the double bonds to be determined.

The majority of C_{25} HBIs in sediments contain 2 to 5 double bonds, with minor mono- and poly-unsaturated isomers. Some relationships between the positions of the double bonds and the source diatoms have been identified. For example, generally, HBIs are biosynthesized by *Haslea spp*. possess a double bond in the C6-C17 or C5-C6 positions, while counterparts from *Pleurosigma spp*. usually contain double bonds between C7 and C20 (Figure 1-9 (b)). A further difference between HBIs from *Haslea spp.* with those from *Pleurosigma spp.* is that both E and Z stereoisomers are usually observed with HBIs from the latter genera. This unusual structural feature is also exhibited by C_{25} and C_{30} HBIs made by *R.*

setigera. The biosynthesis of HBIs by a limited number of diatom genera has also been demonstrated using molecular phylogeny techniques. Despite these advances in source identification and structural determination, the function(s) or role(s) of HBIs in diatoms remain unknown. What is clear, however, is that the source-specific nature of HBIs makes them potentially useful biomarkers for paleoenvironment studies. Despite the near-ubiquity of HBIs in marine and lacustrine locations worldwide, the sources and distributions of some HBIs make them good candidates for proxies of the Arctic and Antarctic sea ice, and in a range of different sea ice settings.

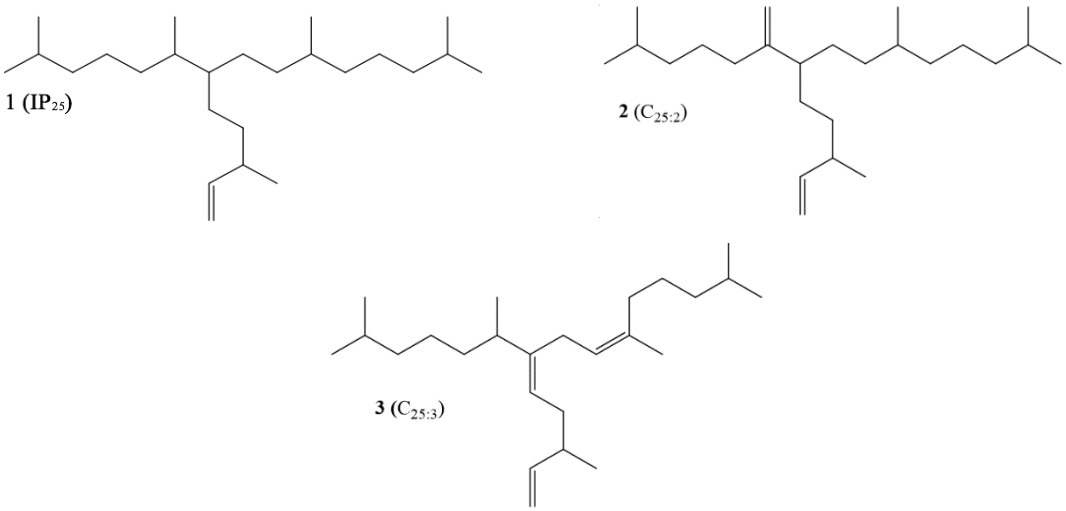

Figure 1-11. Structures of HBI biomarkers

1.6.1 The mono-unsaturated C_{25} HBI – IP_{25}

IP_{25} refers to Ice Proxy with 25 carbon atoms (Figure 1-11 (1)). It is a mono-unsaturated C_{25} HBI produced by certain Arctic sympagic diatoms but has thus far not been identified in the Antarctic. Since the initial discovery of IP_{25} (Belt et al., 2007), this biomarker has been identified in numerous Arctic and subarctic sea ice (e.g. Brown et al., 2014b, 2017), surface sediments (e.g. Müller et al., 2011; Smik & Belt, 2017; Xiao et al., 2015), and sediment trap (e.g. Fahl & Stein, 2012; Lalande et al., 2016) thereafter and used to indicate the presence of the Arctic sea ice.

It was not until Brown et al. (2014b) carried out the analysis of individual sympagic diatom species that confirmed the solid link between several diatom species and the production of IP_{25}. Three (or four) individual sympagic diatom taxa have been identified as producers of IP_{25} – *Pleurosigma stuxbergii* var.

rhomboides, *Haslea kjellmanii*, *H. crucigeroides* and/or *H.spicula*. Besides these, IP_{25} has not been identified in any other diatoms, whether sympagic, pelagic or lacustrine.

In spite of highly source-specificity, however, Belt et al. (2007) caution that IP_{25} can only be used as a binary or semi-quantitative sea ice indicator and more work needs to be done to quantify and characterise sea ice cover.

1.6.2 The di-unsaturated C_{25} HBI – HBI diene/$IPSO_{25}$

Another close structural analogue of IP_{25}, with an additional double bone, the di-unsaturated C_{25} HBI was first reported in Antarctic Sea ice and sediments by Nichols et al. (1988) (Figure 1-11 (2)). Unlike IP_{25} just found in the Arctic, it was also detected in the Antarctic and the source of $IPSO_{25}$ is less specific than that of IP_{25}, it has also been identified in the benthic diatom *Haslea ostrearia* (Jones et al., 1999) and in sediments from some temperate locations. Belt et al. (2016) identified the source of this di-unsaturated HBI - a common constituent of Antarctic sympagic diatom communities *Berkeleya adeliensis*, and introduced the term $IPSO_{25}$ (Ice proxy for the Southern Ocean with 25 carbon atoms), at least when it was detected in the Antarctic.

Massé et al. (2011) found $IPSO_{25}$ in nine sediment samples collected from two well-separated regions in the Antarctic. The stable carbon isotopic compositions ranged from -8.5‰ to -5.7‰, which were close to those reported previously in sediments from Ellis Fjord (-9.1‰ to -9.4‰) (Sinninghe Damsté et al., 2007). They suggested that the $IPSO_{25}$ in the Antarctic sediment originated from sea ice diatoms, where CO_2 supply was often limited (Belt et al., 2008; Gibson et al., 1999; Kennedy et al., 2002). In addition, the carbon isotopic signatures of $IPSO_{25}$ were greatly enriched in ^{13}C compared to other co-occurred polyunsaturated HBIs (-36.1‰ to -41.6‰), clearly indicating different environmental conditions/settings during the biosynthesis of HBI diene. Hence, Massé et al. (2011) hypothesized that the presence of $IPSO_{25}$ in the Antarctic sediments can indicate the contribution of organic matter derived from sea-ice diatoms.

Although the study by Massé et al. (2011) provided preliminary evidence of the biosynthesis of HBI diene in sea ice, on the whole, the sedimentary distribution

of this biomarker for paleo reconstructions in Antarctica is limited to a small number of surface sediments and water column samples. Despite this, a number of sea-ice reconstruction studies based on the variable abundance of HBI diene in Antarctic sediments have already begun to appear (e.g. Barbara et al., 2016; Barbara et al., 2010; Barbara et al., 2013; Campagne et al., 2015; Campagne et al., 2016; Collins et al., 2013; Denis et al., 2010; Etourneau et al., 2013).

1.6.3 The tri-unsaturated C_{25} HBI – HBI triene

A tri-unsaturated HBI, sometimes referred to as HBI III (Figure 1-11 (3)), has been linked with open-water (pelagic) conditions in both the Arctic and the Antarctic. Although a common constituent of marine setting, this HBI III is also showing potential as a proxy for the MIZ in both Polar Regions. The tri-unsaturated isomer (triene) may be biosynthesized within the open ocean areas of the marginal ice zone, near the sea ice edge (Collins et al., 2013; Denis et al., 2010; Etourneau et al., 2013).

1.6.4 Coupling biomarkers

Given the potential limitations of the HBIs mentioned above, new research is directed toward combining the HBI(s) with other sea ice proxies, including newly developing phytoplankton biomarkers, which can be used to identify ice-free or non-seasonal sea ice conditions.

Based on work in surface sediments from East Greenland and West Spitsbergen, Müller et al. (2011) pioneered a PIP_{25} index to be applied in ice-free regions. This index was a ratio of IP_{25} versus combined IP_{25} and phytoplankton biomarkers (Eqn. (1-1)) where the square brackets denotes concentrations. In their initial study, brassicasterol was used as a phytoplanktonic indicator, while they stated that it should also be feasible to determine related PIP_{25} indices using other marine biomarkers derived from organisms living in ice-free conditions. In addition, they noted that a balance factor c was required (Eqn. (1-2)) to compensate the distinctly higher phytoplankton biomarker content compared to the relatively low IP_{25} concentrations within sediments from East Greenland and West Spitsbergen.

Generally speaking, higher PIP_{25} values are consistent with frequent or extensive sea ice cover, intermediate PIP_{25} values imply marginal sea ice or ice edge conditions, and lower PIP_{25} indicates minimum sea ice coverage. The lower limit (PIP_{25} = 0) means the absent or below the detection limit of IP_{25}, which has been frequently interpreted as representing either ice-free or permanent ice cover conditions.

$$PIP_{25} = \frac{[IP_{25}]}{[IP_{25}]+c*[phytoplankic\ lipids]} \quad (1\text{-}1)$$

$$c = \frac{mean\ [IP_{25}]}{mean\ [phytoplankic\ lipids]} \quad (1\text{-}2)$$

To date, PIP_{25} has been tested and applied more recently by several other researchers. For example, Stoynova et al. (2013) analysed the biomarkers in surface sediments from regions of the Arctic and subarctic Atlantic and Pacific, and their results have shown a correlation between PIP_{25} and satellite-derived sea ice concentrations. While relatively poor correlations between near-surface PIP_{25} data and sea ice concentrations have been observed for the Barents Sea (Navarro-Rodriguez et al., 2013) and the Kara & Laptev Seas (Xiao et al., 2013).

Another combined approach is based on the observation of an HBI diene that co-occurs with IP_{25}. Vare et al. (2009) observed an extremely close correlation and similar isotopic compositions ($\delta^{13}C$= -19‰ to -21‰) of IP_{25}. Fahl & Stein (2012) suggested the use of a ratio of diene versus IP_{25} (DIP_{25}) and has been supported by Cabedo-Sanz et al. (2013) and (Xiao et al. (2013). Results from numerous studies are promising and suggest DIP_{25} values may be able to constrain sea ice conditions in highly variable local sites and its applicability to both Antarctic and Arctic Sea ice environments has started to fuel research into possible global-scale sea ice reconstructions.

In addition, the ratio of diene versus triene has been used as a proxy for the ratio of sea ice to the open ocean surrounding the west Antarctic Peninsula (Etourneau et al., 2013) and the Scotia Sea (Collins et al., 2013).

Recently, Smik et al. (2016) used HBI triene as the phytoplankton biomarker in PIP_{25} calculations rather than sterols. Postulating that it could provide more quantitative paleo Arctic Sea ice reconstructions due to its similar stereochemical configuration and closer concentration to IP_{25}.

1.7 Isotope geochemistry in sea-ice reconstructions

1.7.1 The background of isotopes

Isotopes are atoms of the same element which contain the same numbers of protons and electrons but different neutrons. Each atom has a nucleus containing positively charged proton(s) in the centre and electron(s) which carries the same number of negative charges orbiting around. While in some elements, there are also uncharged particles called neutrons in the nucleus. The mass of the electron can be negligible while the mass of a neutron is similar to the proton and considerably greater than the electron and together, they make up the mass of the atom. Hence, isotopes of an element are chemically identical while differing in atomic mass. As the isotopes are unevenly distributed among and within different compounds, this isotopic distribution can reveal information about the physical, chemical, and metabolic processes involved in element transformations.

The relative abundances of stable isotopes are usually expressed as a ratio of heavy isotope (^{h}X) versus light isotope (^{l}X), e.g. $^{2}H/^{1}H$, $^{13}C/^{12}C$. As the variations in isotope ratios are small and measured against standards of known isotopic composition, the isotopic compositions of natural materials are reported as a delta value $\delta^{h}X$ in parts per mil (‰).

$$\delta^{h}X = (\frac{R_X}{R_{std}} - 1) \times 1000,\ R_X = {}^{h}X/{}^{l}X \quad (1\text{-}3)$$

Where a positive $\delta^{h}X$ means the sample is enriched in the heavy isotope relative to the standard and a negative refers to the sample being depleted in the heavy isotope.

The difference in δ-value after a physiochemical process is called isotopic fractionation, which can occur during chemical reactions, phase changes and molecular diffusion. The fractionation factor (α) is defined as:

$$\alpha = \frac{R_{products}}{R_{reactants}} \quad (1\text{-}4)$$

It describes the degree of depletion in the instantaneous product of a reaction. Another parameter called isotope effect or enrichment factor (ε) is also commonly used to report the changes in isotopic composition associated with a reaction.

$$\varepsilon = \delta_{products} - \delta_{reactants} \text{ (1-5)}$$

If the fractionation factor differs from 1 by less than 5‰, it can also be described as:

$$\varepsilon \approx (\alpha - 1) \times 1000 \text{ (1-6)}$$

1.7.2 Hydrogen isotopes and hydrologic cycle

The hydrologic cycle can be investigated by using the isotopes of hydrogen and oxygen. Due to a relatively larger molecular mass, the heavier isotopes have lower vapor pressures than the lighter ones, resulting in an enrichment of ^{2}H and ^{18}O in the ocean compared to the atmospheric water vapor. In turn, the air becomes progressively depleted in ^{2}H and ^{18}O. Hydrologic activities such as rainfall and evaporation influence the hydrogen and oxygen isotopic composition of the environmental water. Hence, paleo archives records, such as continental ice cores, are critical tools to reconstruct the hydrological cycle over a range of geological timescales. Suitable sites for ice-core drilling are, however, constrained to the high-latitude regions of Earth, which significantly limit our understanding of linkages between continental hydrology and global paleoclimate.

Since environmental water is the sole source of hydrogen of photo-autotrophic organisms, the organic matter, mainly lipids, produced by phytoplankton is highly correlated with the stable hydrogen isotope ratio ($^{2}H/^{1}H$) of environmental water. Organic matter in sediments is, however, a highly complex mixture of various organic compounds produced by different organisms via varying biosynthetic pathways. The varying composition of individual lipids can result in a considerate difference in the isotopic composition of bulk sedimentary organic matter and highly hinders the function of it as a robust palaeohydrological proxy.

1.7.3 Compound-specific isotope measurements

Advances in gas chromatography and mass spectrometry (GC-MS) in the 1990s made it possible for the very first time to analyse the $\delta^{2}H$ compositions on an individual lipid level. Since then, the hydrogen isotope composition of the lipid biomarkers (fatty acids, wax esters, ketones, hopanols, sterol, etc) in marine and lacustrine sediments are increasingly being applied to reconstruct the water cycle and paleoclimate.

In the past few decades, the hydrogen isotope composition of alkanes and fatty acids from the waxy coating of vascular plant leaves has been well studied owing to its relatively high yield, which significantly reduces the difficulty in δ^2H values measurement. However, since almost all plants can produce the same wax lipids, this ubiquity remarkably limits their functions in interpreting environmental conditions.

The lipids from algae, on the other hand, though of low biomass, can be quite source specific to the class, genus or even on a species level. And more importantly, based on previous studies, the hydrogen isotope composition of these compounds changes dramatically in responding to certain growth conditions including salinity, temperature, growth rate, irradiance, growth phase.

This allows culture and field-based calibrations of the H isotope response to a variety of environmental conditions to be applied in interpreting microalgal lipids δ^2H values. Quantitative reconstructions of the δ^2H value of environmental water, which can be used in hydrological and climate models, are therefore possible.

1.7.4 Carbon isotopes and environments

The overall abundance of ^{13}C relative to ^{12}C in plant tissue is commonly less than in the carbon of atmospheric carbon dioxide, indicating that carbon isotope discrimination occurs in the incorporation of CO_2 into plant biomass.

Because the isotopes are stable, the information inherent in the ratio of abundances of carbon isotopes, presented by convention as $^{13}C/^{12}C$, is invariant as long as carbon is not lost.

Numerous contributions have been made to our understanding of carbon isotope discrimination in plants since this area was extensively reviewed by (O'Leary, 1988). Here we discuss the physical and enzymatic bases of carbon isotope discrimination during photosynthesis, noting how knowledge of discrimination can be used to provide additional insight into photosynthetic metabolism and the environmental influences on that process.

1.8 Innovation and significance of study

The reconstruction and prediction of the sea ice have been a key challenge for Earth Science. One of the best tools to date to address this challenge is modelling, however, it relies on instrumental observations which just developed in recent decades. A better understanding of the mechanism behind the sea ice dynamics requires more information about past sea ice extent, thickness and other characteristics on a much longer time scale.

Owning to the source-specificity and stability, HBIs hold the potential to serve as binary or, to the best of our knowledge, semi-quantitative proxies to indicate sea ice. In our study, we attempt to characterise the hydrogen and carbon isotopic compositions of HBIs from laboratory cultured HBI-producers under various light conditions. This is also the first attempt to test the effect of irradiance on hydrogen and carbon isotopic compositions of HBIs.

As sea ice directly determines the light intensity underneath, and further influences the photosynthesis rate of the phototrophic organisms, we hypothesize that the variable light conditions, particularly in the range of naturally occurring conditions between nearly-0 to 200 μmol m^{-2} s^{-1}, will affect the isotopic signatures of HBIs (Figure 1-12). The outcomes of this study will thus form the foundation of a novel proxy for reconstructing more detailed sea ice conditions in the past.

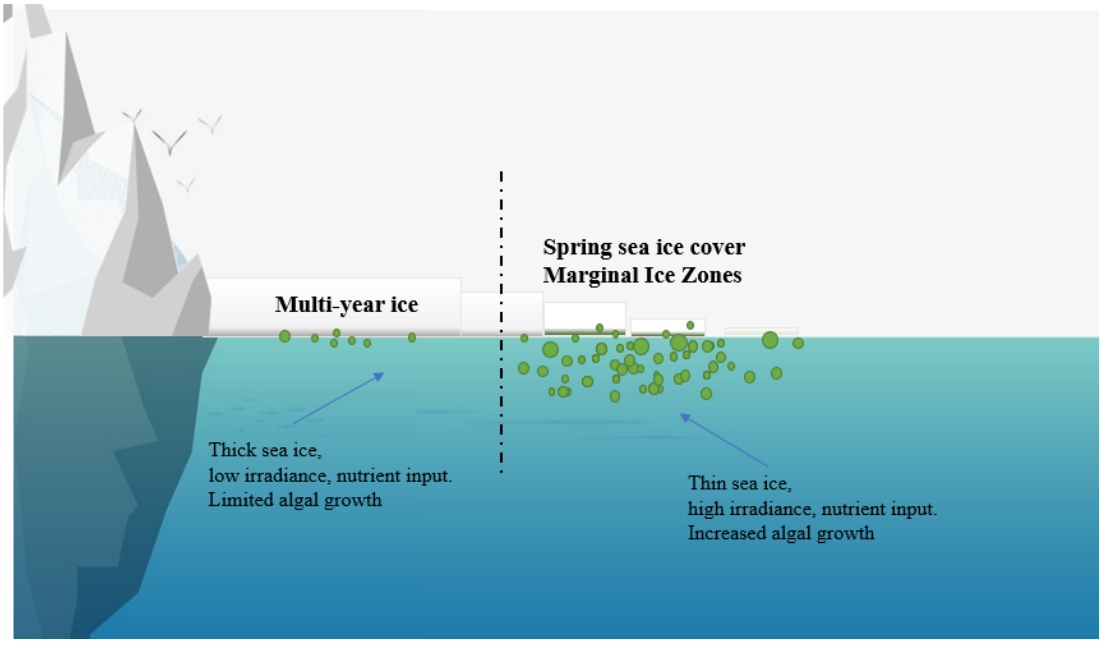

Figure 1-12. Graphical abstract illustrating how the results presented in this study are related to the physical Arctic sea ice environment. Green ovals represent the volume of diatom biomass.

The development of a novel method for identifying variable light transmission through sea ice will positively impact our understanding of related environmental parameters (e.g. ice thickness, under-ice phytoplankton blooms, cloud cover and precipitation) that are currently undergoing rapid change in the polar regions but are extremely poorly understood in the paleo record.

More importantly, this study not only focuses on HBIs but also on more common algal biomarkers such as fatty acids, phytol and sterols. As fatty acids, phytol and sterols are produced by the 3-PGA and/or G3P as the last common precursors from photosynthesis then via three main lipid biosynthesis pathways.

Incorporation of the results of different lipid classes from a series of culture experiments in two species along the light gradients will provide new insights into the fundamental mechanisms which are responsible for determining isotopic compositions of lipids not only in algae but also in other photosynthesising organisms. This will also enhance the use of biomarker-based approaches for reconstructing past climate conditions on Earth.

1.9 Thesis outline

This thesis compromises seven chapters.

Chapter ONE describes the background of this study (**1.1**), sea ice dynamics (**1.2**), how sunlight influences the sea ice (**1.3**), and sea ice as a habitat for primary producers (**1.4**). Various proxies for sea ice reconstructions are introduced in **1.5** and the role of highly branched isoprenoids (HBIs) as geochemical tracers is highlighted in **1.6**. As the application of HBIs has certain limitations, **1.7** demonstrates the incorporation of isotopes in sea ice reconstruction. Chapter one ends with the innovation and significance in **1.8** and the thesis outline in 1.**9**.

Chapter TWO describes the laboratory experiments including the algal culture (**2.1**) and lipids extraction process (**2.2**) and instrumental analysis including gas chromatography–mass spectrometry (GC-MS) screening (**2.3**) and compound-specific stable isotope analysis (CSIA) (**2.4**) in this study.

Chapter THREE is the first result chapter. The effect of light on photosynthesis is first introduced in **3.1**. The results of the growth rate of three marine diatom strains (**3.2**) and lipid concentration of *Pleurosigma intermedium* (**3.3**) and *Rhizosolenia setigera* (**3.4**) are presented, followed by the detailed discussion and conclusion in **3.5** and **3.6**.

Chapter FOUR presents the results of hydrogen isotopic compositions of algal lipids in response to varied irradiance. It begins with the introduction of light-dependent reactions (the first stage) of photosynthesis and three main biosynthesis pathways in **4.1** and the factors controlling hydrogen isotope fractionation in the phototrophic organism in **4.2**. The hydrogen isotopic compositions of algal lipids isolated from *P. intermedium* and *R. setigera* are presented in **4.3** and **4.4** respectively, followed by the discussion and conclusion in **4.5** and **4.6**.

Similarly, Chapter FIVE presents the results of carbon isotopic compositions of algal lipids in response to varied irradiance. It begins with the introduction of the Calvin Cycle (the second stage) of photosynthesis in **5.1** and the factors controlling hydrogen isotope fractionation in the phototrophic organism in **5.2**. The hydrogen isotopic compositions of algal lipids isolated from *P. intermedium* and *R. setigera*

are presented in **5.3** and **5.4** respectively, followed by the discussion and conclusion in **5.5** and **5.6**.

Chapter SIX is a relatively independent chapter, compromising the detection and the identification of the structure of a new HBI produced by laboratory cultured *Navicula salinicola*. The identifications of several HBIs from different diatom species are briefly introduced in **6.1**. The detailed strain information of *N. salinicola* including sample collection, preparation and identification are described in **6.2**. the cultural techniques are introduced in **6.3**. following by the results and discussion in **6.4** and the conclusions in **6.5**.

Chapter SEVEN includes the conclusions in **7.1** and further work in **7.2**.

2 Methodology

Chapter 2 describes the experimental procedures and analytical processes conducted to obtain the data required to achieve the objectives of the projects as described in Chapter 1.

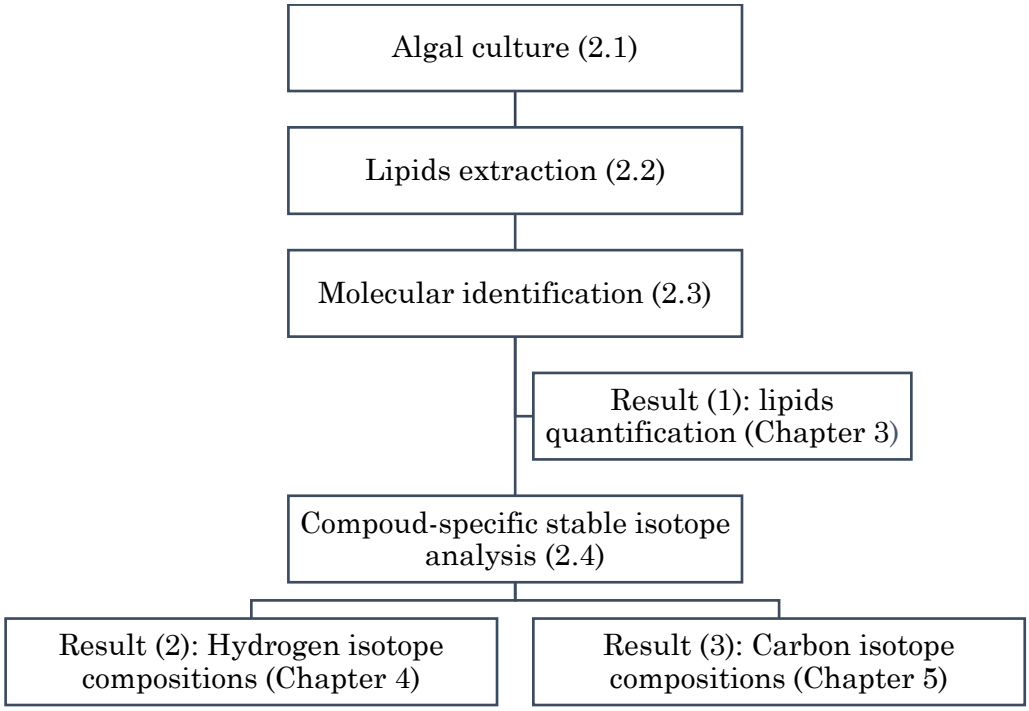

Figure 2-1. Schematic figure showing the experimental procedures and analytical processes described in Chapter 2 and related results in following chapters.

To be specific, **2.1** describes the source of each strain being cultured in this project and the cultural methods. The extraction and purification processes are demonstrated in **2.2**, followed by a description of Gas Chromatography–Mass Spectrometry (GC-MS) for molecular identification (**2.3**). By comparing the peak area of an internal standard, the concentration of the target compounds can be calculated, giving the Result (1) in Chapter 3. Last but not least, samples were then applied to Gas Chromatography – isotope ratio mass spectrometry (GC-IRMS) for the Carbon and Hydrogen isotope measurements. Detailed instrumental parameters and data normalization are introduced in **2.4**. As Hydrogen and Carbon isotope analysis was carried out independently, the results are referred to the relevant chapters (Hydrogen in Chapter 4 and Carbon in Chapter 5).

Most of the methods used in this thesis are adopted and modified from previous studies. The description of methods includes aspects of instrumentation and laboratory operating conditions, in addition to chemical identification and quantification.

2.1 Laboratory algal culture

As introduced in **section 1.6**, only a relatively small number of marine and freshwater diatoms belonging to the *Haslea*, *Navicula*, *Pleurosigma*, *Rhizosolenia* and *Berkeleya* genera can potentially biosynthesis HBI(s). In this study, marine diatoms *Pleurosigma intermedium*, *Rhizosolenia setigera* and benthic diatom *Navicular salinicola* were cultured under laboratory conditions and the HBIs from these strains are listed in Table 2-1.

Table 2-1. Cultural condition, strain information and the associated HBIs of diatom *Pleurosigma intermedium*, *Navicula salinicola* and *Pleurosigma intermedium*.

Name	Strain	Laboratory	Medium	Temp. (°C)	HBIs
Pleurosigma intermedium	RCC 6814	Roscoff culture collection	f/2	15	C25:5
Rhizosolenia setigera	CCMP 1130	Bigelow National Centre for Marine Algae and Microbiota	L1	8	C25:3, C25:4
Navicular salinicola	BTD 1	Laboratory of Molecular Taxonomy of Aquatic Plants Institute of Plant Physiology, Russian Academy of Science	f/2	15	C25:3, C25:2

2.1.1 Strain information and initial treatment

2.1.1.1 *Pleurosigma intermedium* (RCC 6814)

Elongated Diatom *P. intermedium* (RCC 6814) and the initial culture medium were obtained from Roscoff Culture Collection. *P. intermedium* was sampled in Penzé estuary, English Channel, Atlantic Ocean using filters with different mesh sizes with a sampling temperature of 17 °C on the 16th of June 2018, then cultured in f/2 medium under the irradiance of 100 µmol m^{-2} s^{-1} and room temperature of 16 °C at Roscoff Culture Collection.

When culture and culture medium arrived, *P. intermedium* was carefully transferred into the initial medium and stabilized for two weeks. During this period, the temperature was set to 15 °C and irradiance was lowered to approx. 40 µmol m^{-2} s^{-1}. 2 mL of subsample was taken on a daily basis for the measurements of Maximum Quantum Yield of PS-II (fv/fm) by a Multi-wavelength Pulse Amplitude Modulated fluorometry (Phyto - PAM) and microscopic observation.

Once the cells began to reproduce, *P. intermedium* was then transferred into an f/2 enriched natural seawater medium (Guillard & Ryther, 1962). The irradiance was gradually increased while the temperature remained constant at 15 °C. This process has been repeated several times until the value of fv/fm was stable at ca. 0.8. Eventually, *P. intermedium* was maintained in our laboratory at 15 °C, 100 μmol m^{-2} s^{-1} and ready for further culturing experiments.

2.1.1.2 *Rhizosolenia setigera* (CCMP 1330)

Centric diatom *Rhizosolenia setigera* (CCMP 1330) was obtained from the Bigelow National Centre for Marine Algae and Microbiota (NCMA). It was initially collected from Vineyard Sound, Martha's Vineyard, Massachusetts, North Atlantic (approx. 41.9 °N – 70.8 °W) and isolated in 1959. Bigelow used an L1 medium and a culturing temperature of 2 °C for maintenance. The latest testing date of this strain was the 22nd of August in 2006.

Similar treatment with *P. intermedium*, *R. setigera* was carefully transferred into a fresh medium bought from Bigelow and stabilized for two weeks. *R. setigera* was then transferred into L1-enriched natural seawater (Guillard & Ryther, 1962). We increased irradiance and dropped temperature gradually each time transferring culture into the new culturing flask. Eventually, R. setigera was maintained in our laboratory at 8 °C, 100 μmol m^{-2} s^{-1} and ready for further culturing experiments.

2.1.1.3 *Navicular salinicola*

Benthic diatom *N. salinicola* was collected from a coastal marine environment (M. Kulikovskiy, June 2016 at Nha Trang, Vietnam, 12°13'14.5"N 109°12'18.3"E) and kept as strain BTD 1 in the Laboratory of Molecular Taxonomy of Aquatic Plants Institute of Plant Physiology (RAS).

The same treatment with *P. intermedium* was applied to *N. salinicola*. It was maintained in our laboratory at 15 °C, 100 μmol m^{-2} s^{-1} and ready for further culturing experiments.

2.1.2 Microscopy

As mentioned in 1.5.1.2, one of the most unique features of diatom anatomy is that they have a transparent cell wall called frustule which is made of hydrated silicon dioxide. The frustule is composed of two valves that fit into each other like a pill capsule.

Microscopic observation plays an important role in the identification, classification, and monitoring of diatoms. Diatoms are normally divided into two main Orders, which include the Pennales and the Centrales. Pennales are pen-shaped and bilaterally symmetrical (e.g. Figure 2-2 (a)) while Centrales always in a cylindrical shape (e.g. Figure 2-2 (b)). Some diatoms may aggregate during the growth (e.g. Figure 2-2 (c)).

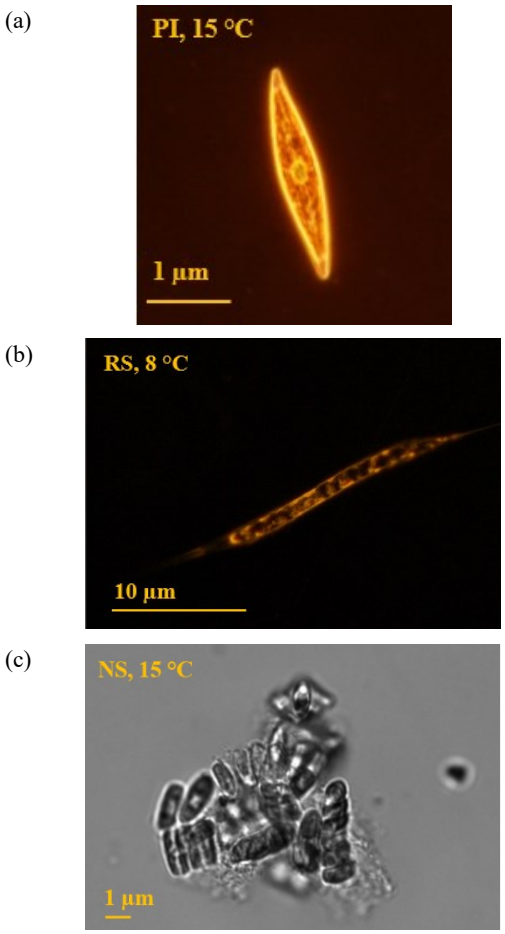

Figure 2-2. The microscopic images of marine diatoms *Pleurosigma intermedium* (a); *Rhizosolenia setigera* (b) and *Navicula salinicola* (c) (author's work; origin: Henry Wellcome microscopic lab, University of East Anglia)

2.1.3 Nutrient-limited light-controlled culture experiment

Ideally given suitable growth conditions such as moderate temperature and salinity, and adequate supply of light and nutrient, algae can grow exponentially at a growth rate of 0.3 to 1 generation per day (Kaiser et al., 2011).

While in laboratory conditions, the growth rate can be expressed by the net changing rate of the increase by reproduction and the decrease by death. Generally speaking, exponential growth ends up by the depletion of essential nutrients. And then stationary phase is reached when the reproduction rate equalise the death rate. it should be noted that even with no net change in cell numbers, algae continues to grow and dead in dynamic balance. Eventually, the death cells outnumber of the living cells and that is the time the stationary phase ends (Figure 2-3).

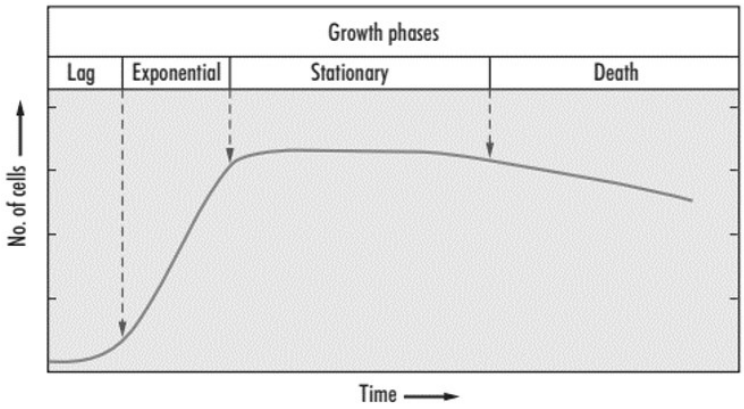

Figure 2-3. Idealized growth curve for a phytoplankton population, from (Kaiser et al., 2011)

In this study, the impact of salinity, temperature and nutrient are beyond the scope. Hence, we trend to set up experiments with suitable temperature and medium and let the growth of laboratory cultured algae being mostly limited by the level of light. The effect of nutrients and light on algal growth can be described by a Michaelis-Menten relationship (Figure 2-4). The increases in nutrient concentration will add progressively less to the growth rate until the maximum growth rate is reached. To equalise the effect of nutrients towards the growth of

diatom in different levels of light intensity, a series of so-called nutrient-limited light-controlled culture experiments were set up.

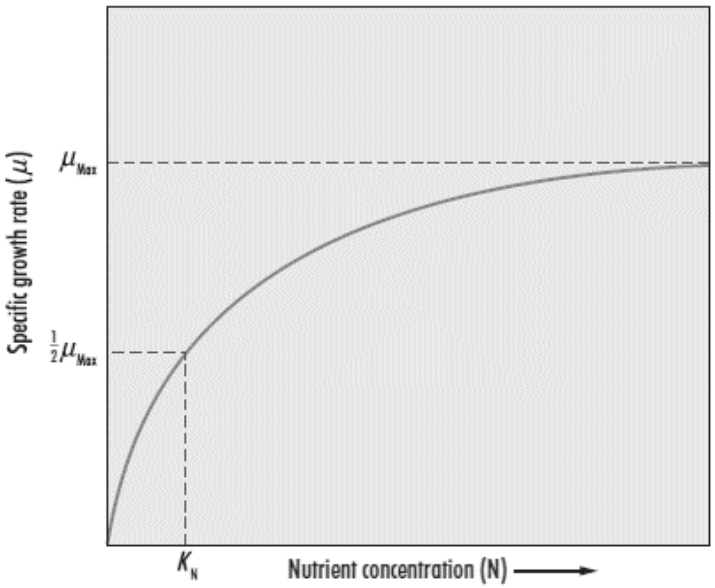

Figure 2-4. Relationship between nutrient concentration (N) and the growth rate of a primary producer. μ_{max} is the maximum growth rate, K_N the nutrient concentration at which growth rate is half the maximum (0.5 μmax)—the half-saturation constant. From (Kaiser et al., 2011)

A reduction of the concentration of nitrate while a doubling of Na_2SiO_3, NaH_2PO_4 and trace metal were applied to ensure that the stationary phase was caused by the unavailability of nitrate. It should be noticed that the reduced amount of nitrate would not affect the growth rate but only limit the yield of biomass (Kaiser et al., 2011). Ultimately, a natural sea water-based nitrate-limited medium with the concentrations of each nutrient 100μM $NaNO_3$, 212 μM Na_2SiO_3 and 72.4μM NaH_2PO_4 was used.

The irradiance gradient was achieved by wrapping the culturing flasks with a series of neutral density lighting gels (produce by Stage Depot limited, specifications No. 299, 201, 211, 210 and 298). The gels can lessen certain overall light output of the source light without altering the colour by adjusting the percentage of light pass through.

Prior to the light experiments, a light sensor QSL 2101-10290 which is a Teflon TM sphere in 1.9 cm diameter on a 25 cm rigid light pipe produced by Biospherical Instruments Inc. co-operated with an output software Logger 2100 was used to measure the overall irradiance.

The area with stable light condition were marked. Once cultured flasks being placed, irradiance inside the flask would be measured 3 times with a stand deviation below 3 μmol m^{-2} s^{-1}, giving the irradiance gradient of 20, 40, 80, 150, 200, 300 (±3) μmol m^{-2} s^{-1}.

R. setigera was cultured at 8 °C while *P. intermedium* was 15 °C. An orbital shaker at 180 rpm was also applied to reduce the potential aggregation of *P. intermedium*. Both *R. setigera* and *P. intermedium* were grown in 250 mL conical flasks and for each light level, three biological replicates were conducted to capture the random biological variation (Figure 2-5). To obtain enough biomass for further isotopic measurements, light-controlled growth experiments have been repeated for several rounds.

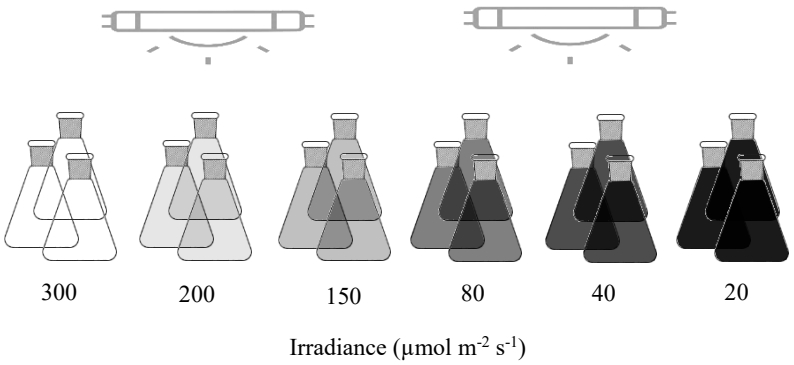

Figure 2-5. A schematic diagram of light-controlled culture experiments. The irradiance gradient (20, 40, 80, 150, 200, 300 μmol m^{-2} s^{-1}) was achieved by wrapping the culturing flasks with a series of neutral density lighting gels which can reduce the light stops without changing colours. For each light level, three biological replicates were conducted.

2.1.4 Growth monitoring

Subsamples (ca. 2 ml) were taken daily for the measurements of the Maximum Quantum Yield of PS-II (Fv/Fm) by Phyto - PAM. Biomass was estimated by measuring the chlorophyll a (Chl a) concentrations *in vivo* fluorescence between 460 nm to 670 nm using the SpectraMax® iD3 Multi-Mode Microplate Reader in a relative fluorescence unit. Growth rates (μ, d^{-1}) were determined using the endpoints of the exponential phase of the growth curves (by curve fitting) and the growth rate equation (2-1).

$$\mu = \frac{ln\frac{N_t}{N_0}}{t} \quad (2\text{-}1)$$

Where N_t and N_0 are the fluorescence values at the end and beginning of exponential phase, and t is the time (day) (Figure 2-6).

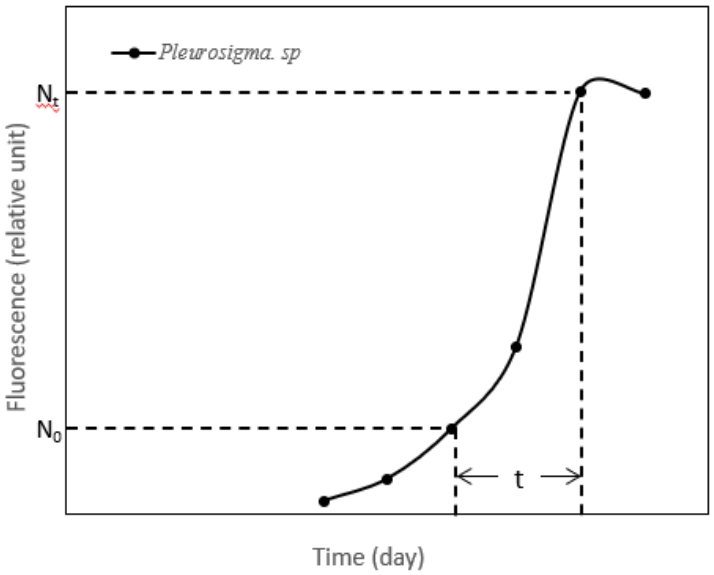

Figure 2-6. A schematic diagram of the growth curve of *P. intermedium*. N_t and N_0 are the fluorescence values (in a relative fluorescence unit) at the end and beginning of exponential phase, and t is the time (day).

2.1.5 Harvest and storage of samples

A ca. 100 mL aliquot was firstly collected from each culture flask and stored in 50 mL acid-washed polypropylene tubes when diatoms reached the exponential phase. The rest of the sample would continue growing until reaching the stationary phase.

For the harvest of each sample, the culture medium would first be removed by centrifugation (4000 rpm, 10 mins). Concentrated samples would then be transferred into 2 mL micro-centrifuge tubes and centrifugated at a higher speed (15000 rpm, 2 min) and stored at -80°C for further lipids extraction.

2.2 Lipids extraction

Before the extraction procedure, it is vital to remove the potential organic matter from the glassware by combustion at 800°C for at least 5 hours. A schematic showing the lipids extraction steps undertaken during the analysis of phytoplankton samples is given in Figure 2-7.

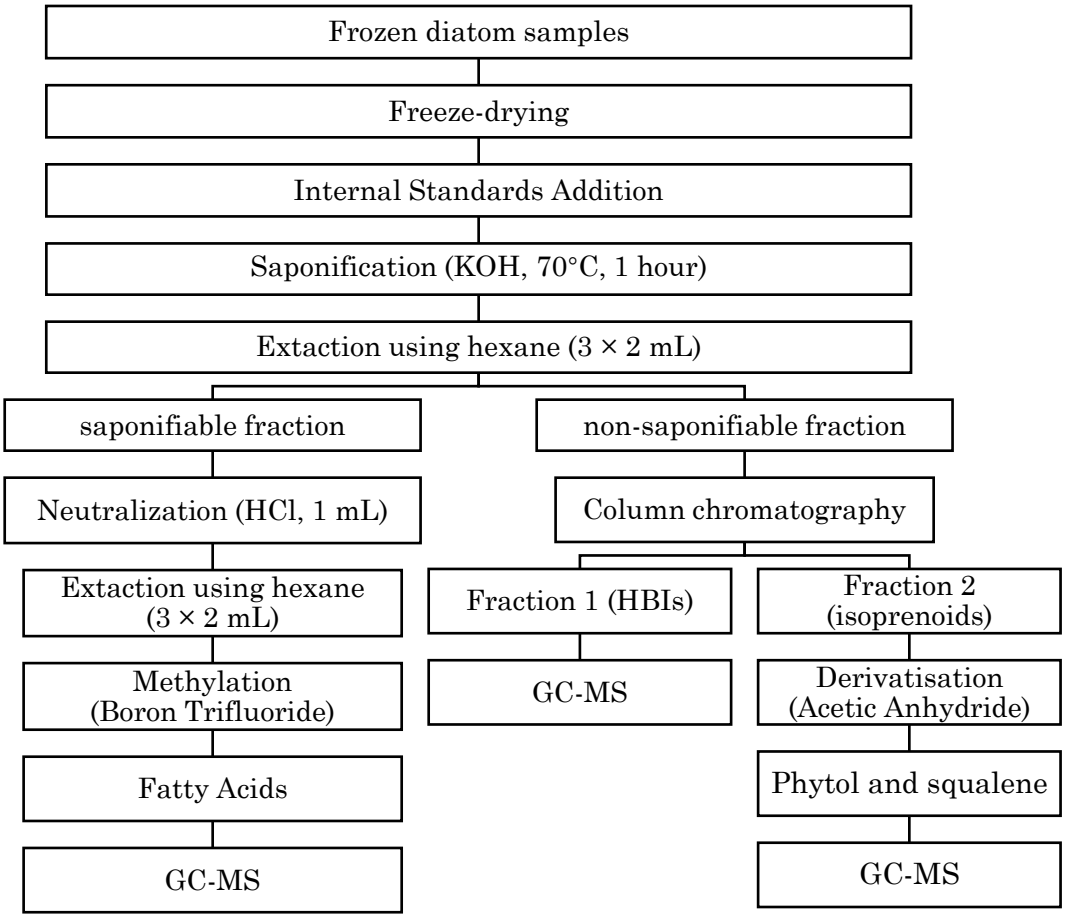

Figure 2-7. A schematic diagram of the lipid extraction steps. Each step including freeze-drying, internal standards addition, saponification, neutralization, Column chromatography, methylation and derivatisation will be demonstrated in the following subsections.

2.2.1 Freeze-drying

The centrifuged samples were freeze-dried in the geochemistry laboratory in University of East Anglia using a ScanVac CoolSafe 4-15 L freeze-dryer. Samples were freeze-dried at -106 ºC and 0.008 – 0.009 hPa for 24-48 hours, depending on the quantity of samples being dried.

The dried sample was then carefully moved into a 4 mL glass vial which had been weighed out (m_g) in advance. The total mass (m_t) was then weighed out using the same methods, giving the net mass of the diatom sample (m_n) by using the equation (2-2) below,

$$m_n = m_t - m_g \quad (2\text{-}2)$$

2.2.2 Internal standards for lipid quantification

Three internal standards were added to quantify the target compounds respectively. To specify, 9-octylheptadec-8-ene (9-OHD, 20 µL; 10 µg mL^{-1}; Figure 2-8 (a)) was added to allow for quantification of HBIs, 5α-androstan-3ß-ol (20 µL; 1 µg mL^{-1}; Figure 2-8 (b)) was added for quantification of sterols, and nonadecanoic acid (10 µL; 1 mg mL^{-1}, Figure 2-8 (c)) was added for quantification of fatty acids.

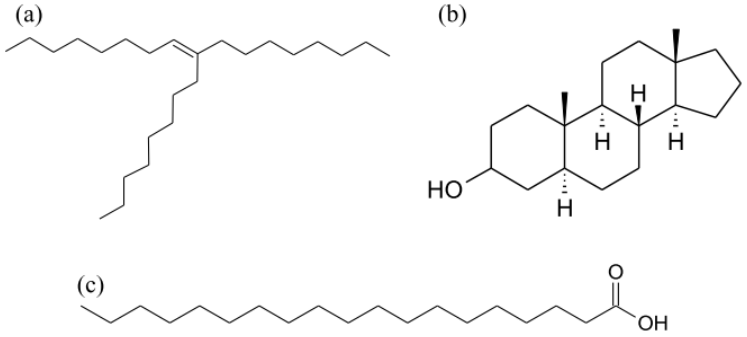

Figure 2-8. Chemical structures of internal standards used for biomarker quantification: (a) 9-octylheptadec-8-ene (9-OHD); (b) 5α-androstanol-3ß-ol; and (c) nonadecanoic acid.

2.2.3 Saponification of fatty acid triglyceride esters

Following the addition of internal standards, freeze-dried samples were saponified with ca. 3 mL methanolic potassium hydroxide (KOH, 5%; MeOH/H_2O, 90/10, v/v) in a 4 mL glass vial capping by a solid top with aluminium lined phenolic screw cap then heated in 70 °C for 1 hour using a heating block. Parafilm Laboratory Sealing Film was applied to prevent the potential leakage of the MeOH vapour.

After samples cooled down to room temperature, the non-saponifiable fraction, including HBIs and sterols, were first extracted by adding 2 mL hexane, vertexing for 1 min and centrifuging at 1500 rpm for 2 mins and transferring to a clean 8 mL vial using a glass pipette. The process was repeated 3 times.

The saponifiable fraction, mainly fatty acids, was first neutralized by adding 1 mL concentrated HCl (35.0-36.6%). Decanted supernatant containing fatty acids was then extracted with hexane using the same method and transferred to a clear 8 mL vial for further methylation.

2.2.4 SiO_2 chromatography column

Following the extractions by hexane, the solvent of the non-saponifiable fraction was removed under a mild helium flow. Before GC-MS analysis, the extracts required partial purification by a SiO_2 chromatography column. The column was made of a glass pipette containing a small plug of glass wool on the bottom and deactivated chromatography grade silica (non-dried, ambient moisture, ca 0.7g; 60-200 μm). The silica was pre-conditioned with ca. 3 mL hexane to homogenise the stationary phase (Figure 2-9).

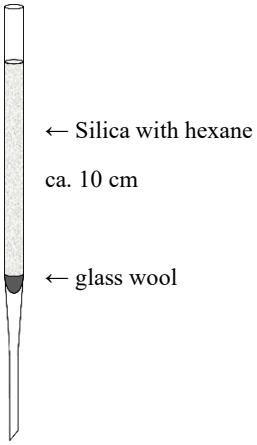

Figure 2-9. A schematic diagram of the SiO_2 chromatography column. The column was made of a glass pipette containing a small plug of glass wool on the bottom and deactivated chromatography grade silica with hexane (ca. 10 cm).

Once the column was stuffed, the dried extracts were re-suspended in ca. 1 mL hexane and sonicated for 3 minutes, then transferred into the SiO_2 column. HBIs (fraction 1) were firstly eluted by ca. 8 ml hexane. The solvent was then removed under a mild helium flow giving a concentration of HBIs down to ca. 150 μL in a glass-inserted 2 mL vial. The HBIs were then ready for GC-MS analysis. Following fraction 2 with phytol and squalene were eluted with ca. 8 ml methanol and kept in a clear glass vial for further purification.

2.2.5 Methylation of fatty acids

Following 2.3.2, the saponifiable fraction containing fatty acids was subjected to a mild helium flow until the solvent was evaporated just to dryness. 500 μL boron trifluoride methanol solution ($BF_3 \cdot CH_3OH$, 14% in methanol) was added into the vial and capped by a solid phenolic screw cap with aluminium lined. Parafilm Laboratory Sealing Film was applied to prevent the potential leakage of methanol vapour. The reaction would be taking ca. 30 minutes at 75°C to complete. 1 mL of hexane was then added into the vial and shaken vigorously by hand for 30 seconds and allowed to stand for 10 minutes to separate into aqueous and hexane phases. The hexane phase containing fatty acids was transferred into a 2 mL vial and the solvent was removed under a mild helium flow. Due to a relatively high concentration of fatty acids, the samples need to be diluted 100-1000 times before further analysis.

2.2.6 Derivatisation of sterols

Fraction 2 was subjected to a mild helium flow until the solvent was evaporated just to dryness. 200 μL each of acetic anhydride and pyridine were added into the vial. The mixture was agitated to ensure homogenization of the reactants. The reaction was carried to completion at 75°C overnight. 800 μL of 4 M HCl and 1 mL of hexane were then added to the vial and shaken vigorously by hand for 30 seconds and allowed to stand for 10 minutes to separate into aqueous and hexane phases. The hexane phase containing sterols and other isoprenoids was transferred into a 2 mL vial and the solvent was removed under a mild helium flow giving a concentration of sterols down to ca. 150 μL in a glass-inserted 2 mL vial. The samples were then ready for further analysis.

A schematic figure of the individual step of the extraction and partial purification procedure can be seen in Figure 2-10.

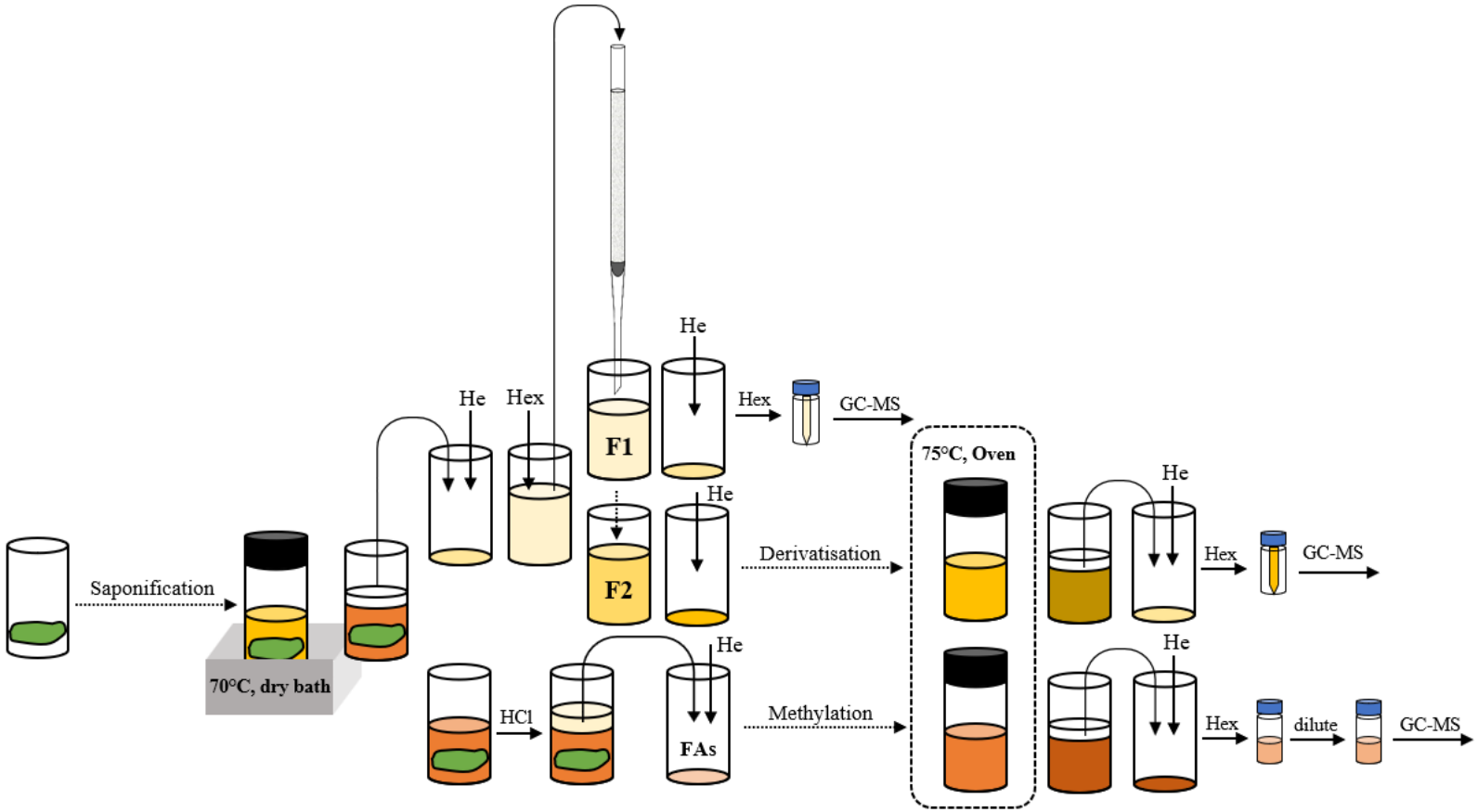

Figure 2-10. A schematic figure showing individual step of the extraction and partial purification of laboratory cultured samples.

2.3 Gas Chromatography – Mass Spectrometry (GC-MS) for molecular identification

2.3.1 GC-MS analysis

Prior to GC-MS analysis, samples containing analytes of interest were transferred to GC-vials and diluted to an appropriate concentration (100 – 500 μL). All of the fractions were analysed by GC-MS using a Thermo Scientific Trace 1300 gas chromatograph equipped with an HP-5ms fused-silica column (30 m; 0.25 μm film thickness; 0.25 mm internal diameter) in Isotopomics in Chemistry Biology & Shaanxi Key Laboratory of Chemical Additives for Industry, School of Chemistry & Chemical Engineering, Shaanxi University of Science & Technology.

2.3.1.1 Method for fatty acids and HBIs analysis

1μL of each sample was injected by Thermo Scientific AS 1310 autosampler and ran splitless mode at 300 °C with a helium carrier gas (1 mL min^{-1} constant flow). The GC oven was heated from 40 °C to 300 °C with a rate of 10 °C min^{-1}, giving a total method time of 26 minutes (Figure 2-11). The MS solvent delay was 5 min and collected scans from m/z 50 - 650.

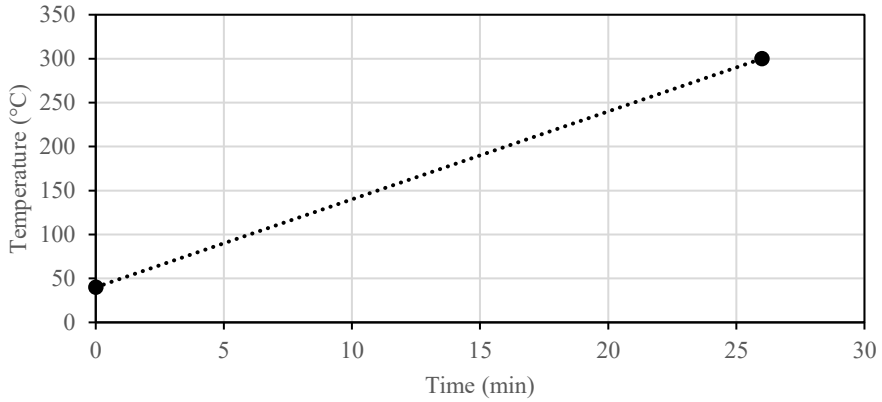

Figure 2-11. GC oven temperature programme for fatty acids and HBIs analysis. The oven temperature was heated from 40 °C to 300 °C by 10 °C min^{-1}, giving a total method time of 26 minutes.

2.3.1.2 Method for sterols and other isoprenoids analysis

1μL of each sample was injected by Thermo Scientific AS 1310 autosampler and ran splitless mode at 310 °C with a helium carrier gas (1 mL min^{-1} constant flow). The oven temperature was ramped from 80 ° to 240 °C with a rate of 20 °C min^{-1} then climbed to 310 °C with a rate of 10 °C min^{-1} and held for 10 mins, giving a

total method time of 25 minutes (Figure 2-12). The MS solvent delay was 5 min and collected scans from m/z 50 - 650.

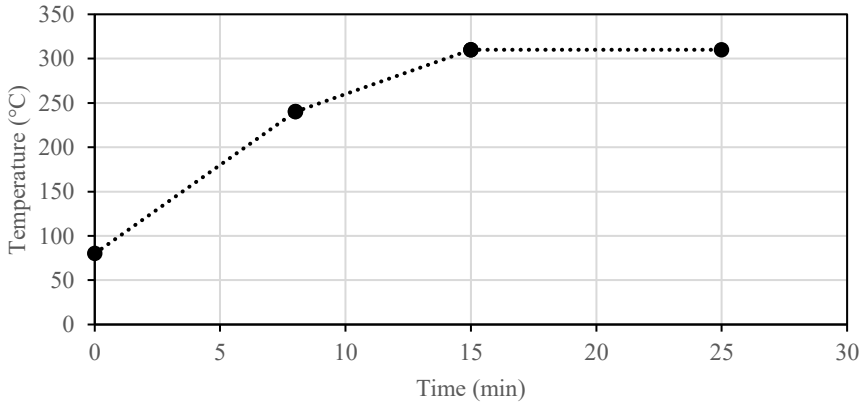

Figure 2-12. GC oven temperature programme for sterols and other isoprenoids analysis. The oven temperature was ramped from 80 ° to 240 °C with a rate of 20 °C min^{-1} then climbed to 310 °C with a rate of 10 °C min^{-1} and held for 10 mins, giving a total method time of 25 minutes.

2.3.2 The identification of fatty acids

The identification of molecules by GC-MS mainly is based on comparing the molecular ion, and characteristic mass spectra of the target compound to previous studies and internal standards. As fatty acids from plants and phytoplankton have been well studied and the establishment of the mass spectra pool made the identification of fatty acids possible.

The methylated products of myristic acid (C14:0, Retention Time (RT) = 15.32 min), palmitoleic acid (C16:1, RT = 17.24 min), palmitic acid (C16:0, RT = 17.44 min) and the internal standard (IS, C19:0, RT = 20.19 min) were found both in cultures of *R. setigera* and *P. intermedium* (Figure 2-13, Figure 2-14).

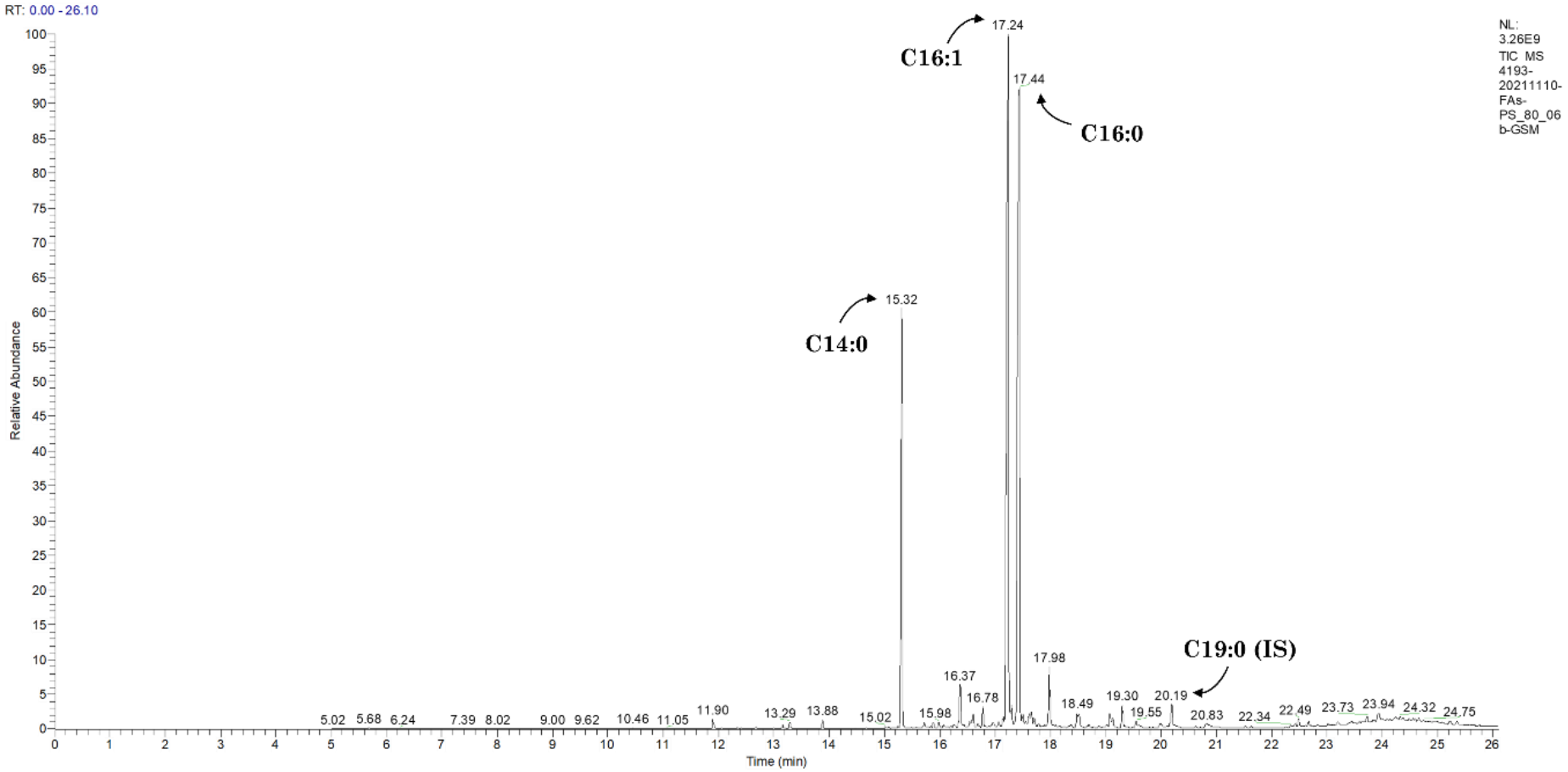

Figure 2-13. Gas chromatogram of the methylated products of fatty acids from laboratory cultured marine diatom *P. intermedium* and *Rhizosolenia setigera*. Myristic acid (C14:0, Retention Time (RT) = 15.32 min), palmitoleic acid (C16:1, RT = 17.24 min), palmitic acid (C16:0, RT = 17.44 min) and the internal standard (IS, C19:0, RT = 20.19 min).

(a)

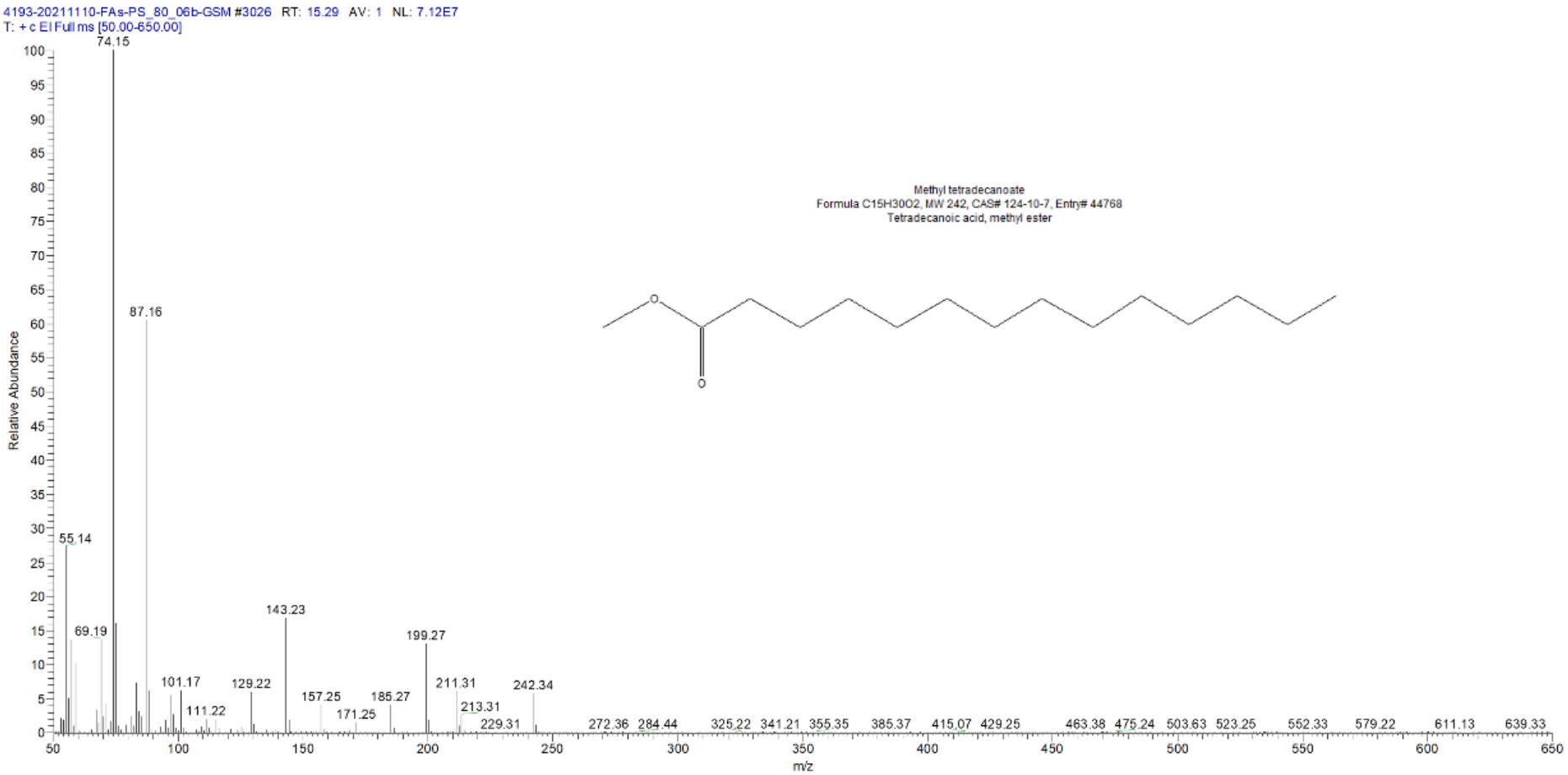
4193-20211110-FAs-PS_80_06b-GSM #3026 RT: 15.29 AV: 1 NL: 7.12E7
T: + c EI Full ms [50.00-650.00]
Methyl tetradecanoate
Formula C15H30O2, MW 242, CAS# 124-10-7, Entry# 44768
Tetradecanoic acid, methyl ester
Relative Abundance
m/z
74.15
87.16
55.14
69.19
143.23
199.27
101.17
129.22
111.22
157.25
171.25
185.27
211.31
213.31
229.31
242.34
272.36
284.44
325.22
341.21
355.35
385.37
415.07
429.25
463.38
475.24
503.63
523.25
552.33
579.22
611.13
639.33

(b)

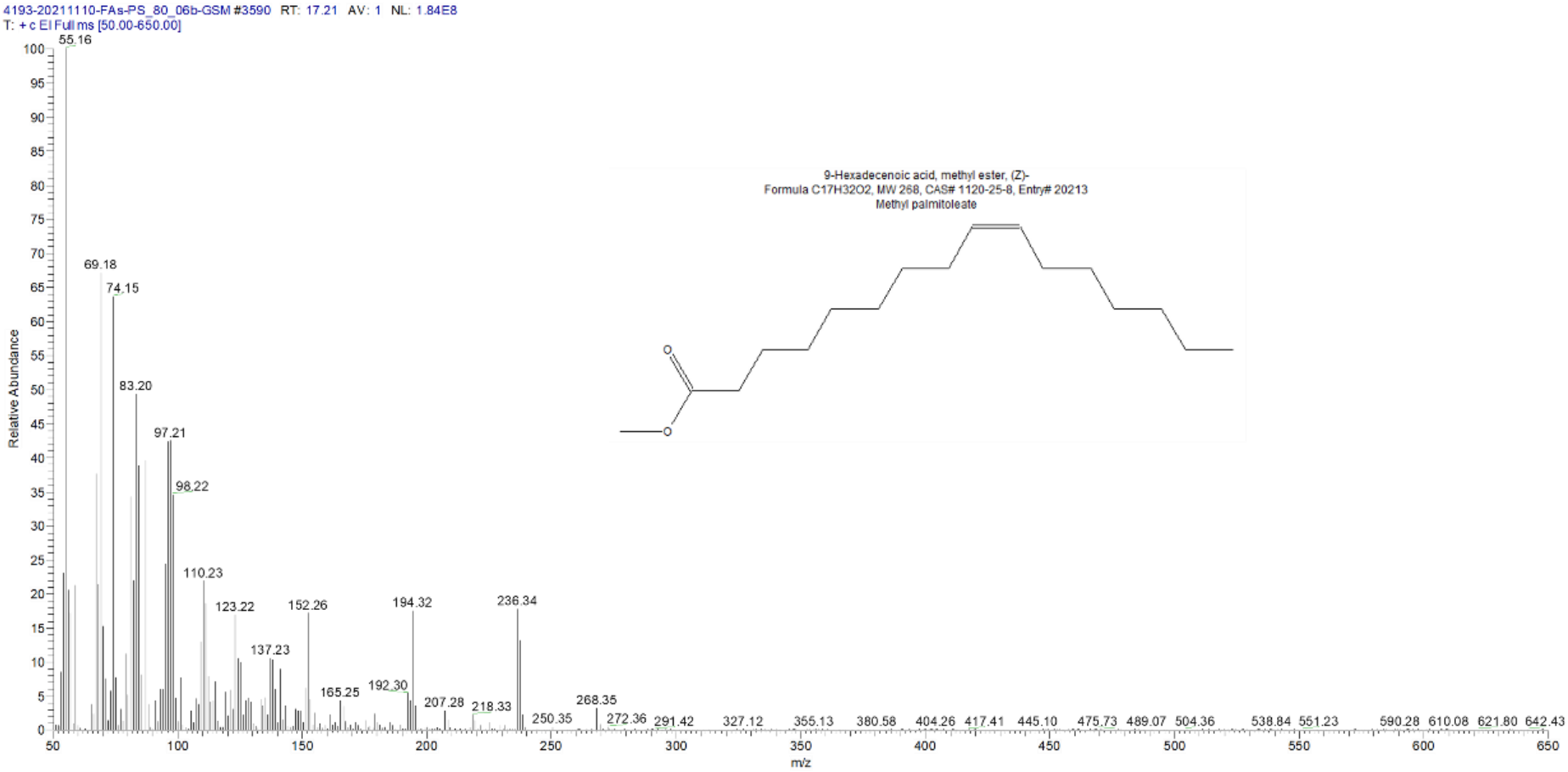
4193-20211110-FAs-PS_80_06b-GSM #3590 RT: 17.21 AV: 1 NL: 1.84E8
T: + c EI Full ms [50.00-650.00]
9-Hexadecenoic acid, methyl ester, (Z)-
Formula C17H32O2, MW 268, CAS# 1120-25-8, Entry# 20213
Methyl palmitoleate
Relative Abundance
m/z
55.16
69.18
74.15
83.20
97.21
98.22
110.23
123.22
137.23
152.26
165.25
192.30
194.32
207.28
218.33
236.34
250.35
268.35
272.36
291.42
327.12
355.13
380.58
404.26
417.41
445.10
475.73
489.07
504.36
538.84
551.23
590.28
610.08
621.80
642.43

(c)

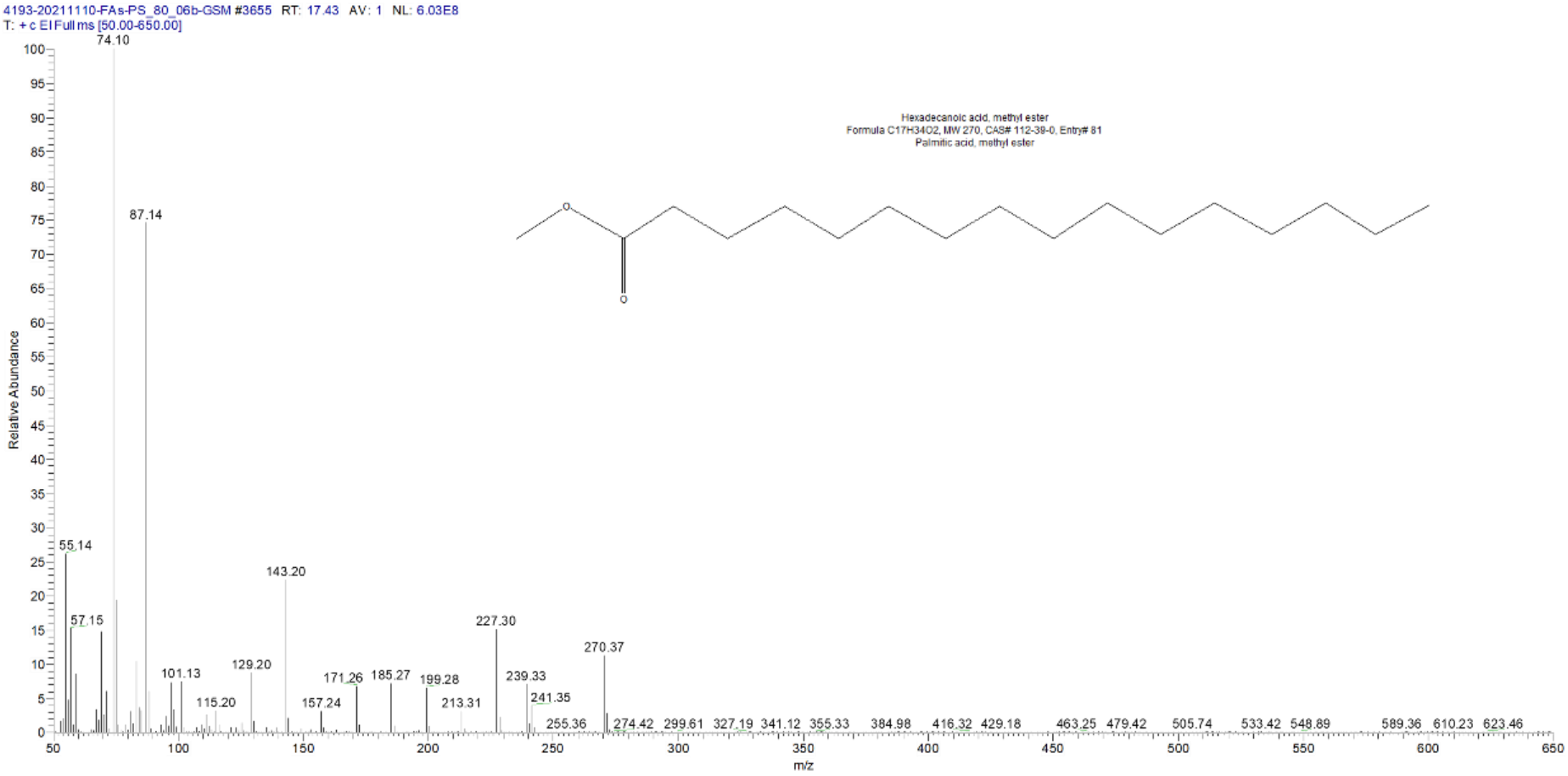

Figure 2-14. Mass Spectrometry and structure of the methylated product of fatty acids C14:0 (a), C16:1 (b), C16:0 (c) from laboratory cultured marine diatom *P. intermedium* and *Rhizosolenia setigera.*

2.3.3 The identification of HBIs

The identification of HBIs extracted from laboratory cultured diatom was mainly established by comparing their respective mass spectra with those published studies. Specifically, each HBI was identified from its molecular ion (M^+), characteristic mass spectrum and retention indices.

HBI triene (C25:3, m/z = 346.53; RT = 18.82 min) and HBI tetraene (C25:4, m/z = 344.53; RT = 19.17 min) were detected from the cultures of *P. intermedium* in this study (Figure 2-15, Figure 2-16). These were consistent with the results of Brown & Belt (2016), of which they identified the structure of the triene and tetraene produced by laboratory cultured *P. intermedium* using a combination of NMR spectroscopy and GC-MS (Figure 2-16).

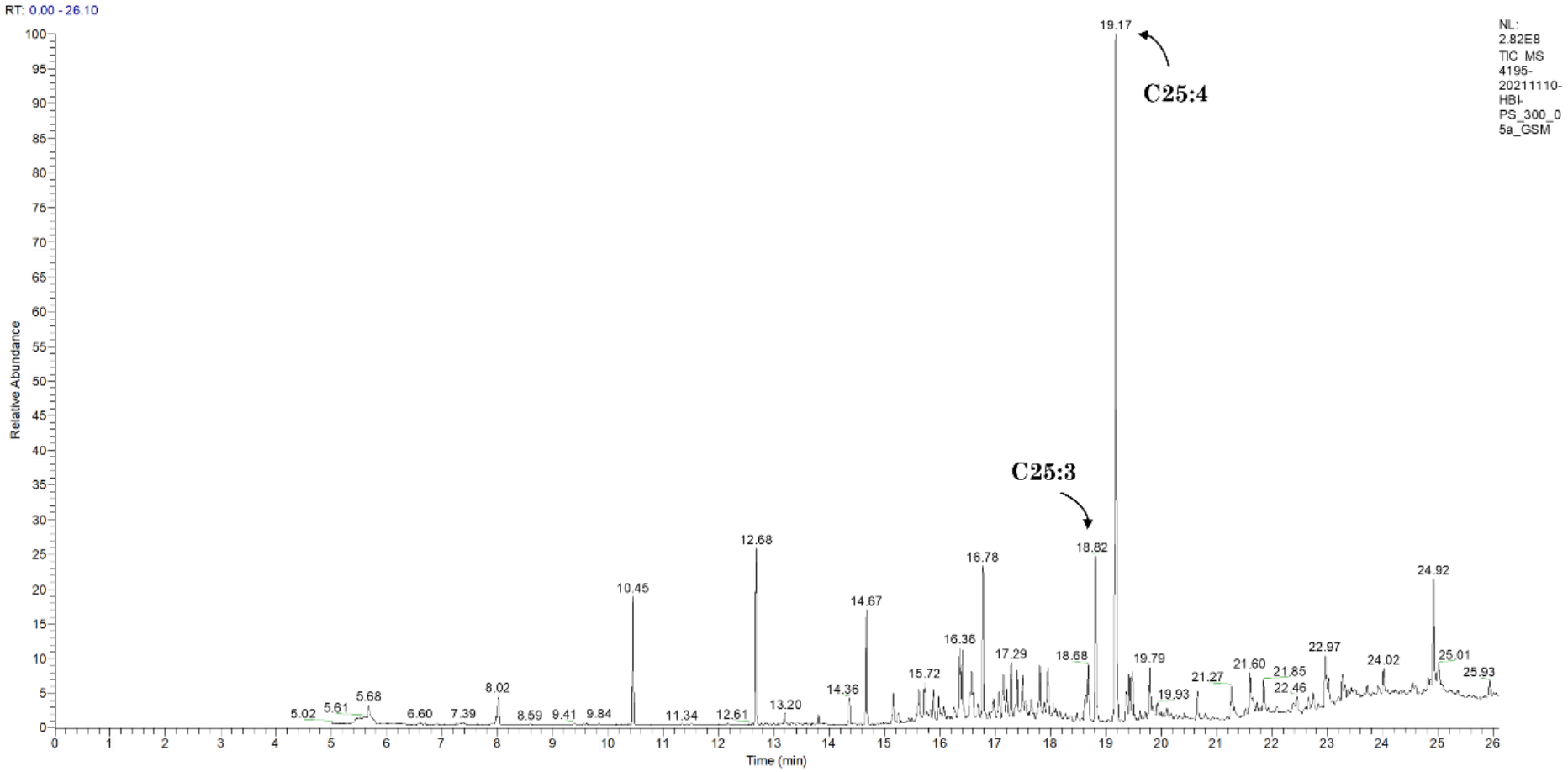

Figure 2-15. Gas chromatography of HBIs from laboratory cultured marine diatom *P. intermedium*. HBI triene (C25:3, m/z = 346.53; RT = 18.82 min) and HBI tetraene (C25:4, m/z = 344.53; RT = 19.17 min) were detected.

(a)

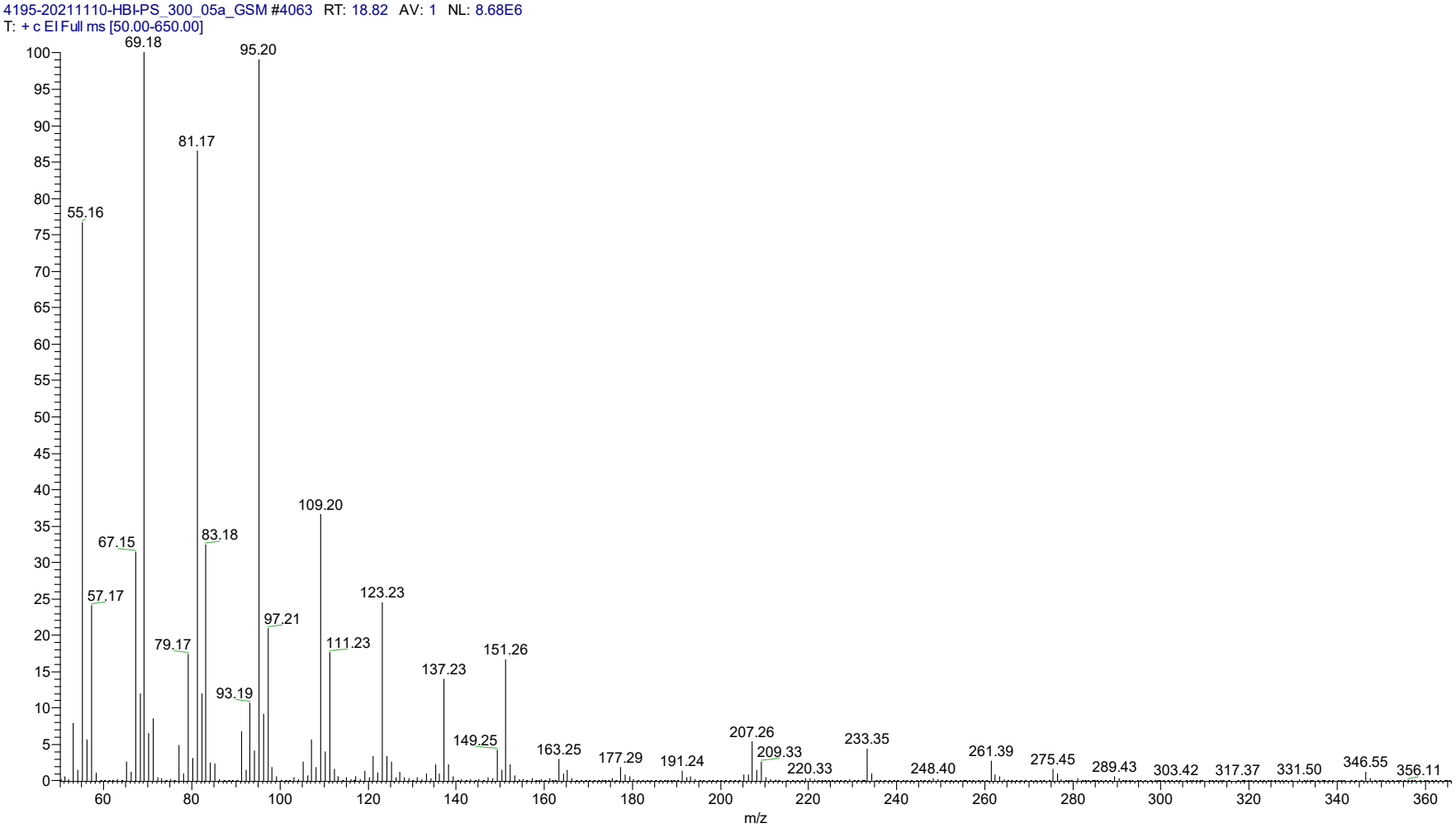
4195-20211110-HBI-PS_300_05a_GSM #4063 RT: 18.82 AV: 1 NL: 8.68E6
T: + c EI Full ms [50.00-650.00]
69.18
95.20
81.17
55.16
109.20
67.15
83.18
123.23
57.17
97.21
79.17
111.23
151.26
137.23
93.19
149.25
207.26
209.33
233.35
163.25
177.29
191.24
220.33
248.40
261.39
275.45
289.43
303.42
317.37
331.50
346.55
356.11
m/z

(b)

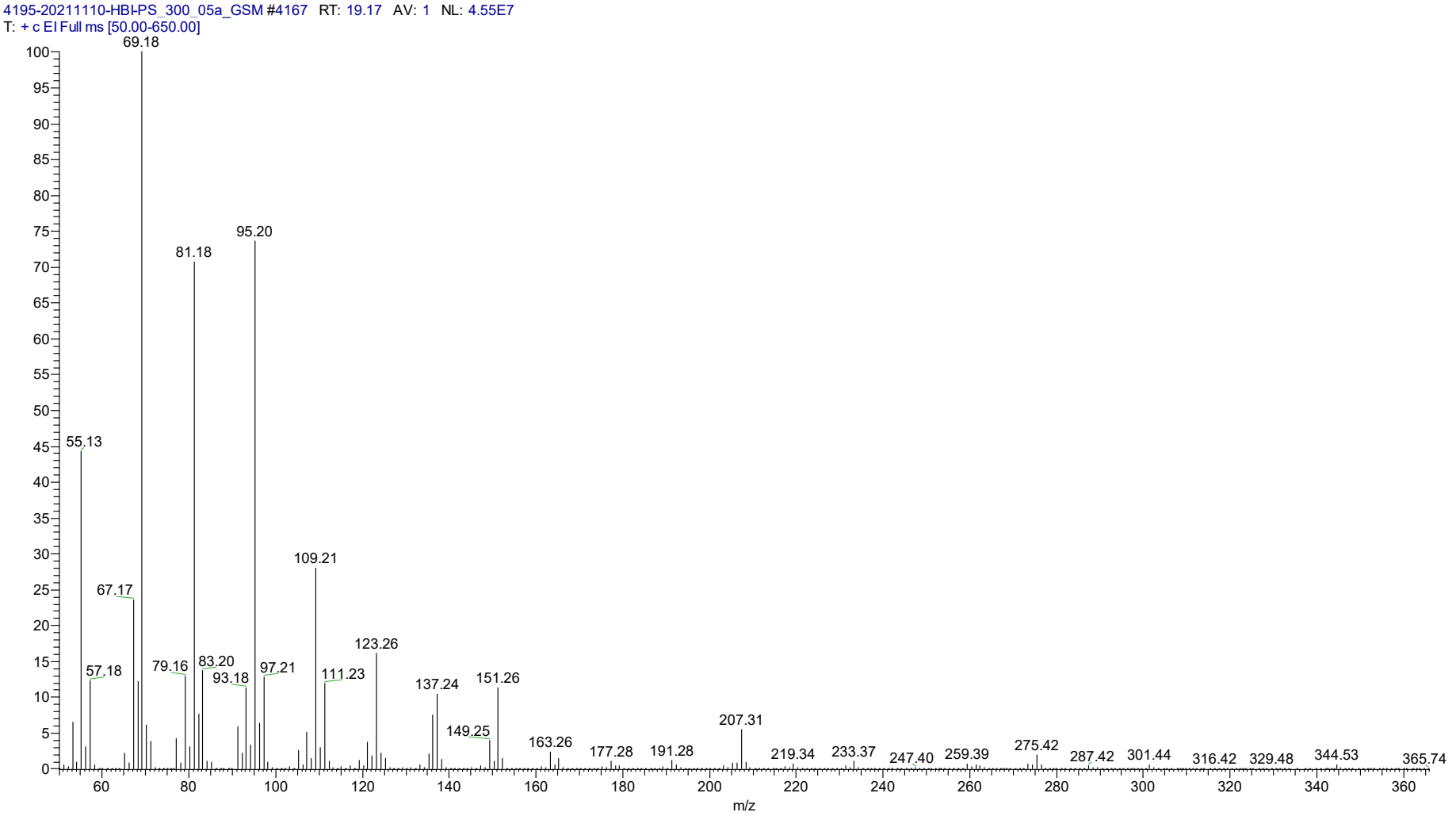
4195-20211110-HBI-PS_300_05a_GSM #4167 RT: 19.17 AV: 1 NL: 4.55E7
T: + c EI Full ms [50.00-650.00]
69.18
95.20
81.18
55.13
109.21
67.17
123.26
57.18
79.16
83.20
93.18
97.21
111.23
137.24
151.26
149.25
207.31
163.26
177.28
191.28
219.34
233.37
247.40
259.39
275.42
287.42
301.44
316.42
329.48
344.53
365.74
m/z

(c)

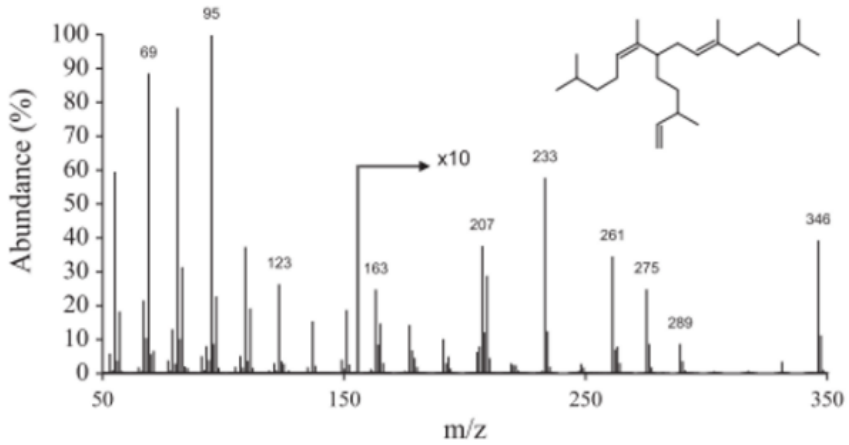

(d)

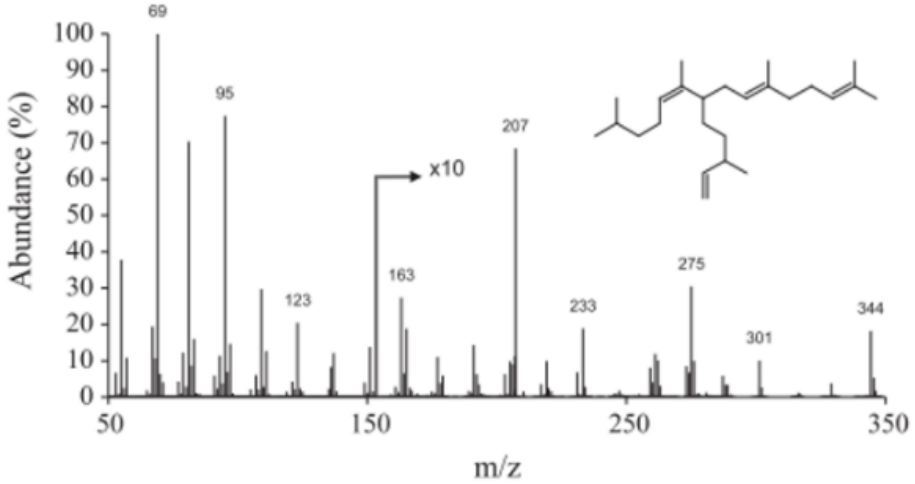

Figure 2-16. The accordance of mass spectrometry of HBIs C25:3 (a) and C25:4 (b) detected from *P. intermedium* in this study and the published mass spectrometry and structures of C25:3 (c) and C25:4 (d) from the same diatom specie (Brown & Belt, 2016).

Another HBI pentane (C25:5, m/z = 342.46; RT = 19.82 min) was detected from the cultures of *R. setigera*. The gas chromatography and mass spectrometry are shown in (Figure 2-17). The structure of C25:5 was confirmed by comparing with (Sinninghe Damsté et al., 2000).

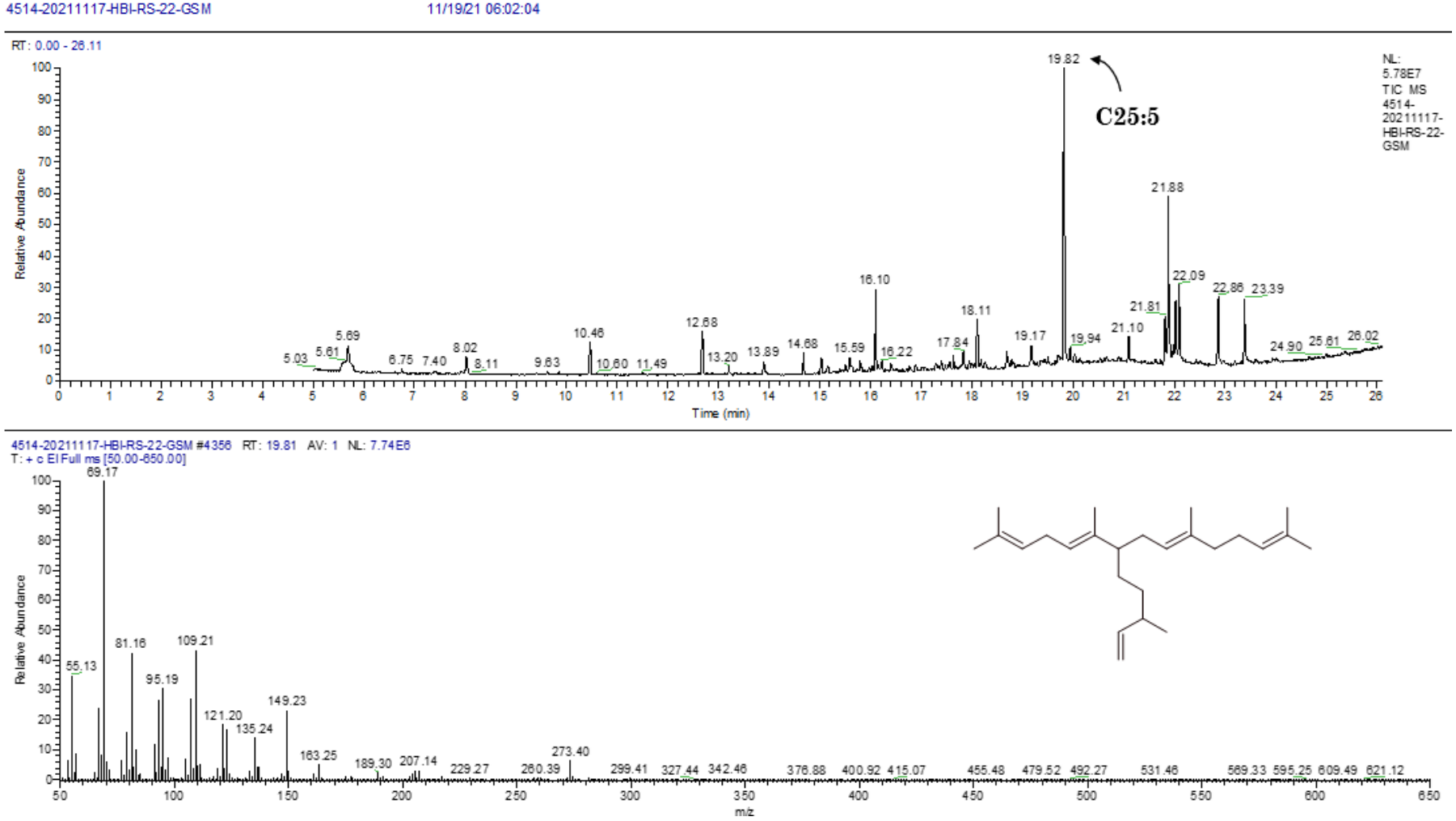

Figure 2-17. Gas chromatography and mass spectrometry of HBI C25:5 (m/z = 342.46; RT = 19.82 min) from laboratory cultured marine diatom *R. setigera*.

2.3.4 The identification of phytol and squalene

Unfortunately, we could not find the sterols and internal standards in most samples. Instead, relatively high yields of neophytadiene (RT = 7.54 min), phytol (RT = 9.50), and squalene (RT = 13.21) were detected from cultures of *P. intermedium*. The gas chromatography and mass spectrometry of phytol and squalene are shown in Figure 2-18 and Figure 2-19, respectively.

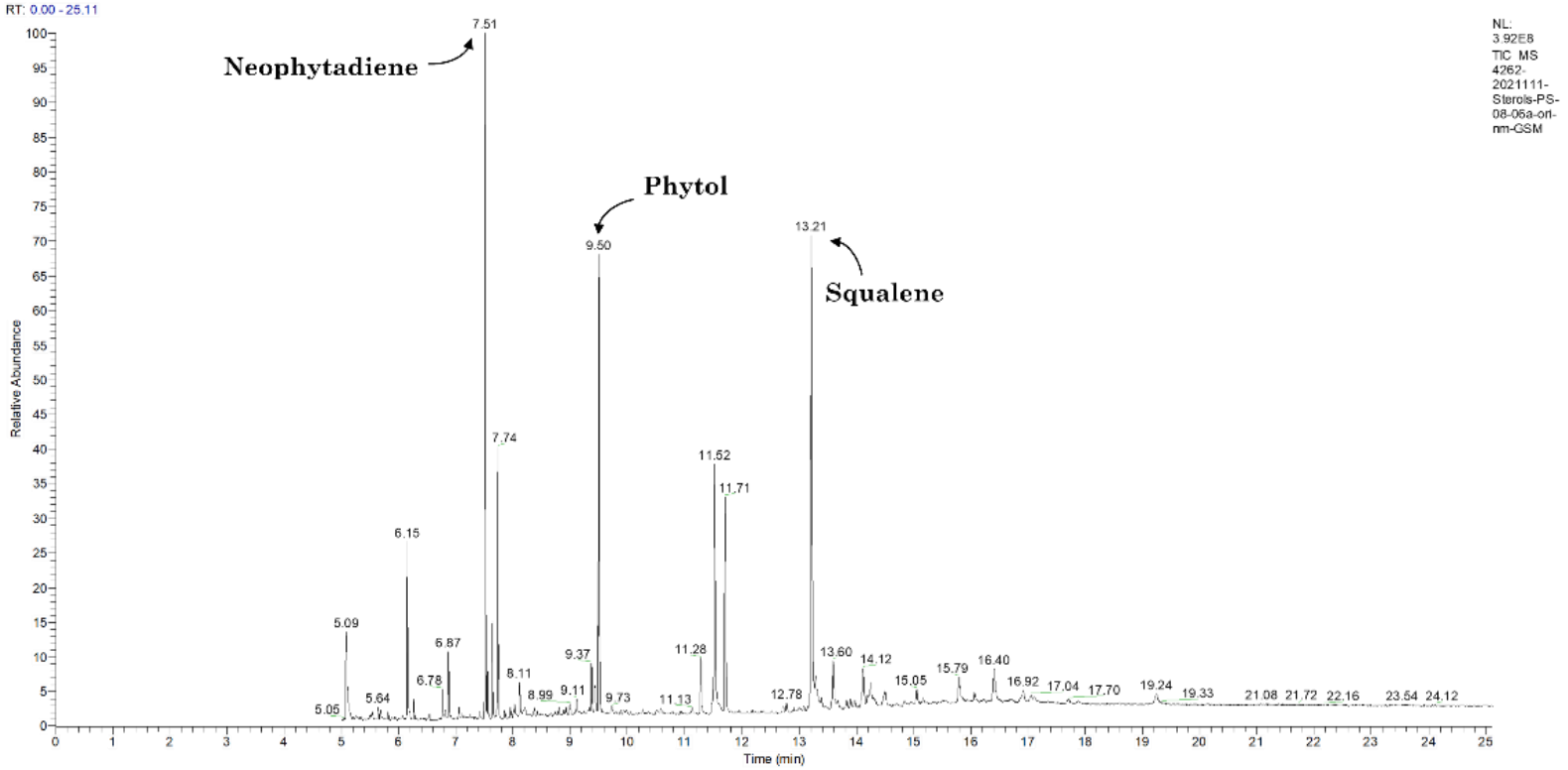

Figure 2-18. Gas chromatography of phytol and squalene from laboratory cultured marine diatom *P. intermedium*.

(a)

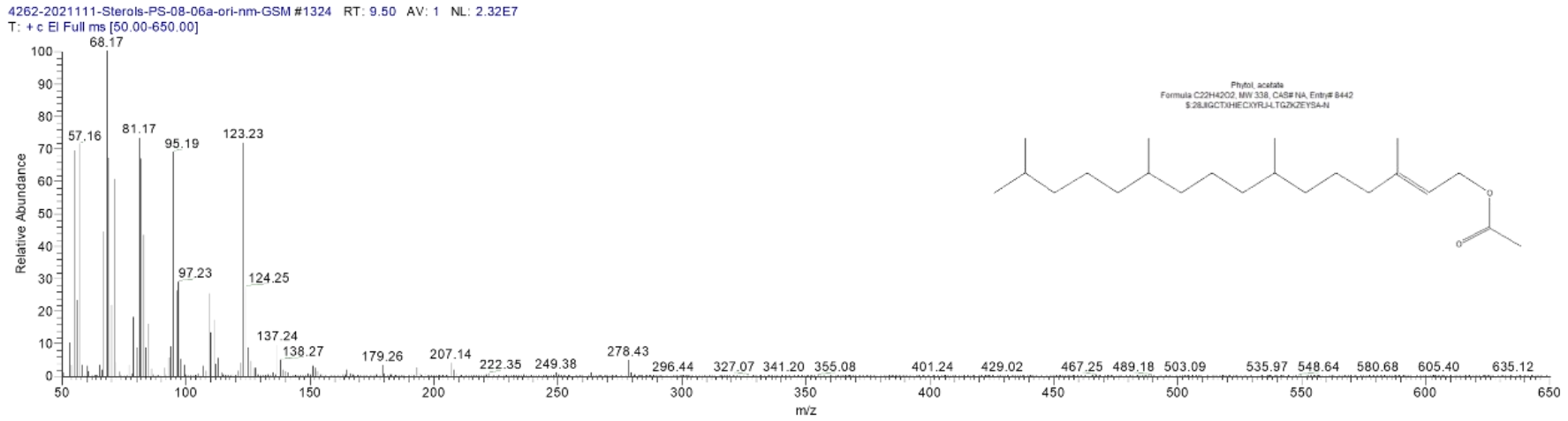

(b)

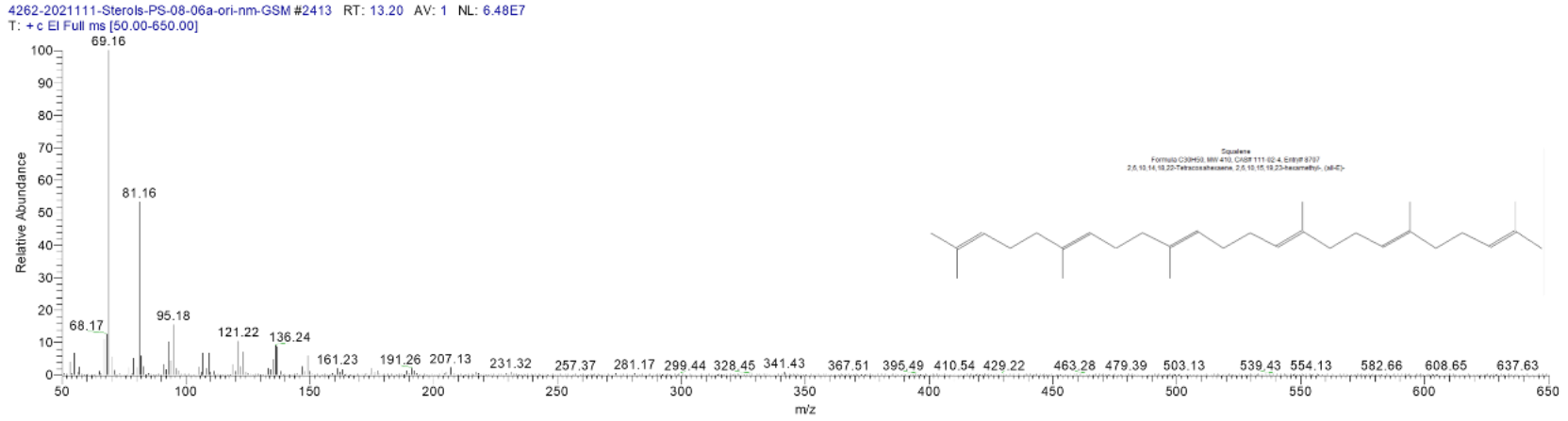

Figure 2-19. Mass Spectrometry and structure of phytol (a), squalene (b) from laboratory cultured marine diatom *P. intermedium*.

2.3.5 The quantification of lipids

Quantifications were made by gas chromatography by comparing the analyte peak area to a known amount of internal standard added to the sample.

$$\frac{P_{IS}}{V_{IS}C_{IS}} = \frac{P_{spl}}{m_{spl}} \quad (2\text{-}3)$$

Where P_{IS} and P_{spl} are the peak areas of the internal standard and analyte, V_{IS} and C_{IS} are the volume and concentration of the internal standard added previously. Rearrange the Eqn. (2-3), the analyte can be quantified by Eqn. (2-4)

$$m_{spl} = \frac{V_{IS}C_{IS} \cdot P_{spl}}{P_{IS}} \quad (2\text{-}4)$$

Last but not least, the absolute value of each analyte needs to be normalised by Eqn. (2-5), giving a unit of ng g^{-1} or ug g^{-1}.

$$m_{(ng/\mu g\ g^{-1})} = \frac{m_{spl}}{m_n} \quad (2\text{-}5)$$

Where m_n is the net mass of the freeze-dried diatom sample described in 2.1.1. Here, we managed to quantify the concentration of fatty acids and HBIs (see 3.4 results (3)).

2.4 Compound-specific Stable Isotope Analysis (CSIA)

The delta values of ^{13}C and ^{2}H of purified algal samples were determined by Gas Chromatography – isotope ratio mass spectrometry (GC-IRMS) using a Thermo Scientific TRACE 1310 GC coupled via a reaction unit (GC Isolink II) and a reference (Conflow IV) to a Thermo Scientific Delta V Plus Isotope Ratio MS in International Centre for Isotope Effects Research, Nanjing University. To keep consistent with the previous GC-MS screening, the same HP-5ms fused-silica column (see **2.3.1**) was used in CSIA.

2.4.1 High Temperature Conversion (HTC) Mode for $^{2}H/^{1}H$ analysis

Compound-specific hydrogen isotopic compositions of fatty acids, HBIs, and other isoprenoids isolated from laboratory cultured marine diatom *P. intermedium* and *R. setigera* were determined by GC-IRMS using High Temperature Conversion (HTC) Mode (Figure 2-20).

In HTC Mode, the compounds from the GC column would then go through a reaction tube typically comprises an outer tube made from fused alumina and an inner tube made from glass carbon. The conversion occurred at temperatures between 1350 and 1450 °C and both organic and inorganic compounds were converted into H_2, N_2, and CO gases. The reactors were followed by a water-separation device to remove the water.

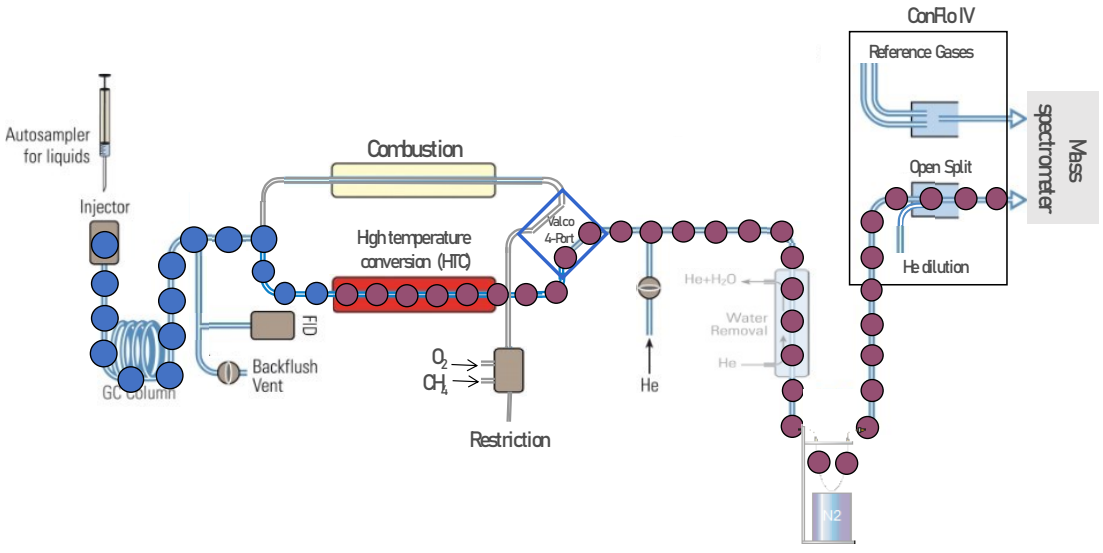

Figure 2-20. A schematic diagram of GC-IRMS in High Temperature Conversion (HTC) Mode for $^{2}H/^{1}H$ analysis. The conversion of organic and inorganic compounds into H_2, N_2 and CO gases occurred at a reaction tube (red) at temperatures between 1350 and 1450 °C.

To increase the efficiency of measurements, the GC condition for fatty acids and HBI analysis was slightly modified. The initial GC oven temperature was set at 100 °C and then raised at a rate of 20 °C min $^{-1}$ to 300 °C. The final temperature was held for 6 minutes, giving a total method time of 16 minutes (Figure 2-21).

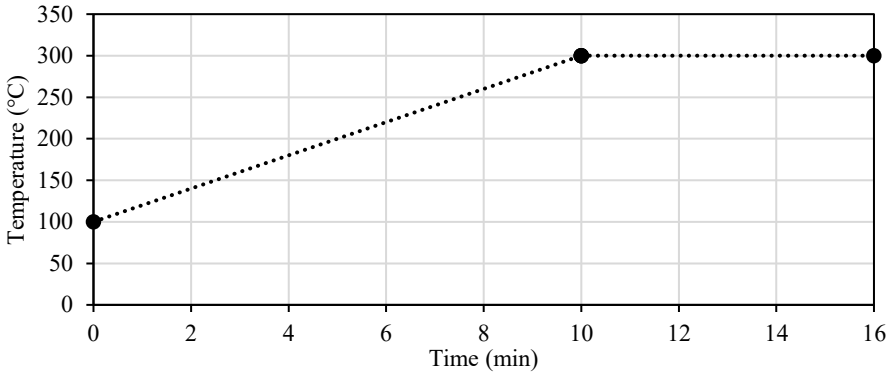

Figure 2-21. GC oven temperature programme for fatty acids and HBIs (a) analysis. The GC oven was heated from 100 °C to 300 °C at a rate of 20 °C min $^{-1}$ and held the final temperature for 6 minutes, giving a total method time of 16 minutes.

The δ^2H values were based on duplicate analyses of well-resolved peaks based on in-house reference gases (H_2, >99.995% purity). A certified Reference Material from the United States Geological Survey, Hydrogen and Carbon Isotopes in Icosanoic Acid Methyl Esters C20 FAMEs, short for USGS72, was injected every three samples.

The main reason I used duplicates instead of triplicates here is the limitations in terms of the low concentration of individual samples, time and access to the partner laboratory at Nanjing University during the COVID-19 pandemic. For some samples harvest from low light conditions, after several steps of extraction and purification, the biomass can hardly meet the lowest standard of isotopic measurements, even with a single injection. To tackle this situation, we thereby test the in-house reference gases to prove the stabilization of the instrument and increase the number of biological replicates. Nevertheless, I would highly recommend that both hydrogen and carbon isotopic analyses should be conducted on triplicates.

During all samples and standard measurements, eight reference gas pulses were passed through the mass spectrometer. Reproducibility of H_2 reference gas δ^2H values after $H3^+$ correction replicates of the same sample did not exceed 3‰. The H_2 signals generated by GC-IRMS of reference gas, fatty acids (Figure 2-22)

isolated from laboratory cultured marine diatom *P. intermedium* and *R. setigera*; HBIs C25:3, C25:4 (Figure 2-23 (a)); phytol and squalene (Figure 2-23 (b)) from P. intermedium and HBI C25:5 (Figure 2-24) from *R. setigera* are shown below.

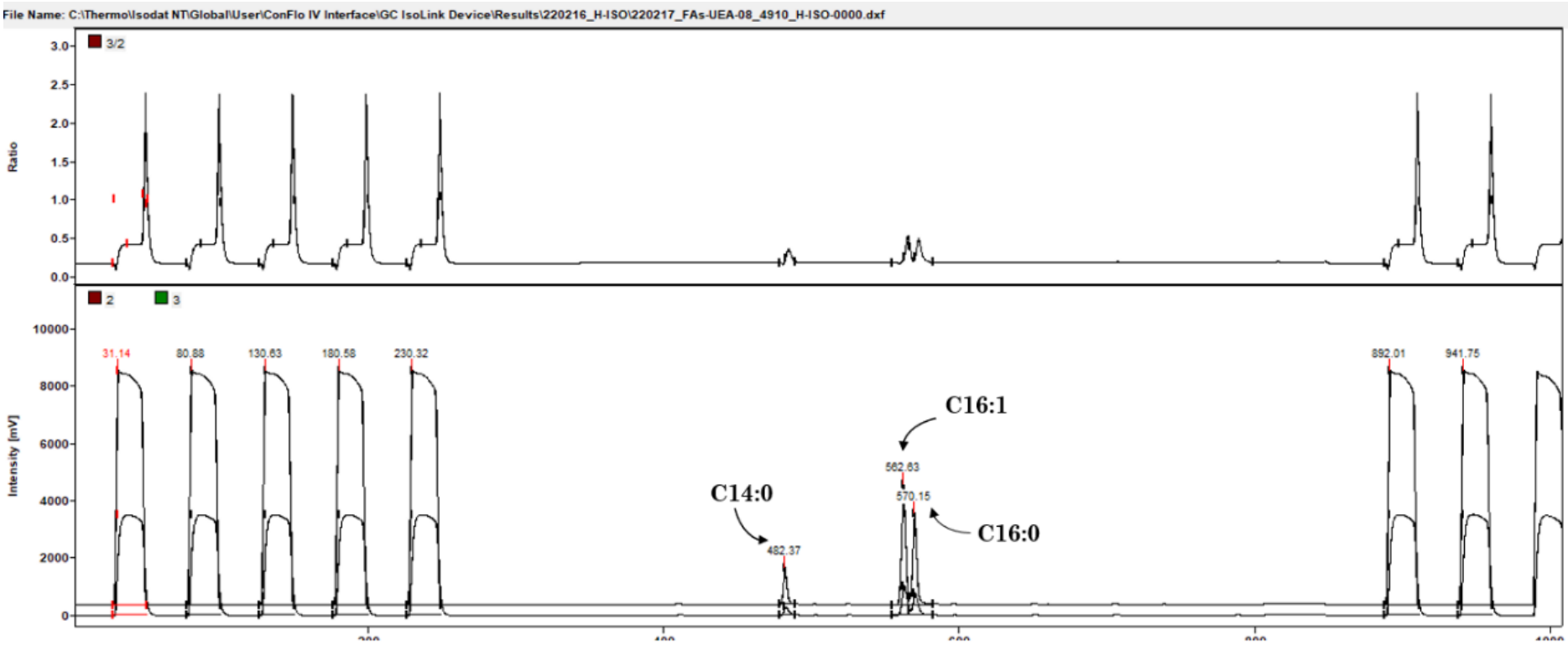

Figure 2-22. The H_2 signals generated by GC-IRMS of fatty acids C14:0 (RT = 482.37), C16:1 (RT = 562.63) and C16:0 (RT = 570.15) isolated from laboratory culture marine diatom *P. intermedium* and *R. setigera*. The upper chamber shows the mass ratio of 3 ($^2H^1H$)/2 ($^1H_2$) and lower chamber shows the intensity of H_2 along with time (second). The first five and last three peaks are references gases.

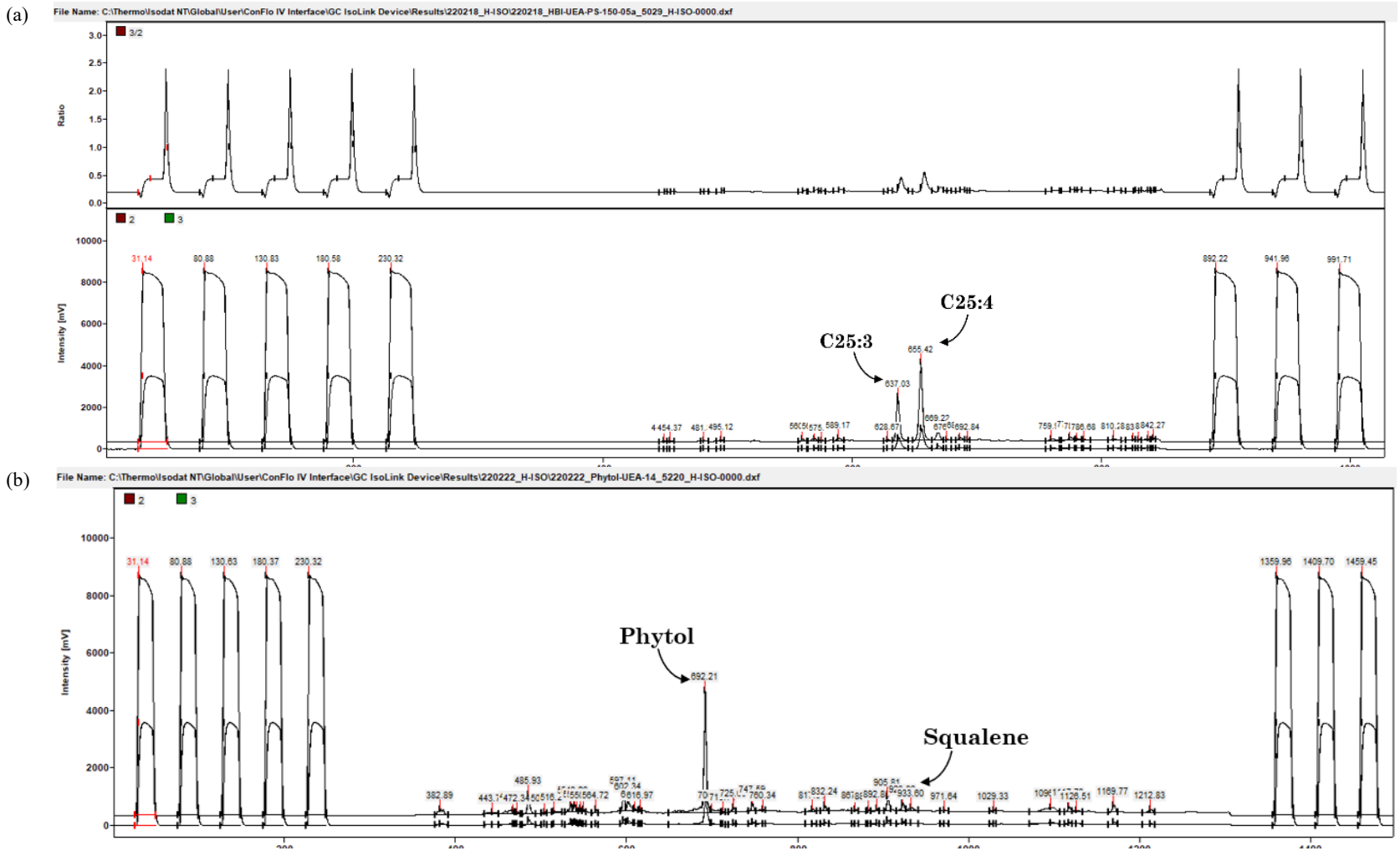

Figure 2-23. The H_2 signals generated by GC-IRMS of (a) HBIs C25:3 (RT = 637.03), C25:4 (RT = 655.42) and (b) phytol (RT = 692.21), squalene (RT = 933.60) isolated from laboratory culture marine diatom *P. intermedium* showing the intensity of H_2 along with time (second). The first five and last three peaks are references gases.

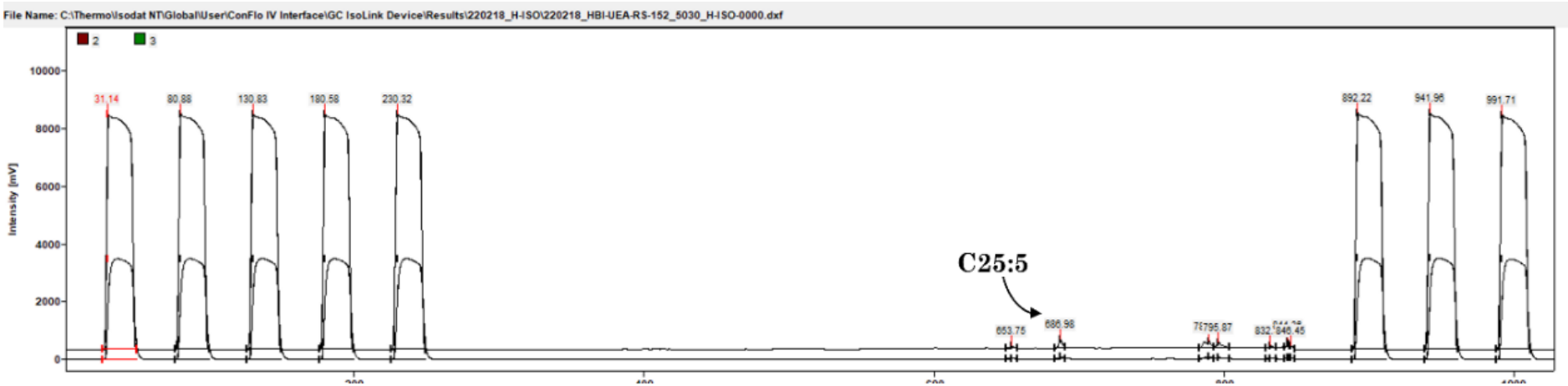

Figure 2-24. The H_2 signals generated by GC-IRMS of HBI C25:5 (RT = 686.98) isolated from laboratory culture marine diatom *R. setigera* showing the intensity of H_2 species (3 ($^2H^1H$)/2 (H_2) along with time (second). The first five and last three peaks are references gases.

Due to the relatively low contraction of squalene, phytol and HBI C25:5 and the nature of hydrogen isotopic composition measurement, the H_2 signals generated by GC-IRMS are extremely low with high background noise. These signals are less robust and require further concentration or more biomass from culture experiments.

However, the measurement of the hydrogen and carbon isoprenoid lipids is supposed to be an essential chain of the whole project as they present completely different biosynthesis pathways. The failed measurement of these compounds was mainly due to the misprediction of the pilot experiments and the limitation of time and access to the lab.

Here, these data are presented as a part of Ph.D. work to maintain the logical chain of this project. The additional measurements of isoprenoid lipids will be included in further work.

2.4.2 The normalization of measured Hydrogen stable isotopic compositions

Using stable isotope ratio mass spectrometry, the stable isotopic composition of samples can be measured by comparing the isotopic composition of a reference gas. This measured isotope value, however, must be converted into a so-called true value which is relative to the international stable isotope reference scale (e.g. Vienna Standard Mean Ocean Water, VSMOW; Vienna Peedee belemnite, VPDB; Vienna Canyon Diablo Troilite, VCDT) so that results can be compared between different laboratories. This isotopic composition normalization procedure requires a series of calculations and can vary from operators and depend on the methods for data generation and the situation of the instrument itself.

Here, a modified single-point anchoring method by referencing versus a certified reference standard (USGS72) and further corrections was used. Based on the Identical Treatment (IT) principle, we assumed that both the standards and samples went through exact same analytical preparation pathways and measurement strategy. The isotopic compositions of the standard and the samples were measured with respect to the working gas. As the stable hydrogen and carbon isotopic compositions of USGS72 with combined standard uncertainties were reported as +348.3 ± 1.5‰ and –1.54 ± 0.03‰ (Schimmelmann et al., 2016),

the respective raw δ-values then can be used to compute the true δ-values of the samples. The mathematical formulation for this normalization is described below, and the notations used in the mathematical derivation are presented in Table 2-2.

Table 2-2. The notations used in the normalization procedure.

Notation	Description
spl	Sample
std	Standard
int	international stable isotope reference scale
R_x	The concentration ratio of the heavy isotope of the material 'x' versus the light isotope
RG	Reference Gas, the reference laboratory cylinder gas
δ_x^M	The measured (relative to the reference gas) δ-value of the material 'x'
δ_x^T	The true (relative to the international stable isotope reference scale) δ-value of the material 'x'
δ_x^{det}	The detrended δ-value of the material 'x'
δ_x^{amt}	The area-correction δ-value of the material 'x'

As introduced in **1.7.1**, the δ-value of a sample is defined as the relative difference in parts per thousand (‰) between the isotopic ratio of the sample (R_{spl}) and the reference standard (R_{std}) using the equation below:

$$\delta_{spl} = (\frac{R_{spl}}{R_{std}} - 1) \times 1000 \quad (2\text{-}6)$$

where R is the concentration ratio of a heavy isotope versus a light one, e.g. $^2H/^1H$ for hydrogen, $^{13}C/^{12}C$ for carbon. The raw δ-values of the sample generated by GC-IRMS can be expressed as:

$$\delta_{spl}^M = (\frac{R_{spl}}{R_{FG}} - 1) \times 1000 \quad (2\text{-}7)$$

Similarly the raw δ-values of the standard can be expressed as:

$$\delta_{std}^M = (\frac{R_{std}}{R_{FG}} - 1) \times 1000 \quad (2\text{-}8)$$

And the true δ-values of the sample and standard can be expressed as:

$$\delta_{spl}^T = (\frac{R_{spl}}{R_{int}} - 1) \times 1000 \quad (2\text{-}9)$$

$$\delta_{std}^T = (\frac{R_{std}}{R_{int}} - 1) \times 1000 \quad (2\text{-}10)$$

Rearrange Eqn. (2-7), (2-8), (2-9) and (2-10), we get:

$$\frac{R_{spl}}{R_{FG}} = \frac{\delta_{spl}^M + 1000}{1000} \quad (2\text{-}11)$$

$$\frac{R_{std}}{R_{FG}} = \frac{\delta_{std}^M + 1000}{1000} \quad (2\text{-}12)$$

$$\frac{R_{spl}}{R_{int}} = \frac{\delta_{spl}^T + 1000}{1000} \quad (2\text{-}13)$$

$$\frac{R_{std}}{R_{int}} = \frac{\delta_{std}^T + 1000}{1000} \quad (2\text{-}14)$$

Dividing Eqn. (2-11) by Eqn. (2-12), Eqn. (2-13) by Eqn. (2-14):

$$\frac{R_{spl}}{R_{std}} = \frac{\delta^{M}_{spl}+1000}{\delta^{M}_{std}+1000} = \frac{\delta^{T}_{spl}+1000}{\delta^{T}_{std}+1000} \quad (2\text{-}15)$$

Rearranged the Eqn. (2-15), the true δ-value of sample (δ^{T}_{spl}) can be computed using the equation below:

$$\delta^{T}_{spl} = \left[\frac{(\delta^{M}_{spl}+1000)(\delta^{T}_{std}+1000)}{(\delta^{M}_{std}+1000)}\right] - 1000 \quad (2\text{-}16)$$

The main critical disadvantage of this method is that only one certified reference was used. In order to obtain accurate results, the true δ-value of the sample should be close to the true δ-value of the standard. The normalization error gets systematically larger as the difference between the δ-values of the sample and standard.

The other downside of this method is, for continuous flow IRMS analyses, although the mass spectrometer remains stable, the conditions at the sample preparation during each analysis sequence may vary depending on several parameters including carrier gas flow rate, condition of the oxidation and reduction columns in the elemental analyser and the temperature of the reaction. The IT principle is actually not strictly followed. Therefore, standard was injected and its δ-value was measured every three samples to check the stability of the instrument and minimise the inaccuracy introduced by the difference δ-value between the sample and certified standard. The normalization used in this study contains several steps below.

2.4.2.1 Linear normalization

This normalization is applied under the assumption that any systematic error introduced during mass spectrometric analyses is linear in a dynamic range. Here, the raw δ-values of the certified standard were plotted on the y-axis and the analysis running sequence number of the individual standard was plotted on the x-axis (Figure 2-25).

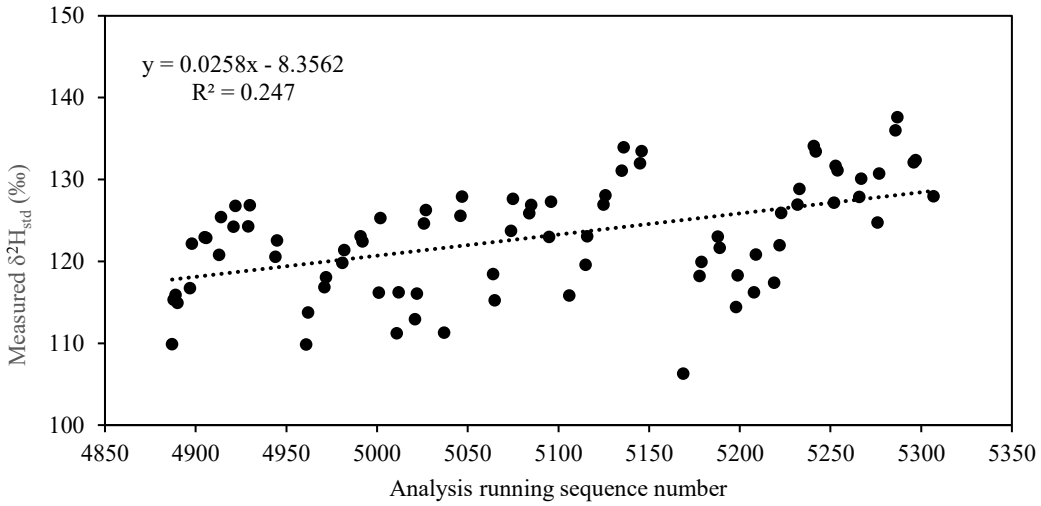

Figure 2-25. The linear shift of the raw δ^2H values of standard along with the analysis running sequence.

By fitting a linear regression line among samples, the equation of the regression line can be calculated as y = 0.0258x – 8.3562 with a coefficient of determination R^2 of 0.247. Due to a small R^2 value (< 0.3), the analysis process was divided into three parts (analysis numbers 4887 - 4945, 4961 – 5146, and 5169 - 5307) based on the sample analysing date and the situation of the instrument. Each piecewise linear regression was calculated as $y = k_d x + b$, where $k_{d1} = 0.1741$ (Figure 2-26 (1)), $k_{d2} = 0.0727$ (Figure 2-26 (2)), and $k_{d3} = 0.1455$ (Figure 2-26 (3)).

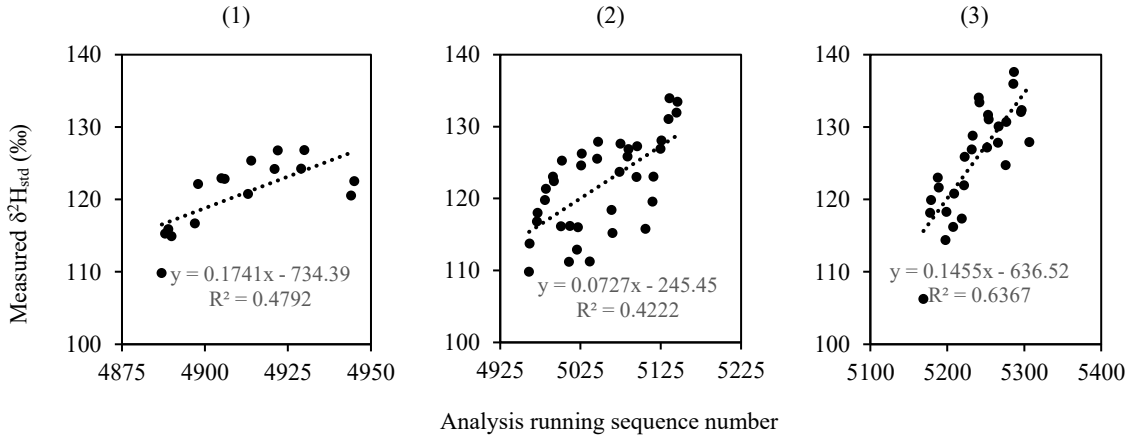

Figure 2-26. The piecewise linear regression of the raw δ^2H values of standard versus analysis running sequence number. Each piecewise linear regression was calculated as $y = k_{dx} + b$, where $k_{d1} = 0.1741$ (analysis number 4887 – 4945, $R^2 = 0.48$, (1)); $k_{d2} = 0.0727$ (analysis number 4961 – 5146, $R^2 = 0.42$, (2)); and $k_{d3} = 0.1455$ (analysis number 5169 – 5307, $R^2 = 0.64$, (3)).

2.4.2.2 The detrending of the raw δ^2H values of standard

The slope of each regression line refers to the mean changes of the raw δ^2H values of standard over time. To remove this distortion, the raw δ^2H values need to be detrended by using the equation below.

$$\delta_{std}^{det} = \delta_{std}^{M} - k_{dx} \times (ARN - STA) \quad (2\text{-}17)$$

where k_{dx} was the slope of the piecewise regression line, ARN referred to the analysis running number of the individual sample and STA was the first analysis running number of each piecewise. The detrending of the samples can also apply to a similar equation below.

$$\delta_{spl}^{det} = \delta_{spl}^{M} - k_{dx} \times (ARN - STA) \quad (2\text{-}18)$$

2.4.2.3 Amount correction of the detrended δ^2H values standard

One more step was required to remove the systematic errors introduced by the variation of the peak area. Here, the peak area of the individual standard was plotted on the x-axis and the corresponding detrended δ^2H values were on the y-axis. Similar with the piecewise regression in data detrending, the regression was calculated in three parts (analysis number 4887 - 4945, 4961 - 5146 and 5169 - 5307) as $y = k_a x + b$, whereas $k_{a1} = 1.4839$ (Figure 2-27 (1)), $k_{a2} = 0.6725$ (Figure 2-27 (2)), $k_{a3} = 1.4769$ (Figure 2-27 (3)).

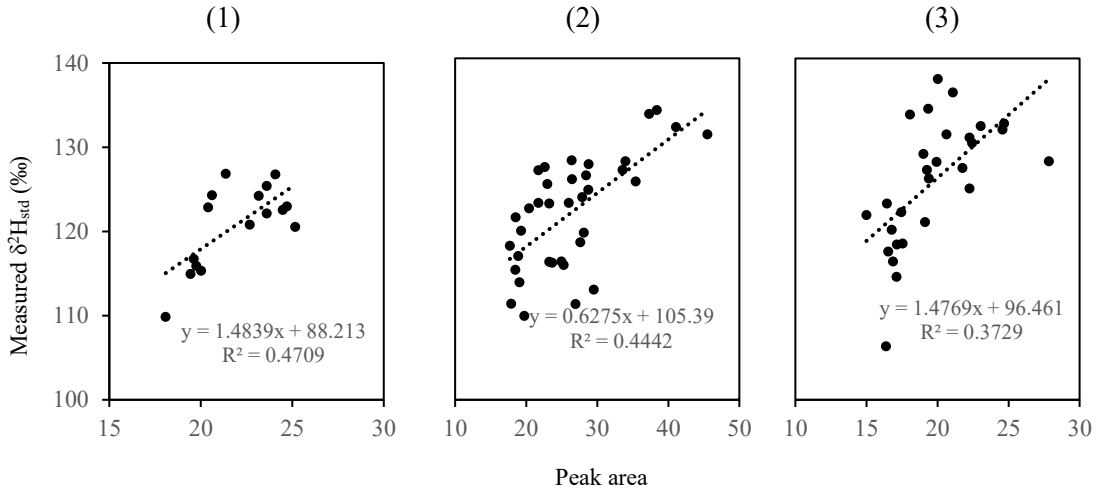

Figure 2-27. The piecewise linear regression of the detrended δ^2H values of standard versus varied amount of peak area. Each piecewise linear regression was calculated as k_{d1} =1.4839 (analysis number 4887 – 4945, R^2 = 0.47, (1)); k_{d2} = 0.6275 (analysis number 4961 – 5146, R^2 = 0.44, (2)); and k_{d3} = 1.4769 (analysis number 5169 – 5307, R^2 = 0.37, (3)).

The correction of the peak area was then completed by using the equation below,

$$\delta_{std}^{amt} = \delta_{std}^{det} - k_{ax} \times (A_{std} - aveA_{std}) \quad (2\text{-}19)$$

where k_{ax} was the slope of the regression line of the piecewise area correction, A_{std} referred to the peak area of an individual standard while $aveA_{std}$ was the average peak area.

Similarly, the amount correction of the samples could also be done by the equation below,

$$\delta_{spl}^{amt} = \delta_{spl}^{det} - k_{ax} \times (A_{spl} - aveA_{std}) \quad (2\text{-}20)$$

Last but not least, the true δ-value of the sample could be calculated by applying a modified equation of Eqn. (2-16) below,

$$\delta_{spl}^{T} = \left[\frac{(\delta_{spl}^{amt}+1000)(\delta_{std}^{T}+1000)}{(ave\delta_{std}^{amt}+1000)}\right] - 1000 \quad (2\text{-}21)$$

where δ_{spl}^{amt} was a corrected δ_{spl}^{M} after detrending and area correction, $ave\delta_{std}^{amt}$ was the average value of the corrected δ^2H value of the measured standard.

2.4.3 Combustion Mode for Carbon isotopic screening

Compound-specific carbon isotopic compositions of fatty acids, HBIs, and other isoprenoids isolated from laboratory cultured marine diatom *P. intermedium* and *R. setigera* were determined by GC-IRMS using Combustion Mode (Figure 2-28). The combustion occurred in an O_2 atmosphere in a quartz reactor to produce CO_2, NO_x and H_2O with reactor temperatures typically between 900-1050 °C.

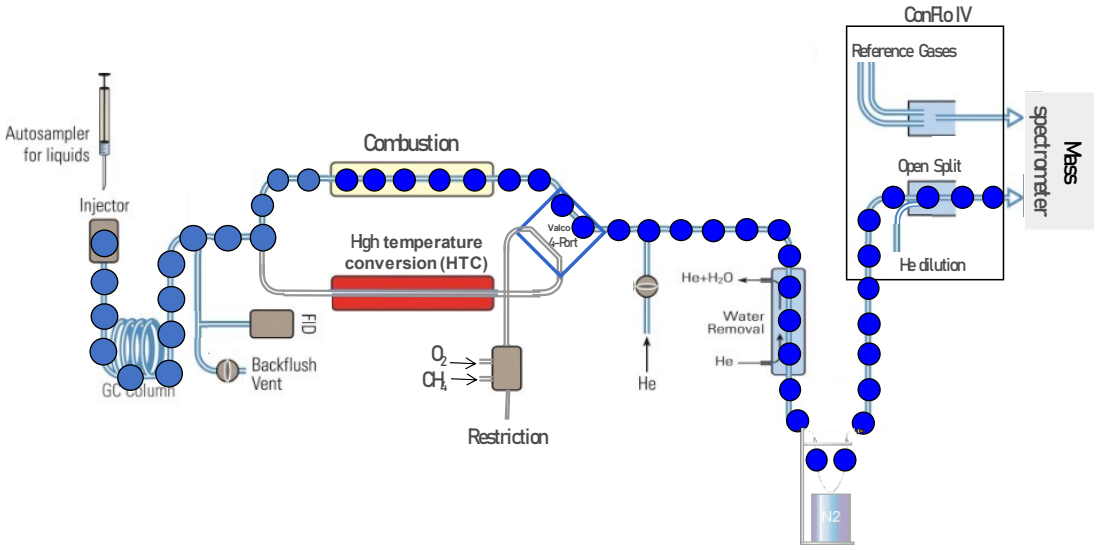

Figure 2-28. A schematic diagram of GC-IRMS in High Temperature Conversion (HTC) Mode for $^{13}C/^{12}C$ analysis. The combustion occurred in an O_2 atmosphere in a quartz reactor (yellow) to produce CO_2, NO_x and H_2O with reactor temperatures typically between 900-1050 °C.

The combustion system was maintained at 1020 °C for $\delta^{13}C$ analysis. The GC programme remained the same with HTC. Carbon isotope compositions were reported based on duplicate analyses of well-resolved peaks. $\delta^{13}C$ values were expressed relative to VPDB, based on in-house reference gases (CO_2) adjusted daily using the USGS72 standard. During all sample and standard measurements, eight reference gas pulses were passed through the mass spectrometer. Reproducibility of H2 reference gas $\delta^{13}C$ values did not exceed 0.2‰.

The CO_2 signals generated by GC-IRMS of reference gas, fatty acids (Figure 2-29) isolated from laboratory cultured marine diatom *P. intermedium* and *R. setigera*; HBIs C25:3, C25:4 (Figure 2-30 (a)); phytol and squalene (Figure 2-30 (b)) from P. intermedium and HBI C25:5 (Figure 2-31) from *R. setigera* are shown below.

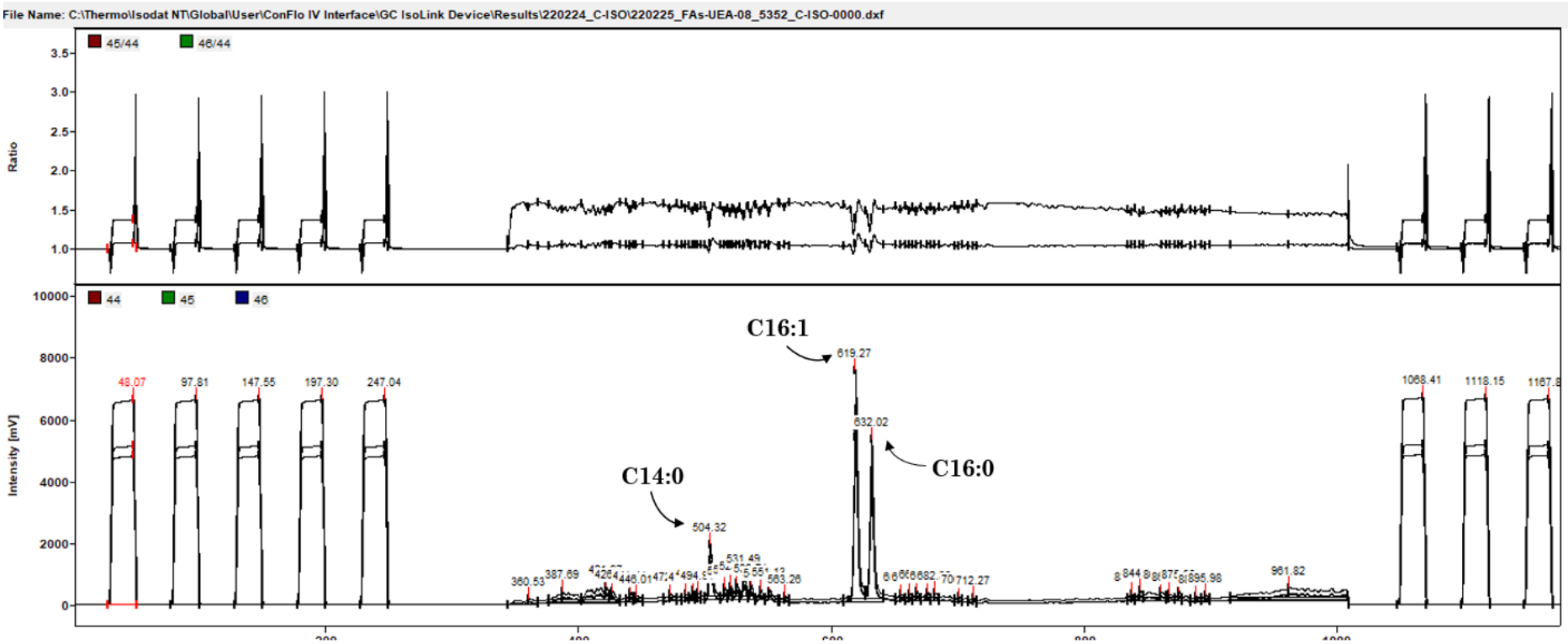

Figure 2-29. The CO_2 signals generated by GC-IRMS of (a) fatty acids C14:0 (RT = 504.32); C16:1 (RT = 619.27), C16:0 (RT = 632.02); (b) HBIs C25:3 (RT = 745.71), C25:4 (RT = 778.94) and (c) phytol (RT = 695.13) squalene (RT = 928.38) isolated from laboratory culture marine diatom *P. intermedium*. The upper chamber shows the mass ratio of 45 ($^{13}CO_2$ and/or $C^{17}O^{16}O$)/44 (CO_2) and 46 ($C^{18}O^{16}O$, $^{13}C^{17}O^{16}O$ and/or $C^{17}O_2$) and the lower chamber shows the intensity of mass CO_2 along with time (second). The first five and last three peaks are references gases.

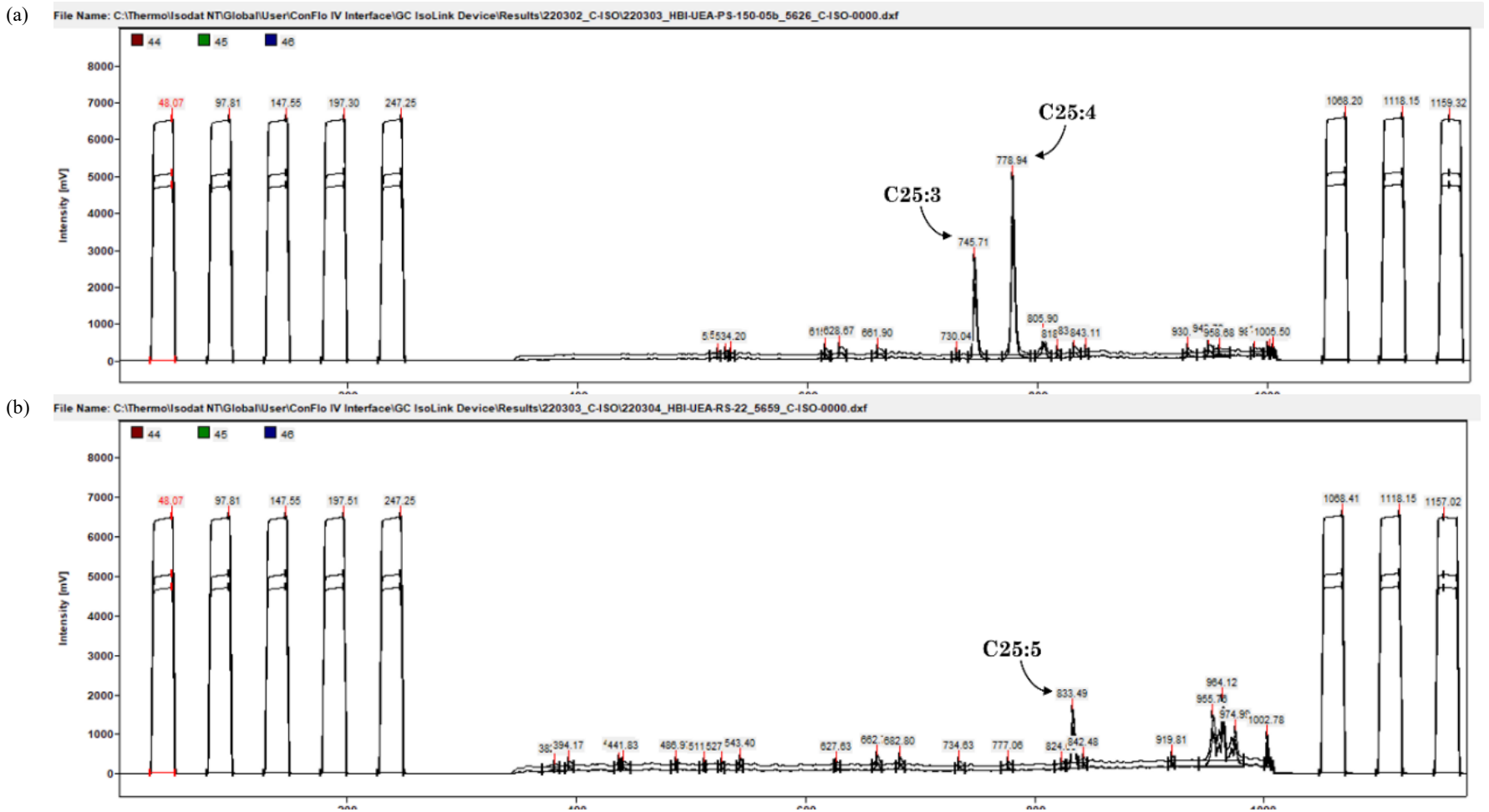

Figure 2-30. The CO_2 signals generated by GC-IRMS of (a) HBIs C25:3 (RT = 745.71), C25:4 (RT = 778.94) and (b) phytol (RT = 695.13) and squalene (RT = 928.38) isolated from laboratory culture marine diatom *P. intermedium* showing the intensity of CO_2 species (44 (CO_2), 45 ($^{13}CO_2$ and/or $C^{17}O^{16}O$) and 46 ($C^{18}O^{16}O$, $^{13}C^{17}O^{16}O$ and/or $C^{17}O_2$)) along with the time (second). The first five and last three peaks are references gases.

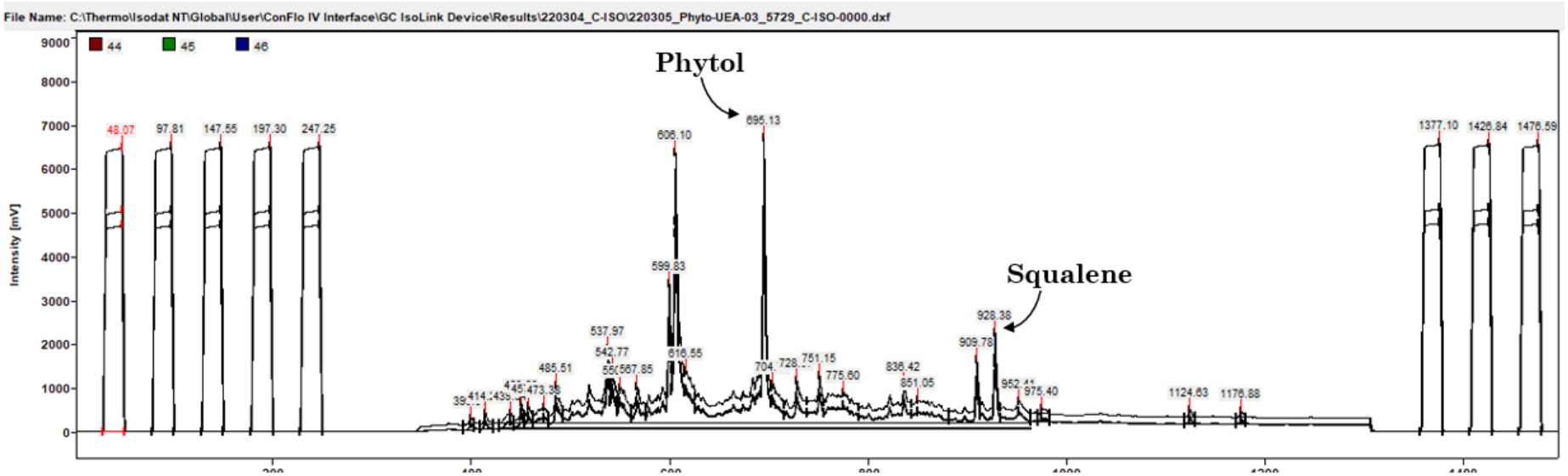

Figure 2-31. The CO_2 signals generated by GC-IRMS of HBI C25:5 (RT = 833.49) isolated from laboratory culture marine diatom *R. setigera* showing the intensity of CO_2 species (44 (CO_2), 45 ($^{13}CO_2$ and/or $C^{17}O^{16}O$) and 46 ($C^{18}O^{16}O$, $^{13}C^{17}O^{16}O$ and/or $C^{17}O_2$)) along with the time (second). The first five and last three peaks are references gases.

2.4.4 The normalization of measured Carbon stable isotopic compositions

The same normalization procedure of measured hydrogen isotopic compositions was applied to that of carbon. It came with the first step of plotting the raw δ-value of the certified standard on the y-axis and the analysis running sequence number of the individual standard on the x-axis (Figure 2-32).

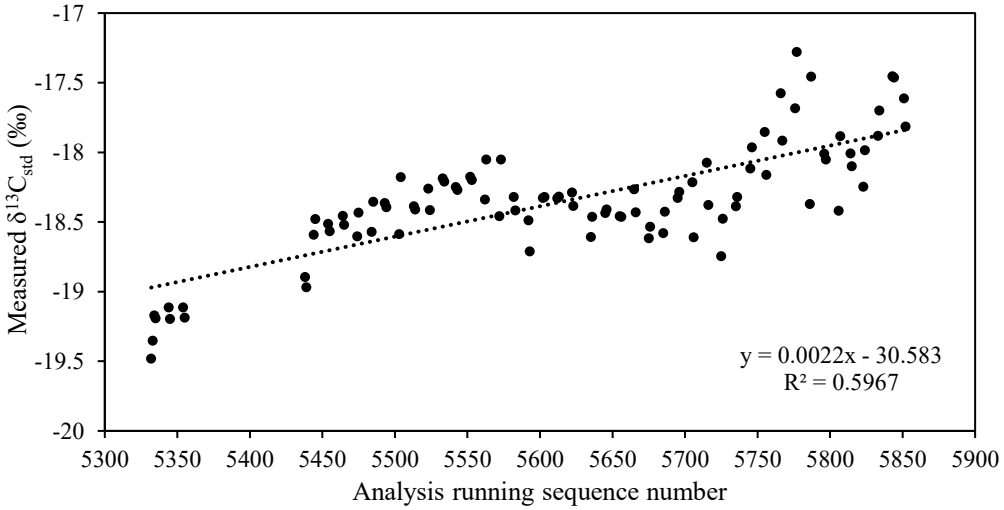

Figure 2-32. The linear shift of the raw $\delta^{13}C$ values of standard along with the analysis running sequence.

By fitting a linear regression line among samples, the equation of the regression line can be calculated as y = 0.0022x – 30.583 with a coefficient of determination R2 of 0.5967. As the carbon isotopic measurement required the additional step of oxidation before each injection, it took longer time than that of hydrogen. The analysis process was divided into five parts (analysis numbers 5332 – 5355, 5438 – 5485, 5493 – 5623, 5635 – 5815 and 5823 - 5852) based on the sample analysing date and the situation of the instrument. The linear regression was calculated in each piecewise expressed as y = kdx + b, where kd1 =0.0084 (Figure 2-33, (1)) , kd2 = 0.0070 (Figure 2-33, (2)), kd3 = -0.0002 (Figure 2-33, (3)), kd4=0.0039 (Figure 2-33, (4)), kd5=0.0172 (Figure 2-33, (5)).

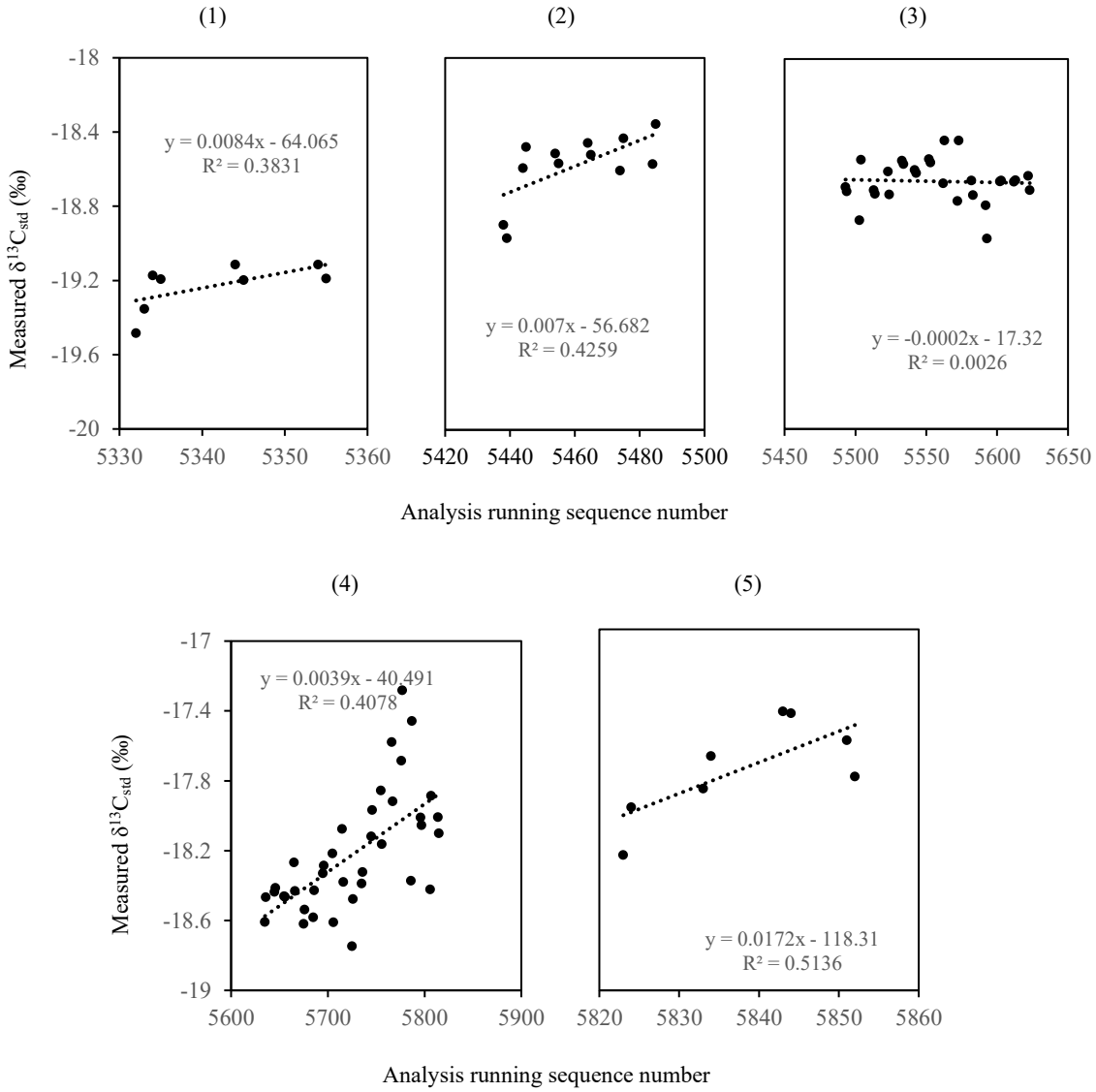

Figure 2-33. The piecewise linear regression of the raw $\delta^{13}C$ values of standard versus analysis running sequence number. Each piecewise linear regression was calculated as $y = k_{dx} + b$, where $k_{d1} = 0.0084$ (analysis number 5332 – 5355, $R^2 = 0.38$, (1)); $k_{d2} = 0.007$ (analysis number 5438 – 5485, $R^2 = 0.43$, (2)); $k_{d3} = -0.0002$ (analysis number 5493 – 5623, $R^2 = 0.0026$, (3)); $k_{d4} = 0.0039$ (analysis number 5635 – 5815, $R^2 = 0.41$, (4)); and $k_{d5} = 0.0172$ (analysis number 5823 - 5852, $R^2 = 0.51$, (5)).

The detrending of the raw $\delta^{13}C$ values of standard and sample was exactly the same as that of hydrogen by using the Eqn. (2-17) and (2-18).

Similarly, the regression of amount correction was calculated in five parts (analysis number 5332 – 5355, 5438 – 5485, 5493 – 5623, 5635 – 5815 and 5823 - 5852) as $y = k_a x + b$, whereas $k_{a1} = -0.0066$ (Figure 2-34 (1)), $k_{a2} = 0.0695$ (Figure 2-34 (2)), $k_{a3} = -0.0039$ (Figure 2-34 (3)), $k_{a4} = 0.1513$ (Figure 2-34 (4)) and $k_{a5} = -0.9626$ (Figure 2-34 (5)).

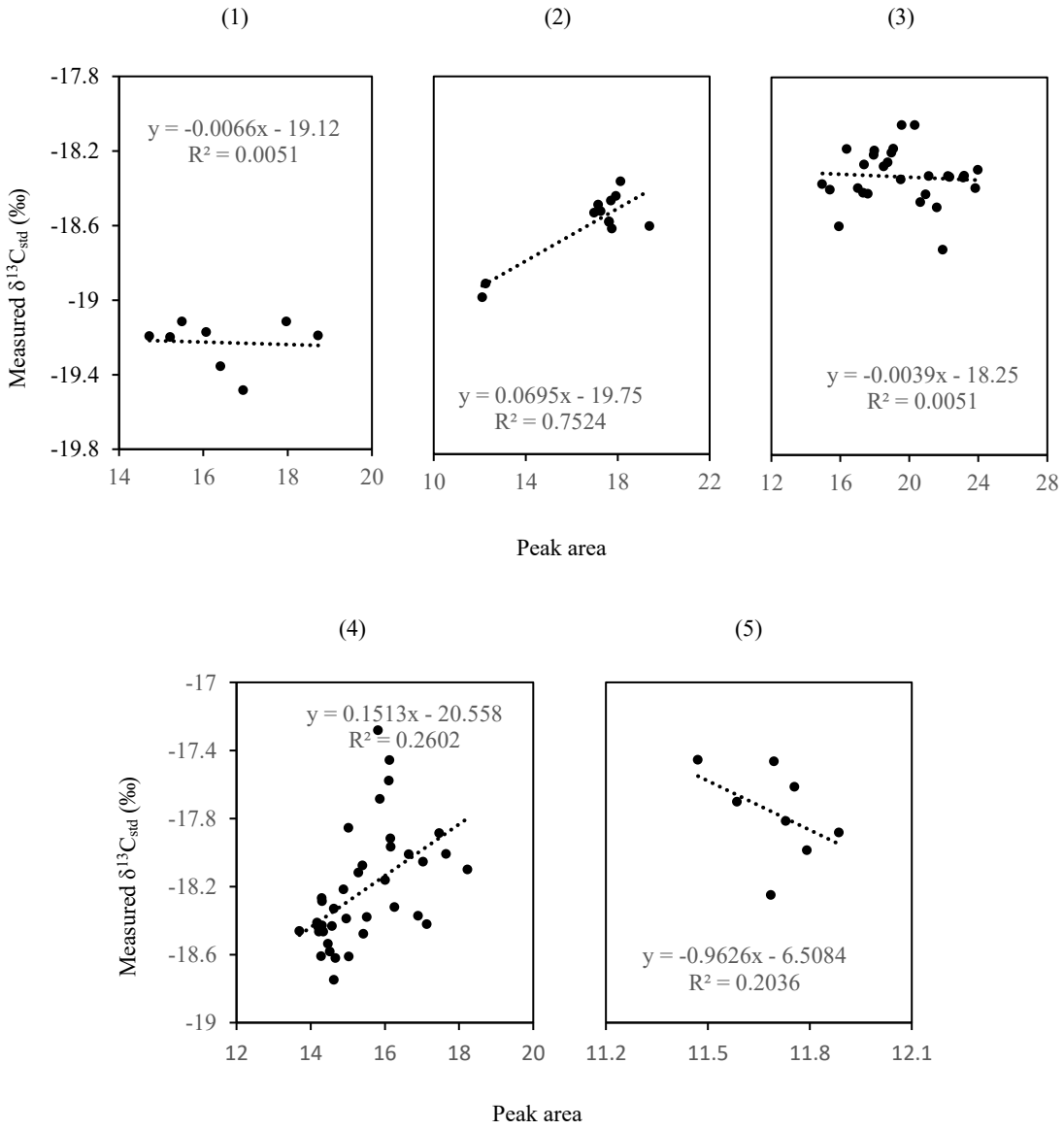

Figure 2-34. The piecewise linear regression of the detrended $\delta^{13}C$ values of standard versus varied amount of peak area. Each piecewise linear regression was calculated as $y = k_{dx} + b$, where $k_{d1} = -0.0066$ (analysis number 5332 – 5355, $R^2 = 0.0051$, (1)); $k_{d2} = 0.0695$ (analysis number 5438 – 5485, $R^2 = 0.75$, (2)); $k_{d3} = -0.0039$ (analysis number 5493 – 5623, $R^2 = 0.0051$, (3)); $k_{d4} = 0.1513$ (analysis number 5635 – 5815, $R^2 = 0.26$, (4)); and $k_{d5} = -0.9626$ (analysis number 5823 - 5852, $R^2 = 0.20$, (5)).

The correction of the peak area was then completed by applying the Eqn. (2-19) for the standards and Eqn. (2-20) for the samples. The normalisation of the measured carbon isotopic compositions of samples would be completed by applying the Eqn. (2-21).

2.5 Analytical uncertainty and error propagation

As real concern was posed over the performance of the analytical facility up to 30‰ using linear normalisation and detrending approach for the measured standard over time. Data was recalculated to reduce the analytical uncertainty and error propagation based on (Polissar & D'Andrea, 2014).

Here a spreadsheet created by Polissar & D'Andrea (2014) was used to calculate and propagate errors involved in δ2H analysis of molecular compounds following the directions below.

Prior to the recalculation, the number of measurements, mean, and the standard deviation of each standard on the reference gas scale were collated and calculated. The offline values of standards for hydrogen and carbon were reported as 348.3‰ and -1.54‰.

The reference gas value and uncertainty were first determined by inputting values of the mean, standard deviation and the number of measurements for each reference molecule on the reference gas scale, and the offline measurements on VSMOW scale on the spreadsheet "1 - Reference Gas". The mean of the mean reference gas δD values determined from difference reference molecules on the VSMOW scale (Mean δDrefgas, VSMOW) and uncertainty in the δDrefgas value were calculated as 202.2‰ and 9.3‰.

On the spreadsheet "2 - Analytical Uncertainty", the values for standard deviation and the number of replicate sample measurements were input, giving the pooled 1σ standard deviation for replicate measurement data as weighted by number of replicates (n -1) (Wt Average 1σ δDsample, refgas*) value as the analytical uncertainty for sample measurements.

The sample values on the VSMOW scale were determined on the spreadsheet "3 - Calculate Sample Composition" by inputting values for sample mean δD values on reference gas scale and the number of replicate sample measurements.

The related spreadsheet can be found in supplementary material. Here I only present the comparison of fatty acids C14:0, C16:1 and C16:0 isolated from marine diatom *Pleurosigma intermedium* harvested from stationary phase (Figure 2-35).

(a)

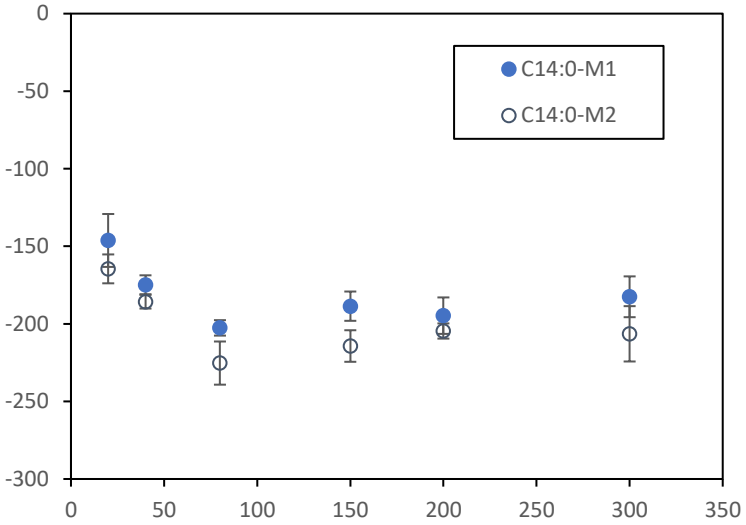

(b)

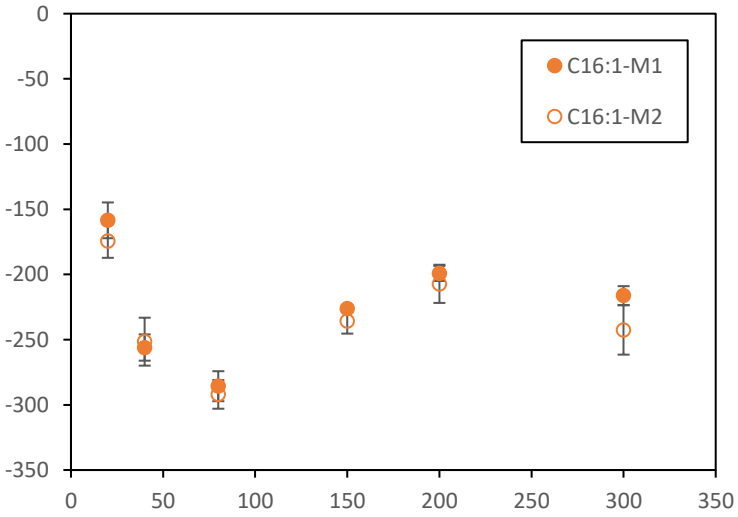

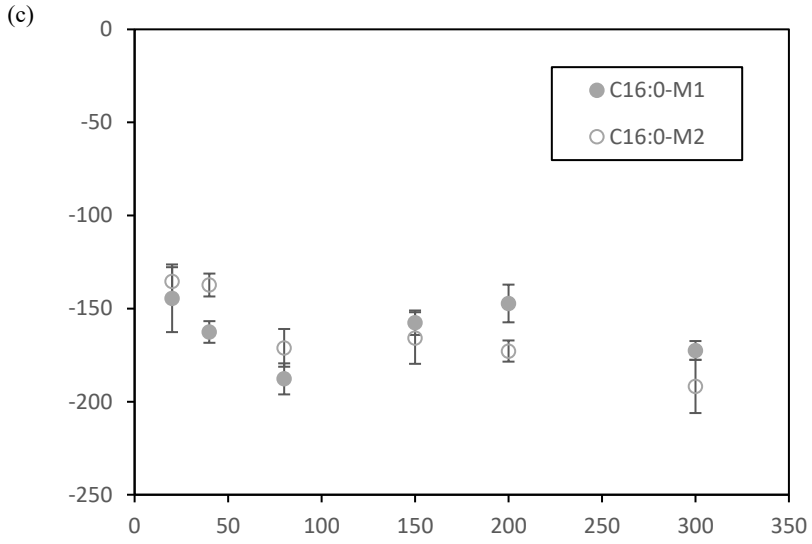

Figure 2-35. The comparison of the normalised hydrogen isotopic composition of fatty acid C14:0 (a), C16:1 (b) and C16:0 (c) isolated from laboratory cultured marine diatom *Pleurosigma intermedium* using linear normalisation and detrending (M1) versus analytical uncertainty and error propagation (M2).

The data calibrated according to Polissar & D'Andrea (2014) are relatively depleted by 10 - 20‰ compared to the data using linear normalisation and detrending. Two datasets fit most between light ranging from 80 – 200 μmol m^{-2} s^{-1} and both of these showed the same direction and responses to the varying high conditions. Considering the difficulty in hydrogen isotope measurements and error propagation occurring during the measurements and calibrations, I using high quantity of biological replicates to increase the accuracy and unfortunately this is the best I can do at this point. For the some samples, especially those harvested from low light and high light, re-analysis would be required in the future work.

To keep the consistent of this study, the following chapters would be discussed based on the data using linear normalisation and detrending.

3 The effect of irradiance on the growth rate and concentration of lipids from laboratory cultured marine diatom

Chapter three presents the results of the growth rate and concentration of lipids of laboratory cultured marine diatom *Navicula salinicola*, *Rhizosolenia setigera* (CCMP1330) and *Pleurosigma intermedium* (RCC6814) in varied light conditions.

First, the effect of light on diatom photosynthesis is briefly introduced in **3.1**. The growth rate of each specie at varied light levels is presented in **3.2**. The concentrations of fatty acids and HBI(s) of *P. intermedium* and *R. setigera* are shown in **3.3** and **3.4**. Actually, HBIs were detected in all three strains, including a new HBI triene (three double bonds) being discovered in *N. salinicola*. The full structure of this new HBI was determined and published (see Chapter 6). Unfortunately, we are not able to present the results of lipid yields of *N. salinicola* as the biomass has been used for structure identification. The discussion and conclusion are in **3.5** and **3.6**.

3.1 The effect of light on photosynthesis in diatoms

Photosynthesis is a process that phototrophic organisms capture light energy and assimilate carbon dioxide and water into sugar. Light is an essential element for photosynthesis. In laboratory conditions, where water, carbon dioxide, and moderate temperature are offered, the effect of light on algal growth can be described as a P/E curve (Figure 3-1). The compensation irradiance E_c represents the irradiance when the photosynthetic rate equals the respiration rate. The photosynthetic rate increases when the irradiance increases irradiance is relatively low. While the increase of light will then have progressively less effect on the photosynthetic rate. Once the light intensity gets high enough (E_k), the maximum rate of photosynthetic (P_{max}) will be reached. At this point, the increase of light will not affect photosynthesis owing to the limited amount of chlorophyll molecules. When light continues increasing, photoinhibition will occur and result in a decrease in photosynthetic rate.

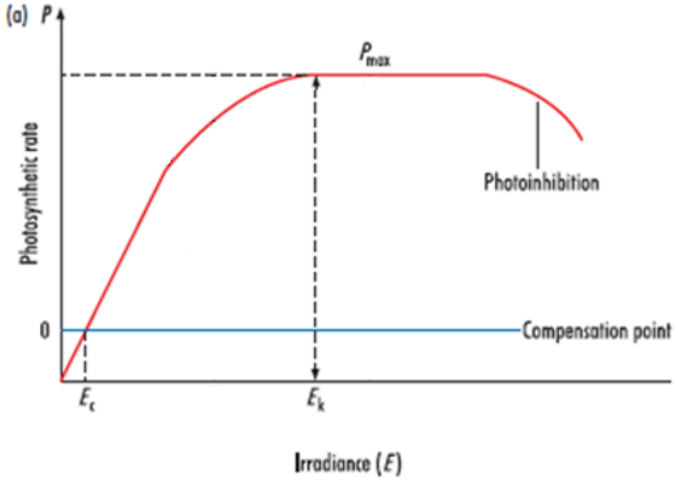

Figure 3-1. The photosynthesis (P) in response to increasing irradiance (E) - P/E curve. At the compensation irradiance E_c the photosynthetic rate is equal to the respiration rate. The photosynthetic rate increases with the irradiance when irradiance is relatively low. At the saturation irradiance (E_k), the rate of photosynthesis is saturated (P_{max}). In some organisms, there can be a decrease in photosynthetic rates at very high irradiance (photoinhibition). Modified from (Kaiser et al., 2011).

3.2 Result (1) The effect of irradiance on growth rate of laboratory cultured marine diatom *N. salinicola, R. setigera* and *P. intermedium*

N. salinicola was grown at a light gradient from 10 μmol m^{-2} s^{-1} to 270 μmol m^{-2} s^{-1} at 15°C. The growth rate was 0.10 d^{-1} at the light intensity of 10 μmol m^{-2} s^{-1} and increased as light increased. The maximum growth rate of 1.11 d^{-1} was reached at the light intensity of 150 μmol m^{-2} s^{-1}. When the light intensity continued increasing to 270 μmol m^{-2} s^{-1}, the growth rate was slightly dropped to 0.9538 d^{-1} (Figure 3-2 (square), Table 3-1).

P. intermedium were grown under irradiance ranging from 20 μmol m^{-2} s^{-1} to 300 μmol m^{-2} s^{-1} at 8 °C and 15 °C, respectively. Similarly pattern and magnitude responses to light with *N. salinicola* were observed in *P. intermedium*. The growth rate increased from 0.14 day^{-1} at the light intensity of 200 μmol m^{-2} s^{-1} to the maximum growth rate of 0.80 d^{-1} at the light intensity of 150 μmol m^{-2} s^{-1}, then remained constant at 200 μmol m^{-2} s^{-1} and slightly decreased at 300 μmol m^{-2} s^{-1} (Figure 3-2 (circle), Figure 3-3, Table 3-1).

The same light conditions were set up for *R. setigera*, while the growth temperature was dropped to 8°C because we failed to grow them at 15°C. The growth rate of *R. setigera* was significantly slower than other two strains, ranging from a minimum of 0.01 d^{-1} at the irradiance of 20 μmol m^{-2} s^{-1} to the maximum of 0.35 d^{-1} at 200 μmol m^{-2} s^{-1}. The growth of *R. setigera* slightly slow down to 0.33 d^{-1} when the light was 300 μmol m^{-2} s^{-1} (Figure 3-2 (triangle), Table 3-1).

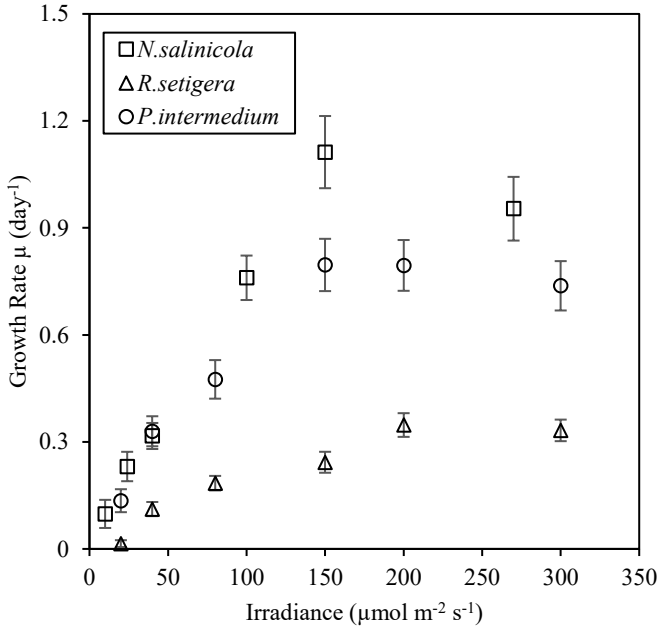

Figure 3-2. Growth rate μ plotted against irradiance of laboratory cultures of *N. salinicola* (□), *R. setigera* (○) and *P. intermedium* (△).

Cultures were harvested in the exponential phase and stationary phase respectively. The length of time (day) for each strain to reach the exponential phase and stationary phase are listed in Table 3-1. For the cultures at 15°C (*N. salinicola* and *P. intermedium*), the life span ranged from 12 days to 50 days depending on irradiance; while for *R. setigera* (cultured at 8 °C), it took almost 4 months to reach the stationary phase at lowest light intensity.

Table 3-1. The growth rate of *N. salinicola*, *R. setigera* strain CCMP 1330 and *P. intermedium* strain RCC6814 under different levels of light intensity and the amount of time (day) for each stain to reach the exponential (exp) phase and stationery (sta) phase.

Light intensity (μmol m^{-2} s^{-1})	Growth rate (μ, day^{-1})	Harvest time (exp/sta, day)
*N. salinicola,*15 ºC		
270	0.95	6/12
150	1.11	6/12
100	0.76	7/14
40	0.32	17/24
24	0.23	24/40
10	0.10	35/50
R. setigera strain CCMP 1330, 8 ºC		
300	0.33	20/27
200	0.35	20/27
150	0.24	20/29
80	0.18	27/44
40	0.11	48/71
20	0.01	53/114
P. intermedium strain RCC6814, 15 ºC		
300	0.74	6/12
200	0.79	8/16
150	0.80	8/20
80	0.48	12/25
40	0.33	15/28
20	0.14	21/46

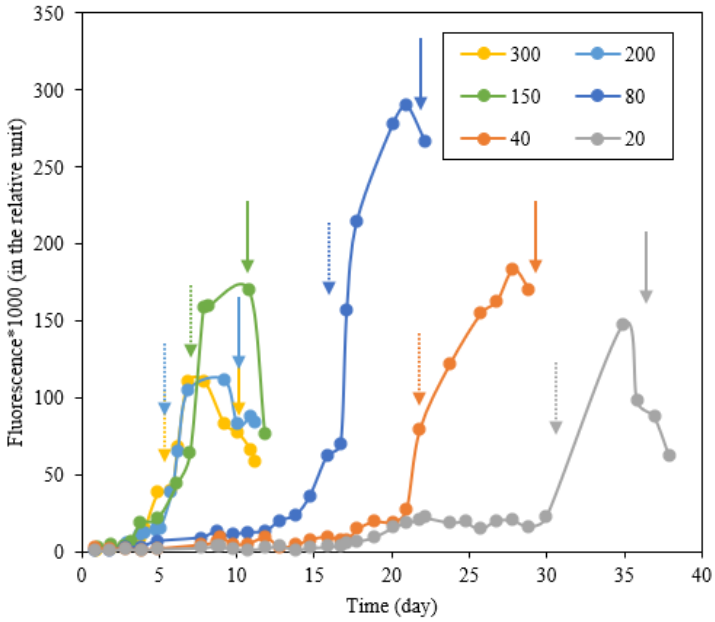

Figure 3-3. The growth curve of laboratory cultured marine diatom *Pleurosigma intermedium*. the biomass was estimated as fluorescence in the relative unit. The errors represent the sampling time point (dash, exponential phase; solid, stationary phase) of each samples cultured under varying light conditions.

3.3 Result (2) The lipid concentrations of laboratory cultured marine diatom *Pleurosigma intermedium*

Lipids of *P. intermedium* were harvested from exponential phase and stationary phase respectively. Fatty acids C14:0, C16:1 and C16:0, HBIs C25:3 and C25:4, phytol and squalene were detected in most samples, however, concentrations of phytol and squalene failed to calculate as the lack of the internal standard.

3.3.1 Fatty acids

For the samples from exponential phase, concentrations of fatty acids were between 0.34 – 4.22 mg g-1 for C14:0, 1.94 – 10.45 mg g-1 for C16:1 and 2.32 – 14.71 mg g-1 for C16:0 (Figure 3-4 (a), Table 3-2). For the samples from stationary phase, the concentrations of fatty acids were significantly higher by 5.24 - 26.36 mg g-1 for C14:0, 12.91 - 76.81 mg g-1 for C16:1 and 19.75 - 59.09 mg g-1 for 16:0 (Figure 3-4 (b), Table 3-3). The concentration of three fatty acids were positively correlated with irradiance in both growth phases, regardless the growth rate remained the same when irradiance was over 150 μmol m-2 s-1 (Figure 3-2).

No significant variation was observed in the relative concentrations of three fatty acids in response to varied light conditions in two growth phases. There seems to be a shift from fatty acid C16:0 to C16:1 in the growth of *P. intermedium* as C16:0 was the most abundant fatty acids in exponential phase while in stationary phase, C16:1 became the dominant fatty acids (Figure 3-4 (c, d)).

3.3.2 HBIs

Compared to fatty acids, concentrations of HBIs were significantly lower. The concentrations of C25:3 and C25:4 harvested from exponential phase were 7.01 – 265.44 μg g^{-1} and 4.01 – 451.61 μg g^{-1} respectively (Figure 3-5 (a), Table 3-2). For the samples harvested from stationary phase, the concentrations of C25:3 and C25:4 were 11.96 – 381.56 μg g^{-1} and 3.55 – 769.94 μg g^{-1} respectively (Figure 3-5 (b), Table 3-3).

HBIs concentrations of samples harvested from exponential phase were positively correlated with irradiance, increasing by 1.49 μg (μmol m^{-2} $s^{-1})^{-1}$ and 0.74 μg (μmol m^{-2} $s^{-1})^{-1}$ (C25:3, R^2=0.90; C25:4, R^2=0.95, Figure 3-5 (a)). While for the samples harvested from stationary phase, concentrations of C25:3 and C25:4 increased as light levels increased from 20 to 150 μmol m^{-2} s^{-1} and dropped after the maximum

growth rate was reached, giving a maximum yield of 356.12 μg g^{-1} for C25:3 and 718.43 μg g^{-1} for C25:4 (Figure 3-5 (b)).

The ratio of C25:3 versus C25:4 decreased sharply from 1.64 at the light intensity of 40 μmol m^{-2} s^{-1} to 0.46 at 300 μmol m^{-2} s^{-1} in exponential phase. Similar responses while greater sensitivity was observed in stationary phase. The ratio dropped from 2.77 at irradiance of 20 μmol m^{-2} s^{-1} to 0.37 at 300 μmol m^{-2} s^{-1} (Figure 3-5 (c, d)).

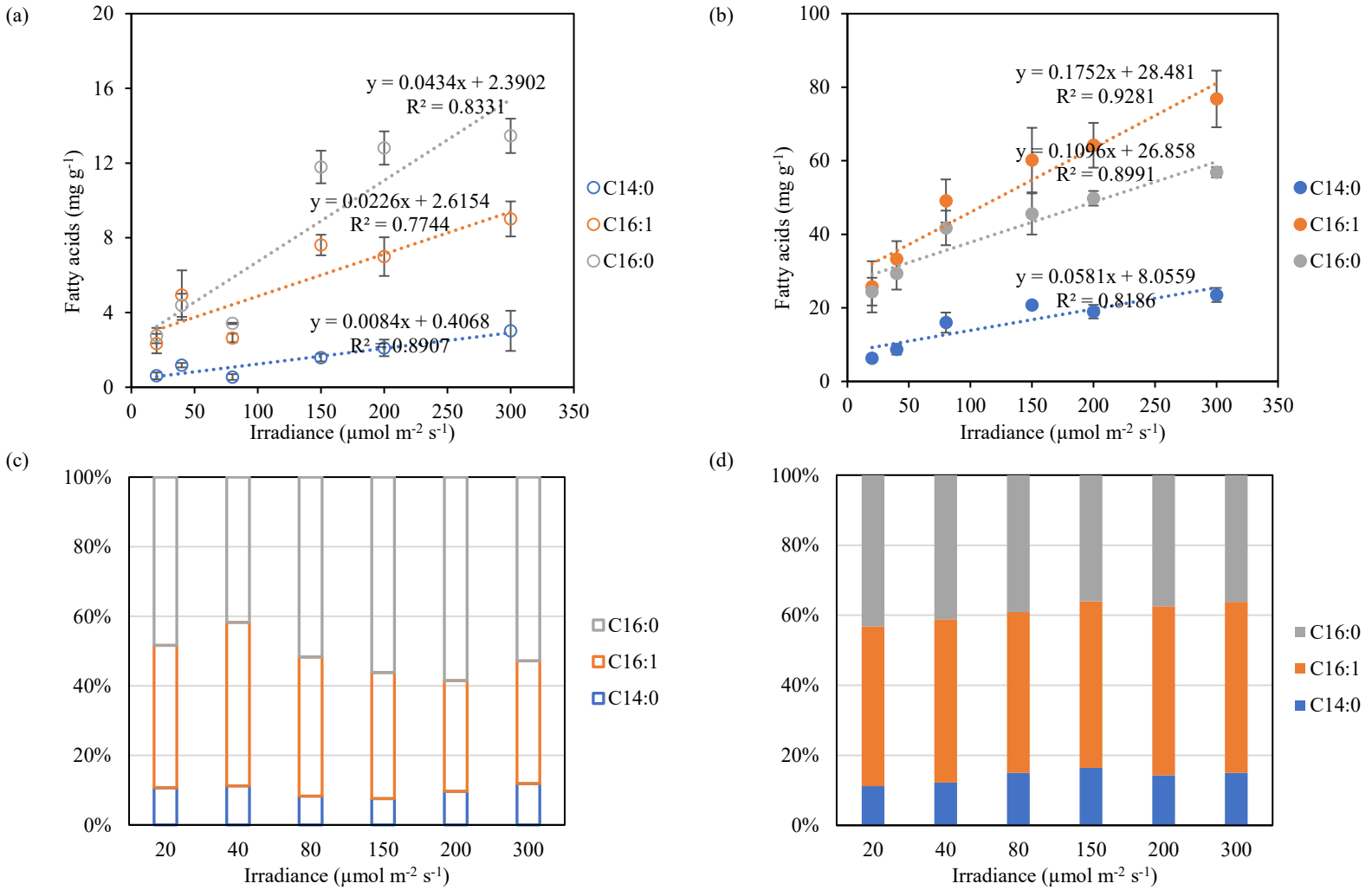

Figure 3-4. The concentrations (scatter) and relative values (100% stacked column) of fatty acids C14:0, C16:1 and C16:0 harvested from exponential phase (a, c) and stationary phase (b, d) of laboratory cultured marine diatom *P. intermedium* with different irradiance.

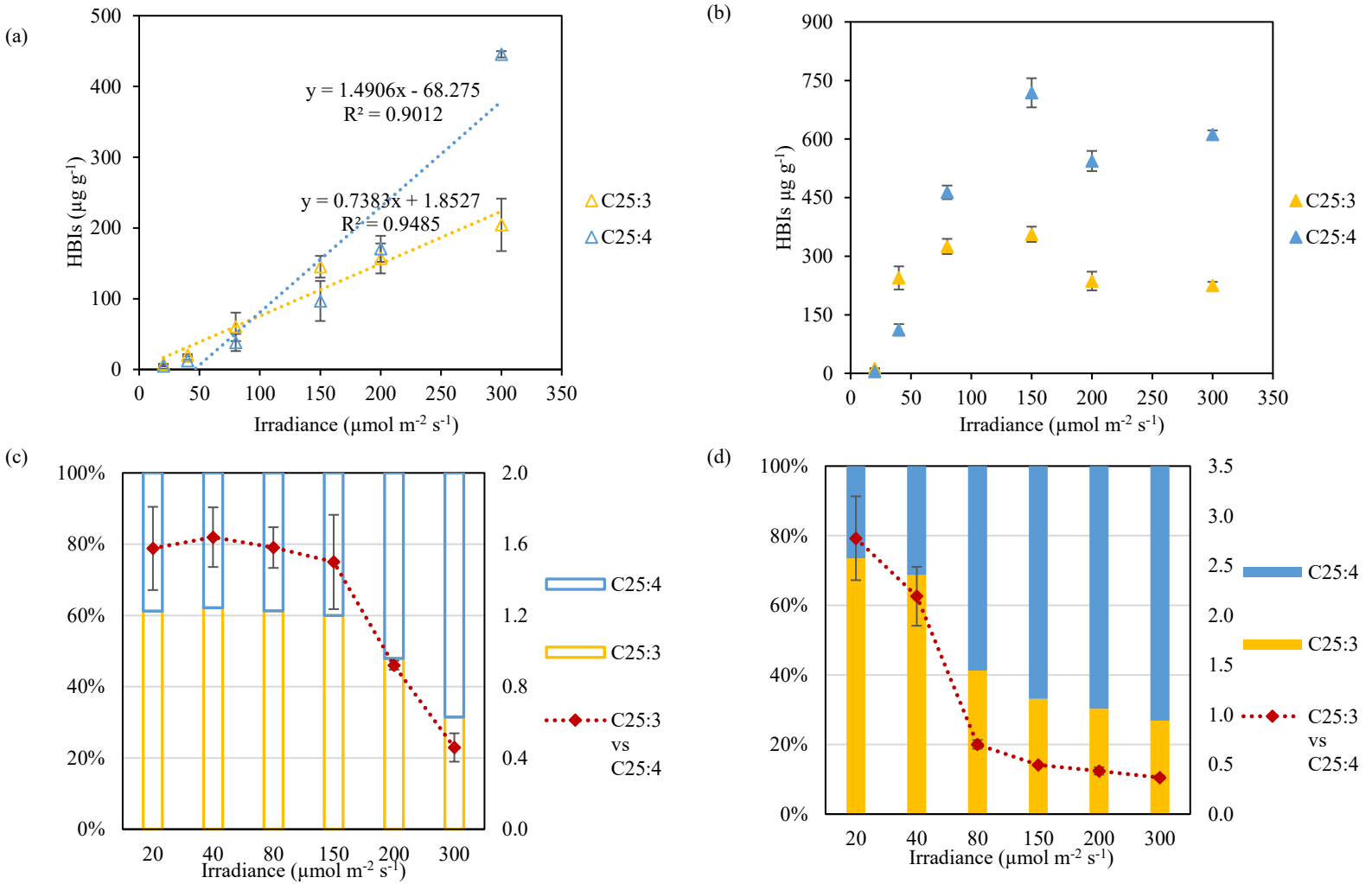

Figure 3-5. The concentrations (scatter) and relative values (100% stacked column) of HBIs C25:3 and C25:4 harvested from exponential phase (a, c, N=20) and stationary phase (b, d, N=18) of laboratory cultured marine diatom *P. intermedium* with different irradiance.

Table 3-2. The concentrations of fatty acids C14:0, C16:1, C16:0 and HBIs C25:3 and C25:4 harvested from exponential phase of laboratory cultured marine diatom *P. intermedium* with different irradiance. The alphabet represents biological repeats.

Irradiance ($\mu mol\ m^{-2}\ s^{-1}$)	Sample	Mass (freeze-dried, mg)	FAs ($mg\ g^{-1}$)			HBIs ($\mu g\ g^{-1}$)		C25:3 vs C25:4
			C14:0	C16:1	C16:0	C25:3	C25:4	
20	PI_20_01a_exp	2.51	N.A.	N.A.	N.A.	8.40	4.27	1.97
20	PI_20_01c_exp	2.32	N.A.	N.A.	N.A.	7.25	4.96	1.46
20	PI_20_02a_exp	2.70	0.71	1.94	2.32	7.44	5.32	1.40
20	PI_20_03a_exp	2.60	0.83	3.22	3.44	7.14	4.01	1.78
20	PI_20_04a_exp	2.40	0.34	1.98	2.63	7.01	5.06	1.38
20	PI_20_04b_exp	2.90	0.56	2.21	2.67	N.A.	N.A.	N.A.
Ave			0.61	2.34	2.77	7.45	4.72	1.60
Stdev			0.18	0.52	0.41	0.50	0.50	0.23
40	PI_40_03a_exp	4.50	1.25	6.80	4.28	19.66	13.75	1.43
40	PI_40_03b_exp	4.50	1.28	3.86	5.20	22.13	12.06	1.83
40	PI_40_03c_exp	2.60	1.01	4.14	3.70	18.88	11.19	1.69
Ave			1.18	4.93	4.39	20.22	12.34	1.65
Stdev			0.12	1.33	0.62	1.39	1.06	0.17
80	PI_80_01a_exp	0.27	N.A.	N.A.	N.A.	40.54	28.42	1.43
80	PI_80_02a_exp	3.10	0.40	2.88	3.45	87.85	55.19	1.59
80	PI_80_02b_exp	2.70	0.70	2.41	3.38	52.28	30.67	1.70
Ave			0.55	2.64	3.42	60.23	38.09	1.57
Stdev			0.15	0.23	0.04	20.12	12.12	0.11
150	PI_150_01a_exp	0.73	N.A.	N.A.	N.A.	144.23	84.70	1.70
150	PI_150_01b_exp	0.74	N.A.	N.A.	N.A.	121.59	64.95	1.87
150	PI_150_03a_exp	2.30	1.54	9.26	14.14	N.A.	N.A.	N.A.
150	PI_150_03b_exp	3.40	1.86	7.52	10.62	164.05	141.94	1.16
150	PI_150_03c_exp	3.10	1.36	6.99	12.03	150.75	95.45	1.58
Ave			1.59	7.61	11.59	145.15	96.76	1.58
Stdev			0.21	0.55	0.87	15.37	28.28	0.26
200	PI_200_03a_exp	2.70	1.94	7.09	12.20	135.79	152.12	0.89
200	PI_200_03b_exp	2.80	2.72	8.21	12.15	178.08	188.91	0.94
200	PI_200_03c_exp	1.60	1.67	4.73	11.72	N.A.	N.A.	N.A.
Ave			2.11	6.68	12.03	156.94	170.51	0.92
Stdev			0.44	1.45	0.21	21.15	18.39	0.03

(Continued on next page)

Table 3-2 (continued). The concentrations of fatty acids C14:0, C16:1, C16:0 and HBIs C25:3 and C25:4 harvested from exponential phase of laboratory cultured marine diatom *P. intermedium* with different irradiance. The alphabet represents biological repeats.

300	PI_300_01a_exp	0.67	N.A.	N.A.	N.A.	191.90	439.04	0.44
300	PI_300_01b_exp	1.48	1.28	8.12	12.24	195.18	444.83	0.44
300	PI_300_03a_exp	4.00	3.35	8.24	14.71	265.44	451.61	0.59
300	PI_300_03b_exp	4.20	3.24	9.24	13.03	N.A.	N.A.	N.A.
300	PI_300_03c_exp	4.20	4.22	10.45	13.86	165.18	446.47	0.37
Ave			3.02	9.01	13.46	204.42	445.49	0.46
Stdev			1.08	0.94	0.92	37.10	4.48	0.08

n.d. not detected
n.a. not available

Table 3-3. The concentrations of fatty acids C14:0, C16:1, C16:0 and HBIs C25:3 and C25:4 harvested from stationary phase of laboratory cultured marine diatom *P. intermedium* with different irradiance. The alphabet represents biological repeats.

Irradiance ($\mu mol\ m^{-2}\ s^{-1}$)	Sample	Mass (freeze-dried, mg)	FAs ($mg\ g^{-1}$)			HBIs ($\mu g\ g^{-1}$)		C25:3 vs C25:4
			C14:0	C16:1	C16:0	C25:3	C25:4	
20	PI_20_06a	5.10	7.97	32.97	29.17	N.A.	N.A.	N.A.
20	PI_20_06c	4.60	5.54	12.91	21.83	11.96	5.07	2.36
20	PI_20_08c	8.20	5.24	27.39	22.76	n.d.	n.d.	n.a.
20	PI_20_09a	7.80	6.65	30.44	28.59	13.30	4.82	2.76
20	PI_20_09c	8.30	6.13	24.92	19.75	12.01	3.55	3.38
Ave			6.31	25.73	24.42	12.43	4.48	2.83
Stdev			0.97	6.96	3.77	0.62	0.67	0.42
40	PI_40_01a	5.08	6.42	32.82	23.41	n.d.	n.d.	n.a.
40	PI_40_06a	5.80	8.73	31.71	27.42	215.31	92.85	2.32
40	PI_40_06b	5.90	9.52	41.00	35.18	285.12	113.39	2.51
40	PI_40_06c	6.10	10.15	27.51	31.48	232.50	128.34	1.81
Ave			8.70	33.26	29.37	244.31	111.52	2.22
Stdev			1.41	4.89	4.40	29.70	14.55	0.30
80	PI_80_01c	2.34	12.50	52.56	41.72	n.d.	n.d.	n.a.
80	PI_80_06a	8.80	20.04	54.85	47.91	334.96	488.07	0.69
80	PI_80_06b	6.80	16.51	49.38	42.64	342.20	449.28	0.76
80	PI_80_06c	7.90	14.90	39.52	34.69	297.67	453.19	0.66
Ave			15.99	49.08	41.74	324.94	463.51	0.70
Stdev			2.74	5.85	4.70	19.51	17.44	0.04
150	PI_150_05a	7.70	21.71	71.88	53.44	333.94	682.64	0.49
150	PI_150_05b	8.00	20.23	57.95	42.05	352.86	702.70	0.50
150	PI_150_05c	7.30	20.43	50.71	41.14	381.56	769.94	0.50
Ave			20.79	60.18	45.54	356.12	718.43	0.50
Stdev			0.65	8.79	5.60	19.58	37.33	0.01
200	PI_200_01b	2.17	18.93	58.76	48.32	n.d.	n.d.	n.a.
200	PI_200_05a	5.00	17.77	69.84	51.85	247.75	578.56	0.43
200	PI_200_05b	6.70	21.97	70.72	51.65	202.98	516.52	0.39
200	PI_200_05c	5.10	17.19	57.55	47.34	258.36	536.08	0.48
Ave			18.97	64.22	49.79	236.37	543.72	0.43
Stdev			1.84	6.09	1.99	24.00	25.90	0.04

(Continued on next page)

Table 3-3 (continued). The concentrations of fatty acids C14:0, C16:1, C16:0 and HBIs C25:3 and C25:4 harvested from stationary phase of laboratory cultured marine diatom *P. intermedium* with different irradiance. The alphabet represents biological repeats.

300	PI_300_01b	1.04	N.A.	N.A.	N.A.	237.01	605.88	0.39
300	PI_300_01c	1.02	26.36	67.01	56.59	n.d.	n.d.	n.a.
300	PI_300_05a	6.30	24.12	88.56	59.09	214.45	626.65	0.34
300	PI_300_05b	6.00	22.16	76.64	56.59	223.57	602.98	0.37
300	PI_300_05c	6.00	21.42	75.03	55.18	n.d.	n.d.	n.a.
Ave			23.51	76.81	56.86	255.01	611.84	0.37
Stdev			1.91	7.71	1.41	9.27	10.54	0.02

n.d. not detected
n.a. not available

3.4 Result (3) The lipid concentrations from laboratory cultured marine diatom *Rhizosolenia setigera*

The concentrations of fatty acids and HBI C25:5 were significantly lower than that of *P. intermedium*. Here we only presented the lipid concentration of *R. setigera* harvested from stationary phase.

The concentrations of fatty acids were between 1.31 – 8.48 mg g^{-1} for C14:0; 0.91 – 3.22 mg g^{-1} for C16:1 and 3.8 – 6.62 mg g^{-1} for C16:0. The yield of fatty acids first increased with light and reached the maximum concentration at the irradiance of 150 µmol m^{-2} s^{-1} then decreased along with the increase of light (Figure 3-6, Table 3-4).

The concentrations of HBI C25:5 showed a negative correlation with light, ranging from 3.06 µg g^{-1} at the light intensity of 300 µmol m^{-2} s^{-1} to 28.12 µg g^{-1} at the light intensity of 20 µmol m^{-2} s^{-1} (Figure 3-7, Table 3-4).

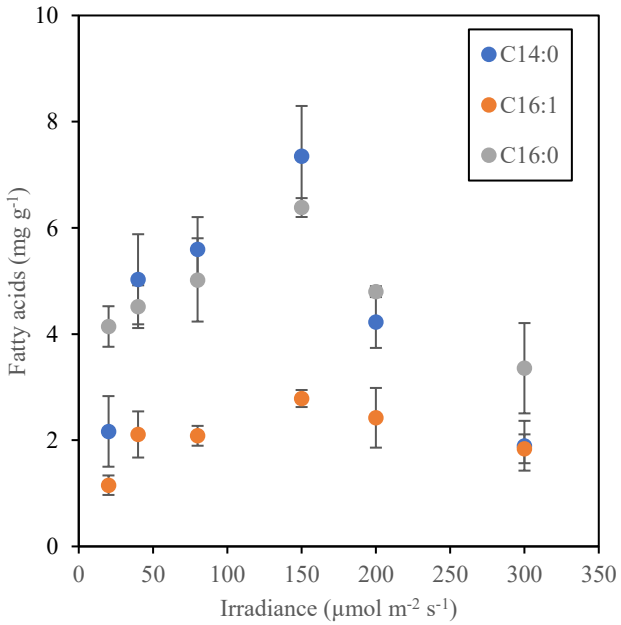

Figure 3-6. The concentrations of fatty acids C14:0, C16:1 and C16:0 harvested from stationary phase of laboratory cultured marine diatom *R. setigera* with varying irradiance, N=18.

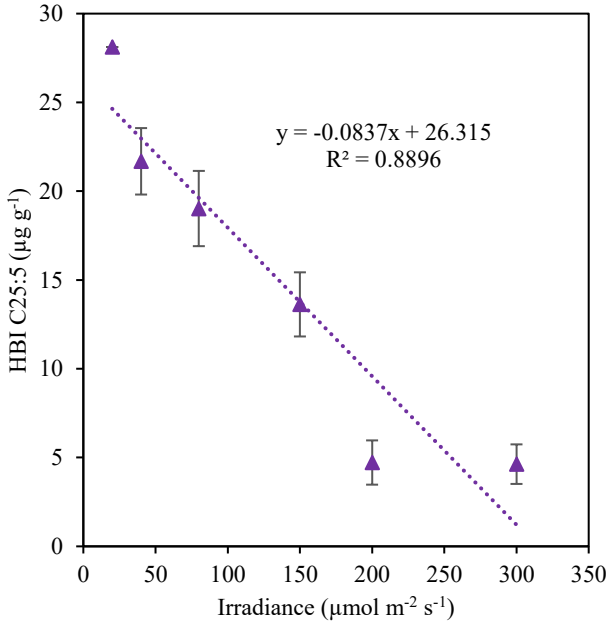

Figure 3-7. The concentrations of HBI C25:5 harvested from stationary phase of laboratory cultured marine diatom *R. setigera* with varying irradiance. The concentrations of HBI C25:5 decreased as irradiance increased by 0.084 µg g^{-1} (µmol m^{-2} s^{-1})$^{-1}$, N=15.

Table 3-4. The concentrations of fatty acids C14:0, C16:1, C16:0 and HBI C25:5 harvested from stationary phase of laboratory cultured marine diatom *R. setigera* with different irradiance. The alphabet represents biological repeats.

Irradiance (µmol m^{-2} s^{-1})	Sample	Mass (freeze-dried, mg)	FAs (mg g^{-1})			HBI (µg g^{-1})
			C14:0	C16:1	C16:0	
20	RS_20a	0.34	2.25	1.35	3.94	N.A.
20	RS_20b	0.88	2.94	1.21	3.81	28.12
20	RS_20c	0.10	1.31	0.91	4.68	N.A.
	Ave		2.17	1.15	4.14	28.12
	Stdev		0.66	0.18	0.38	N.A.
40	RS_40a	1.75	6.23	2.59	5.08	23.44
40	RS_40b	2.81	4.44	1.53	4.32	19.09
40	RS_40c	1.18	4.42	2.20	4.15	22.52
	Ave		5.03	2.11	4.52	21.68
	Stdev		0.85	0.43	0.40	1.87
80	RS_80a	4.30	6.38	2.05	5.92	16.46
80	RS_80b	3.23	5.51	2.33	5.13	21.65
80	RS_80c	6.03	4.90	1.88	4.01	18.96
	Ave		5.60	2.08	5.02	19.02
	Stdev		0.61	0.19	0.78	2.12
150	RS_150a	9.01	6.18	2.86	6.34	N.A.
150	RS_150b	6.21	8.48	2.56	6.19	15.43
150	RS_150c	4.93	7.40	2.94	6.62	11.82
	Ave		7.35	2.79	6.38	13.63
	Stdev		0.94	0.16	0.18	1.81
200	RS_200a	7.65	4.83	3.22	4.80	4.98
200	RS_200b	4.66	4.20	2.04	4.67	3.08
200	RS_200c	6.55	3.64	2.01	4.92	6.10
	Ave		4.22	2.42	4.80	4.72
	Stdev		0.49	0.56	0.10	1.25
300	RS_300a	7.31	1.33	1.54	2.16	3.06
300	RS_300b	2.51	1.89	1.77	4.03	5.54
300	RS_300c	5.03	2.47	2.20	3.88	5.29
	Ave		1.90	1.84	3.36	4.63
	Stdev		0.47	0.27	0.85	1.11

3.5 Discussion

3.5.1 The concentration of lipids as a function of growth rate

The correlation between the growth rate of laboratory cultures and irradiance showed a good agreement with the theoretical P/E curve (Figure 3-1). The maximum growth rate of 1.11 d^{-1} and 0.80 d^{-1} was observed at the light intensity of 150 µmol m^{-2} s^{-1} in *N. salinicola* and *P. intermedium*, and 0.35 day^{-1} at 200 µmol m^{-2} s^{-1} in *R. setigera*.

In this study, growth rate served as a function of light and will further lead to great variations in the yield of lipids. The magnitude of these variations may differ from lipid class. Here, we observed the different directions of fatty acids and HBIs C25:3 and C25:4 harvested from stationary phase of *P. intermedium* in response to varied light conditions. The yields of fatty acids and HBIs both showed a positive correlation with light before reaching the maximum growth rate. Once light intensity was saturated (E_k), the concentration of fatty acids continued increasing and remained in the linear correlation with irradiance, while the yield of HBIs greatly dropped. It should be noted that this was only observed in samples from the stationary phase.

As the energy storage compound, fatty acids hold the highest priority among all lipid classes. The yield of fatty acids can be up to a hundredfold greater than that of HBIs. It seems that the cell stopped producing more HBIs at stationary phase when the maximum growth rate was reached. Actually, the yield of HBI produced by *R. setigera* deceased as light increased. For the increasing yields of fatty acids at high irradiance, it can be seen as a response for storing excess reductant produced in the light reaction of photosynthesis since fatty acids synthesis consumes twice as much NADPH as protein or carbohydrate synthesis.

3.5.2 Decreasing ratio of C25:3 versus C25:4 with the increase of irradiance

Very few studies investigated the effect of growth conditions on HBI distributions within a species in the past. The most definitive relationship was identified by (Rowland et al., 2001). Their cultures experiments of *Haslea ostrearia* at different

temperatures showed that predominant HBI produced by *H. ostrearia* had more double bonds in higher growth temperatures.

A significant decrease in the ratio of C25:3 versus C25:4 along with the increase of light was observed in both the exponential phase and stationary phase (Figure 3-5 (c, d)). Unfortunately much remains unknown about the biosynthesis pathway, function of HBIs and the mechanism underlying the HBI distribution in response to varied growth conditions so far. Based on the observations from our experiments and (Rowland et al., 2001), the number of double bonds likely benefits from a higher growth rate either by higher growth temperature or higher irradiance.

3.6 Conclusion

Light-controlled growth experiments of *N. salinicola*, *P. intermedium* and *R. setigera* showed the growth rate of all three strains increased as the light increased until the maximum growth rate was reached. The yields of fatty acids produced by *P. intermedium* remained proportionate to the irradiance even at the highest irradiance, while the yield of HBIs dropped after reaching the maximum growth rate. In addition, an inversed correlation between the concentration of HBI C25:5 produced by *R. setigera* and light intensity was observed.

In terms of the relative amount of HBIs C25:3 and C25:4 produced by *P. intermedium*, a sharp diminishing of the fraction of C25:3 was observed both in the exponential phase and stationary phase as the light increased. However, this link requires more growth experiments at light levels between 40 - 200 μmol m^{-2} s^{-1} to support. Once confirmed, the ratio of C25:3 versus C25:4 can be potentially used as a proxy to indicate light conditions. However, in practical application, the biodegradation and shift between HBIs should be taken into consideration.

The observation of the responses of HBI(s) concentration to varied growth rate/light conditions might provide new insights into understanding the function and mechanism regulating the distribution of HBI(s) in different strains.

The results of this chapter will also help us decipher the hydrogen and carbon isotopic data in Chapter 4 5and Chapter 5.

4 The effect of irradiance on Hydrogen isotopic compositions of lipids from laboratory cultured marine diatom *Pleurosigma intermedium* and *Rhizosolenia setigera*

The study of hydrogen and carbon stable isotopic compositions of lipids from environmental samples and laboratory cultures has become an integral component of research in Earth sciences. Lipids may differ greatly in their chemical structure and function within and among different organisms, ultimately, the biosynthesis of all lipids requires inorganic sources of carbon and hydrogen. This makes the link between the isotopic composition of lipids and various environmental parameters such as salinity, temperature, CO_2 concentrations, etc.

Pioneering studies of compound-specific $^{13}C/^{12}C$ (Freeman et al., 1990; Hayes et al., 1990) and $^{2}H/^{1}H$ (Sauer et al., 2001; Sessions et al., 1999) analyses have shown the potential of the compound-specific isotopes to reconstruct various environmental conditions. However, much remains unknown about the detailed biosynthetic process of the inorganic elements to a specific lipid compound and the mechanisms underlying the influence of internal and external factors on isotopic signatures of different lipid classes.

To narrow this gap, we have conducted a series of light-controlled laboratory culture experiments and measured the hydrogen isotopic compositions of different lipid classes from two diatom strains.

Chapter four first describes the photosynthesis and biosynthetic process and highlights the steps which might result in large $^{2}H/^{1}H$ fractionation in **4.1**. Followed by a summary of factors controlling the hydrogen isotope fractionation of algal lipids and related published work in **4.2**. The hydrogen isotopic compositions and fractionation factor (α) of fatty acids, highly branched isoprenoids (HBIs), phytol and squalene from laboratory cultured marine diatom *Pleurosigma intermedium* and *Rhizosolenia setigera* are shown in **4.3** and **4.4**, following with detailed discussions in **4.5** and conclusion in **4.6**.

Frequently used abbreviations in this chapter are listed in Table 4-1. Carbon isotope-related results will be discussed in Chapter 5.

Table 4-1. Frequent used abbreviations in Chapter FOUR.

Abbreviation	Description
3-PGA	3-PhosphoGlyceric Acid
ACT	Acetogenic
ADP	Adenosine DiPhosphate
ATP	Adenosine TriPhosphate
CoA	Coenzyme A
DMAPP	DiMethylAllyl PyroPhosphate
FNR	Ferredoxin–NADP Reductase
G3P	Glyceraldehyde 3-Phosphate
HBIs	Highly Branched Isoprenoids
IPP	Isopentenyl PyroPhosphate
KIE	Kinetic Isotope Effect
DOXP/MEP	1-deoxy-D-xylulose-5-phosphate/2-methylerythroyl-4-phosphate
MVA	Mevalonate
$NADP^+$	Nicotinamide Adenine Dinucleotide Phosphate
NADPH	Reduced Nicotinamide Adenine Dinucleotide Phosphate
PS-I	PhotoSystem I
PS-II	PhotoSystem II
RuBP	Ribulose-1,5-BisPhosphate

4.1 Introduction

As briefly introduced in 1.7.2, water is the sole hydrogen source of photosynthesizing organisms and their products. Hence, understanding the process of hydrogen from the water source into organic compounds during photosynthesis and biosynthesis is of great importance. An overview of this process and the main lipid classes discussed in this chapter is shown in Figure 4-1 (a).

4.1.1 Photosynthesis

Photosynthesis is the process that phototrophic organisms capture energy from light to convert carbon dioxide into carbohydrates and fuel the organism's activities. This is the very first step that environmental water being converted into organic matter.

Photosynthesis occurs in two stages – light-dependent reactions (short as light reactions) which capture the energy of light and then produce the hydrogen carrier NADPH and the energy-storage molecule ATP; and light-independent reactions (Calvin-Benson-Bassham Cycle) which use the production of light reactions to assimilate carbon dioxide.

Light reactions take place on the thylakoid membranes (Figure 4-1 (b)) which contain some integral membrane protein complexes including Photosystem II (PS-II), Cytochrome b6f complex, Photosystem I (PS-I), and ATP synthase (Figure 4-1 (b) (c)).

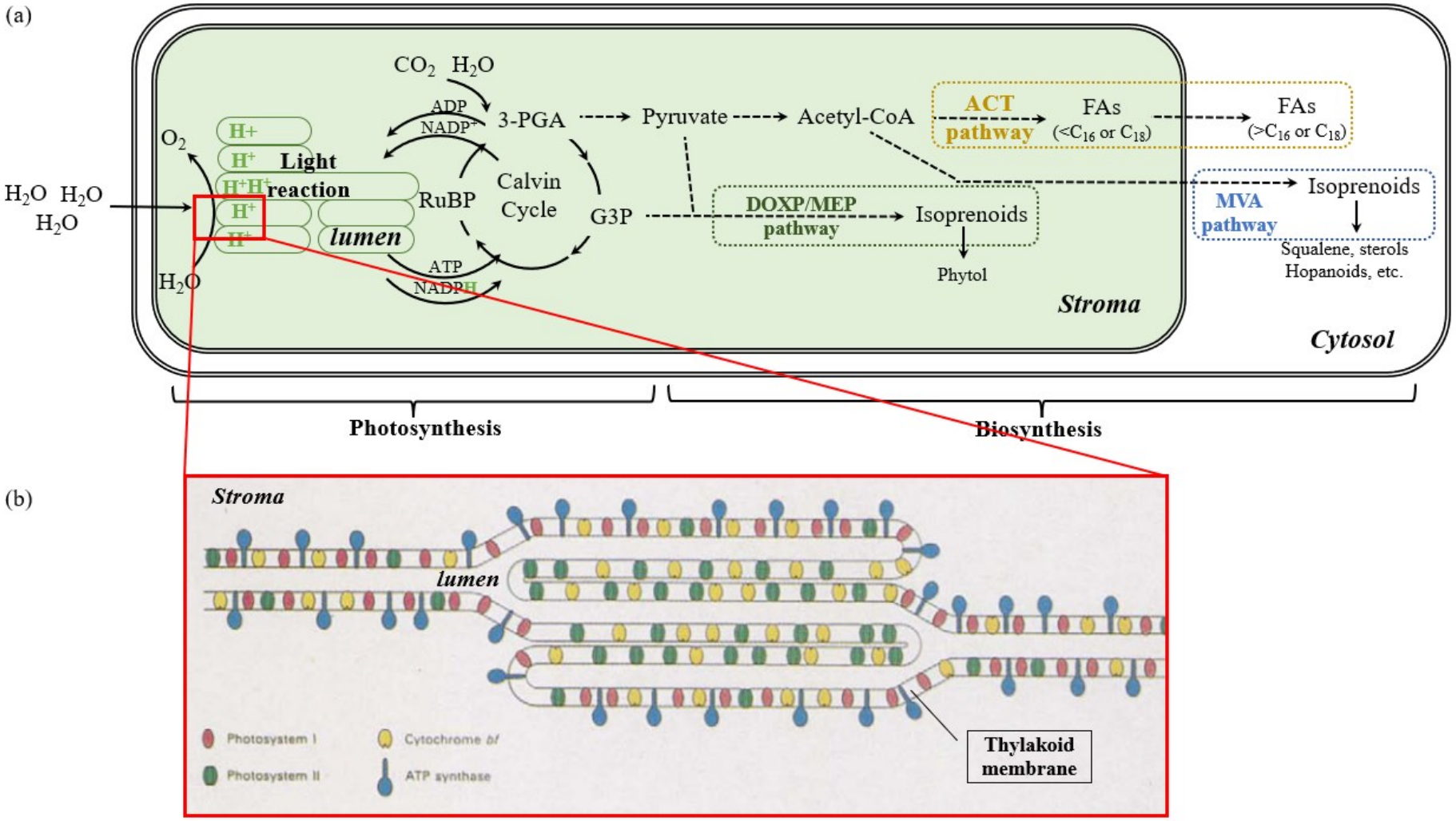

(figure to be continued)

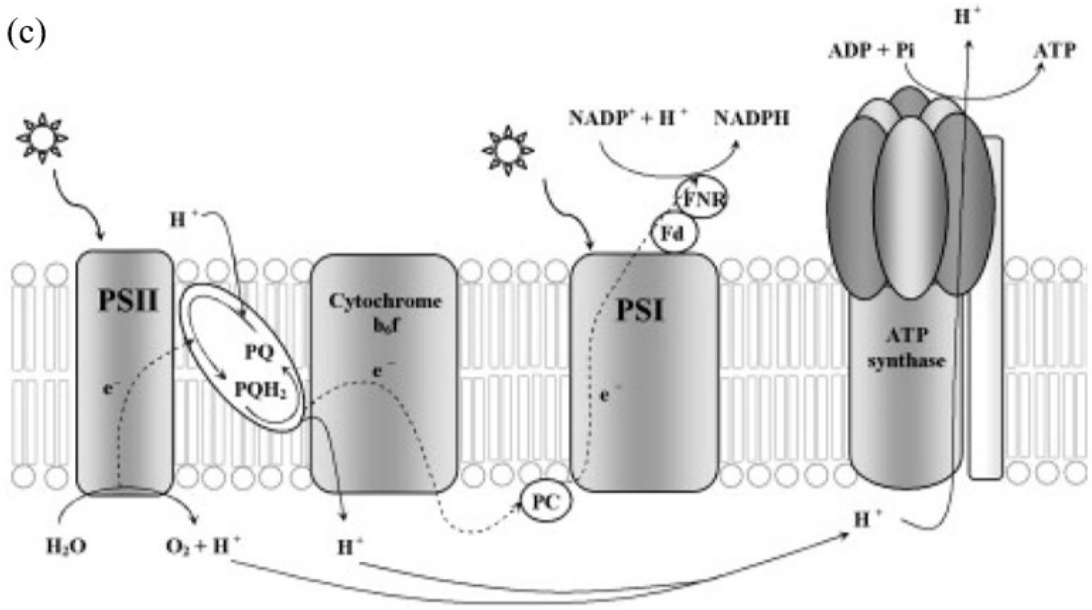

Figure 4-1. Overview of the synthesis of lipid biomarkers in phototrophic organisms, where water first is split into H^+ and O_2 during light reactions on the membrane of thylakoid. ATP and NADPH produced in light reactions are then used in Calvin Cycle to yield 3-PGA, G3P for the biosynthesis of FAs and isoprenoid lipids via ACT, MVA and DOXP/MEP pathway (a). The structure of thylakoid membrane of four integral membrane protein complexes including PS-II (green), Cytochrome b6f (yellow), PS-I (red) and ATP synthase blue) (b); the process of light reactions on thylakoid membrane (c). The dashed and solid lines indicate electron and proton transports, respectively. Abbreviations are listed in Table 4-1.

In short, when the reaction centre is excited by light, water will be split into protons (H^+), electrons (e^-) and O_2 as the reaction below,

$$2H_2O \rightarrow 4H^+ + 4e^- + O_2$$

O_2 will then be released into the atmosphere as a by-product. The electrons will be transferred by a mobile electron carrier called the plastoquinone (PQ) to Cytochrome b6f and to PS-I through plastocyanin (PC) molecules. Ultimately, the electrons will be transferred to Ferredoxin-$NADP^+$ Reductase (FNR) on PS-I. This is the place where $NADP^+$ being reduced to NADPH. The overall process of the photosynthetic electron transport chain in chloroplasts is

$$H_2O \rightarrow \text{PS-II} \rightarrow \text{PQ} \rightarrow \text{Cytochrome b6f} \rightarrow \text{PC} \rightarrow \text{PS-I} \rightarrow \text{NADPH}$$

And the net-reaction of all light-dependent reactions is

$$2H_2O + 2NADP^+ + 3ADP + 3Pi \rightarrow O_2 + 2H^+ + 2NADPH + 3ATP$$

During this procedure, the protons experience the very first kinetic fractionation via being catalysed by FNR, resulting in highly ^2H-depleted NADPH.

The production of light reactions will then be utilized in the second stage of photosynthesis - Calvin-Benson-Bassham Cycle, where 3-PGA and G3P are

produced for further lipids biosynthesis. A detailed description of Calvin-Benson-Bassham Cycle can be seen in section 5.1.

4.1.2 Three main biosynthesis pathways for different lipid classes

The productions of photosynthesis 3-PGA and G3P then become common precursors for the biosynthesis of different lipids via three main biosynthesis pathways. Varied $^{2}H/^{1}H$ fractionation may occur during these processes.

4.1.2.1 Acetogenic (ACT) pathway

Photosynthesizing plants, algae, and cyanobacteria use the ACT pathway to synthesis straight carbon chain compounds such as fatty acids and alkenes inside the plastid (Figure 4-1 (a)).

The biosynthesis of saturated fatty acids begins with the formation of acetyl-CoA by removing one molecule of CO_2 from pyruvate in chloroplast (step ①). (This decarboxylation process may result in significant carbon isotopic heterogeneity, see Chapter 5.2.4). One molecule of acetyl-CoA undergoes addition of CO_2 to form malonyl-ACP (step ②③).The malonyl-ACP is then added to the acetyl-CoA (derived from chloroplastic pyruvate), producing a ß-ketoacul-ACP by loss of a molecule of CO2(step ④). The subsequent extension of acetyl-CoA by repetitive addition of C_2 unit from malonlyl-CoA (step ④⑤⑥⑦) with two molecules of NADPH being consumed to yield chain-length up to C_{16} or C_{18} fatty acids in chloroplast (Figure 4-2). Enzymatic desaturation of these acids (i.e. dehydrogenation) can occur, resulting in unsaturated products.

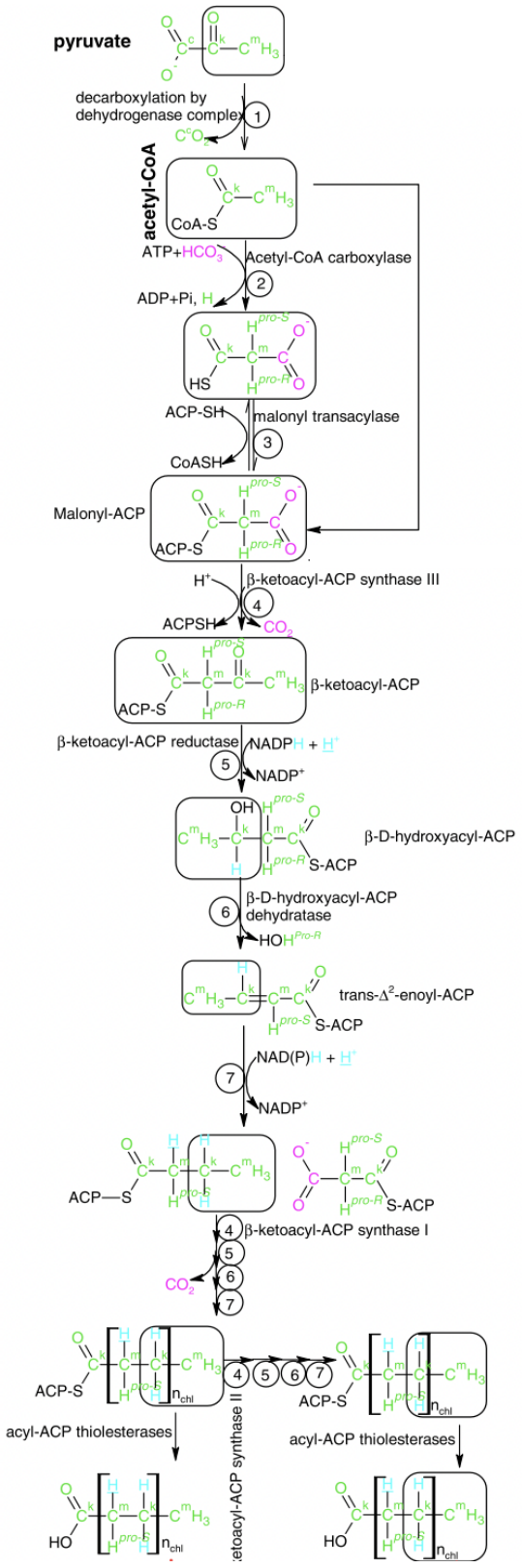

Figure 4-2. Fatty acid and alkane syntheses in higher plants. Acetyl-CoA is formed by removing one molecule of CO_2 from pyruvate in chloroplast (step ①) then undergoes addition of CO_2 to form malonyl-ACP (step ②③). Subsequent extension of acetyl-CoA (derived from chloroplastic pyruvate) by repetitive addition of C2 unit from malonlyl-CoA yields fatty acids of chain-length up to C_{16} or C_{18} in chloroplast (step ④⑤⑥⑦). The steps involving the comsuming of NADPH and lose of CO_2 are highlighted in blue and pink. From (Zhou et al., 2010). Abbreviations are listed in Table 4-1.

4.1.2.2 The Mevalonate (MVA) pathway

The MVA pathway is an essential metabolic pathway that only operates in higher eukaryotes and some heterotrophic bacteria. Located in the cytosol, this pathway produces two C5 units named isopentenyl pyrophosphate (IPP) and dimethylallyl pyrophosphate (DMAPP) for the biosynthesis of isoprenoid lipids such as steroid, terpenoid and hopanoid.

MVA pathway begins with condensing two molecules of acetyl-CoA to yield one molecule of acetoacetyl-CoA and then the second condensation of acetyl-CoA to form HMG-CoA. Mevalonate is generated by the reduction of HMG-CoA by two molecules of NADPH and then phosphorylated to yield fundamental isoprenoid unit IPP and/or DMAPP (Figure 4-3).

4.1.2.3 The 1-deoxy-D-xylulose-5-phosphate (DOXP)/2-methylerythroyl-4-phosphate (MEP) pathway

An alternative pathway for isoprenoid lipids such as phytol is DOXP/MEP pathway (short as MEP pathway) inside the plastid. DOXP/MEP pathway involves the condensation of G3P and pyruvate to form the intermediate 1-deoxy-d-xylulose 5-phosphate. IPP/DMAPP is then produced by a series of enzymic reactions using one molecule of NADPH (Figure 4-3).

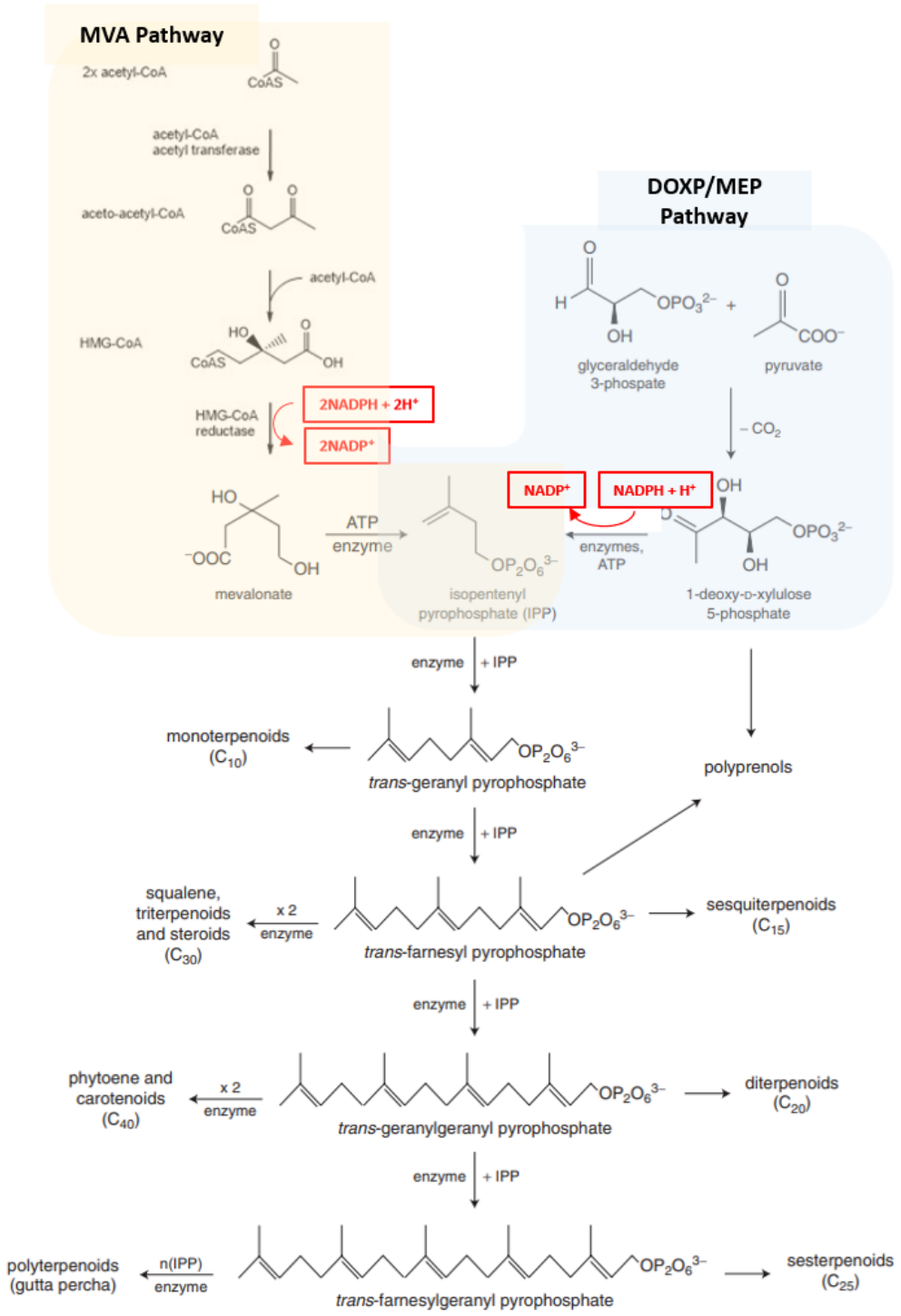

Figure 4-3 Biosynthesis of terpenoids via the MVA and DOXP/MEP pathways and the synthsis of futther isoprenoid lipids. The steps involving the comsuming of NADPH are highlighted in red. Modified from (Killops & Killops, 2005). Abbreviations are in accordance with previous figures and listed in Table 4-1.

4.2 Factors controlling hydrogen isotope fractionation of phototrophic organism

The isotopic composition of lipids from algae can be linked to various environmental parameters. Hence, lipids can reveal much information about biological, chemical, and physical processes in the environment.

As source water directly provides the hydrogen atoms, it (δD_e) decides the $^2H/^1H$ compositions of the lipids from phototrophic organisms. Besides source water, empirical studies have shown a strong link between the δ^2H value of microalgal lipids and other environmental controls such as salinity, temperature and light. Figure 4-4 lists factors that may externally and/or internally control the $^2H/^1H$ fractionation in the biosynthesis of individual lipids.

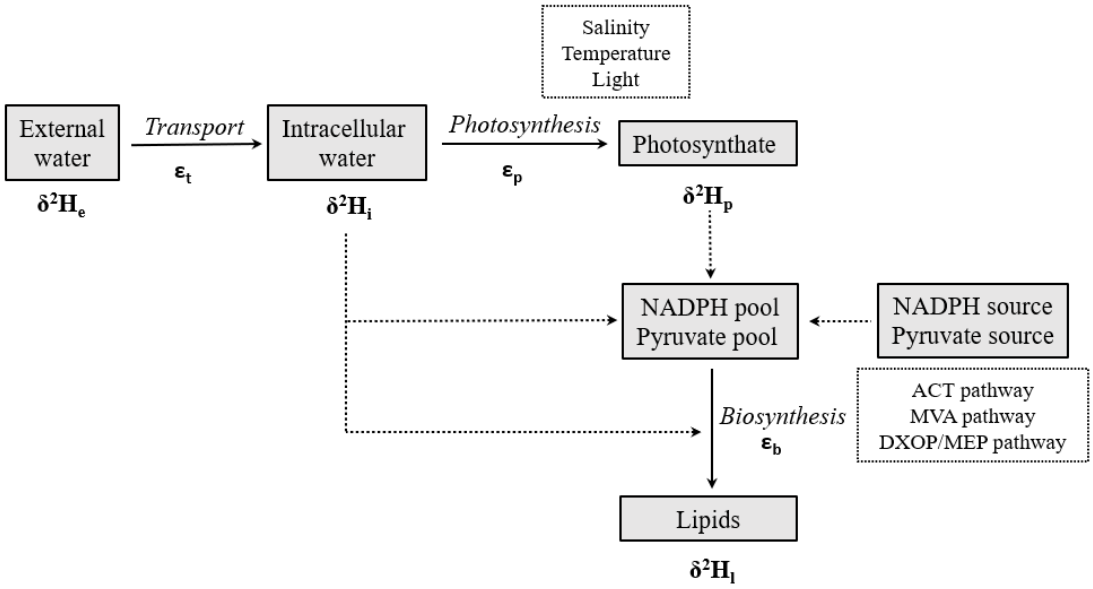

Figure 4-4. Overview of the processes affecting the $^2H/^1H$ fractionation of lipid biomarkers from phototrophic organisms. Modified from (Sachse et al., 2012). Abbreviations are in accordance with previous figures and listed in Table 4-1.

4.2.1 Source water

Estep & Hoering (1980) first reported a -93‰ to -178‰ hydrogen isotope fractionation in photosynthesis and an additional -30‰ to -60‰ ^2H depletion during the lipids and proteins synthesis by laboratory cultures of a series of algae. They concluded that photosynthesis was the primary process causing hydrogen isotopic fractionation. After that, several studies have shown that the hydrogen derived from NADPH produced in photosynthesis is likely to have δ^2H values between ca. –250‰ and -600‰ (Cormier et al., 2018; Luo et al., 1991; Schmidt et

al., 2003; Yakir & DeNiro, 1990). This large $^{2}H/^{1}H$ fractionation during photosynthesis results in ^{2}H-depletion relative to environmental water in almost all biosynthetic products in the phototrophic organism.

Since the first attempt of using hydrogen isotopic analyses of algal sterols as a viable means to reconstruct the $^{2}H/^{1}H$ ratio of environmental water (Sauer et al., 2001), the link between the $\delta^{2}H$ value of lipids and source water has been explored both in the field-based and laboratory culture studies.

For example, hydrogen isotopic compositions of lipid biomarkers *n*-C29 alkane (Garcin et al., 2012; Polissar & Freeman, 2010; Sachse et al., 2004), *n*-C17 alkane (Garcin et al., 2012; Huang et al., 2004; Polissar & Freeman, 2010; Sachse et al., 2004; Sauer et al., 2001), *n*-C28 alkanoic acid (Hou et al., 2008; Huang et al., 2004), C16:0 (Huang et al., 2002) and 18Δ5 sterol (Sauer et al., 2001) all showed correlation with $\delta^{2}H$ values of source water across climatic gradients from tropical Africa to western Europe and America.

Laboratory culture experiments of several freshwater and marine algal species have further provided solid confirmation of this relationship (Englebrecht & Sachs, 2005; Zhang & Sachs, 2007).

4.2.2 Salinity

Schouten et al. (2006) first reported ca. 3‰ decreasing in $^{2}H/^{1}H$ fractionation per salinity unit in alkenones from cultured coccolithophorids *E. huxleyi* and *G. oceanica*. A similar trend was observed in algal and cyanobacterial lipids of environmental samples from Christmas Island in the Pacific (Sachse & Sachs, 2008).

More recent studies of laboratory culture (Heinzelmann et al., 2015; Maloney et al., 2016; Sachs et al., 2016) and field studies (Chivall et al., 2014; M'boule et al., 2014; Nelson & Sachs, 2014a, 2014b; Sachs & Schwab, 2011) supported their results and presented a systemic linear increase of 1-2‰ per salinity unit of $\delta^{2}H$ lipids with the increase of salinity.

The underlying mechanism remains unknown though, a greater salinity is hypothesized to restrict the exchange of water between algal cells and lead to greater recycling of ^{2}H-enriched internal water. Higher salinities can also reduce growth rates and lead to a reduction of $^{2}H/^{1}H$ fractionation during biosynthesis. In addition, the osmolytes production rate may increase under high salinity conditions, which would potentially consume ^{2}H-depleted water molecules and lead to a more ^{2}H-enriched water pool (Sachs, 2014).

The observation and quantification of the link between the $\delta^{2}H$ values of lipid biomarkers from algae and salinity have provided significant implications for paleo salinity reconstruction.

4.2.3 Temperature

(Schouten et al., 2006) cultures of *E. huxleyi* at three temperatures showed an increase of $^{2}H/^{1}H$ fractionation in alkenoes by 0.4-1‰ $(°C)^{-1}$ along with the temperature.

Batch culturing of two species of freshwater green algae *E. unicocca* and *V. aureus* at 15 °C and 25°C by (Zhang et al., 2009b) showed a 20-40‰ increase of $^{2}H/^{1}H$ fractionation in fatty acids in higher temperature. He concluded that the enzyme activities, KIEs and hydrogen tunnelling may be influenced by temperature, and further affect the $\delta^{2}H$ values of the lipids. While Sachse et al. (2012) hypothesized that the effect of temperature may be the function of changes in the isotopic composition of intracellular water since different classes of lipids were influenced by a similar magnitude.

4.2.4 Irradiance

Studies of the effect of irradiance on $^{2}H/^{1}H$ fractionation have shown the direction of response might be lipid-dependent. A decrease of ca. 40‰ in $^{2}H/^{1}H$ fractionation was observed in alkenones from the haptophyte *Emiliania huxleyi* when irradiance was increased from 15 to 200 μmol m^{-2} s^{-1} (van der Meer et al., 2015). The same direction was found in phytol and C14:0 fatty acid from the diatom *Thalassionsira pseudonana* at irradiance between 6 and 47 μmol m^{-2} s^{-1}, while an opposite response was observed in the sterol biomarker (Sachs et al., 2017).

The discrepancy in lipid response was expected to be a result of the relative proportion of ^{2}H-depleted NADPH and common precursors (such as pyruvate) contributing to the biosynthesis of different lipids classes and the inhibition of biosynthesis pathways under different light conditions (Sachs et al., 2017). As light directly controls the photons input in PS-II, it is expected to be a primary factor that impacts the $^{2}H/^{1}H$ fractionation in the phototropic organisms. Here, we presented our results of hydrogen isotopic compositions of different lipid classes in response to varied irradiance in 4.3 and 4.4 with certain explanations in 4.5.

4.2.5 Lipid biosynthetic pathway

Photosynthesis provides ^{2}H-depleted NADPH and common precursors for further biosynthesis. Different biosynthetic pathways can lead to a difference up to 170‰ depletion of ^{2}H in algal lipids.

Field and laboratory studies investigating the differences in the $\delta^{2}H$ values of various algal biomarker lipids have shown that the ACT pathway for the straight chain lipids is enriched in ^{2}H by 100-200‰ relative to isoprenoid lipids (Chikaraishi & Naraoka, 2003; Chikaraishi et al., 2004a; Cormier et al., 2018; Ladd et al., 2021; Sauer et al., 2001; Sessions et al., 1999; Zhang & Sachs, 2007; Zhou et al., 2016). Isoprenoid lipids produced via the MVA pathway show a depletion in ^{2}H by approximately 200-250‰ relative to source water (Chikaraishi, Naraoka, et al., 2004; Li et al., 2009; Sauer et al., 2001; Sessions et al., 1999). Phytol and related compounds produced via the DOXP/MEP pathway are generally observed to have the largest ^{2}H depletions of any lipids (Li et al., 2009) (Lichtenthaler, 1999; Rohmer et al., 1993; Schwender et al., 1996).

Laboratory cultures of the marine diatom *Thalassiosira pseudonana* under nitrogen replete and nitrogen limited conditions showed that the sterols produced by MVA and/or DOXP/MEP pathways were enriched in ^{2}H by 37‰ in nitrogen limited relative to nitrogen replete condition (Zhang et al., 2009b). As the IPPs/DMAPPs produced in the MVA pathway in the cytosol are generally enriched in ^{2}H than that in DOXP/MEP pathway in the plastid. They proposed a 'cross-talk' of the IPPs between these two pathways, where under fast-growing

conditions the IPPs from the plastid DOXP/MEP pathway might cross into the cytosol to provide additional IPPs to the MVA pathways, resulting in a 37‰ more negative in ^{2}H. Their study highlights the molecule yields and exchanges and the associated $^{2}H/^{1}H$ variation in different growth conditions.

4.2.6 Growth phase

20–30‰ larger $^{2}H/^{1}H$ fractionation in alkenones harvested in stationary phase relative to exponential phase from batch cultures of *Emiliania huxleyii* was observed (Wolhowe et al., 2009).

A marked decrease in the sensitivity of fractionation factor $\alpha_{alkenones\text{-}water}$ to salinity was observed both in coastal haptophytes *Isochrysis galbana* and *Chrysotila lamellosa* from earlier growth phase (exponential phase, early stationary phase) to late growth phase (stationary phase, late stationary phase) (Chivall et al., 2014). Their results suggest the alkenone salinity proxy is likely to be most sensitive to salinity when alkenones are produced in a state similar to the exponential phase.

4.2.7 Growth Rate

Schouten et al., (2006) first reported a negative correlation between $\alpha_{alkenones\text{-}water}$ and growth rate from laboratory cultures of haptophye algae *Emiliania huxleyi* and *Gephyrocapsa oceanica*. They concluded that lower growth rates can limit the $^{2}H/^{1}H$ fractionation during biosynthesis.

Similar results were found in the culture experiment of *Emiliania huxleyi* by Sachs & Kawka, (2015). Their results showed an increase of $^{2}H/^{1}H$ fractionation in all lipids as the growth rate increased by 24‰ to 79‰ $(d^{-1})^{-1}$. This is likely because of a proportional increase in the fraction of NADPH from PS-II relative to NADPH from the cytosolic oxidative pentose phosphate pathway when the growth rate increases.

4.3 Result (1) Hydrogen isotopic compositions of lipids from laboratory cultured marine diatom *Pleurosigma intermedium*

Hydrogen isotopic compositions of acetogenic lipids (C14:0, C16:1 and C16:0 fatty acids) and isoprenoid lipids (C25:3, C25:4 HBIs, phytol and squalene) harvested from stationary phase of laboratory cultured marine diatom *P. intermedium* under six levels of light intensity ranging from 20 to 300 μmol m^{-2} s^{-1} were measured to study the influence of irradiance on $^{2}H/^{1}H$ fractionation of algal lipids.

In general, the $\delta^{2}H$ values of isoprenoid lipids showed a negative correlation with irradiance; while the $\delta^{2}H$ values of fatty acids first decreased when light was lower than 150 μmol m^{-2} s^{-1} then increased with the increase of light. Large differences were observed within and between lipid classes in response to varied light conditions.

HBI C25:3 held the smallest $^{2}H/^{1}H$ fractionation, with the hydrogen isotopic compositions ranging from -71.8‰ to -139.7‰. HBI C25:4, squalene and phytol showed similar $\delta^{2}H$ values, ranging from -148.6‰ to -228.0‰, -122.3‰ to -237.7‰ and -132.8‰ to -269.5‰ respectively. Fatty acids showed the largest variation in response to irradiance, C14:0 and C16:0 ranged from -124.1‰ to -245.2‰ while the lowest $\delta^{2}H$ value of -303.2‰ was observed in C16:1 (Figure 4-5).

Besides stationary phase, the $\delta^{2}H$ values of fatty acids and HBIs harvested from exponential were measured to compare the hydrogen isotopic compositions in different growth phases.

Each lipid class will be discussed separately in the following sections.

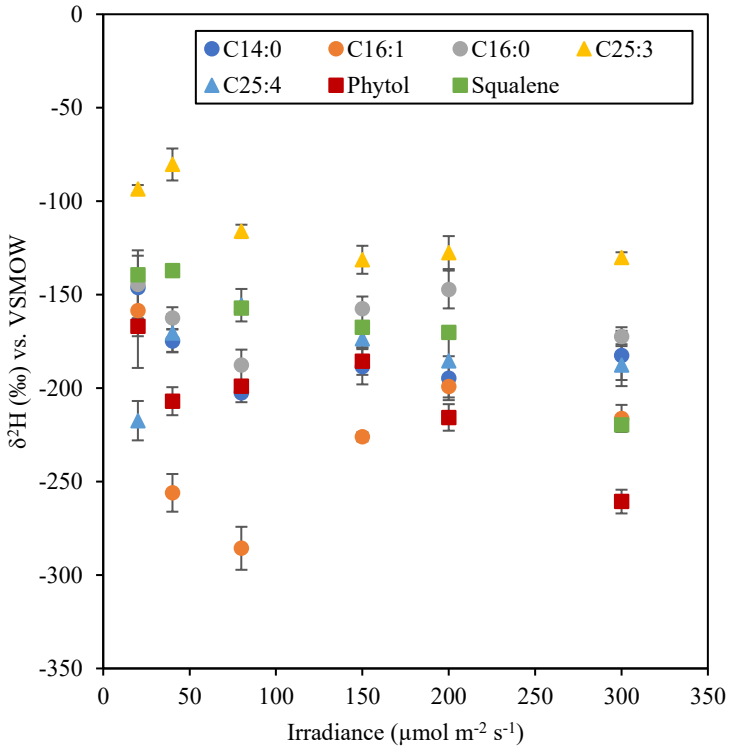

Figure 4-5. Relationships between irradiance and hydrogen isotopic composition of fatty acids (●), HBIs (▲), and other isoprenoids (■) harvested from stationary phase of laboratory cultured marine diatom *P. intermedium*.

4.3.1 Fatty acids

Stable hydrogen isotopic compositions of fatty acids (C14:0, C16:1, C16:0) produced by *P. intermedium* in exponential phase and stationary phase were measured respectively.

For the samples harvested from exponential phase, the hydrogen isotopic composition of C14:0 fatty acid ranged from -112.9‰ at light intensity of 40 µmol m^{-2} s^{-1} to -213.9‰ at highest irradiance (300 µmol m^{-2} s^{-1}). C16:1 fatty acid had very close δ^2H values with C14:0 fatty acid, ranging from -101.1‰ at the lowest irradiance to -226.3‰ at the highest irradiance. C16:0 fatty acid holds the smallest fractionation, ranging from -52.3‰ at light intensity of 40 µmol m^{-2} s^{-1} to -178.9‰ at an irradiance of 200 µmol m^{-2} s^{-1} (Figure 4-6, Table 4-2).

δ^2H values of three fatty acids harvested from exponential phase decreased with the increasing of irradiance in all three fatty acids by 0.31‰, 0.34‰ and 0.38‰ (µmol m^{-2} s^{-1})$^{-1}$ for C14:0, C16:1 and C16:0 (Figure 4-6).

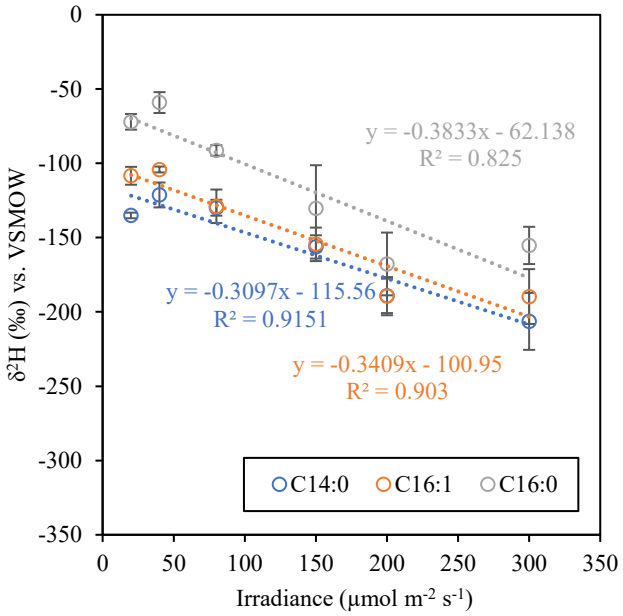

Figure 4-6. Relationships between irradiance and hydrogen isotopic composition of fatty acids C14:0 (blue), C16:1 (orange) and C16:0 (grey) harvested from exponential phase of laboratory cultured marine diatom *P. intermedium*.

For the samples harvested from stationary phase, the hydrogen isotopic composition of C14:0 fatty acid ranged from -124.1‰ at light intensity of 20 µmol m^{-2} s^{-1} to -245.2‰ at light intensity of 150 µmol m^{-2} s^{-1}). The δ^2H values of C16:1 ranged from -143.8‰ at the lowest irradiance to -303.2‰ at light intensity of 80 µmol m^{-2} s^{-1}. Similar to samples from exponential phase, C16:0 fatty acid held the smallest fractionation, ranging from -121.9‰ at light intensity of 20 µmol m^{-2} s^{-1} to -196.3‰ at an irradiance of 80 µmol m^{-2} s^{-1} (Figure 4-7, Table 4-3).

The responses of fatty acids to increasing light intensity seemed cannot be simply described as positive or negative as a turning point was observed in all three fatty acids. The δ^2H values of fatty acids first decreased in low light conditions then increased with the increasing of light intensity. Significant changes were expected between irradiance of 80 and 150 µmol m^{-2} s^{-1} that triggered this hydrogen isotope shift.

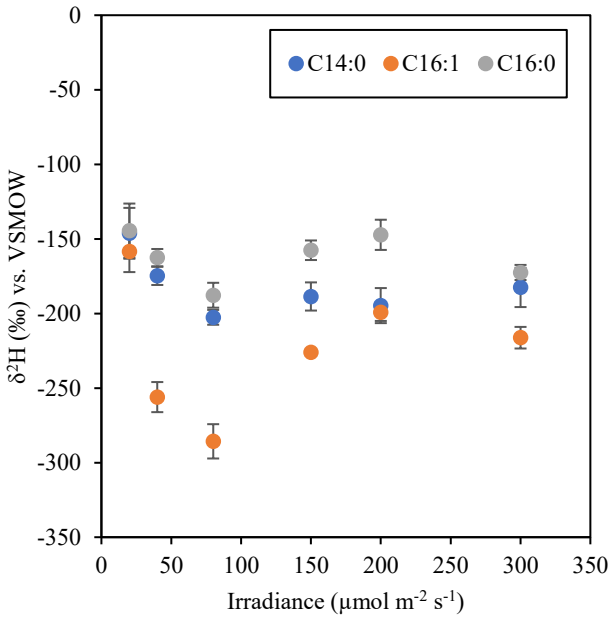

Figure 4-7. Relationships between irradiance and hydrogen isotopic composition of fatty acids C14:0 (blue), C16:1 (orange) and C16:0 (grey) harvested from stationary phase of laboratory cultured marine diatom *P. intermedium*.

Table 4-2. δ^2H values and lipid-water fractionation factor (α) of fatty acids C14:0, C16:1 and C16:0 harvested from exponential phase of laboratory cultured marine diatom *P. intermedium*. The alphabet represents biological repeats.

Irradiance ($\mu mol\ m^{-2}\ s^{-1}$)	Sample	Mass (freeze-dried, mg)	C14:0		C16:1		C16:0	
			δ^2H (‰)	α	δ^2H (‰)	α	δ^2H (‰)	α
20	PI_20_02a_exp	2.70	n.d.	n.a.	-117.8	0.883	-70.1	0.931
20	PI_20_03a_exp	2.60	-137.7	0.863	-101.1	0.900	-81.1	0.920
20	PI_20_04a_exp	2.40	-134.2	0.867	-106.6	0.894	-68.2	0.933
20	PI_20_04b_exp	2.90	-133.3	0.868	-108.0	0.893	-68.8	0.932
Ave			-135.1	0.866	-108.4	0.893	-72.1	0.929
Std			1.9	0.002	6.0	0.006	5.3	0.005
40	PI_40_03a_exp	4.50	-129.7	0.871	-101.3	0.900	-52.3	0.949
40	PI_40_03b_exp	4.50	-112.9	0.888	-105.4	0.895	-68.8	0.932
40	PI_40_03c_exp	2.60	n.d.	n.a.	-105.7	0.895	-56.2	0.945
Ave			-121.3	0.880	-104.1	0.897	-59.1	0.942
Std			8.4	0.008	2.0	0.002	7.0	0.007
80	PI_80_01a_exp	0.27	n.d.	n.a.	n.d.	n.a.	-95.3	0.906
80	PI_80_02a_exp	3.10	-128.6	0.872	-133.7	0.867	-91.8	0.909
80	PI_80_02b_exp	2.70	-124.0	0.877	-113.3	0.888	-85.6	0.915
80	PI_80_02c_exp	5.80	-137.0	0.864	-139.7	0.861	-92.5	0.908
Ave			-129.9	0.871	-128.9	0.872	-91.3	0.910
Std			5.3	0.005	11.3	0.011	3.6	0.004
150	PI_150_01a_exp	0.73	n.d.	n.a.	-159.7	0.841	-126.4	0.875
150	PI_150_01b_exp	0.74	n.d.	n.a.	-167.6	0.833	-124.0	0.877
150	PI_150_03a_exp	2.30	-146.1	0.855	-139.4	0.861	-138.2	0.863
150	PI_150_03b_exp	3.40	-157.5	0.843	-142.9	0.858	-129.8	0.871
150	PI_150_03c_exp	3.10	-165.2	0.836	-163.0	0.838	-152.3	0.849
Ave			-156.3	0.845	-154.5	0.846	-134.1	0.867
Std			7.9	0.008	11.3	0.011	10.3	0.010
200	PI_200_01a_exp	0.67	-186.2	0.815	-173.5	0.827	-178.9	0.822
200	PI_200_01b_exp	0.62	-203.7	0.797	-208.0	0.793	-162.4	0.838
200	PI_200_03a_exp	2.70	-172.2	0.829	-193.6	0.807	-150.9	0.850
200	PI_200_03b_exp	2.80	-194.6	0.806	-182.5	0.818	-151.7	0.849
200	PI_200_03c_exp	1.6	n.d.	n.a.	n.d.	n.a.	-169.3	0.832
Ave			-189.2	0.812	-189.4	0.811	-162.6	0.838
Std			11.6	0.012	12.9	0.013	10.6	0.011

(Continued on next page)

Table 4-2 (continued). δ^2H values and lipid-water fractionation factor (α) of fatty acids C14:0, C16:1 and C16:0 harvested from exponential phase of laboratory cultured marine diatom *P. intermedium*. The alphabet represents biological repeats.

300	PI_300_01a_exp	1.46	-213.9	0.787	-183.8	0.817	-142.3	0.859
300	PI_300_01b_exp	1.48	-192.1	0.809	-226.3	0.774	-177.9	0.823
300	PI_300_03a_exp	4.00	-191.8	0.809	-180.2	0.821	-159.0	0.842
300	PI_300_03b_exp	4.20	-196.4	0.804	-176.8	0.824	-148.9	0.852
300	PI_300_03c_exp	4.20	-209.0	0.792	-181.2	0.820	-148.1	0.853
Ave			-200.6	0.800	-189.7	0.811	-155.3	0.846
Std			9.1	0.009	18.5	0.018	12.6	0.013

n.d. not detected
n.a. not available

Table 4-3. δ^2H values and lipid-water fractionation factor (α) of fatty acids C14:0, C16:1 and C16:0 harvested from stationary phase of laboratory cultured marine diatom *P. intermedium.* The alphabet represents biological repeats.

Irradiance ($\mu mol\ m^{-2}\ s^{-1}$)	Sample	Mass (freeze-dried, mg)	C14:0		C16:1		C16:0	
			δ^2H (‰)	α	δ^2H (‰)	α	δ^2H (‰)	α
20	PI_20_01a	3.47	-135.6	0.865	-185.7	0.815	-152.3	0.849
20	PI_20_01c	0.07	-152.3	0.849	-145.7	0.855	-162.3	0.839
20	PI_20_02c	3.40	-143.2	0.858	-165.3	0.836	-131.8	0.869
20	PI_20_06a	5.10	-161.2	0.840	-147.0	0.854	-170.3	0.831
20	PI_20_06c	4.60	-178.2	0.823	-159.7	0.841	-121.9	0.879
20	PI_20_08c	8.20	-124.1	0.877	-162.5	0.838	-128.2	0.873
20	PI_20_09a	7.80	-125.8	0.875	-143.8	0.857	n.d.	n.a.
20	PI_20_09c	8.30	-149.6	0.851	n.d.	n.a.	n.d.	n.a.
Ave			-146.2	0.855	-158.5	0.842	-144.5	0.856
Stdev			17.1	0.017	13.7	0.014	18.2	0.018
40	PI_40_01c	2.24	-165.0	0.836	-268.3	0.732	-170.7	0.830
40	PI_40_06a	5.80	-181.1	0.820	-256.3	0.744	-157.6	0.843
40	PI_40_06b	5.90	-174.7	0.826	-243.6	0.757	n.d.	n.a.
40	PI_40_06c	6.10	-178.4	0.822	n.d.	n.a.	-159.3	0.842
Ave			-174.8	0.826	-256.1	0.745	-162.6	0.838
Stdev			6.1	0.006	10.1	0.010	5.8	0.006
80	PI_80_01b	0.56	n.d.	n.a.	-273.1	0.728	-181.9	0.819
80	PI_80_03a	7.80	-196.4	0.804	-274.2	0.727	-196.3	0.805
80	PI_80_06a	8.80	-199.8	0.801	-284.5	0.716	-194.0	0.807
80	PI_80_06b	6.80	-204.3	0.796	-303.2	0.697	-192.3	0.809
80	PI_80_06c	7.90	-209.7	0.791	-293.6	0.707	-174.3	0.827
Ave			-202.6	0.798	-285.7	0.715	-187.8	0.813
Stdev			5.0	0.005	11.5	0.012	8.3	0.008
150	PI_150_01a	2.41	n.d.	n.a.	-229.3	0.771	-159.3	0.842
150	PI_150_01b	0.25	-189.2	0.812	n.d.	n.a.	n.d.	n.a.
150	PI_150_01c	0.33	n.d.	n.a.	-225.0	0.776	-165.2	0.836
150	PI_150_05a	7.70	-176.7	0.824	-222.9	0.778	-147.1	0.854
150	PI_150_05b	8.00	-199.8	0.801	-227.2	0.774	-158.8	0.842
Ave			-188.6	0.812	-226.1	0.776	-157.6	0.844
Stdev			9.4	0.009	2.4	0.002	6.6	0.008

(Continued on next page)

Table 4-3 (continued). δ^2H values and lipid-water fractionation factor (α) of fatty acids C14:0, C16:1 and C16:0 harvested from stationary phase of laboratory cultured marine diatom *P. intermedium*. The alphabet represents biological repeats.

200	PI_200_01a	3.13	-178.3	0.823	n.d.	n.a.	-160.4	0.840
200	PI_200_01b	2.17	n.d.	n.a.	-206.4	0.794	-157.7	0.843
200	PI_200_01c	1.20	-210.2	0.791	-200.3	0.801	n.d.	n.a.
200	PI_200_04b	4.9	-209.3	0.791	-192.2	0.809	n.d.	n.a.
200	PI_200_05a	5.00	-189.2	0.812	-206.8	0.794	-144.4	0.856
200	PI_200_05b	6.70	-195.2	0.806	-195.6	0.805	-138.9	0.862
200	PI_200_05c	5.10	-186.1	0.815	-193.9	0.807	-134.9	0.866
Ave			-194.7	0.806	-199.2	0.802	-147.3	0.854
Stdev			11.8	0.012	5.8	0.006	10.1	0.010
300	PI_300_01a	2.20	-198.7	0.802	-220.0	0.781	-167.1	0.834
300	PI_300_01b	1.04	-175.3	0.826	-213.8	0.787	-181.2	0.820
300	PI_300_01c	1.02	-165.2	0.836	-228.3	0.772	-172.2	0.829
300	PI_300_05a	6.30	-196.1	0.805	-204.2	0.797	-168.0	0.833
300	PI_300_05b	6.00	-190.6	0.810	-214.3	0.786	n.d.	n.a.
300	PI_300_05c	6.00	-169.3	0.832	-216.8	0.784	-173.9	0.827
Ave			-182.5	0.818	-216.2	0.785	-172.5	0.828
Stdev			13.2	0.013	7.2	0.007	5.1	0.005

n.d. not detected
n.a. not available

4.3.2 HBIs

Stable hydrogen isotopic compositions of HBIs (C25:3, C25:4) produced by *P. intermedium* in exponential phase and stationary phase were measured respectively. Unfortunately, we only managed to measure a small amount of HBI samples from exponential phase due to low concentration, and the results showed large standard deviation. Hence, we decided not to show these data at this stage. Further culture experiments will be required to obtain confident isotope data.

For the samples harvested from stationary phase, the hydrogen isotopic composition of C25:3 ranged from -71.0‰ at light intensity of 40 µmol m^{-2} s^{-1} to -130.1‰ at light intensity of 300 µmol m^{-2} s^{-1}. HBI C25:4 holds lower δ^2H values relative to C25:3, ranging from -228.0‰ at light intensity of 20 µmol m^{-2} s^{-1} to -148.6‰ at an irradiance of 40 µmol m^{-2} s^{-1} (Figure 4-8, Table 4-4).

Eliminating the data point at lowest irradiance (20 µmol m^{-2} s^{-1}) of C25:4, δ^2H values of C25:3 and C25:4 both showed a negative correlation with light by ca. 0.15‰ (µmol m^{-2} s^{-1})$^{-1}$.

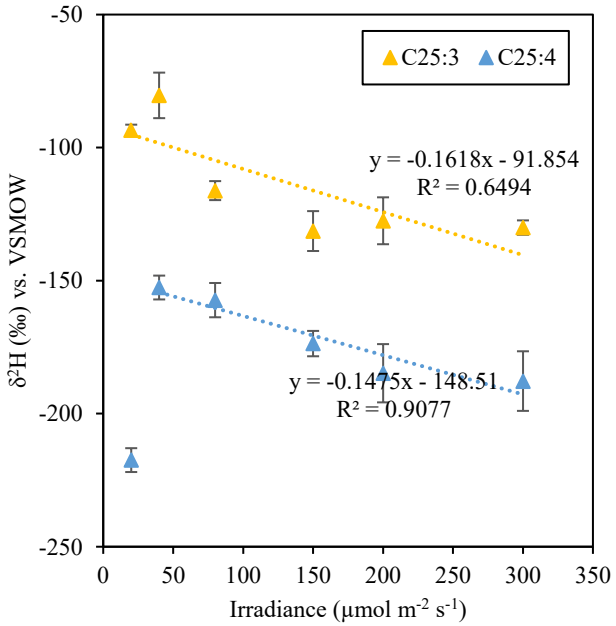

Figure 4-8. Relationships between irradiance and hydrogen isotopic composition of HBIs C25:3 (yellow), C25:4 (blue) harvested from stationary phase of laboratory cultured marine diatom *P. intermedium*. Eliminating the data point of C25:4 at irradiance of 20 µmol m^{-2} s^{-1}, δ^2H values of C25:3 and C25:4 decreased as irradiance increased by 0.16‰ and 0.15‰ (µmol m^{-2} s^{-1})$^{-1}$ (R^2 = 0.65, 0.91) respectively.

Table 4-4. δ^2H values and lipid-water fractionation factor (α) of HBIs C25:3 and C25:4 harvested from stationary phase of laboratory cultured marine diatom *P. intermedium*. The alphabet represents biological repeats.

Irradiance ($\mu mol\ m^{-2}\ s^{-1}$)	Sample	Mass (freeze-dried, mg)	C25:3		C25:4	
			δ^2H (‰)	α	δ^2H (‰)	α
20	PI_20_06a	5.10	-95.6	0.905	-228.0	0.773
20	PI_20_06c	4.60	-91.4	0.910	-206.9	0.794
Ave			-93.5	0.907	-217.4	0.783
Std			2.1	0.002	10.5	0.011
40	PI_40_06a	5.80	-78.5	0.922	-150.3	0.851
40	PI_40_06b	5.90	-71.0	0.930	-158.8	0.842
40	PI_40_06c	6.10	-91.7	0.909	-148.6	0.852
Ave			-80.4	0.921	-152.6	0.848
Std			8.6	0.009	4.5	0.004
80	PI_80_06a	8.80	-111.1	0.890	-164.3	0.837
80	PI_80_06b	6.80	-118.9	0.882	-148.8	0.852
80	PI_80_06c	7.90	-118.5	0.882	-158.9	0.842
Ave			-116.2	0.885	-157.3	0.844
Std			3.6	0.004	6.4	0.006
150	PI_150_01a	2.41	-139.2	0.862	-177.4	0.823
150	PI_150_05a	7.70	-137.8	0.863	-176.6	0.824
150	PI_150_05b	8.00	-121.2	0.880	-166.9	0.834
150	PI_150_05c		-127.2	0.874	n.d.	n.a.
Ave			-131.4	0.870	-173.7	0.827
Std			7.5	0.008	4.8	0.005
200	PI_200_05a	5.00	-123.5	0.877	-182.3	0.819
200	PI_200_05b	6.70	-139.7	0.861	-199.3	0.802
200	PI_200_05c	5.10	-119.3	0.882	-172.8	0.828
Ave			-127.5	0.873	-184.8	0.816
Std			8.8	0.009	10.9	0.011
300	PI_300_01b	2.20	-127.3	0.874	-200.4	0.800
300	PI_300_05a	6.30	-132.8	0.868	-173.2	0.828
300	PI_300_05b	6.00	n.d.	n.a.	-189.6	0.811
Ave			-130.1	0.871	-187.7	0.813
Std			2.7	0.003	11.2	0.011

n.d. not detected
n.a. not available

4.3.3 Phytol and squalene

Due to low concentrations of phytol and squalene, we could only manage to measure stable hydrogen isotopic compositions of samples from stationary phase. Squalene had the hydrogen isotopic compositions of -122.3‰ to -237.76‰. δ^2H values of phytol were generally lower than squalene, ranging from -132.8‰ to -269.5‰. Both phytol and squalene showed larger $^2H/^1H$ fractionations with the increasing of irradiance by 0.31 and 0.27 $(\mu mol\ m^{-2}\ s^{-1})^{-1}$ respectively (Figure 4-9, Table 4-4).

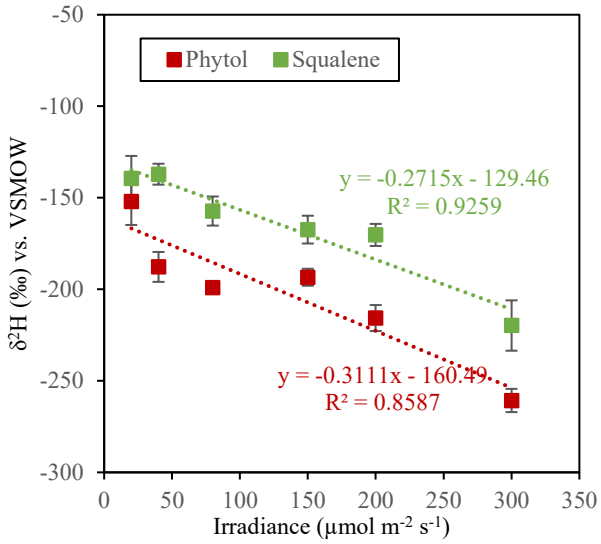

Figure 4-9. Relationships between irradiance and hydrogen isotopic composition of phytol (red), squalene (green) harvested from stationary phase of laboratory cultured marine diatom *P. intermedium*. δ^2H values of phytol and squalene decreased as irradiance increased by 0.27‰ and 0.31‰ (µmol m^{-2} s^{-1})$^{-1}$ (R^2 = 0.93, 0.86) respectively.

Table 4-5. δ^2H values and lipid-water fractionation factor (α) of phytol and squalene harvested from stationary phase of laboratory cultured marine diatom *P. intermedium*. The alphabet represents biological repeats.

Irradiance (µmol m^{-2} s^{-1})	Sample	Mass (freeze-dried, mg)	Phytol		Squalene	
			δ^2H (‰)	α	δ^2H (‰)	α
20	PI_20_06a	5.10	-132.8	0.868	-150.3	0.851
20	PI_20_06b	4.60	-149.3	0.852	-122.3	0.879
20	PI_20_08c	8.20	-159.3	0.842	n.d.	n.a.
20	PI_20_09a	7.80	-166.9	0.834	-145.6	0.855
Ave			-152.1	0.849	-139.4	0.861
Stdev			12.8	0.013	12.3	0.012
40	PI_40_06a	5.80	-198.8	0.802	-143.5	0.857
40	PI_40_06b	5.90	-179.3	0.822	-138.2	0.863
40	PI_40_06c	6.10	-185.2	0.816	-129.6	0.871
Ave			-187.8	0.813	-137.1	0.864
Stdev			8.2	0.008	5.7	0.006
80	PI_80_06a	8.80	-199.3	0.802	-165.2	0.836
80	PI_80_06b	6.80	n.d.	n.a.	n.d.	n.a.
80	PI_80_06c	7.90	-198.8	0.802	-149.3	0.852
Ave			-199.0	0.802	-157.3	0.844
Stdev			0.2	0.000	7.9	0.008
150	PI_150_05a	7.70	-193.2	0.808	-159.1	0.842
	PI_150_05b	8.00	-187.8	0.813	-177.5	0.823
	PI_150_05c		-199.2	0.802	-165.6	0.835
ave			-193.4	0.807	-167.4	0.833
std			4.6	0.005	7.6	0.008
200	PI_200_05a	5.00	-222.8	0.778	-176.9	0.824
	PI_200_05b	6.70	n.d.	n.a.	-162.3	0.839
	PI_200_05c	5.10	-208.6	0.792	-171.7	0.829
ave			-215.7	0.785	-170.3	0.831
std			7.1	0.007	6.0	0.006
300	PI_300_05a	6.30	-254.8	0.746	-204.3	0.796
	PI_300_05b	6.00	-257.8	0.743	-217.3	0.783
	PI_300_05c	6.00	-269.5	0.731	-237.7	0.763
ave			-260.7	0.740	-219.8	0.781
std			6.3	0.006	13.8	0.014

n.d., not detected
n.a., not available

4.4 Result (2) The Hydrogen isotopic compositions of lipids from laboratory cultured marine diatom *Rhizosolenia setigera*

Marine diatom *R. setigera* were cultured under varied irradiance and the hydrogen isotopic compositions of fatty acids and HBI C25:5 harvested during stationary phase were measured.

Similar pattern of fatty acids C14:0 and C16:1 in response to increasing of irradiance were observed in *R. setigera*. Hydrogen isotopic compositions of C14:0 and C16:1 first decreased and reached lowest values of -234.5‰ and -213.4‰ at irradiance of 80 μmol m^{-2} s^{-1} respectively, then increased with the light, giving a highest value of –132.0‰ at irradiance of 200 μmol m^{-2} s^{-1} and -153.1‰ at irradiance of 300 μmol m^{-2} s^{-1}. δ^2H values of C16:0 showed a linear correlation with light (R^2 = 0.87), increasing from -170.4‰ at lowest irradiance to -48.3‰ at highest irradiance by 0.41‰ (μmol m^{-2} $s^{-1})^{-1}$ (Figure 4-10, Table 4-6).

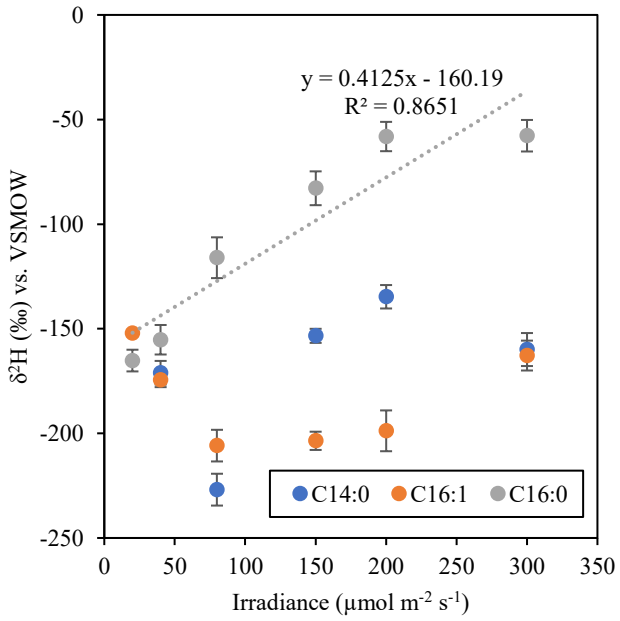

Figure 4-10. Relationships between irradiance and hydrogen isotopic composition of fatty acids C14:0 (blue), C16:1 (orange) and C16:0 (grey) harvested from stationary phase of laboratory cultured marine diatom *R. setigera*. δ^2H values of C16:0 increased along with light by 0.41‰ (μmol m^{-2} $s^{-1})^{-1}$ (R^2 = 0.87).

HBI C25:5 was the only HBI being detacted from *R. setigera*. Its δ^2H values ranged from -196.5‰ at lowest irradiance to -166.8‰ and showed a linear

correlation with light (R^2 = 0.77) with a much smaller sensitivity than fatty acids (0.07‰ (µmol m^{-2} $s^{-1})^{-1}$) though (Figure 4-11, Table 4-6).

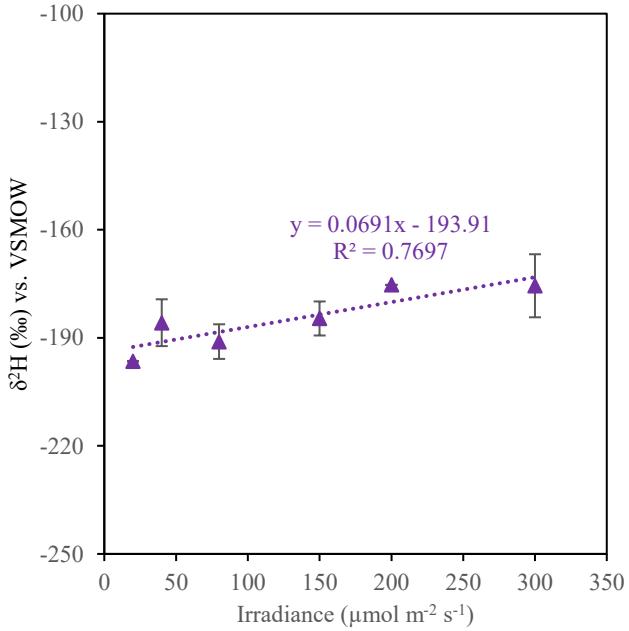

Figure 4-11. Relationships between irradiance and hydrogen isotopic composition of HBI C25:5 harvested from stationary phase of laboratory cultured marine diatom *R. setigera*. δ^2H values of C25:5 increased along with light by 0.07‰ (µmol m^{-2} $s^{-1})^{-1}$ (R^2 = 0.77).

Table 4-6. δ^2H values and lipid-water fractionation factor (α) of fatty acids C14:0, C16:1 and C16:0 and HBI C25:5 harvested from stationary phase of laboratory cultured marine diatom *R. setigera*. The alphabet represents biological repeats.

Irradiance ($\mu mol\ m^{-2}\ s^{-1}$)	Sample	Mass (freeze-dried, mg)	C14:0		C16:1		C16:0		C25:5	
			δ^2H (‰)	α	δ^2H (‰)	α	δ^2H (‰)	α	δ^2H (‰)	α
20	RS_20a	0.34	n.d.	n.a.	-152.1	0.848	-160.0	0.840	n.d.	n.a.
20	RS_20b	0.88	n.d.	n.a.	n.d.	n.a.	-170.4	0.830	-196.5	0.803
Ave			n.a.	n.a.	-152.1	0.848	-165.2	0.835	-196.5	0.803
Stdev			n.a.	n.a.	n.a.	n.a.	5.2	0.005	n.a.	n.a.
40	RS_40a	1.75	-169.2	0.831	-170.9	0.829	-148.2	0.852	-179.3	0.821
40	RS_40b	2.81	-178.7	0.821	n.d.	n.a.	n.d.	n.a.	n.d.	n.a.
40	RS_40c	1.18	-165.2	0.835	-177.9	0.822	-162.3	0.838	-192.3	0.808
Ave			-171.0	0.829	-174.4	0.826	-155.3	0.845	-185.8	0.814
Stdev			5.7	0.006	3.5	0.003	7.1	0.007	6.5	0.007
80	RS_80a	4.3	n.d.	n.a.	n.d.	n.a.	n.d.	n.a.	-186.2	0.814
80	RS_80b	3.23	-234.5	0.765	-198.3	0.802	-106.3	0.894	-195.9	0.804
80	RS_80c	6.03	-219.3	0.781	-213.4	0.787	-125.8	0.874	n.d.	n.a.
Ave			-226.9	0.773	-205.9	0.794	-116.1	0.884	-191.0	0.809
Stdev			7.6	0.008	7.6	0.008	9.8	0.010	4.8	0.005
150	RS_150a	9.01	-149.3	0.851	-206.6	0.793	-93.6	0.906	n.d.	n.a.
150	RS_150b	6.21	-153.3	0.847	-206.7	0.793	-74.2	0.926	-189.3	0.811
150	RS_150c	4.93	-157.5	0.842	-197.4	0.803	-80.7	0.919	-179.9	0.820
Ave			-153.4	0.847	-203.6	0.796	-82.8	0.917	-184.6	0.815
Std			3.4	0.003	4.4	0.004	8.1	0.008	4.7	0.005
200	RS_200a	7.65	-129.6	0.870	-194.8	0.805	-62.1	0.938	n.d.	n.a.
200	RS_200b	4.66	-132.0	0.868	-212.2	0.788	-64.0	0.936	n.d.	n.a.
200	RS_200c	6.55	-142.5	0.858	-189.3	0.811	-48.3	0.952	-175.3	0.825
Ave			-134.7	0.865	-198.8	0.801	-58.1	0.942	-175.3	0.825
Std			5.6	0.006	9.8	0.010	7.0	0.007	n.a.	n.a.
300	RS_300a	7.31	-169.7	0.830	-153.1	0.847	-68.2	0.932	n.a.	n.a.
300	RS_300b	2.51	-150.4	0.850	-165.2	0.835	-54.2	0.946	-184.3	0.816
300	RS_300c	5.03	-159.8	0.840	-170.1	0.830	-50.8	0.949	-166.8	0.833
Ave			-159.9	0.840	-162.8	0.837	-57.7	0.942	-175.6	0.824
Std			7.9	0.008	7.1	0.007	7.5	0.008	8.8	0.009

n.d. not detected
n.a. not available

4.5 Discussion

4.5.1 Mechanisms underlying the effect of irradiance on $^{2}H/^{1}H$ fractionation in algal lipids

Although much remains unknown about the exact physiological and biochemical mechanisms underlying the influence of light on $^{2}H/^{1}H$ fractionation of algal lipids, theoretical, empirical and experimental studies conducted to date have provided certain explanations.

As introduced in 4.1.1, source water splits and generates H^{+} to reduce $NADP^{+}$ to NADPH in light reactions on the thylakoid membrane. The NADPH produced in photosynthesis is highly depleted in ^{2}H (up to -600‰) and results in large ^{2}H-depletion in further lipid biosynthesis (Luo et al., 1991; Schmidt et al., 2003). Sugar metabolism such as the oxidative pentose phosphate pathway in cytosol is another important way to produce NADPH. Studies have shown that the NADPH derived from sugar metabolism is likely enriched in ^{2}H compared to that from photosynthesis (Hayes, 2001; Sachse et al., 2012; Schmidt et al., 2003). Besides photosynthesis and sugar metabolism, the hydrogen in algal lipids can also be directly from intracellular water which is expected to be most enriched in ^{2}H as it is assumed to have nearly the same $\delta^{2}H$ value as the environmental water. Hence, the relative proportion of hydrogen sources of (1) photosynthetic NADPH; (2) metabolic NADPH; and (3) hydrogen derived from intracellular water have been a key factor impacting the $^{2}H/^{1}H$ fractionation in algal lipids (Dirghangi & Pagani, 2013; Gamarra & Kahmen, 2015; Heinzelmann et al., 2015; Maloney et al., 2016; Sachs & Kawka, 2015; Sachs et al., 2016; Zhang et al., 2009a).

In addition to the reductant H^{-}, pyruvate, the last common precursor for three biosynthesis pathways is another factor that decides the hydrogen isotopic composition of algal lipids as it is the source of acetyl-CoA and contributes up to 1/3 of the hydrogen in MEP-derived lipids (Sessions et al., 2002).

Pyruvate can be transferred from a photosynthesis production of 3-PGA inside the chloroplast or produced by glycolysis in cytosol and mitochondrion (Bailleul et al., 2015). The identification of a full set of glycolysis enzymes inside plastids of whole genome sequences of the marine diatom *Phaeodactylum tricornutum* and *Thalassiosira pseudonana* has provided evidence of pyruvate being produced by

glycolysis inside plastid (Kroth et al., 2008; Smith et al., 2012; Smith et al., 2016). In addition, Smith et al., (2016) observed major coordinated shifts in transcript control of primary and intermediate metabolism over light : dark cycles. Their results have shown that plastidic glycolysis predominated in the dark in marine diatom *P. tricornutum,* while cytosolic and mitochondrial glycolysis predominated in the light.

In order to investigate the effect of irradiance on $^{2}H/^{1}H$ fractionation in algae, we conducted cultures experiments with two diatom species at six levels of light intensity ranging from 20 to 300 μmol m^{-2} s^{-1}. Large and systematic changes in hydrogen isotopic compositions related to varied irradiance occurred within and among lipid classes: for fatty acids C14:0, C16:1 and C16:0 harvested from stationary phase, the $\delta^{2}H$ values first decreased when irradiance was below 150 μmol m^{-2} s^{-1} then increased as irradiance increases; for the isoprenoid lipids, including HBIs C25:3 and C25:4, phytol and squalene, a greater fractionation was observed in higher irradiance. The same inverse relationship between $\delta^{2}H$ values and irradiance was also observed for the fatty acid from exponential phase.

Incorporating our results of growth rates (see 3.2) and concentrations of each lipid class (see 0) with regards to different light conditions, distinguishing metabolic pathways and molecules exchanging may explain the mechanisms underlying the effect of light on $^{2}H/^{1}H$ fractionation in algal lipids.

4.5.1.1 Inverse directions of fatty acids in response to irradiance

The effect of light on $^{2}H/^{1}H$ fractionation of fatty acids C14:0, C16:1 and C16:0 cannot be simply described as a positive or negative correlation. A “turning point” was observed in all three fatty acids. It seems that when light intensity was lower than 80 μmol m^{-2} s^{-1}, $\delta^{2}H$ values of fatty acids decreased as light intensity increased, while when light intensity was over 150 μmol m^{-2} s^{-1}, the $\delta^{2}H$ values of fatty acids showed an opposite direction in response to light. A “turning point” was expected at the irradiances between 80 to 150 μmol m^{-2} s^{-1} where the largest $^{2}H/^{1}H$ fractionation in the biosynthesis of fatty acids occurred (Figure 4-7).

Different sources for NADPH and pyruvate for fatty acids biosynthesis with regard to varied light may account for these changes. Here we hypothesize a schematical Figure 4-12 of different sources of NADPH (●/○), pyruvate (■/▨/□),

IPP (△) and DMAPP (▲) in low light (a), mediate light (b) and high light conditions (c).

When light intensity was low, photosynthesis was greatly inhibited, resulting in limited yields of photosynthetic NADPH (○) and pyruvate (□). The NADPH (●) used for fatty acids and other lipids inside the plastid was likely transported from the cytosol and/or mitochondria via the oxidative pentose phosphate pathway. Since plastidic glycolysis was mainly predominated in the dark (Smith et al., 2016), as a result, cytosolic and mitochondrial NADPH (●) and plastidic pyruvate (▨) became the major sources for fatty acids synthesis (Figure 4-12 (a)).

The increase of light intensity will largely increase the photosynthesis rate, especially during relatively low light conditions. During this process, ^{2}H-depleted NADPH (○) and pyruvate (□) gradually became the main source for fatty acids synthesis, resulting in a decreasing $\delta^{2}H$ value of fatty acids (Figure 4-12 (b)).

When light continues increasing, ultimately, the maximum growth rate would reach, and the increase of light would not increase or even inhibit photosynthesis (see section 3.1, Figure 3-2). At this point, photosynthesis could not provide enough NADPH (○) and pyruvate (□) to synthesize the increasing concentrations of fatty acids. It was likely that a greater proportion of pyruvate from the cytosol and mitochondrion was imported to the plastid. Fatty acids, therefore, became ^{2}H-enriched from increased proportional cytosolic and mitochondrial NADPH (●) and cytosolic pyruvate (■) (Figure 4-12 (c)).

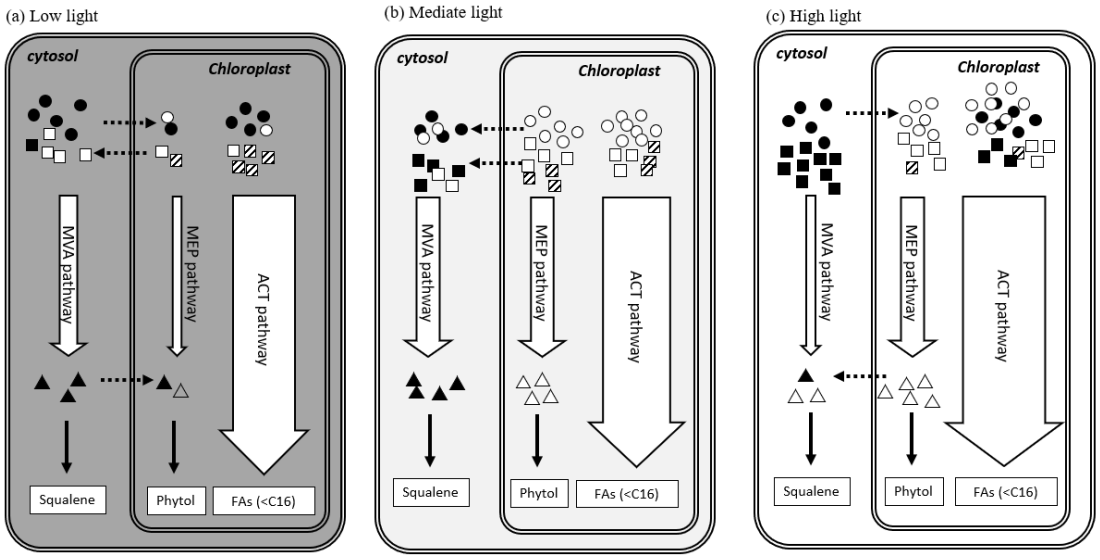

		Pathway	Location	Isotopic signature
○	NADPH	photosynthesis	chloroplast	Highly depleted in ^{2}H
●	NADPH	sugar metabolism	cytosol/mitochondria	Less depleted in ^{2}H
□	pyruvate	photosynthesis	chloroplast	Highly depleted in ^{2}H
▨	pyruvate	glycolysis	chloroplast	Moderately depleted in ^{2}H
■	pyruvate	glycolysis	cytosol	Less depleted in ^{2}H
△	DMAPP	MEP pathway	chloroplast	Highly depleted in ^{2}H
▲	IPP	MVA pathway	cytosol	Less depleted in ^{2}H

Figure 4-12. Schematic of hypothetical photosynthetic NADPH (○), cytosolic and mitochondrial NADPH (●); photosynthetic pyruvate (□), plastidic pyruvate (▨), cytosolic pyruvate (■), DMAPP (△), IPP (▲) changes in low light (a), mediate light (b) and high light (c) conditions. Dashed arrows indicate the molecule transports and open arrows represent three metabolic pathways. The amount of symbol and the width of the arrow are associated with the contribution of precursors and the exhibition of biosynthesis pathway (not to scale). In low light (a), fatty acids were synthesized predominately with ^{2}H-depleted pyruvate originating in the chloroplast (▨) and cytosolic and mitochondrial NADPH (●) transported from cytosol. Phytol and squalene unutilized IPP (▲) from MVA pathway in cytosol. In mediate light (b), photosynthetic NADPH (○) photosynthetic pyruvate (□) and plastidic pyruvate (▨) were the main sources from phytol and fatty acids biosynthesis, squalene were produced via MVA pathway using the NADPH (●) and pyruvate (■) produced locally in cytosol. NADPH and pyruvate may transport from chloroplast to cytosol as the light increased. In high light (c), both squalene and phytol were biosynthesise from DMAPP (△) as MVA pathway were largely inhibited. ^{2}H-enriched NADPH (●) and pyruvate (■) produced in cytosol were transported into chloroplast when the maximum photosynthetic rated reached.

4.5.1.2 Decreasing $\delta^{2}H$ values of isoprenoid lipids (HBIs, phytol and squalene) response to light

Isoprenoid lipids can be produced either by MVA pathway or MEP pathway. It has been well established that squalene and sterols are mainly produced via MVA pathway in cytosol while phytol is produced via MEP pathway inside the chloroplast.

Located in different organisms though, there are intermediates exchanges between two biosynthesis pathways (Zhang et al., 2009b). In addition, gene expression studies have shown that light plays as a key factor to modulate the expression of the genes associated with two pathways (Rodríguez-Concepción, 2006; Rodríguez-Concepción & Boronat, 2015). Rodríguez-Concepción (2006) found expression of genes related with MEP pathway increased while the ones associated with the MVA pathway decreased after *Arabidopsis* seedlings were exposed to light for just 45 min.

Here, a negative correlation between $\delta^{2}H$ values and irradiance was observed in all isoprenoid lipids. The exchanges of certain intermediates such as IPP and DMAPP produce by two biosynthesis pathways may explain this negative correlation.

Similar with fatty acids, in low light conditions, cytosolic and mitochondrial NADPH (●) and plastidic pyruvate (▨) were the major sources for lipids synthesis. Besides photosynthesis, MEP pathway was also likely restricted by low irradiance. ^{2}H-enriched IPP produced via MVA pathway were actually the precursors of all isoprenoid lipids, either to synthesize locally in cytosol or transported into chloroplast for the MEP-derived lipids like phytol (Figure 4-12 (a)).

In mediate light, the increasing contributions of ^{2}H-depleted photosynthetic NADPH (○) and pyruvate (□) account for the larger ^{2}H/^{1}H fractionation in isoprenoid lipids, both in MVA and MEP pathways (Figure 4-12 (b)).

In high light, mitochondrial NADPH (●) and cytosolic pyruvate (■) were imported into the chloroplast for the increasing concentration of lipids, however, the majority of these molecules were actually used for fatty acids synthesis instead of isoprenoid lipids. The quantification of lipids from *P. intermedium* shown that the concentrations of fatty acids were almost hundredfold of isoprenoids lipids (Table 3-2). The concentrations of HBIs even decreased when light was higher than 150 μmol m^{-2} s^{-1}. The influence of light on isoprenoid lipids were minor at this point (Figure 4-12 (c)).

4.5.1.3 Distinct ^{2}H-enrichment of HBI C25:3 – the implication for HBI biosynthesis pathway

The generally accepted principle by several studies is that lipids synthesized via the acetogenic pathway are the most ^{2}H-enriched relative to isoprenoid lipids synthesized by either the MVA or MEP pathway (Chikaraishi & Naraoka, 2003; Chikaraishi et al., 2004a; Sauer et al., 2001; Sessions et al., 1999; Zhang & Sachs, 2007). Isoprenoid lipids such as phytol and related compounds produced by DOXP/MEP pathway is expected to have largest ^{2}H/^{1}H fractionation (Li et al., 2009; Lichtenthaler, 1999; Rohmer et al., 1993; Schwender et al., 1996).

A summary of individual step of hydrogen being added, removed, exchanged and transferred from NADPH (red arrow) in each biosynthesis pathways by (Sachse et al., 2012) gave exhaustive explanations of this difference in ^{2}H/^{1}H fractionation among three biosynthesis pathway (Figure 4-13).

In acetogenic pathway, of the seven hydrogen atoms in a butyryl chain, three inherited from the original acetyl-CoA, two derived from NADPH and two directly

transferred from intracellular water. In higher plants, fatty acids with 16 or 18 carbon atoms are exported from the chloroplasts for further elongation in the endoplasmic reticulum. In MVA pathway, two molecules of NADPH being consumed during the formation of MVA and more NADPH are used during combination of two molecules of FPP to squalene. While in MEP pathway, DOXP being reduced by one molecule of NADPH to MEP and three molecules are consumed during from GGPP to Phytol (Figure 4-13).

Our result, however, showed a distinct ^{2}H-enrichement of HBI C25:3 (-78.5‰ to -139.7‰). This was the most ^{2}H-enriched lipid among all the lipid classes we have observed in this study. Up to date, there is still much remains unknown about the exact biosynthesis pathway of HBIs. It can be species-dependent and influenced by growth conditions (Massé et al., 2004a). Here, we hypothesize that the HBI C25:3 is likely biosynthesized via MVA pathway in cytosol. Although the same amount of NADPH is utilized during the biosynthesis of IPP and as fatty acids, the formation of HMG-CoA requires an addition of one molecule of water. As MVA pathway locates in cytosol, it is possible that this H_2O molecule came from intracellular water which has a $\delta^{2}H$ value somewhat 200-600‰ higher than photosynthetically produced NADPH (Hayes, 2001; Schmidt et al., 2003; Yakir & DeNiro, 1990). Besides, the acidic hydrogen atoms on MVA readily exchange with intracellular water. These result in ^{2}H-enrichemnt in IPP and HBI C25:3. Using the same MVA pathway, the ^{2}H-depletion squalene can be benefited from two molecules of NADPH being used to reduce FPP (Figure 4-13).

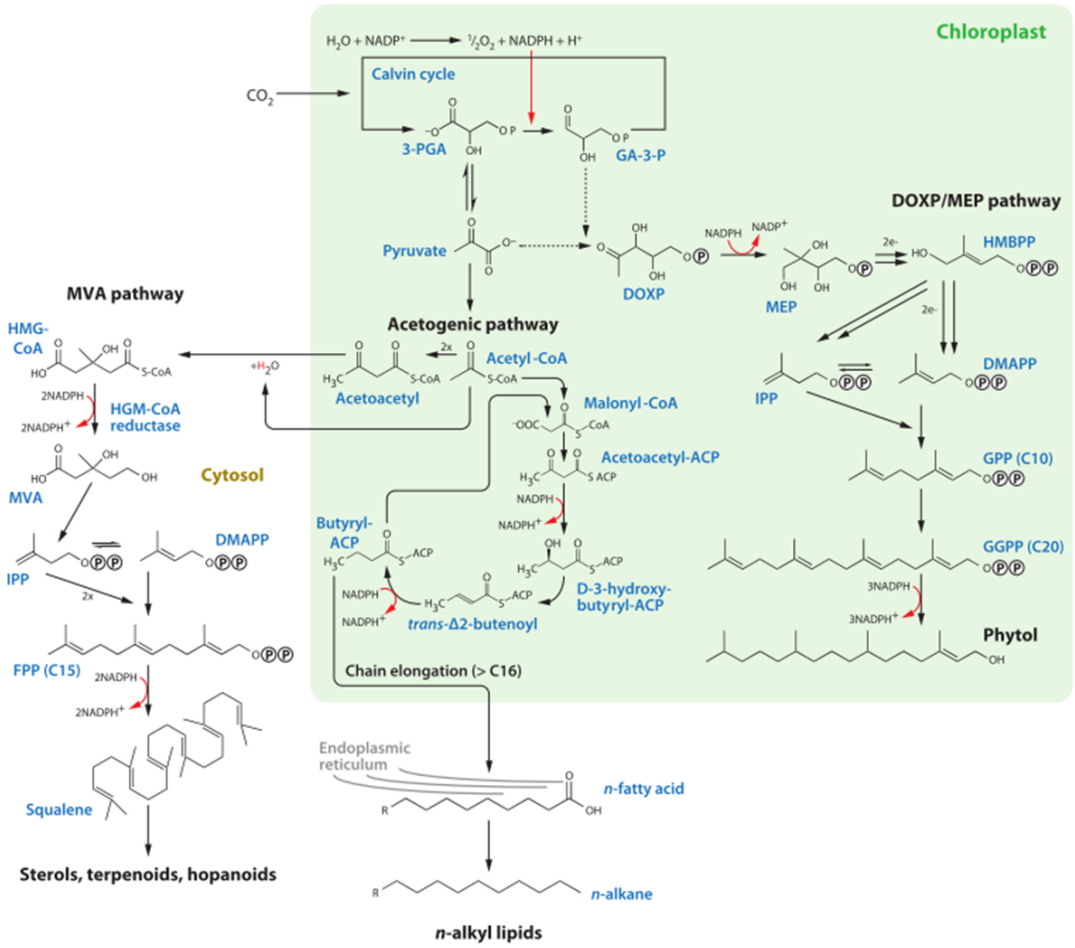

Figure 4-13. Overview of acetogenic, MVA and DOXP/MEP pathways of lipid biosynthesis in photosynthesizing organisms. Red arrows indicate where Hydrogen is transferred from reduced $NADP^+$ (NADPH), causing depletion in ^2H of the product. Double arrows indicate that several transition steps are involved in these reactions. Abbreviations are accordance with previous figured and listed in Table 4-1. Drawn by (Sachse et al., 2012), modified from (Chikaraishi et al., 2004a), (Lichtenthaler, 1999), (Schmidt et al., 2003), and (Zhang & Sachs, 2007).

4.5.2 Larger $^2H/^1H$ fractionations observed in stationary phase relative to exponential phase

Lower δ^2H values of fatty acids produced by *P. intermedium* in stationary phase compared to that from exponential phase were observed when light was below 200 µmol m^{-2} s^{-1}. Largest ^2H-depletion of 72.7‰ for C14:0, 156.8‰ for C16:1 and 96.5‰ for C16:0 were found at an irradiance of 80 µmol m^{-2} s^{-1}. There was no predominance difference of $^2H/^1H$ ratio of fatty acids harvest between stationary phase and exponential phase when light intensity was higher than 200 µmol m^{-2} s^{-1} (Figure 4-14, Table 4-2, Table 4-3).

Explanations for the general depletion of ^{2}H of fatty acids from stationary phase relative to exponential phase can be concluded as the accumulation of photosynthetic NADPH originated lipids. Wolhowe et al. (2009) also found 20-30‰ greater $^{2}H/^{1}H$ fractionation in alkenones from cultures of *E. huxleyi* in the stationary phase compared to the exponential phase. This difference was particular significant in low/mediate light conditions. With a relatively low growth rate, the cell required longer time to reach stationary phase, for example, when light intensity was 80 µmol m^{-2} s^{-1}, it took 13 days for *P. intermedium* growing from exponential phase to stationary phase, while when irradiance was 20 µmol m^{-2} s^{-1} and 300 µmol m^{-2} s^{-1}, the time interval was 25 days and 6 days respectively. In addition, the impact of light on photosynthetic rate was much stronger when light was insufficient (see chapter **2.1.3**). The large depletion of ^{2}H in fatty acids at 80 µmol m^{-2} s^{-1} was a result of cumulative photosynthetic NADPH originating lipids and long life span.

While when light was saturated (over 200 µmol m^{-2} s^{-1}) and photosynthesis could not provide enough ^{2}H-depleted NADPH for the increasing yield for fatty acids biosynthesis, ^{2}H-enriched NADPH from sugar metabolism was involved. The short time interval between exponential phase and stationary phase resulted in a similar hydrogen isotopic compositions in two growth phases.

Our results suggest the hydrogen isotopic compositions of fatty acids are likely to be most sensitive to low and intermate light conditions (lower than 150 µmol m^{-2} s^{-1}) from algae grown from stationary phase.

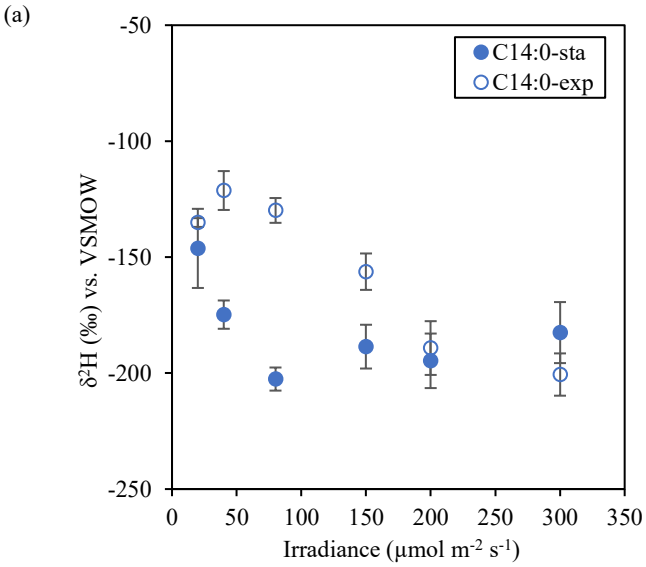

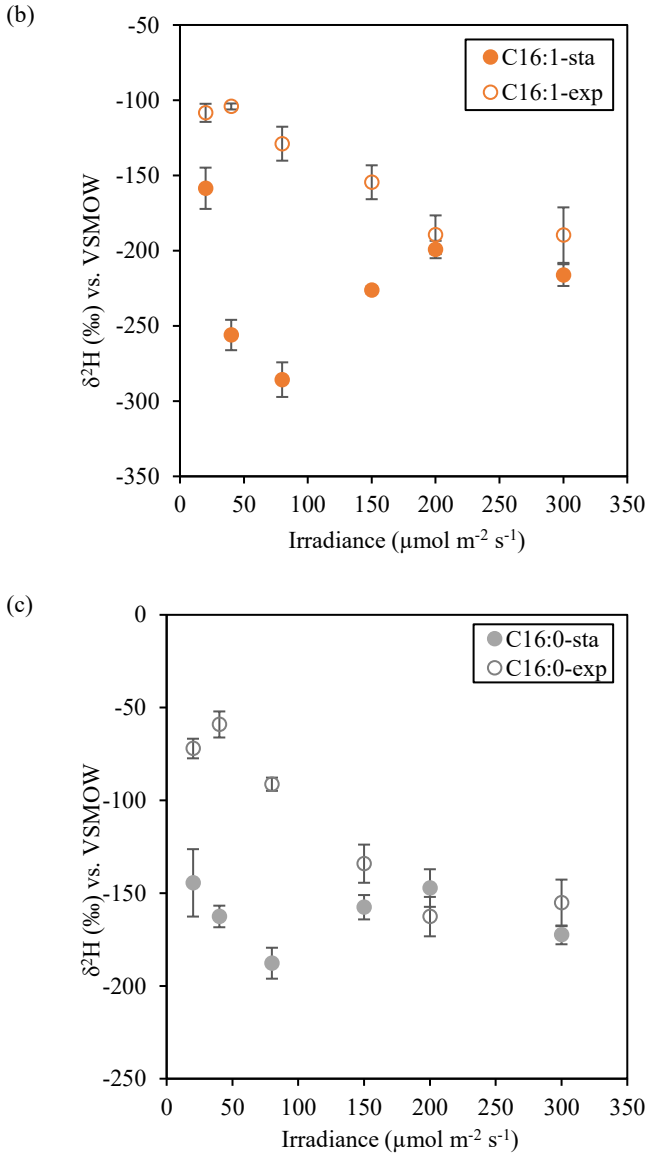

Figure 4-14. The comparison of the δ^2H values of fatty acids C14:0 (a); C16:1 (b); and C16:0 (c) harvested from exponential phase (exp,○) and stationary phase (sta,●) of laboratory cultured marine diatom *P. intermedium* in response to the increasing of irradiance.

4.5.3 The comparison between species: *P. intermedium* vs *R. setigera*

4.5.3.1 Large difference in δ^2H values of the same fatty acid compounds between difference species

As all the reactions in lipids biosynthesis are enzyme-mediated, the algal physiological state, growth condition will certainly impact each KIE being performed during individual step. For example, grown under similar growth conditions, alkenones synthesized by *G. oceanica* were on average depleted in ^2H by 30‰ compared to those of *E. huxleyi* (Schouten et al., 2006). C16:0 fatty acid

produced by Chlorophyceae (*E. unicocca* and *V. aureus*) and Trebouxiophyceae (*B. braunii*) differed by 160‰ relative to source water (Zhang & Sachs, 2007).

Besides the magnitude of the KIE expressed in each step of lipid synthesis differing between species, the enzymes used for a particular reaction can differ between species, as it the case for fatty acid desaturase enzymes in eukaryotic phytoplankton and cyanobacteria. In addition, the biosynthesis pathways, especially for isoprenoid lipids can be species dependent.

In this study, hydrogen isotopic compositions of fatty acids C14:0, C16:1 and C16:0 from marine diatom *P. intermedium* and *R. setigera* were measured respectively. Samples from *R. setigera* were generally enriched in ^{2}H-enriched by up to 120‰ than *P. intermedium*, except C14:0 at 80 µmol m^{-2} s^{-1} and C16:0 at 20 µmol m^{-2} s^{-1}. The shift in direction of $^{2}H/^{1}H$ fractionation in response to irradiance was observed in C14:0 and C16:1 fatty acids from *R. setigera* as well. While hydrogen isotopic composition of C16:0 showed a positive relationship with irradiance (Figure 4-15).

Our results of varied magnitude of hydrogen isotopic compositions and responses to environmental parameter in two marine species suggest when using the ubiquitous lipids such as C14:0 and C16:0 as a hydrogen isotope based proxy for hydrologic reconstructions, the result may be highly impacted by species.

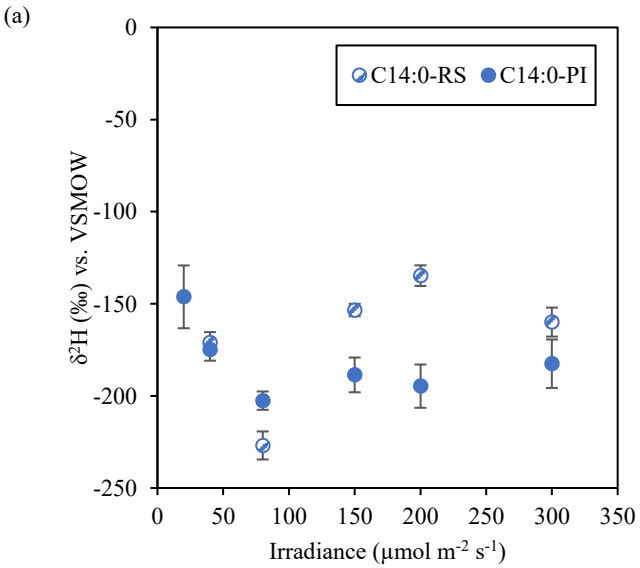

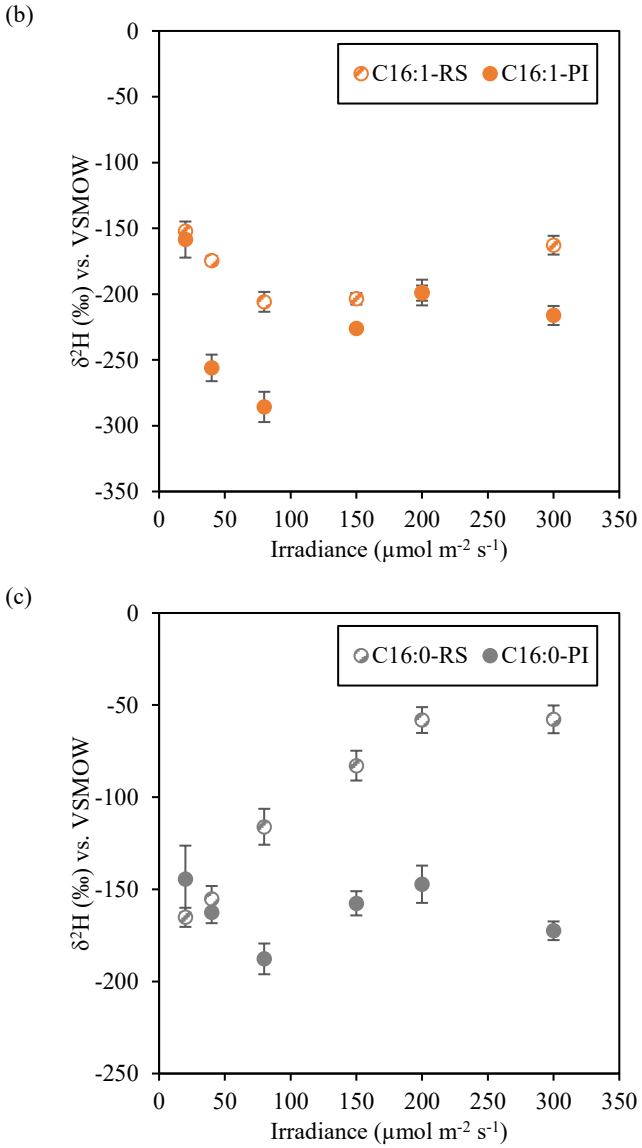

Figure 4-15. The comparison of the δ^2H values of fatty acids C14:0 (a); C16:1 (b); and C16:0 (c) harvested from stationary phase of laboratory cultured marine diatom *R. setigera* (RS, stripped) and *P. intermedium* (PI, closed) in response to the increasing of irradiance.

4.5.3.2 Inverse direction of HBIs produced by *P. intermedium* (C25:3, C25:4) and *R. setigera* (C25:5) responding to irradiance

An inverse direction of HBIs produced by *P. intermedium* (C25:3, C25:4) and *R. setigera* (C25:5) responses to irradiance was observed Figure 4-16. For C25:3 and C25:4, the δ^2H values decreased with irradiance by ca. 0.15‰ $(\mu mol\ m^{-2}\ s^{-1})^{-1}$, while the δ^2H values of *R. setigera*-produced C25:5 showed a positive correlation with light with a relatively smaller sensitivity of ca. 0.07‰ $(\mu mol\ m^{-2}\ s^{-1})^{-1}$.

Both being able to produce HBI(s), however, it should be noted that *P. intermedium* and *R. setigera* actually belong to different phylogenetic clusters and physiologically differ from each other (Figure 1-10) (Sinninghe Damsté et al., 2004).

At this point, we are not able to provide solid explanation on this inverse direction of responses between two species as much about the biosynthesis pathway and function of HBIs in diatom still remain unclear. Massé et al. (2004b) determined the different biosynthetic pathways of sesterterpenes (isoprenoid lipids with a C25 skeleton) in *R. setigera* and another HBI-producer *Haslea ostrearia* by specific inhibition of MVA and MEP pathways and comparison with the natural $^{13}C/^{12}C$ isotope ratios of the ^{13}C labelled lipids. Their results showed that the sesterterpenes and the related sterols were produced by MVA pathway in *R. setigera*; while for the structurally similar compounds in *H. ostreasria* were biosynthesized by MEP pathway. Their results suggested that the biosynthesis of HBI(s) can be species-dependent and cannot simply be grouped according to structural type.

The ^{2}H-enriched hydrogen isotopic compositions of HBIs produced by *P. intermedium* suggested that they were likely produced via MVA pathway in cytosol as well. However, when compared the relative concentrations of HBI(s) and fatty acids in stationary phase of two diatom species. C25:5 is significantly lower (less than 10%) relative to C25:3 and C25:4 and showed a negative correlation with light (see 3.4, Figure 3-7). It seems that C25:5 was progressively less prior in lipid biosynthesis relative to fatty acids with increasing of light intensity. It seems there was no further requirement for NADPH from photosynthesis as ^{2}H-enriched NADPH and pyruvate produced locally in cytosol can already fulfil the small amount of C25:5 biosynthesis.

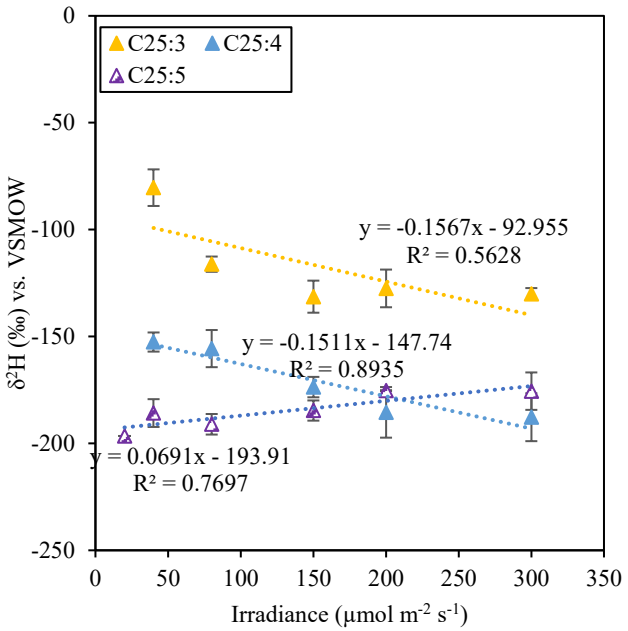

Figure 4-16. The comparison of the δ^2H values of HBIs harvested from stationary phase of laboratory cultured marine diatom *P. intermedium* (C25:3, yellow; C25:4, blue) and *R. setigera* (C25:5, stripped) in response to the increasing of irradiance.

4.6 Conclusion and potential implication for sea ice reconstruction

As photosynthesis is the primary process causing hydrogen isotopic fractionation in phototrophic organisms. Light is expected to hold the potential to drive large changes in the $^{2}H/^{1}H$ fractionation in microalgal lipids.

Our results of hydrogen isotopic compositions of several lipid classes from two marine species cultured under varied irradiance conditions showed different directions and magnitude of $^{2}H/^{1}H$ fractionation within and among lipid classes as irradiance increased.

A turning point of hydrogen isotopic composition of fatty acids harvested from stationary phase in response to the increase of the light was observed both in *P. intermedium* and *R. setigera*. The $\delta^{2}H$ values first decreased because more ^{2}H-depleted photosynthetic NADPH was produced as light increased. When light continued getting higher and the cell eventually reach the highest growth rate, more ^{2}H-enriched metabolic NADPH was involved to fulfil the increasing yields of fatty acids, hence minimising the $^{2}H/^{1}H$ fractionation.

$\delta^{2}H$ values of the isoprenoid lipid classes (HBIs C25:3, C25:4; phytol and squalene) from *P. intermedium* were negatively correlated with light. The increasing NADPH and pyruvate produced by photosynthesis in high light conditions were responsible for this larger $^{2}H/^{1}H$ fractionation.

Besides, fatty acids harvested in the stationary phase experienced greater $^{2}H/^{1}H$ fractionation than that from the exponential phase as a result of accumulated photosynthetic NADPH originated lipids.

In addition, significant differences in algal lipids produced by two diatom species were observed as well. HBI C25:5 produced by *R. setigera* showed an opposite direction and smaller sensitivity in response to light compared to the HBIs produced by *P. intermedium*.

Laboratory culture and field-based studies of $^{2}H/^{1}H$ fractionation of algal lipids response to a variety of environmental conditions have been applied to interpret hydrological and climate models. However, the mechanisms underly the effect of light on hydrogen isotopic compositions of algal lipids can be of great complexity as light can not only impact the growth rate of cells but also directly control the light reactions in photosynthesis. The only two papers to date presenting their

studies on the effect of irradiance on hydrogen isotopic compositions of algal lipids by laboratory cultures were Sachs et al. (2017) and van der Meer et al. (2015). Here we broadened the light range from 20 to 300 and provided the very first hydrogen isotopic data of HBIs. Based on the papers above, we hypothesised that the hydrogen isotopic compositions in microalgal lipids can be controlled by the relative fraction of the sources of hydrogen (intracellular water, metabolic NADPH and photosynthetic NADPH); relative fraction of the sources of pyruvate (cytosolic and mitochondria pyruvate, plastidic pyruvate and photosynthetic pyruvate); and biosynthesis pathway. Significant advances are required to increase our level of understanding of the exact biosynthesis pathway and function of algal lipids, especially distinguishing biomarkers like HBIs, so that the magnitude and details of the differences between and within individual algal lipid classes can be better interrupted with regards to the environmental parameters such as salinity, temperature, and irradiance.

We believe the results of this study can provide new insights into the fundamental mechanisms responsible for determining the isotopic composition of lipid biomarkers. Importantly, the characterisation of the relationship between $^{2}H/^{1}H$ fractionation of HBIs and light can potentially develop a new method for identifying variable light transmission through sea ice.

5 The effect of irradiance on carbon isotopic compositions of lipids from laboratory cultured marine diatom *Pleurosigma intermedium* and *Rhizosolenia setigera*

Carbon isotopic fractionations in physical, chemical and biological processes have led to an uneven distribution of ^{12}C and ^{13}C among organic carbon products. Stable carbon isotopic compositions of plant and algal lipids are generally enriched in ^{12}C relative to environmental carbon (e.g. atmospheric CO_2, dissolved CO_2 and bicarbonate) owing to their preferential uptake of the lighter isotope (^{12}C) in carbon fixation processes during photosynthesis. Photosynthates then become precursors or substrates for further lipids biosynthesis. Hence, carbon isotopic signature of the natural products from phototrophic organisms can be linked with various environmental parameters. The additional carbon isotopic fractionations associated with the individual biosynthesis processes however, will lead to large differences of carbon isotopic compositions among different plant/algal species, lipid classes and even carbon atom positions within the single compound.

Pioneered by Freeman et al. (1990) and Hayes et al. (1990), compound-specific isotopic composition has been applied to a board range of studies including biochemical process and carbon cycle reconstruction (Pagani, 2014).

Here, stable carbon isotopic compositions of fatty acids, HBIs and other isoprenoid lipids from laboratory cultured marine diatom *Pleurosigma intermedium* and *Rhizosolenia setigera* in six levels of light intensity ranging from 20 to 300 μmol m^{-2} s^{-1} were measured.

To better interpret the observed isotopic compositions, Chapter 5 first demonstrates the well-established process from inorganic carbon being transported into cell to the biosynthesis of individual lipid (**5.1**). Factors controlling on $^{13}C/^{12}C$ fractionation during this process are discussed in **5.2**, following by a brief review of previous work on carbon isotopic signatures responding to varied growth conditions. Our results of carbon isotopic compositions of algal lipids from laboratory cultures of two diatom species under different irradiance are shown in **5.3** and **5.4** respectively, following with detailed discussion in **5.5** and conclusion in **5.6**.

Frequent used abbreviations in this chapter are listed in Table 5-1.

Table 5-1. Frequent used abbreviations in Chapter five.

Abbreviation	Description
3-PGA	3-PhosphoGlyceric Acid
ACT	Acetogenic
ADP	Adenosine DiPhosphate
ATP	Adenosine TriPhosphate
CO_2 (aq)	Dissolved carbon dioxide
CoA	Coenzyme A
DMAPP	DiMethylAllyl PyroPhosphate
FNR	Ferredoxin–NADP Reductase
G3P	Glyceraldehyde 3-Phosphate
HBIs	Highly Branched Isoprenoids
IPP	Isopentenyl PyroPhosphate
KIE	Kinetic Isotope Effect
MEP	2-C-Methyl-D-Erythritol 4-Phosphate
MVA	Mevalonate
$NADP^+$	Nicotinamide Adenine Dinucleotide Phosphate
NADPH	Reduced Nicotinamide Adenine Dinucleotide Phosphate
PEP	PhosphoenolPyruvate
Pi	inorganic Phosphate
PS-I	PhotoSystem I
PS-II	PhotoSystem II
RuBisCO	Ribulose-1,5-Bisphosphate Carboxylase/Oxygenase
RuBP	Ribulose-1,5-BisPhosphate

5.1 Introduction

Algae can utilize either dissolved carbon dioxide (CO_2 (aq)) or bicarbonate (HCO_3^-) as carbon source. The whole process of carbon assimilation and associated carbon isotopic fractionations can be simplified as three phases – transport, photosynthesis and biosynthesis (Figure 5-1).

Environmental CO_2 and HCO_3^- molecules first percolate into cell by diffusion and/or active transport. This is a dynamics process with the leaking of carbon from cell to environmental simultaneously. In chloroplast stroma, CO_2 molecules are then assimilated into biomaterials with a series of enzymatic carbon fixation reactions called Calvin-Benson-Bassham cycle, mostly referred as Calvin Cycle, (Buchanan, 2016; Calvin, 1962).

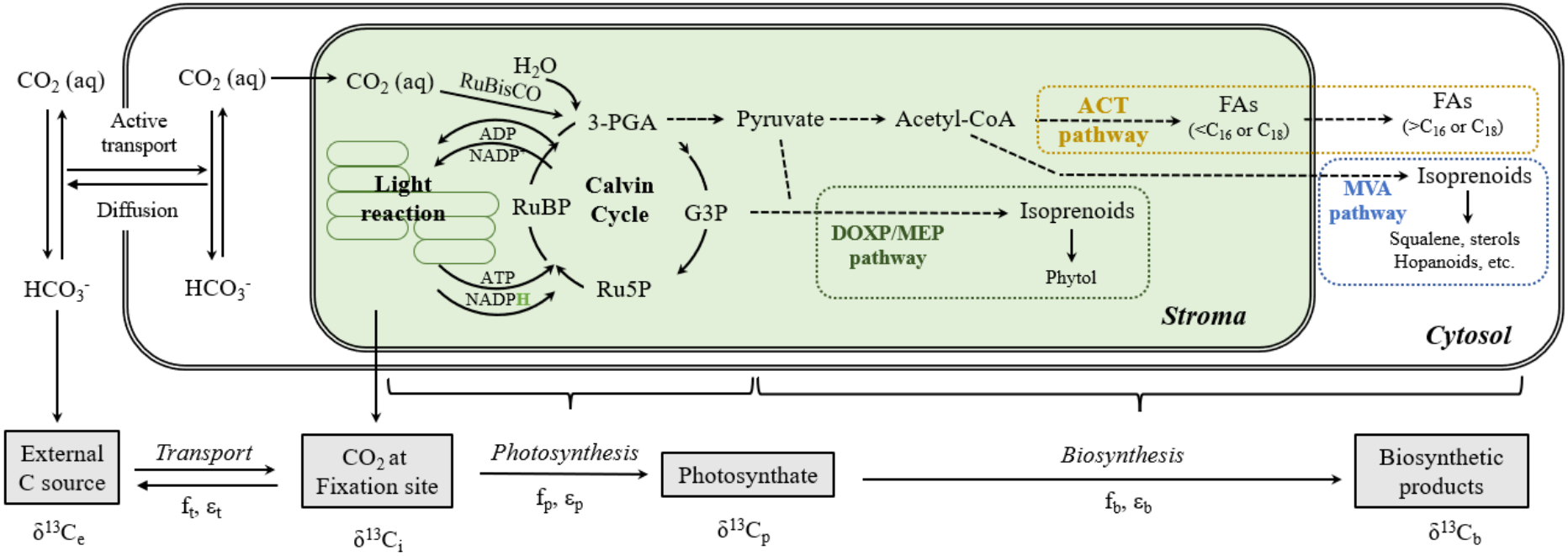

Figure 5-1. Overview of photosynthetic and biosynthetic pathways in algae, where CO_2 and HCO_3^- molecules diffuse and/or actively transport in to chloroplast and be assimilated by RuBisCO in Calvin Cycle. The Productions of Calvin Cycle then become precursors for further biosynthesis of fatty acids and isoprenoid lipids via ACT, MVA and DOXP/MEP pathway. Abbreviations: 3-PGA, 3-PhosphoGlyceric Acid; ATP, Adenosine TriPhosphate; G3P, Glyceraldehyde 3-Phosphate; MEP, 2-C-Methyl-D-Erythritol 4-Phosphate; MVA, Mevalonate; $NADP^+$, Nicotinamide Adenine Dinucleotide Phosphate; NADPH, Reduced Nicotinamide Adenine Dinucleotide Phosphate; RuBisCO, Ribulose-1,5-Bisphosphate Carboxylase/Oxygenase; RuBP, Ribulose-1,5-BisPhosphate; Ru5P, Ribulose-5-Phosphate. Modified from (Chikaraishi, 2014).

As the second stage of photosynthesis, Calvin Cycle utilizes ATP and NADPH from light-dependent reactions (see chapter **4.1.1**) and perform a series of reduction-oxidation reactions to produce sugars in a step-wise process (Figure 5-2).

In short, three molecules of CO_2, three molecules of water and three molecules of Ribulose-1,5-Bisphosphate (RuBP, a C_5 compound) are incorporated into six molecules of glyceraldehyde 3-phosphate (G3P, a C_3 compound) by catalysation of the key enzyme named Ribulose-1,5-Bisphosphate Carboxylase/Oxygenase (RuBisCO). During this process, six molecules of ATP and six molecules of NADPH produced in light-dependent reactions are used. Of six molecules of produced G3P, five are used to regenerate five molecules of RuBP consuming three molecules of ATP, leaving a net gain of one G3P molecule for further biosynthesis (Bassham et al., 1950).

The sum of reactions in the Calvin cycle is the following:

$$3CO_2 + 6NADPH + 6H^+ + 9ATP + 5H_2O \rightarrow G3P + 6NADP^+ + 9ADP + 8Pi$$

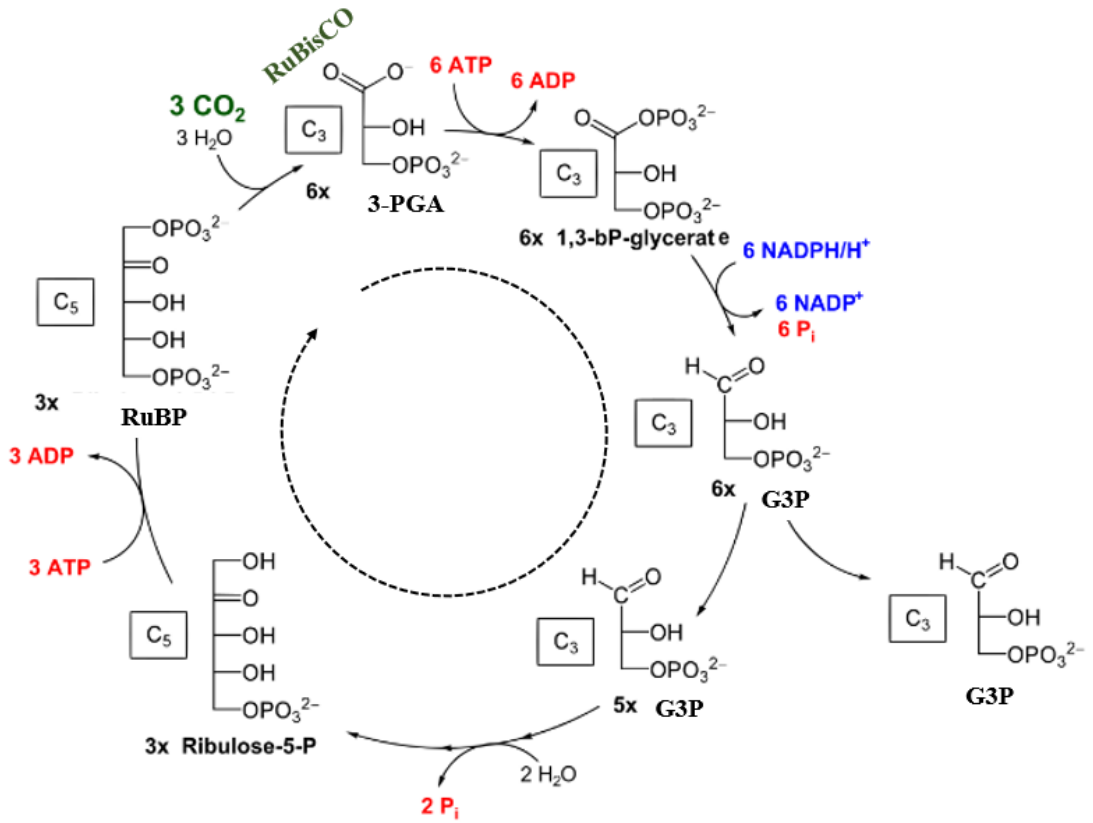

Figure 5-2. Overview of a Simplified Calvin cycle with structural formula. Three molecules of CO_2, three molecules of water and three molecules of RuBP are incorporated into six molecules of G3P by catalysation of RuBisCO. During this process, six molecules of ATP and six molecules of NADPH are used. Of six molecules of produced G3P, five are used to regenerate five molecules of RuBP consuming

three molecules of ATP, leaving a net gain of one G3P molecule for further biosynthesis. Abbreviations are accordance with previous figures and listed in Table 5-1.

The production of photosynthesis, 3-PGA and G3P then will be used to biosynthesis a variety of functional organic compounds via different secondary biosynthetic pathways. In this study, we mainly focus on ATC, DOXP/MEP and MVA pathways and the associated additional $^{13}C/^{12}C$ fractionations (Figure 5-1). Detailed biosynthesis steps of three pathways have been described in Chapter 4.1.2.

5.2 Factors controlling $^{13}C/^{12}C$ fractionation during biosynthesis of lipids by phototrophic organisms

The major focus of previous investigations on carbon isotopic compositions of higher plant and algal lipids has been on understanding the influence of factors on the link between environmental parameters.

The overall fractionation observed between external DIC ($\delta^{13}C_e$) and biosynthetic products ($\delta^{13}C_b$) via photosynthetically fixed CO_2 can be controlled sequentially by several processes (Figure 5-1).

5.2.1 Dynamics of inorganic carbon in water

Not like plants in terrestrial environments can only assimilate gaseous CO_2 for photosynthesis, aquatic plants and algae can selectively use CO_2 (aq) and/or HCO_3^- as carbon sources.

These chemical species of CO_2 are linked by a series of equilibria reactions below,

$$CO_2 + H_2O \Leftrightarrow H_2CO_3 \Leftrightarrow H^+ + HCO_3^- \Leftrightarrow 2H^+ + CO_3^{2-}$$

$$\underset{\delta^{13}C_{gas}}{CO_2\ (gas)} \xleftrightarrow{\varepsilon_{gas-aq}} \underset{\delta^{13}C_{aq}}{H_2CO_3/CO_2\ (aq)} \xleftrightarrow{\varepsilon_{aq-HCO_3^-}} \underset{\delta^{13}C_{HCO_3^-}}{HCO_3^-} \xleftrightarrow{\varepsilon_{HCO_3^- - CO_3^{2-}}} \underset{\delta^{13}C_{CO_3^{2-}}}{CO_3^{2-}}$$

However, the isotopic compositions of the different CO_2 species are not equal because of isotopic fractionation associated with different equilibria processes. A number of factors including pH, temperature, total dissolved inorganic carbon (DIC) primarily control the isotopic compositions of plants and algae via equilibria reactions involving CO_2 species.

As this reaction leads to a release of protons, pH controls the relative abundance of different CO_2 species. For example, a higher pH results in an increases of the ratio of HCO_3^- related to CO_2, makes HCO_3^- a primary carbon source for plants and algae. As a result, the isotopic composition of plants and algae can indirectly reflect the pH of the environment.

The equilibrium isotope effect in the hydration/dehydration reactions between chemical species of CO_2 is also sensitive with temperature. Mook et al. (1974) first summarized the isotopic fractionation between CO_2 (aq) and HCO_3^- as

$$\varepsilon_{c_{aq}} \equiv \left[\frac{\delta^{13}CO_{2_{aq}} + 1000}{\delta^{13}C_{HCO_3^-} + 1000} - 1\right] \times 1000$$

$$\equiv 24.12 - \frac{9866}{T}, \text{ T is absolute temperature (5-1)}$$

CO_2 (aq) is typically 12‰ depleted in ^{13}C than those of HCO_3^- at 0°C and 8.4‰ depleted in ^{13}C at 30°C (Mook et al., 1974). This will result in a ^{13}C-depletion of 8 to 12‰ in the organism using CO_2 (aq) than the ones using HCO_3^-.

5.2.2 CO_2 concentration

CO_2 concentration is essentially determined by the partial gaseous CO_2 pressure (pCO_2) in the atmosphere upon the interface of water and air. According to Henry's law,

$$C = k \times P \text{ (5-2)}$$

C = concentration; k = Henry's Law constant; P = partial pressure of the gas

At 20°C, k for CO_2 in water is 3.4×10^{-2} M atm^{-1} and the pCO_2 is 3.9×10^{-4} atm, giving a theoretical concentration of 13.26 μM of CO_2 (aq) in water. This concentration is significantly lower than the Michaelis constant (Km, see chapter **2.1.3**) of CO_2 for RubisCO (25-68 μM) in marine diatom (Young et al., 2016).

While with an alkaline pH ranging from 8.0 to 8.2 and a high salinity in seawater, HCO_3^- concentration can reach as high as 2000 μM (Matsuda et al., 2001; Stumm & Morgan, 1995). Since CO_2 (aq) is distinctively able to permeate biological membranes (Gutknecht et al., 1977) among all CO_2 species, diatoms have developed a high DIC affinity mechanism to take up HCO_3^- actively from the environment and accumulate it inside the chloroplast.

Hence, the magnitude of $^{13}C/^{12}C$ fractionation during carbon transport and fixation in algae depends on the concentration of extra- and intracellular CO_2.

5.2.3 Fractionation during carbon uptake

Laboratory experiments show that the isotopic fractionations associated with the steps of CO_2 (aq) and/or HCO_3^- being processed across the cell membranes by diffusion or actively transport are small, usually less than l‰ (O'Leary, 1981). While the $^{13}C/^{12}C$ fractionation during photosynthesis when CO_2 was fixed by RuBisCO in Calvin Cycle is relative larger. Laboratory experiments have shown that $^{13}C/^{12}C$ fractionation by RuBisCO is approximately 29‰ versus aqueous CO_2,

or 37‰ versus total DIC at 30°C (Bidigare et al., 1997) (Guy et al., 1987; Roeske & O'Leary, 1984).

However, this maximum value is rarely expressed in marine photoautotrophs in natural settings due to the limitation in growth rate and cell geometry. Smaller *in situ* fractionations have been attributed to differences in growth rate and cell geometry (Bidigare et al., 1997; Popp et al., 1998). In addition, phosphoenolpyruvate (PEP) carboxylase in plants and some bacteria can catalyse the HCO_3^- to PEP (Kai et al., 2003).

5.2.4 Lipid classes and secondary metabolic pathways

Additional $^{13}C/^{12}C$ fractionations may occur during the secondary biosynthesis and lead to a significant variation in the $\delta^{13}C$ values among different algal lipid classes. A thorough understanding of the mechanism of varied isotopic composition of biosynthetic products requires the identification of carbon in biosynthetic substrates/precursors corresponding to the products on the level of specific carbon atoms.

Three major biosynthetic pathways – the acetogenic pathway for alkyl lipids, the MVA and DOXP/MEP pathways for isoprenoid lipids result in post-photosynthesis isotopic heterogeneity. The common precursors of all three pathways are G3P and pyruvate originating directly either from Calvin Cycle or sugar metabolism (Figure 5-1).

Rossmann et al. (1991) first determined the relative carbon isotopic composition of each position of glucose from a C4 plant and a C3 plant by stepwise chemical and biochemical degradation of the molecule and stable isotope ratio measurement of the fragments. Their results showed a relative 13C enrichment by 5 to 6‰ in C-4 position and a depleted by ca. 5‰ in C-6 position (Table 5-3 (a)), supported by recently work of Gilbert et al. (2009) using 13C NMR where they reported up to 10‰ differences of δ13C values within carbohydrates for glucose and sucrose from plant starch. The C-1, C-2 and C-3 positions are enriched in 13C by 0 to 2‰, the C-5 and C-6 position are depleted in 13C by up to 6‰, while the C-4 position is enriched in 13C by up to 6% (Table 5-3 (b)).

(a)

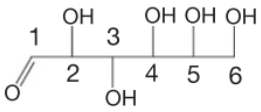

(b)

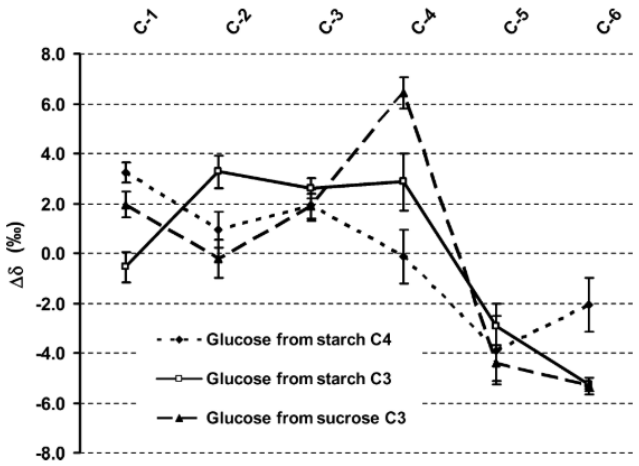

Figure 5-3. (a) The carbon positions in a C6 sugar unit; (b) $\delta^{13}C$ values of specific carbon atoms in glucose from starch C4, C3 and sucrose C3 higher plant, from (Gilbert et al., 2009). Values are described as isotope shift Δδ (‰) (Δδ = mean isotope deviation ($\delta i^{13}C$) - $\delta_g{}^{13}C$). The error bars are the standard deviations from the mean value observed for the set of samples (n = 4 for each origin).

The isotopic heterogeneity of glucose may be attributed to the different isotopic compositions within the starting substate (3-PGA). Figure 5-4 describes the sources of carbon atoms with respect to positions in lipids associated with three biosynthesis pathways. One molecule of glucose associated with two molecules of 3-PGA, of which C-3 and C-4 (diamond), C-2 and C-5 (circle), C-1 and C-6 (cube) in glucose corresponding with C-1 (diamond), C-2 (circle), C-3 (cube) in 3-PGA. The carbon atoms in G3P and pyruvate are inherited from those of 3-PGA.

Acetyl-CoA is the common precursor for both the ACT pathway and MVA pathway. It is formed by removing the carbon in the C-1 positions in pyruvate by decarboxylation. The carbon chain is then elongated by addition of malonyl CoA (detailed description of MVA pathway given in Chapter 4.1.2.2, Figure 4-2), result in long fatty acid chain made up with equal amount of C-2 carbon and C-3 carbon (Figure 5-4).

In MVA pathway, there is one more step involving removal of CO_2 in C-2 position during the formation of IPP from MVA. As a result, a five-carbon unit (IPP) contains two of C-2 carbons and three of C-3 carbons. Further decarboxylation may occur during the synthesis of functional compounds such as sterol afterwards (Figure 5-4).

In MEP pathway, one molecule of CO_2 was dropped from GAP when combing with pyruvate to yield MEP (detailed description of MEP pathway please see Chapter 4.1.2.3, Figure 4-3), resulting in a five carbon unit (IPP/DMAPP) with one of C-1 carbon, two of C-2 carbons and two of C-3 carbons (Figure 5-4).

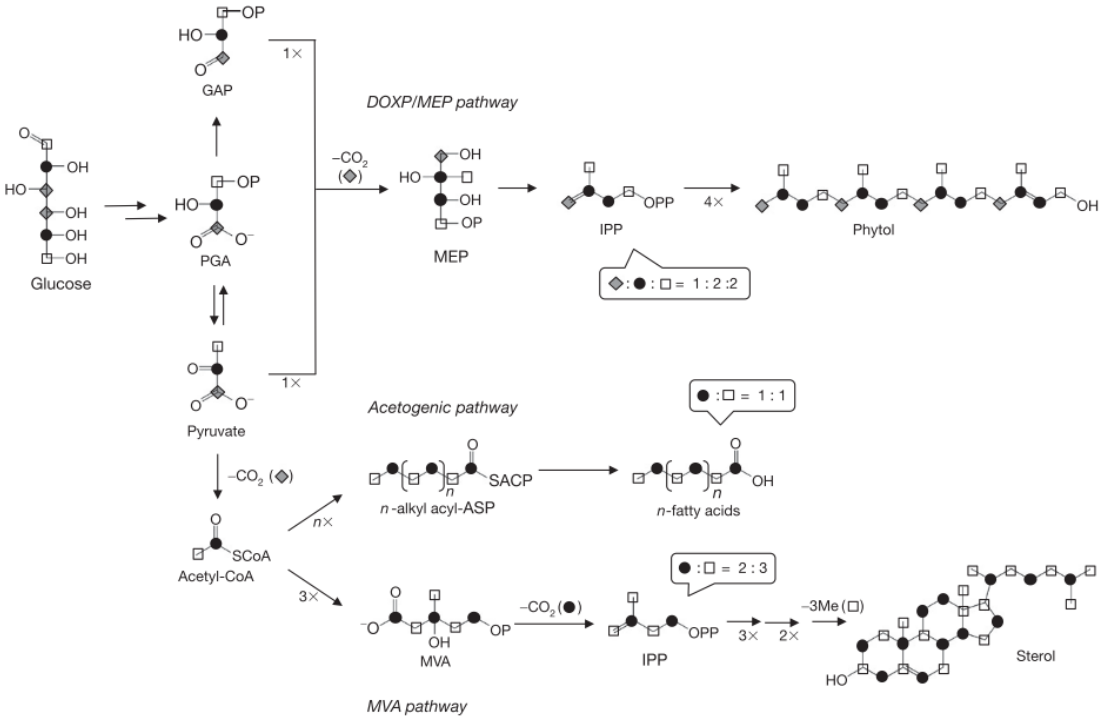

Figure 5-4. Sources of carbon atoms with respect to positions in lipids associated with the acetogenic, MVA, and DOXP/MEP pathways. Drawn by (Chikaraishi, 2014), after (Chikaraishi et al., 2004a; Lichtenthaler, 1999; Schwender et al., 1996). Carbon atoms derived from the C-1, C-2, and C-3 positions of PGA are represented by an open diamond, filled circle, and open square, respectively. Abbreviations are accordance with previous figures and listed in Table 5-1.

Generally speaking, in algae, *n*-alkanoic acids are expected to be 4.6-5.4‰ ^{13}C-depleted relative to biomass carbon (Chikaraishi et al., 2004a; Chikaraishi et al., 2004b; Hayes, 1993; Schouten et al., 1998; van Dongen et al., 2002); 9.6‰ for n-alkanes (Chikaraishi & Naraoka, 2003) and 3.1-4.5‰ for alkenone (Bidigare et al., 1997; Schouten et al., 1998; van Dongen et al., 2002). The magnitude of ^{13}C-depleteion of isoprenoid lipids is relatively variable, for example, sterols are 1.3-6.5‰ depleted in ^{13}C relative to biomass (Chikaraishi, 2006; Chikaraishi et al., 2004a; Schouten et al., 1998; van Dongen et al., 2002), and phytol is normal 2.5-3.8‰ depleted (Chikaraishi et al., 2004a; van Dongen et al., 2002).

5.3 Result (1) Stable Carbon isotopic compositions of lipids from laboratory cultured marine diatom *Pleurosigma intermedium*

Carbon isotopic compositions of acetogenic lipids (C14:0, C16:1 and C16:0 fatty acids) and isoprenoid lipids (C25:3, C25:4 HBIs, phytol and squalene) harvested from stationary phase of laboratory cultured marine diatom *P. intermedium* under six levels of light intensity ranging from 20 to 300 μmol m^{-2} s^{-1} were measured to explore the influence of irradiance on $^{13}C/^{12}C$ fractionation of algal lipids.

Overall, the $\delta^{13}C$ values of all lipid classes showed a positive correlation with irradiance. Up to 12.5‰ of difference of $^{13}C/^{12}C$ fractionation were observed within a single lipid under different light levels.

HBIs held the smallest $^{13}C/^{12}C$ fractionation, with the carbon isotopic compositions ranging from -19.7‰ to -8.2‰. Fatty acids had the intermediate $\delta^{13}C$ values of -38.5‰ to -17.5‰. Squalene showed the similar $\delta^{13}C$ values ranging from -30.4‰ to -21.8‰ but relative less sensitive in response to the increase of light. Lowest carbon isotopic compositions were observed in phytol ranging from -39.8‰ to -27.3‰ (Figure 5-5).

Besides, the $\delta^{13}C$ values of fatty acids and HBIs harvested from exponential were measured to compare the carbon isotopic compositions in different growth phases.

Each lipid class will be discussed separately in the following sections.

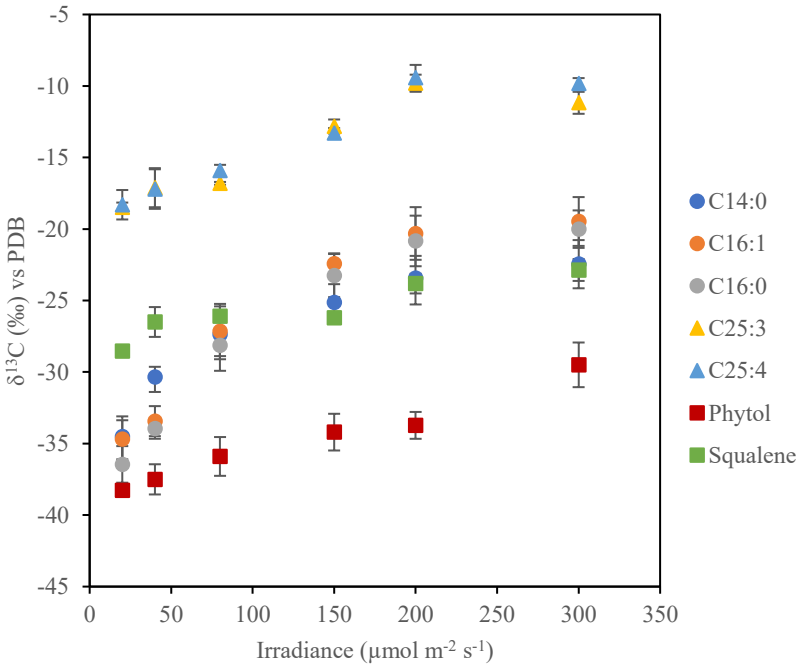

Figure 5-5. Relationships between irradiance and carbon isotopic composition of fatty acids (●), HBIs (▲), phytol and squalene (■) harvested from stationary phase of laboratory cultured marine diatom *P. intermedium*.

5.3.1 Fatty acids

Stable carbon isotopic compositions of fatty acids (C14:0, C16:1, C16:0) produced by *P. intermedium* in exponential phase and stationary phase were measured respectively.

For the samples harvested from exponential phase, the carbon isotopic composition of C14:0 fatty acid ranged from -46.6‰ at lowest irradiance (20 µmol m^{-2} s^{-1}) to -24.4‰ at highest irradiance (300 µmol m^{-2} s^{-1}). C16:1 and C16:0 had very close $\delta^{13}C$ values (as they had the same carbon skeleton) ranging from -40.1‰ and -40.2‰ at the lowest irradiance to -26.1‰ and -24.9‰ at highest irradiance respectively (Figure 5-6, Table 5-2).

Samples harvested from stationary phase were generally ^{13}C-enriched than these from exponential phase. Carbon isotopic compositions of C14:0 fatty acid ranged from -36.1‰ to -20.7‰, occurred at lowest irradiance and highest irradiance respectively. C16:1 and C16:0 showed the similar patten in response to increasing light conditions, ranging from to -37.6‰ to -17.5‰, -38.5‰ to -18.0‰ respectively (Figure 5-6, Table 5-3).

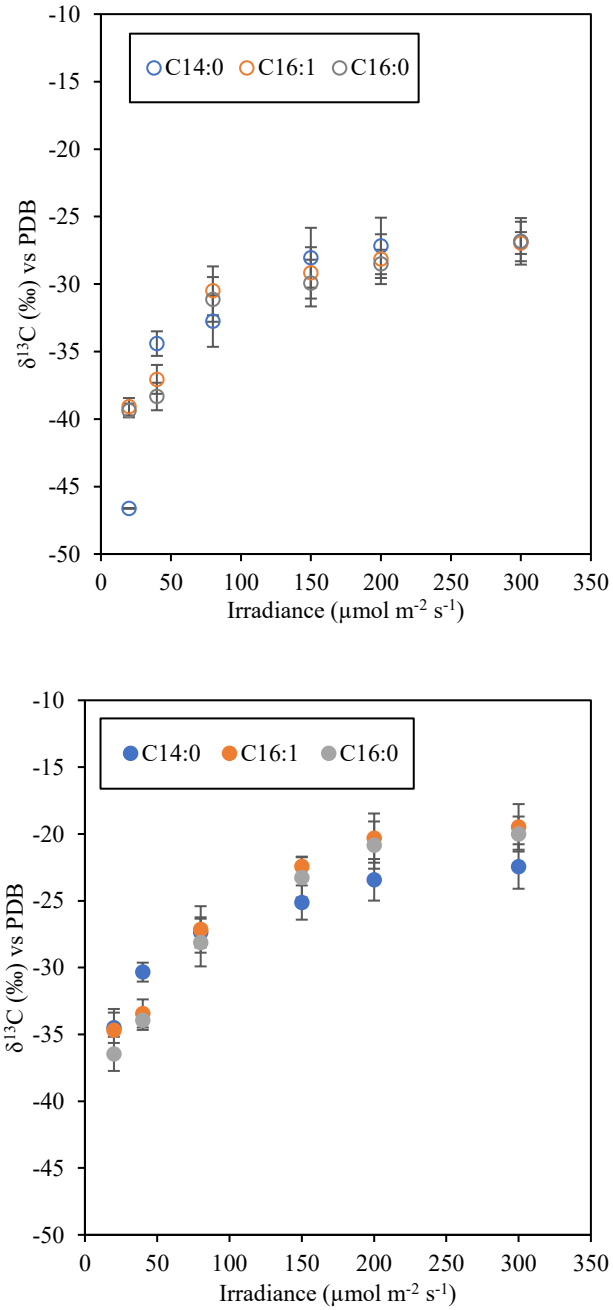

Figure 5-6. Relationships between irradiance and carbon isotopic composition of fatty acids C14:0 (blue), C16:1 (orange) and C16:0 (grey) harvested from exponential phase (○) and stationary phase (●) of laboratory cultured marine diatom *P. intermedium*.

Table 5-2. $\delta^{13}C$ values and lipid-water fractionation factor (α) of fatty acids C14:0, C16:1 and C16:0 harvested from exponential phase of laboratory cultured marine diatom *P. intermedium*. The alphabet represents biological repeats.

Irradiance ($\mu mol\ m^{-2}\ s^{-1}$)	Sample	Mass (freeze-dried, mg)	C14:0		C16:1		C16:0	
			$\delta^{13}C$ (‰)	α	$\delta^{13}C$ (‰)	α	$\delta^{13}C$ (‰)	α
20	PI_20_02a_exp	2.70	n.d.	n.d.	-38.6	0.961	-38.9	0.961
20	PI_20_03a_exp	2.60	n.d.	n.d.	-40.1	0.960	-39.3	0.961
20	PI_20_04a_exp	2.40	-46.6	0.953	-39.2	0.961	-39.0	0.961
20	PI_20_04b_exp	2.90	n.d.	n.d.	-38.5	0.962	-40.2	0.960
Ave			-46.6	0.953	-39.1	0.961	-39.4	0.961
Stdev			n.a.	n.a.	0.6	0.001	0.5	0.001
40	PI_40_03a_exp	4.50	-33.1	0.967	-36.3	0.964	-39.2	0.961
40	PI_40_03b_exp	4.50	-34.9	0.965	-36.3	0.964	-36.9	0.963
40	PI_40_03c_exp	2.60	-35.2	0.965	-38.6	0.961	-38.9	0.961
Ave			-34.4	0.966	-37.1	0.963	-38.3	0.962
Stdev			0.9	0.001	1.1	0.001	1.0	0.001
80	PI_80_01a_exp	0.27	-31.2	0.969	-29.0	0.971	-29.0	0.971
80	PI_80_02a_exp	3.10	-33.2	0.967	-32.7	0.967	-33.4	0.967
80	PI_80_02b_exp	2.70	-35.7	0.964	-31.8	0.968	-31.9	0.968
80	PI_80_02c_exp	5.80	-30.9	0.969	-28.4	0.972	-30.2	0.970
Ave			-32.7	0.967	-30.5	0.970	-31.1	0.969
Stdev			1.9	0.002	1.8	0.002	1.7	0.002
150	PI_150_01a_exp	0.73	-27.9	0.972	-26.0	0.974	-28.9	0.971
150	PI_150_01b_exp	0.74	-24.5	0.976	-29.4	0.971	-27.9	0.972
150	PI_150_03a_exp	2.30	-30.2	0.970	-30.5	0.970	-30.4	0.970
150	PI_150_03b_exp	3.40	-29.6	0.970	-30.8	0.969	-32.5	0.968
Ave			-28.0	0.972	-29.2	0.971	-29.9	0.970
Stdev			2.2	0.002	1.9	0.002	1.7	0.002
200	PI_200_01a_exp	0.67	-25.1	0.975	-26.2	0.974	-28.3	0.972
200	PI_200_01b_exp	0.62	-26.0	0.974	-28.2	0.972	-28.5	0.972
200	PI_200_03a_exp	2.70	-30.6	0.969	-31.1	0.969	-30.1	0.970
200	PI_200_03b_exp	2.80	-27.0	0.973	-27.1	0.973	-27.2	0.973
Ave			-27.2	0.973	-28.2	0.972	-28.5	0.971
Stdev			2.1	0.002	1.8	0.002	1.0	0.001

(Continued on next page)

Table 5-2. $\delta^{13}C$ values and lipid-water fractionation factor (α) of fatty acids C14:0, C16:1 and C16:0 harvested from exponential phase of laboratory cultured marine diatom *P. intermedium*. The alphabet represents biological repeats.

300	PI_300_01a_exp	1.46	-27.9	0.972	-26.3	0.974	-24.9	0.975
300	PI_300_01b_exp	1.48	-24.4	0.976	-28.4	0.972	-25.7	0.974
300	PI_300_03a_exp	4.00	n.d.	n.d.	-26.9	0.973	-29.1	0.971
300	PI_300_03b_exp	4.20	-28.2	0.972	-27.1	0.973	-27.4	0.973
300	PI_300_03c_exp	4.20	n.d.	n.d.	-26.1	0.974	-27.1	0.973
Ave			-26.8	0.973	-27.0	0.973	-26.8	0.973
Stdev			1.7	0.002	0.8	0.001	1.5	0.001

n.d. not detected
n.a. not available

Table 5-3. $\delta^{13}C$ values and lipid-water fractionation factor (α) of fatty acids C14:0, C16:1 and C16:0 harvested from stationary phase of laboratory cultured marine diatom *P. intermedium*. The alphabet represents biological repeats.

Irradiance ($\mu mol\ m^{-2}\ s^{-1}$)	Sample	Mass (freeze-dried, mg)	C14:0		C16:1		C16:0	
			$\delta^{13}C$ (‰)	α	$\delta^{13}C$(‰)	α	$\delta^{13}C$(‰)	α
20	PI_20_01a	3.47	n.d.	n.d.	-35.5	0.965	-36.5	0.963
20	PI_20_01b	4.35	n.d.	N.A.	-33.9	0.966	-35.1	0.965
20	PI_20_02c	3.40	-36.1	0.964	-37.6	0.962	-38.5	0.962
20	PI_20_06a	5.10	n.d.	n.d.	-33.2	0.967	-38.0	0.962
20	PI_20_06c	4.60	n.d.	n.d.	-32.7	0.967	-34.7	0.965
20	PI_20_08c	8.20	-32.9	0.967	-33.2	0.967	-35.3	0.965
20	PI_20_09a	7.80	-34.7	0.965	-35.6	0.964	-36.5	0.963
20	PI_20_09c	8.30	-34.3	0.966	-35.8	0.964	-37.0	0.963
Ave			-34.5	0.965	-34.7	0.965	-36.5	0.964
Stdev			1.1	0.001	1.6	0.002	1.3	0.001
40	PI_40_01a	5.08	-30.5	0.970	-32.6	0.967	-33.6	0.966
40	PI_40_01b	1.10	-31.1	0.969	-35.1	0.965	-35.1	0.965
40	PI_40_01c	2.24	-30.3	0.970	-33.6	0.966	-33.9	0.966
40	PI_40_06a	5.80	-30.9	0.969	-32.5	0.968	-33.1	0.967
40	PI_40_06b	5.90	-30.4	0.970	n.d.	n.d.	n.d.	n.d.
40	PI_40_06c	6.10	-28.9	0.971	n.d.	n.d.	n.d.	n.d.
Ave			-30.3	0.970	-33.4	0.967	-33.9	0.966
Stdev			0.7	0.001	1.1	0.001	0.7	0.001
80	PI_80_01a	3.88	-27.5	0.973	-28.8	0.971	-29.0	0.971
80	PI_80_01b	0.56	-28.4	0.972	-30.1	0.970	-30.7	0.969
80	PI_80_03a	7.80	-26.6	0.973	-26.5	0.974	-26.6	0.973
80	PI_80_06a	8.80	-25.5	0.974	-25.6	0.974	-29.6	0.970
80	PI_80_06b	6.80	-27.3	0.973	-26.6	0.973	-27.2	0.973
80	PI_80_06c	7.90	-29.0	0.971	-25.3	0.975	-25.6	0.974
Ave			-27.4	0.973	-27.1	0.973	-28.1	0.972
Stdev			1.1	0.001	1.7	0.002	1.8	0.002
150	PI_150_01b	0.25	-24.5	0.976	-21.9	0.978	-21.9	0.978
150	PI_150_01c	0.33	-26.2	0.974	-22.5	0.978	-24.7	0.975
150	PI_150_05a	7.70	-26.2	0.974	-23.6	0.976	-24.5	0.976
150	PI_150_05b	8.00	-22.9	0.977	-21.5	0.979	-21.0	0.979
150	PI_150_05c	7.30	-25.9	0.974	-22.6	0.977	-24.2	0.976
Ave			-25.1	0.975	-22.4	0.978	-23.3	0.977
Stdev			1.3	0.001	0.7	0.001	1.5	0.002

(Continued on next page)

Table 5-3 (continued). $\delta^{13}C$ values and lipid-water fractionation factor (α) of fatty acids C14:0, C16:1 and C16:0 harvested from stationary phase of laboratory cultured marine diatom *P. intermedium*. The alphabet represents biological repeats.

200	PI_200_01a	3.13	-24.2	0.976	-21.8	0.978	-22.7	0.977
200	PI_200_01b	2.17	-25.9	0.974	-20.1	0.980	-23.1	0.977
200	PI_200_01c	1.20	-24.6	0.975	-23.6	0.976	-21.9	0.978
200	PI_200_05a	5.00	-22.3	0.978	-18.6	0.981	-18.9	0.981
200	PI_200_05b	6.70	-21.9	0.978	-18.4	0.982	-19.2	0.981
200	PI_200_05c	5.10	-21.8	0.978	-19.4	0.981	-19.2	0.981
Ave			-23.4	0.977	-20.3	0.980	-20.8	0.979
Stdev			1.6	0.002	1.8	0.002	1.8	0.002
300	PI_300_01a	2.20	-20.7	0.979	-22.0	0.978	-21.8	0.978
300	PI_300_01b	1.04	-21.9	0.978	-17.5	0.983	-19.2	0.981
300	PI_300_05a	6.30	-21.4	0.979	-20.9	0.979	-20.9	0.979
300	PI_300_05b	6.00	-25.5	0.975	-19.1	0.981	-20.1	0.980
300	PI_300_05c	6.00	-22.8	0.977	-18.0	0.982	-18.0	0.982
Ave			-22.4	0.978	-19.5	0.981	-20.0	0.980
Stdev			1.7	0.002	1.7	0.002	1.3	0.001

n.d. not detected

5.3.2 HBIs

HBIs showed the smallest $^{13}C/^{12}C$ fractionation among all lipid classes in this study. For the samples harvested from exponential phase, C25:3 had lowest $\delta^{13}C$ value of -38.2‰ at light intensity of 20 µmol m^{-2} s^{-1}. The $\delta^{13}C$ values of C25:3 then increased with the increasing of light intensity and reached the highest value of -17.1‰ at light intensity of 200 µmol m^{-2} s^{-1}. C25:4 showed similar responses (ranging from -38.9‰ to -17.9‰) but slightly larger $^{13}C/^{12}C$ fractionation relative to C25:3 (Figure 5-7, Table 5-4).

Compared to exponential phase, samples from stationary phase were greatly enriched in ^{13}C and less sensitive to the varied light conditions. Carbon isotopic compositions of HBIs C25:3 and C25:4 ranged from -18.9‰ and -19.7‰ at light intensity of 20 µmol m^{-2} s^{-1} to -9.2‰ and 8.2‰ at light intensity of 200 µmol m^{-2} s^{-1} (Figure 5-7,Table 5-5).

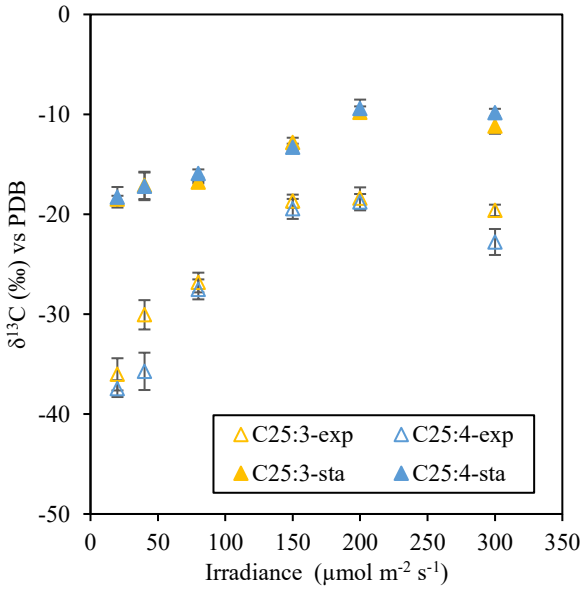

Figure 5-7. Relationships between irradiance and carbon isotopic composition of HBIs C25:3 (yellow) and C25:4 (blue) harvested from exponential phase (exp, △) and stationary phase (sta, ▲) of laboratory cultured marine diatom *P. intermedium*.

Table 5-4. $\delta^{13}C$ values and lipid-water fractionation factor (α) of HBIs C25:3, C25:4 harvested from exponential phase of laboratory cultured marine diatom *P. intermedium*. The alphabet represents biological repeats.

Irradiance ($\mu mol\ m^{-2}\ s^{-1}$)	Sample	Mass (freeze-dried, mg)	C25:3		C25:4	
			$\delta^{13}C$ (‰)	α	$\delta^{13}C$ (‰)	α
20	PI_20_01a_exp	2.51	-33.9	0.966	-36.9	0.963
20	PI_20_02a_exp	2.70	-38.2	0.962	-37.1	0.963
20	PI_20_03a_exp	2.60	-37.5	0.962	-38.9	0.961
20	PI_20_04a_exp	2.40	-35.6	0.964	n.d.	n.d.
20	PI_20_04b_exp	2.90	-34.9	0.965	-36.9	0.963
Ave			-36.0	0.964	-37.5	0.963
Stdev			1.6	0.002	0.8	0.001
40	PI_40_03a_exp	4.50	-28.7	0.971	-33.1	0.967
40	PI_40_03b_exp	4.50	-29.4	0.971	-36.8	0.963
40	PI_40_03c_exp	2.60	-32.1	0.968	-37.3	0.963
Ave			-30.1	0.970	-35.7	0.964
Stdev			1.5	0.001	1.9	0.002
80	PI_80_02a_exp	3.10	-28.2	0.972	-28.9	0.971
80	PI_80_02b_exp	2.70	-26.4	0.974	-27.1	0.973
80	PI_80_02c_exp	5.80	-25.9	0.974	-26.6	0.973
Ave			-26.8	0.973	-27.5	0.972
Stdev			1.0	0.001	1.0	0.001
150	PI_150_01a_exp	0.73	-18.1	0.982	-19.0	0.981
150	PI_150_03a_exp	2.30	-19.8	0.980	-21.0	0.979
150	PI_150_03b_exp	3.40	-18.6	0.981	-18.3	0.982
150	PI_150_03c_exp	3.10	-18.3	0.982	-19.6	0.980
Ave			-18.7	0.981	-19.5	0.981
Stdev			0.7	0.001	1.0	0.001
200	PI_200_01a_exp	0.67	-18.2	0.982	-17.9	0.982
200	PI_200_03a_exp	2.70	-18.2	0.982	-18.8	0.981
200	PI_200_03b_exp	2.80	-17.1	0.983	-18.4	0.982
200	PI_200_03c_exp	1.60	-20.1	0.980	-20.1	0.980
Ave			-18.4	0.982	-18.8	0.981
Stdev			1.1	0.001	0.8	0.001
300	PI_300_01b_exp	1.48	-19.4	0.981	-21.4	0.979
300	PI_300_03a_exp	4.00	-19.6	0.980	-21.6	0.978
300	PI_300_03b_exp	4.20	-20.5	0.979	-24.4	0.976
300	PI_300_03c_exp	4.20	-18.9	0.981	-23.7	0.976
Ave			-19.6	0.980	-22.8	0.977
Stdev			0.6	0.001	1.3	0.001

n.d. not detected

Table 5-5. $\delta^{13}C$ values and lipid-water fractionation factor (α) of HBIs C25:3, C25:4 harvested from stationary phase of laboratory cultured marine diatom *P. intermedium*. The alphabet represents biological repeats.

Irradiance ($\mu mol\ m^{-2}\ s^{-1}$)	Sample	Mass (freeze-dried, mg)	C25:3		C25:4	
			$\delta^{13}C$ (‰)	α	$\delta^{13}C$ (‰)	α
20	PI_20_06a	5.10	-18.1	0.982	-18.0	0.982
20	PI_20_06b	1.00	-18.9	0.981	-17.2	0.983
20	PI_20_08c	8.20	-18.5	0.981	-19.7	0.980
Ave			-18.5	0.982	-18.3	0.982
Stdev			0.3	0.000	1.0	0.001
40	PI_40_06a	5.80	-16.8	0.983	-15.7	0.984
40	PI_40_06b	5.90	-18.8	0.981	-19.1	0.981
40	PI_40_06c	6.10	-15.6	0.984	-16.8	0.983
Ave			-17.1	0.983	-17.2	0.983
Stdev			1.4	0.001	1.4	0.001
80	PI_80_06a	8.80	-16.8	0.983	-16.0	0.984
80	PI_80_06b	6.80	-16.9	0.983	-15.4	0.985
80	PI_80_06c	7.90	-16.7	0.983	-16.4	0.984
Ave			-16.8	0.983	-15.9	0.984
Stdev			0.1	0.000	0.4	0.000
150	PI_150_05a	7.70	-12.2	0.988	-13.2	0.987
150	PI_150_05b	8.00	-12.9	0.987	-12.9	0.987
150	PI_150_05c	7.30	-13.4	0.987	-13.8	0.986
Ave			-12.8	0.987	-13.3	0.987
Stdev			0.5	0.000	1.1	0.000
200	PI_200_05a	5.00	-10.6	0.989	-9.8	0.990
200	PI_200_05b	6.70	-9.6	0.990	-8.2	0.992
200	PI_200_05c	5.10	-9.2	0.991	-10.3	0.990
Ave			-9.8	0.990	-9.4	0.991
Stdev			0.6	0.001	0.9	0.001
300	PI_300_05a	6.30	-10.4	0.990	-9.4	0.991
300	PI_300_05b	6.00	-11.9	0.988	-10.2	0.990
Ave			-11.2	0.659	-9.8	0.990
Stdev			0.8	0.466	0.4	0.000

5.3.3 Phytol and squalene

Linear correlation was observed both in phytol and squalene in response to increasing irradiance. The $\delta^{13}C$ values of phytol increased from -39.8‰ at lowest light intensity to -27.3‰ at highest light intensity by 0.029‰ (µmol m^{-2} $s^{-1})^{-1}$ (R^2 = 0.98). Squalene increased from -30.4‰ to -21.8‰ by 0.018‰ (µmol m^{-2} $s^{-1})^{-1}$ (R^2 = 0.86, Figure 5-8, Table 5-6).

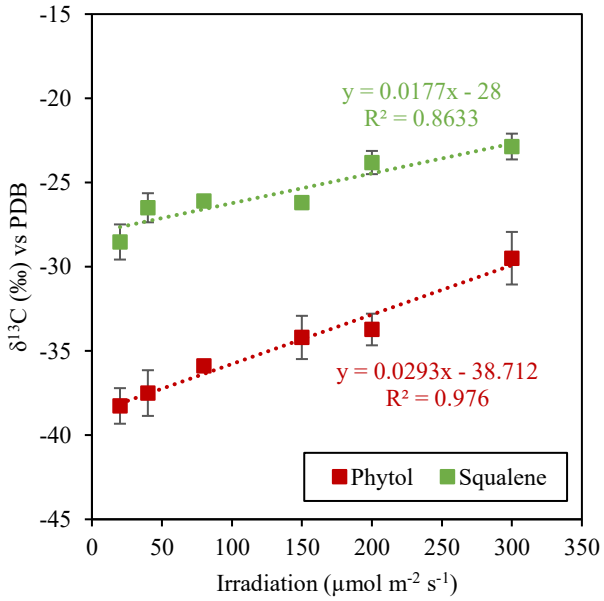

Figure 5-8. Relationships between irradiance and carbon isotopic composition of phytol (red) and squalene (green) harvested from laboratory cultured of marine diatom *P. intermedium*. $\delta^{13}C$ values of phytol and squalene increased as irradiance increased by 0.018‰ and 0.029‰ (µmol m^{-2} $s^{-1})^{-1}$ (R^2 = 0.86, 0.98) respectively.

Table 5-6. $\delta^{13}C$ values and lipid-water fractionation factor (α) of phytol and squalene harvested from stationary phase of laboratory cultured marine diatom *P. intermedium*. The alphabet represents biological repeats.

Irradiance ($\mu mol\ m^{-2}\ s^{-1}$)	Sample	Mass (freeze-dried, mg)	Phytol		Squalene	
			$\delta^{13}C$ (‰)	α	$\delta^{13}C$ (‰)	α
20	PI_20_06a	5.1	-37.6	0.962	-28.8	0.971
20	PI_20_06b	1.0	-37.0	0.963	-28.4	0.972
20	PI_20_08c	8.2	-39.8	0.960	-27.6	0.972
20	PI_20_09a	7.8	n.d.	n.d.	-27.5	0.972
20	PI_20_09c	8.3	-38.6	0.961	-30.4	0.970
Ave			-38.3	0.962	-28.5	0.971
Stdev			1.1	0.001	1.0	0.001
40	PI_40_06a	5.8	-39.4	0.961	-25.3	0.975
40	PI_40_06b	5.9	-36.8	0.963	-26.9	0.973
40	PI_40_06c	6.1	-36.3	0.964	-27.3	0.973
Ave			-37.8	0.962	-26.5	0.974
Stdev			1.4	0.001	0.9	0.001
80	PI_80_06a	8.8	-35.9	0.964	-26.1	0.974
80	PI_80_06b	6.8	n.d.	n.d.	n.d.	n.d.
80	PI_80_06c	7.9	n.d.	n.d.	n.d.	n.d.
80	PI_80_03a	7.8	n.d.	n.d.	n.d.	n.d.
Ave			-35.9	0.964	-26.1	0.974
Stdev			n.a.	n.a.	n.a.	n.a.
150	PI_150_05a	7.7	-33.1	0.967	-25.7	0.974
150	PI_150_05b	8.0	-36.0	0.964	-26.6	0.973
150	PI_150_05c	7.3	-33.5	0.967	-26.3	0.974
Ave			-34.2	0.966	-26.2	0.974
Stdev			1.3	0.001	0.4	0.000
200	PI_200_05a	5.0	-32.6	0.967	-22.9	0.977
200	PI_200_05b	6.7	-33.7	0.966	-24.6	0.975
200	PI_200_05c	5.1	-34.9	0.965	-24.0	0.976
Ave			-33.7	0.966	-23.8	0.976
Stdev			0.9	0.001	0.7	0.001
300	PI_300_05a	6.3	-30.4	0.970	-23.1	0.977
300	PI_300_05b	6.0	-27.3	0.973	-21.8	0.978
300	PI_300_05c	6.0	-30.8	0.969	-23.7	0.976
Ave			-29.5	0.971	-22.9	0.977
Stdev			1.6	0.002	0.8	0.001

n.d. not detected
n.a. not available

5.4 Result (2) The stable Carbon isotopic compositions of lipids from laboratory cultured marine diatom *Rhizosolenia setigera*

Carbon isotopic compositions of fatty acids C14:0, C16:1 and C16:0 and isoprenoid lipid C25:5 from laboratory cultured marine diatom *R. setigera* were measured. $\delta^{13}C$ values of C14:0 and C16:1 at 20 µmol m^{-2} s^{-1} were not detected due to low concentrations.

Our results suggested light mainly influenced the $^{13}C/^{12}C$ fractionation of three fatty acids in irradiance below 100 µmol m^{-2} s^{-1}. $\delta^{13}C$ values of C14:0 increased from -34.0‰ at irradiance of 40 µmol m^{-2} s^{-1} to -29.2‰ at irradiance of 300 µmol m^{-2} s^{-1}. $\delta^{13}C$ values of C16:1 ranged from -31.3‰ at irradiance of 40 µmol m^{-2} s^{-1} to -28.9‰ at irradiance of 150 µmol m^{-2} s^{-1} and remained an average of ca. -29‰ when light was higher. C16:0 increased from -35.3‰ to -28.3‰ from 20 to 300 µmol m^{-2} s^{-1} (Figure 5-9, Table 5-7).

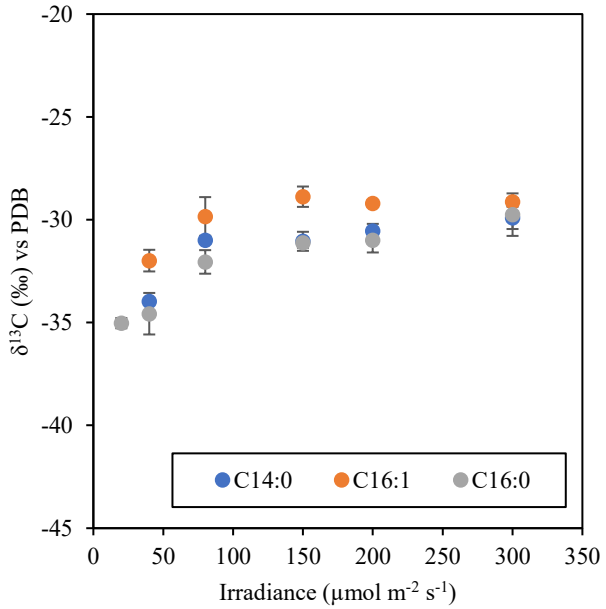

Figure 5-9. Relationships between irradiance and carbon isotopic composition of fatty acids C14:0 (blue), C16:1 (orange) and C16:0 (grey) harvest from stationary phase of laboratory cultured marine diatom *R. setigera*.

Only one HBI C25:5 was detected in laboratory cultured marine diatom *R. setigera*. The $\delta^{13}C$ values of HBI C25:5 increased from -35.1‰ at irradiance of 20 µmol m^{-2} s^{-1} to -28.6‰ at irradiance of 200 µmol m^{-2} s^{-1} then slightly decreased to -30.5 ‰ at irradiance of 300 µmol m^{-2} s^{-1}.

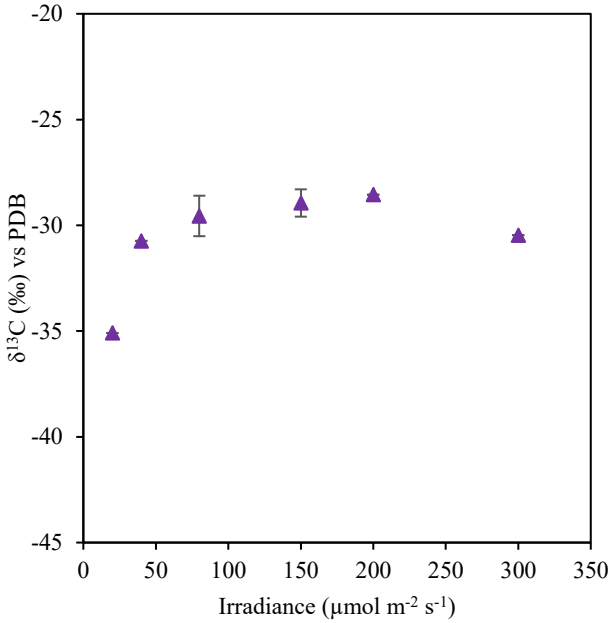

Figure 5-10. Relationships between irradiance and carbon isotopic composition of HBI C25:5 harvest from stationary phase of laboratory cultured marine diatom *R. setigera*.

Table 5-7. $\delta^{13}C$ values and lipid-water fractionation factor (α) of fatty acids C14:0, C16:1, C16:0 and HBI C25:5 harvested from stationary phase of laboratory cultured marine diatom *R. setigera.* The alphabet represents biological repeats.

Irradiance		Mass	C14:0		C16:1		C16:0		C25:5	
(µmol m^{-2} s^{-1})	Sample	(freeze-dried, mg)	$\delta^{13}C$ (‰)	α	$\delta^{13}C$ (‰)	α	$\delta^{13}C$ (‰)	α	$\delta^{13}C$ (‰)	α
20	RS_20a	0.34	n.d.	n.d.	n.d.	n.d.	-35.3	0.965	n.d.	n.d.
20	RS_20b	0.88	n.d.	n.d.	n.d.	n.d.	-34.8	0.965	-35.1	0.965
Ave			n.a.	n.a.	n.a.	n.a.	-35.0	0.965	-35.1	0.965
Stdev			n.a.	n.a.	n.a.	n.a.	0.3	0.000	n.a.	n.a.
40	RS_40a	1.75	-34.0	0.966	-32.6	0.967	-33.2	0.967	-30.7	0.969
40	RS_40b	2.81	n.d.	n.d.	-31.3	0.969	-35.4	0.965	n.d.	n.d.
40	RS_40c	1.18	n.d.	n.d.	-32.0	0.968	-35.1	0.965	n.d.	n.d.
Ave			-34.0	0.966	-32.0	0.968	-34.6	0.965	-30.7	0.969
Stdev			n.a.	n.a.	0.5	0.001	1.0	0.001	n.a.	n.a.
80	RS_80a	4.30	n.d.	n.d.	n.d.	n.d.	n.d.	n.d.	-30.5	0.969
80	RS_80b	3.23	n.d.	n.d.	-28.9	0.971	-32.6	0.967	-28.7	0.971
80	RS_80c	6.03	-31.0	0.969	-30.8	0.969	-31.5	0.969	n.d.	n.d.
Ave			-31.0	0.969	-29.8	0.970	-32.1	0.968	-29.6	0.970
Stdev			n.a.	n.a.	n.a.	n.a.	0.6	0.001	0.9	0.001
150	RS_150a	9.01	-31.7	0.968	-29.3	0.971	-31.2	0.969	n.d.	n.d.
150	RS_150b	6.21	-30.6	0.969	-28.2	0.972	-30.8	0.969	-28.7	0.971
150	RS_150c	4.93	-30.9	0.969	-29.2	0.971	-31.4	0.969	-29.6	0.970
Ave			-31.0	0.969	-28.9	0.971	-31.1	0.969	-29.1	0.971
Stdev			0.5	0.000	0.5	0.000	0.2	0.000	0.4	0.000
200	RS_200a	7.65	-30.3	0.970	-29.4	0.971	-30.6	0.969	n.d.	n.d.
200	RS_200b	4.66	-30.3	0.970	-29.2	0.971	-30.6	0.969	n.d.	n.d.
200	RS_200c	6.55	-31.0	0.969	-29.0	0.971	-31.8	0.968	-28.6	0.971
Ave			-30.5	0.969	-29.2	0.971	-31.0	0.969	-28.6	0.971
Stdev			0.3	0.000	0.1	0.000	0.6	0.001	n.a.	n.a.
300	RS_300a	7.31	-29.2	0.971	-28.9	0.971	-28.3	0.972	n.d.	n.d.
300	RS_300b	2.51	-30.2	0.970	-29.3	0.971	-30.3	0.970	-28.7	0.971
300	RS_300c	5.03	-30.4	0.970	-29.2	0.971	-30.7	0.969	n.d.	n.d.
Ave			-29.9	0.970	-29.1	0.971	-29.8	0.970	-28.7	0.971
Stdev			0.5	0.001	0.2	0.000	1.0	0.001	n.a.	n.a.

n.d., peak not detected or too small may introduce large error
n.a. not available

5.5 Discussion

5.5.1 Mechanism underlying the effect of light on $^{13}C/^{12}C$ fractionation of algal lipids

Light may not directly influence the carbon isotopic composition, however, the Calvin cycle requires the NADPH and ATP be produced in light reaction. Light is also necessary for the activation of RuBisCO. The impact of light on growth rate will further result in large difference in carbon isotopic compositions within and among algal lipid classes.

Here, a linear correlation between growth rate μ and $\delta^{13}C$ values of fatty acids and HBIs from laboratory cultured marine diatom *P. intermedium* was observed both in exponential phase and stationary phase (Figure 5-12).

For fatty acids, the $\delta^{13}C$ values of samples from exponential phase increased along with the increasing of growth rate by 25.6‰ $(day^{-1})^{-1}$ in C14:0; 17.1‰ $(day^{-1})^{-1}$ in 16:1 and 17.6‰ $(day^{-1})^{-1}$ in C16:0 (Figure 5-12, (a)). While for the samples harvested from stationary phase, C14:0 showed less sensitivity towards growth rate with an increase of 15.9‰ $(day^{-1})^{-1}$; while C16:1 and C16:0 seemed more sensitive in response to growth rate by 23.1‰ $(day^{-1})^{-1}$ and 24.3‰ $(day^{-1})^{-1}$ respectively (Figure 5-12, (b)).

Having the same carbon skeleton, HBIs C25:3 and C25:4 showed very similar $\delta^{13}C$ values and patterns in responses to growth rate. $\delta^{13}C$ values of HBIs harvested from exponential increased with growth rate by 26.2 and 28.7‰ $(day^{-1})^{-1}$ (Figure 5-12, (c)); while for the samples from stationary phase, the magnitude of variations in carbon isotopic composition relative to growth rate is significantly smaller (11.1 and 11.8‰ $(day^{-1})^{-1}$ for C25:3 and C25:4 respectively, Figure 5-12, (d)).

Ultimately, in this study, when other growth conditions did not limit the growth of diatom, growth rate played as a function of irradiance. A model of two extreme cases involving low and high growth rates are shown in Figure 5-11 to explain the correlations observed between carbon isotopic compositions and irradiance.

When light is extremely low, the inhibition of light reaction further significantly reduces the carboxylation reactions in Calvin Cycle. This allows the frequent exchanges DIC inside and outside of the cell and greatly minimises the carbon isotopic heterogeneity resulting in similar external ($\delta^{13}C_e$) and internal ($\delta^{13}C_i$)

carbon isotopic compositions. At this point, RuBisCO can always selectively fix the ^{12}C from CO_2 pool and a maximum $^{13}C/^{12}C$ fractionation (ε_p) by RuBisCO is expected (Figure 5-11 (a)).

When it comes to the high growth conditions, most of the DIC is expected to be carboxylated immediately once enters in cells owing to a high rate of photosynthesis. There hardly is opportunity for cell to selectively assimilate lighter CO_2 as all the DIC is used for photosynthesis (Figure 5-11 (b)).

As the fractionation during transport (ε_t) is expected small while the fractionation in carboxylation (ε_p) is potentially large, observed fractionation should theoretically vary from near-zero (<1‰) in low growth rate to ca. 37‰ in high growth rate relative to DIC.

Overall, our model suggests the $^{13}C/^{12}C$ fractionation in algae is primarily effected by the DIC exchange between cell and environment and the photosynthesis rate. Smaller fractionations may associate with an exchange-limited scenario while larger fractionations may indicate a carboxylation-limited scenario.

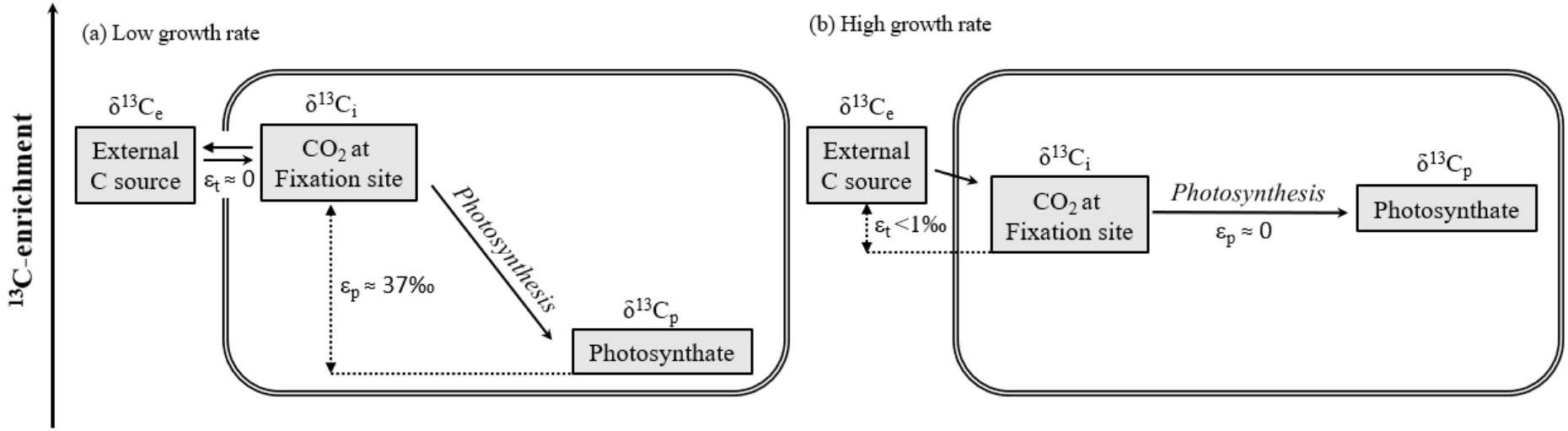

Figure 5-11. Schematic $^{13}C/^{12}C$ fractionation in during carbon transport and photosynthesis in low growth rate (a) and high growth rate (b) conditions (author originated). When growth rate is low (a), frequent exchanges of DIC between cell and environment results in similar external ($\delta^{13}C_e$) and internal ($\delta^{13}C_i$) carbon isotopic compositions. RuBisCO can selectively fix the ^{12}C from carbon pool and a maximum $^{13}C/^{12}C$ fractionation (ε_p) during photosynthesis is expected. When growth rate is high (b), DIC is expected to be fixed by RuBisCO immediately once enters in cells. The $^{13}C/^{12}C$ fractionation during photosynthesis (ε_p) can be as low as near zero.

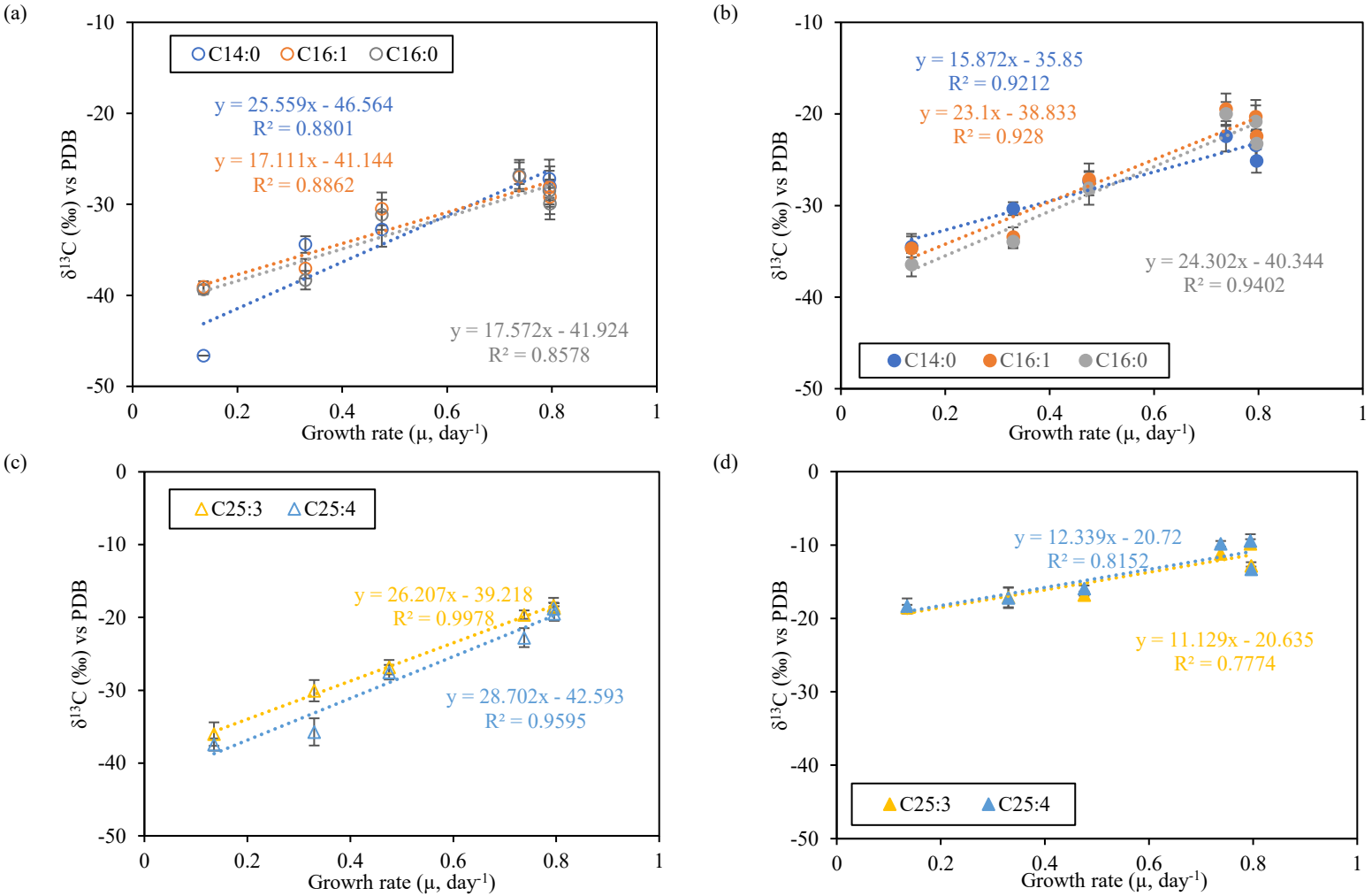

Figure 5-12. Linear correlation between growth rate (μ) and carbon isotopic compositions of fatty acids C14:0, C16:1 and C16:0 (a,b) and HBIs C25:3, C25:4 (c,d) harvested from exponential phase (open) and stationary phase (close) of laboratory cultured marine diatom *P. intermedium*.

5.5.2 Large carbon isotopic fractionation in exponential phase compared to stationary phase

Samples harvested from exponential phase were generally ^{13}C-depleted relative to those from stationary phase.

5.5.2.1 Fatty acids

An average of 5.4‰, 5.6‰ and 5.2‰ ^{13}C-depletion in fatty acids C14:0, C16:1 and C16:0 was observed respectively (Figure 5-13). This might be attributed to more isotopically heavy CO_2 being taken up during the growth of *P. intermedium*. When the carbon uptake rate was greater than the leaking rate of internal DIC, increasing amount of ^{13}C-enriched DIC will be fixed by RuBisCO and resulted in a ^{13}C enrichment.

Except the single data point of C14:0 we obtained from exponential phase with an unexpecting low $\delta^{13}C$ value of -46.6‰, there was no predominance difference of this ^{13}C-enrichement of fatty acids from stationary relative to exponential phase in different growth rate.

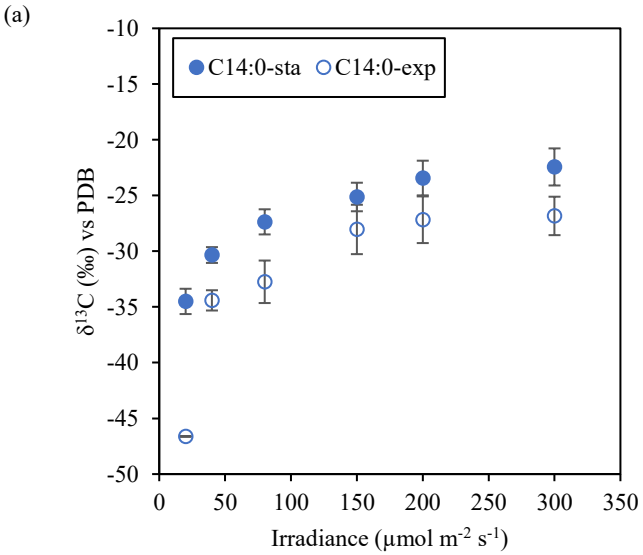

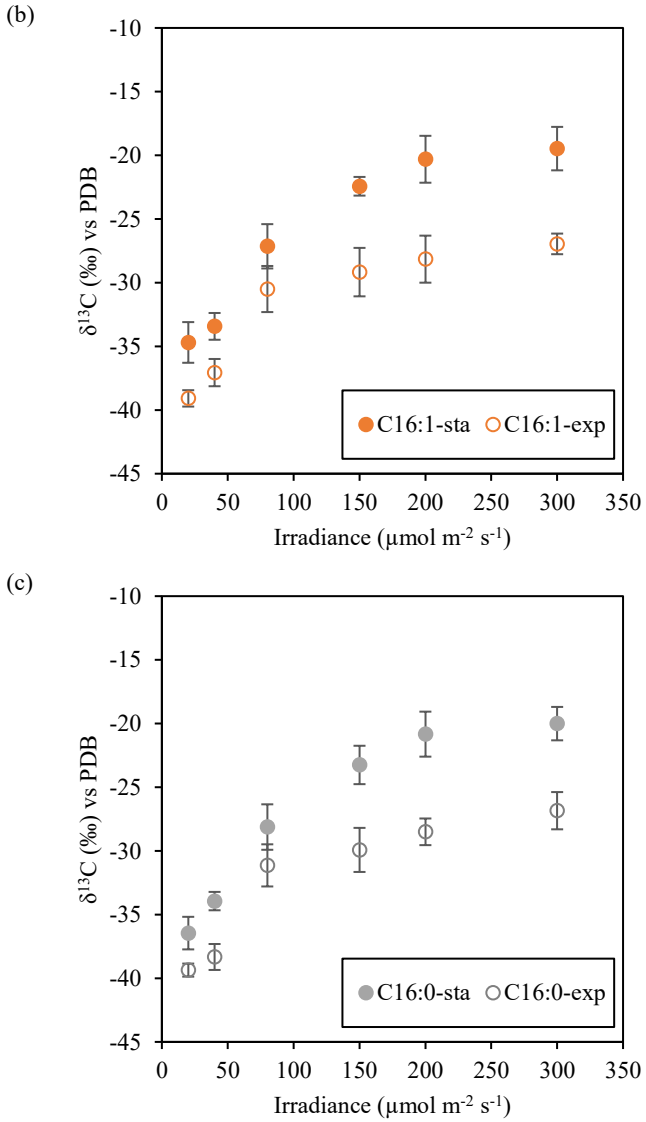

Figure 5-13. The comparison of $\delta^{13}C$ values of fatty acids (a) C14:0; (b) C16:1; and (c) C16:0 harvested from exponential phase (exp,○) and stationary phase (sta,●) of laboratory cultured marine diatom *P. intermedium*.

5.5.2.2 HBIs

The ^{13}C-enrichement of HBIs from stationary phase relative to exponential phase is much more predominant compared to fatty acids and showed a growth rate sensitive manner. A maximum of 17.5‰ in C25:3 and 19.2‰ in C25:4 of ^{13}C-enrichement of samples harvested from stationary phase relative to exponential phase were observed at lowest growth rate; while at highest growth rate, it was 5.7‰ and 6.2‰ (Figure 5-7, Figure 5-14). The differences between two growth phases generally became smaller when growth rate increased.

This is consistent with our pervious results of the concentrations of HBIs in exponential phase and stationary phase (see Chapter **3.3.2**). The yields of HBIs

kept increasing with the increase of irradiance in exponential phase. While in stationary phase, it seems that the biosynthesis of HBIs was significantly reduced when light is higher than 150 μmol m^{-2} s^{-1}, even with the highest growth rate. The majority of ^{13}C-enriched photosynthate were likely used to produce fatty acids instead of HBIs. This also led to a much wider range (up to 21‰ variation, Figure 5-7, Table 5-4) of carbon isotopic compositions of C25:3 and C25:4 from exponential phase in response to growth rate. In addition, the priority of fatty acids biosynthesis may also explain their consistency of ca. 5.5 ‰ ^{13}C-enrichment from stationary phase to exponential phase, regardless of growth rate.

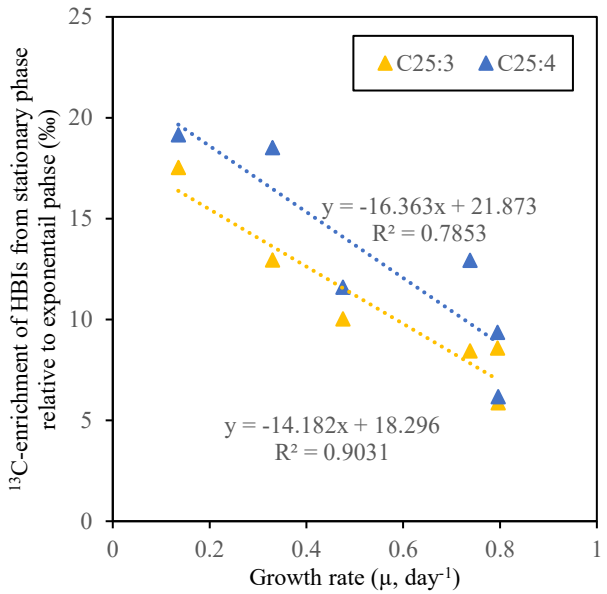

Figure 5-14. The ^{13}C-enrichemnt of HBIs C25:3 (yellow) and C25:4 (blue) harvested from stationary phase relative to exponential phase in different growth rate.

5.5.3 The comparison between two species: *P. intermedium* and *R. setigera*

Carbon isotopic compositions of fatty acids C14:0, C16:1, C16:0 from laboratory cultured marine diatoms *P. intermedium* and *R. setigera* under light conditions ranging from 20 to 300 μmol m^{-2} s^{-1} are plotted in Figure 5-15. In lowest irradiance, fatty acids of *P. intermedium* and *R. setigera* had very close carbon isotopic compositions. However, not like *P. intermedium*, the $^{13}C/^{12}C$ fractionation of fatty acids in *R. setigera* seemed in response to irradiance mainly at low light conditions (below 100 μmol m^{-2} s^{-1}) and remained consistent over 200 μmol m^{-2} s^{-1}. Our results showed up to 10‰ enrichment of ^{13}C in fatty acids from *P. intermedium* than *R. setigera* at light intensity of 300 μmol m^{-2} s^{-1}.

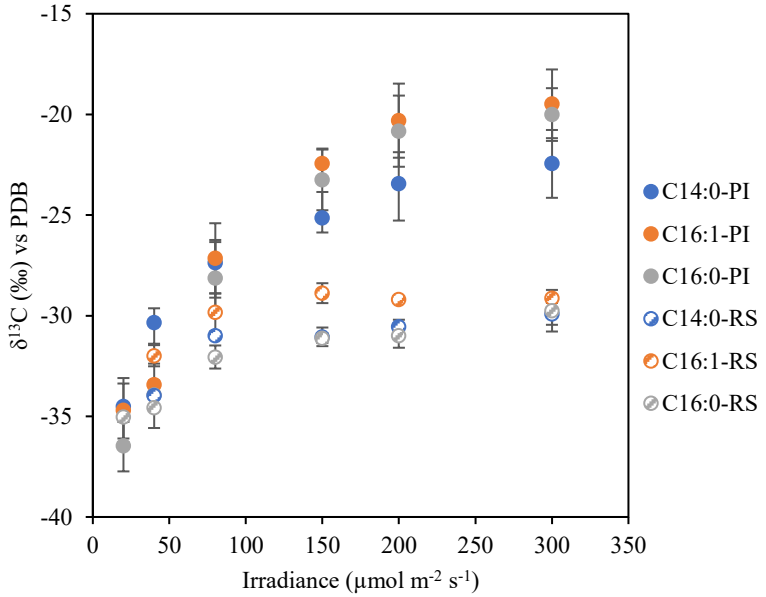

Figure 5-15. Carbon isotopic compositions of fatty acids C14:0 (blue), C16:1 (orange), C16:0 (grey) from stationary phase of laboratory cultured marine diatoms *P. intermedium* (PI, close) and *R. setigera* (RS, stripped) in response to increasing irradiance.

A similar linear relationship between fatty acids and growth rate was observed in *R. setigera* as well. The $\delta^{13}C$ values of C14:0, C16:1 and C16:0 increased with growth rate by 13.5‰, 10.4‰ and 15.3‰ $(day^{-1})^{-1}$ respectively (Figure 5-16, only showed C14:0).

The growth rates of *R. setigera* were significant lower than *P. intermedium* under the same irradiance. It should be noted that the cell size of *R. setigera* (>10 µm in long axes) is much bigger than *P. intermedium* (2-3 µm in long axes) and they were cultured in different temperatures (8°C for *R. setigera* and 15°C for *P. intermedium*). The $\delta^{13}C$ values of three fatty acids from *R. setigera* were generally isotopically heavier by 3-5‰ that from *P. intermedium* with similar growth rate. According to Mook et al. (1974) (see 5.2.1, Eqn. (5-1), the different culturing temperatures may result in ca. 0.85‰ enrichment of ^{13}C in HCO_3^- at 15°C than CO_2 (aq) at 8°C and both *R. setigera* and *P. intermedium* utilize HCO_3^- as main carbon source. Nevertheless, the effect of temperature on $^{13}C/^{12}C$ fractionation of CO_2 species is minor at this point. The yields of fatty acids from P. intermedium was more than ten times of that from *R. setigera* at the similar growth rate. Smaller $^{13}C/^{12}C$ fractionations of fatty acids in *R. setigera* are more likely attributed to the physiological state such as less active of RuBisCO in lower temperature and cell geometry (Popp et al., 1998).

Despite the difference in $\delta^{13}C$ values, our results of two species kept accordance with our expectations and supported our model of the mechanisms underlying the effect of irradiance on $^{13}C/^{12}C$ fractionation in algal biomarkers (see **5.5.1**).

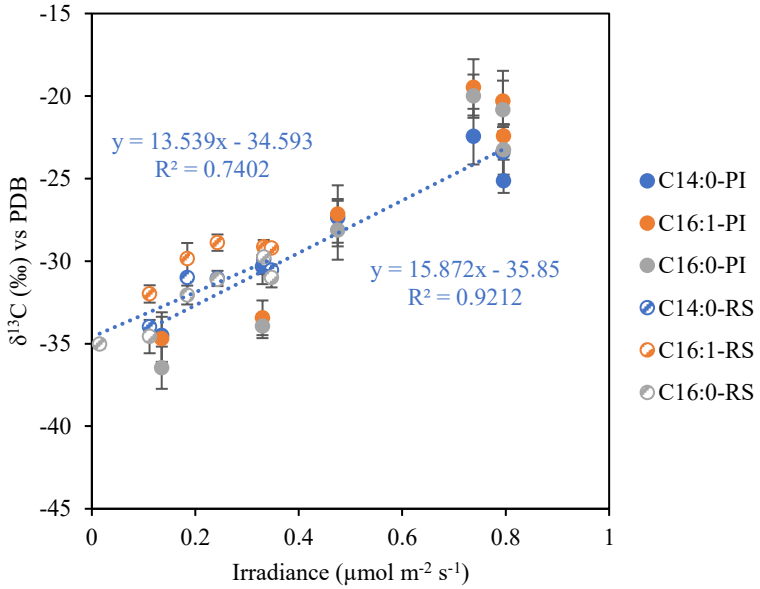

Figure 5-16. Liner relationship between carbon isotopic compositions of fatty acids C14:0, C16:1, C16:0 harvested from stationary phase of laboratory cultured marine diatoms *P. intermedium* (PI, close) and *R. setigera* (RS, stripped) and growth rate.

5.5.3.1 Large effect of irradiance on carbon isotope fractionation of HBIs within and between two diatom species: the implication of HBIs as sea ice proxies

As introduced in section 1.6, some HBIs such as IP_{25} and $IPSO_{25}$ hold the potential to be served as suitable biomarker proxies for sea ice conditions. A summary of published carbon isotopic compositions of HBIs from environmental samples from previous studies are listed in Table 5-8.

Table 5-8. A summary of the published Carbon isotopic data of HBIs from environmental samples.

	$\delta^{13}C$ value (‰)	Location	Reference
IP_{25}	-22.3 ± 0.4	Arctic (in sea ice)	(Belt et al., 2008)
IP_{25}	-19.6 ± 1.1	Arctic (under sea ice)	(Belt et al., 2008)
IP_{25}	-19.3 ± 2.3	Arctic (sediments)	(Belt et al., 2008)
IP_{25}	-17.1 ± 0.5	Arctic	(Brown, 2011)
$IPSO_{25}$	-9.4 to -9.1	Antarctica	(Sinninghe Damsté et al., 2007)
$IPSO_{25}$	-8.5 to -5.7	Antarctica	(Massé et al., 2011)
$IPSO_{25}$	-12.5 ± 3.3	Antarctica (open waters)	(Schmidt et al., 2018)
HBI III	-42.7 to -35	Arctic and Antarctic	(Belt et al., 2008) (Massé et al., 2011) (Schmidt et al., 2018; Smik et al., 2016)
C25:5	-38 to -41	Antarctica	(Massé et al., 2011)

Almost in all studies reported to date, IP_{25} in Arctic Sea ice, under sea ice and/or in sediments have been significantly enriched in ^{13}C than the majority of

phytoplanktonic organic matter from the Arctic and kept consistent with a sea ice origin (see review of Belt & Müller (2013) and references therein). They believed these distinctive isotopically heavy signatures of IP_{25} would support it as an Arctic Sea ice proxy. For the large range of carbon isotopic composition for IP_{25} in sea ice and sediments, they hypothesised that there might be a more variable and open brine channel network in Arctic Sea ice, along with greater replenishment of CO_2 from sub-surface water.

While similar ^{13}C-enrichment of $IPSO_{25}$ was also observed in sediments (Belt et al., 2016; Massé et al., 2011; Sinninghe Damsté et al., 2007) in the Antarctic and in some near-surface waters proximal to melting sea ice (Schmidt et al., 2018), with even smaller $\delta^{13}C$ values.

For HBIs triene (C25:3) and pentaene (C25:5), they can be identified from most locations and are not limited to polar diatoms. The carbon isotopic compositions showed more depleted in ^{13}C, ranging from -35 to -42.7‰ (Belt et al., 2008; Massé et al., 2011) and -38 to -41‰ (Massé et al., 2011).

Actually, Belt et al, (2008) have summarised their data on carbon isotopic compositions of the HBIs, n-alkanes and bulk organic matter in the Arctic sea ice, sediment traps and sediments from seasonally ice-covered locations in the Canadian High Arctic and the related data obtained from the literature (Figure 5-17, see (Belt et al., 2008) and references therein). Based on the similarity between the carbon isotopic compositions of IP_{25} from sea ice ($\delta^{13}C$ = -22.3‰ ± 0.4), sediments ($\delta^{13}C$ = -19.3‰ ± 2.3) and sediment trap samples ($\delta^{13}C$ = -19.6‰ ± 1.1) and the consistency with reported $\delta^{13}C$ values from Arctic sea ice organic matter (−18.3‰ to −20.6‰) (Schubert & Calvert, 2001), they hypothesized a so-called "specificity of IP_{25} to a sea ice origin" meaning wherever detected, its isotopic signature should ideally reflect its formation from within this isolated environment. Considering the ubiquity of other algal biomarkers like *n*-alkanes, they believed that the specificity of IP_{25} made it a more reliable biomarker to represent the bulk sea ice isotopic composition.

Nevertheless, they pointed out that the local environmental conditions such as CO_2 concentrations and temperature might influence the diatom growth and further isotopic compositions of the individual lipids. The magnitude of this influence required the analysis of more sea ice samples from different locations.

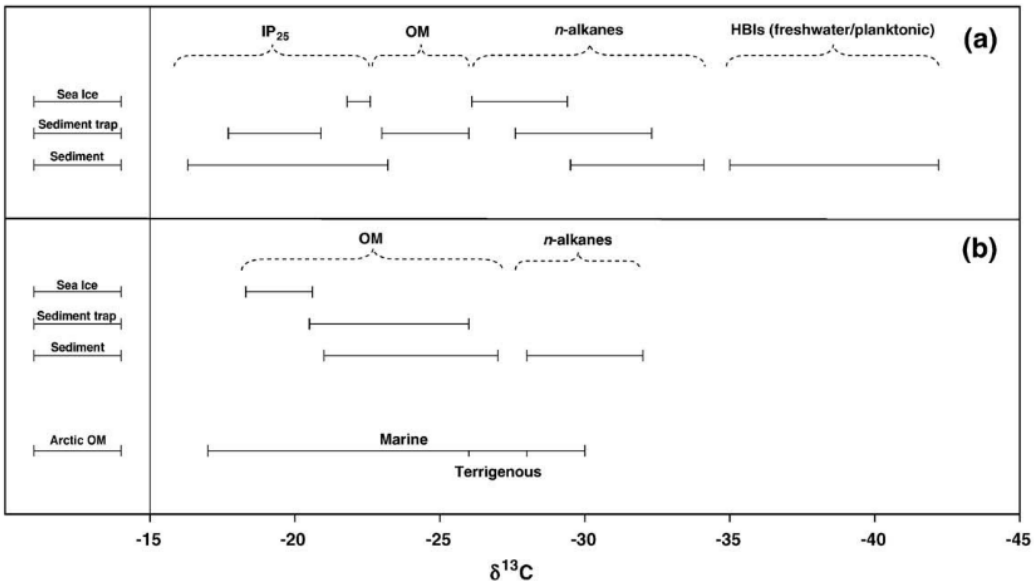

Figure 5-17. A summary of $\delta^{13}C$ values for bulk organic matter and individual biomarkers from (Belt et al., 2008) and references therein; (a)5 sea ice, sediment trap and sediment samples obtained from Franklin Bay, Canadian High Arctic from (Belt et al., 2008); (b) literature data cited in (Belt et al., 2008).

Here, we presented a wide range of carbon isotopic compositions of HBIs (-19.7 to -9.2‰ for HBIs harvested from stationary phase and -38.2 to -17.1‰ for the ones from exponential phase in *P. intermedium*; -35.1 to -28.6‰ for C25:5 in *R. setigera* growing under varied irradiance.

Distinct ^{13}C-enriched HBIs were observed in our laboratory cultured samples of *P. intermedium* from stationary phase. However, large variation of carbon isotopic compositions in response to different irradiance, especially in low light conditions was found. For the samples from exponential phase, $\delta^{13}C$ values were significantly lower and showed an even wider range. We could not explain the distinct isotopic heavy feature of HBIs C25:3 and C25:4, however, it is clear that different growth rate, as a function of varied growth conditions (e.g. irradiance, as in this study) would lead to significant difference in $^{13}C/^{12}C$ fractionation of algal lipids, and the differences of isotopic compositions of lipids from different growth phases can be large.

Our results of $\delta^{13}C$ values of HBI C25:5 from laboratory cultured *R. setigera* are significant lower (more than 10‰ at similar growth rate) than those from *P. intermedium* (Figure 5-18). These differences may attribute to the potential different biosynthesis pathway. Based on our hydrogen isotopic data of HBI C25:3 and C25:4 in Chapter 4.5.1.3, it was likely that C25:3 and C25:4 were produced via MVA pathway while *R. setigera* might use MEP pathway. Physiological state

of *P. intermedium* and *R. setigera* will almost certainly lead to difference in $^{13}C/^{12}C$ fractionation.

A good correlation also observed between C25:5 and growth rate ($R^2 = 0.81$, Figure 5-18). Compared to the environmental samples of several *Rhizosolenia spp.* isolated from polar and sub-polar locations from Arctic and Antarctic Table 5-8, (Belt et al., 2017), our results of *R. setigera* showed ca. 7‰ ^{13}C enrichment.

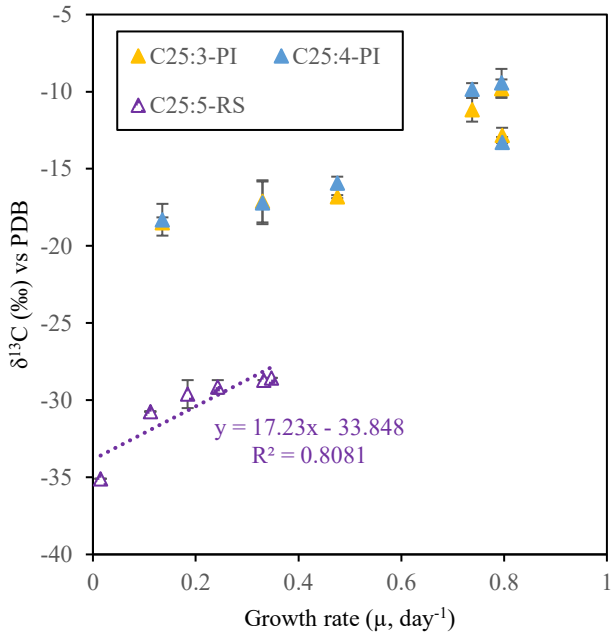

Figure 5-18. Liner relationship between carbon isotopic compositions of HBIs harvested from stationary phase of laboratory cultured marine diatoms *P. intermedium* (PI, C25:3, C25:4, close) and *R. setigera* (RS, C25:5, stripped) and growth rate.

5.6 Conclusion and potential implication for the sea ice reconstruction

Carbon isotopic compositions of lipids from phototrophic organisms have been used as a tool to reflect carbon-related environmental parameters. Here, we presented the first data set of carbon isotopic signatures of several lipid classes from marine diatom *Pleurosigma intermedium* and *Rhizosolenia setigera* in response to six levels of irradiance ranging from 20 to 300 μmol m^{-2} s^{-1}.

Our results of *P. intermedium* showed HBIs C25:3 and C25:4 were the most ^{13}C-enriched lipids, fatty acids C14:0, C16:1 and C16:0 and squalene had the intermediate $\delta^{13}C$ values and phytol had the largest ^{13}C depletion. Same fatty acids produced by *R. setigera* showed similar $\delta^{13}C$ values with HBI C25:5. The sources of each carbon atom and carboxylation step in different biosynthesis pathways may result in this variation among different lipid classes (Figure 5-4, (Chikaraishi, 2014)).

The $\delta^{13}C$ values of all lipid classes showed a positive correlation with irradiance by varied magnitude though. A linear correlation between growth rate and carbon isotopic compositions of fatty acids and HBIs was observed both in P. intermedium and *R. setigera*. The limitation of DIC exchange and/or carboxylation by growth rate is likely responsible for the $^{13}C/^{12}C$ fractionation during photosynthesis (Figure 5-11).

Samples harvested from the stationary phase were generally enriched in ^{13}C compared to those from the exponential phase since an increasing amount of ^{13}C-enriched DIC was fixed by RuBisCO when after ^{12}C-enriched DIC was used up during the earlier growth phase.

Incorporating published carbon isotopic compositions of different HBIs from polar regions, our data showed similar values but a much wider range and high sensitivity towards varied irradiance, especially in low light conditions. The magnitude of differences in carbon isotopic signatures of algal lipids introduced by varied irradiance and growth phase was remarkable and will lead to misinterpretations of HBIs as sea ice proxies.

More field-based studies and laboratory cultures are required to improve our understanding of the link between the carbon isotopic compositions of algal lipids

and environmental parameters and the fundamental processes controlling $^{13}C/^{12}C$ fractionation during photosynthesis and further secondary biosynthesis of individual lipids.

Our observation of HBIs responding to a light gradient may provide some insights with regard to sea ice reconstruction, however, the exact biosynthetic pathway and function of HBIs in different diatom species still needs to be explored.

Further work are required to increase our level of understanding of the magnitude and details of the differences between and within individual algal lipid classes in relation to environmental parameters such as salinity, temperature, and irradiance.

6 A novel tri-unsaturated HBI alkene from the marine diatom *Navicula salinicola*

This chapter has been peer-reviewed at published (see supplementary materials). This work was done by Simin Gao (main experimental work), Lukas Smik (GC-MS analysis, NMR analysis), Maxim Kulikovskiy (strain collection and financial support of laboratory work), Nataliya Shkurina and Evgeniy Gusev (strain isolation and cultivation), Nikolai Pedentchouk (project development and manuscript discussions), Thomas Mock (project development and manuscript discussions) and Simon T. Belt (manuscript main writer).

6.1 Introduction

This chapter is a relatively independent chapter describing our work on the identification of a novel tri-unsaturated C_{25} highly branched isoprenoid (HBI) alkene from laboratory culture of the diatom *Navicula salinicola*.

As described in 1.6, C_{25} HBI alkenes are common components of marine and lacustrine sediments worldwide and are biosynthesised by certain diatoms mainly belonging to the genera *Haslea*, *Navicula*, *Rhizosolenia*, *Pleurosigma, Berkeleya* and *Pseudosolenia* (Belt et al., 2000; Belt et al., 1996; Belt et al., 2001; Brown, Belt, & Cabedo-Sanz, 2014; Grossi et al., 2004; Kaiser et al., 2016; Sinninghe Damsté et al., 1999; Volkman et al., 1994). In terms of *Navicula* genus, a single tri-unsaturated C_{25} HBI (Structure 6; Figure 6-1) has been identified in the freshwater diatom *N. sclesvicensis* (Belt et al., 2001), and the mainly brackish species *N. phyllepta* has also been reported as an HBI-producing diatom (Sinninghe Damsté et al., 2004), although no structures were given. In contrast, no HBIs have as yet been reported in any marine species within the *Navicula* genus.

Here, a novel tri-unsaturated C_{25} HBI was detected from a laboratory culture of the marine diatom *N. salinicola*. This new HBI was then isolated by large-scale culture and its structure was determined by a combination of nuclear magnetic resonance (NMR) spectroscopy and gas chromatography-mass spectrometry (GC-MS). This newly characterised HBI contains a relatively unusual conjugated diene sub-unit (Structure 3; Figure 6-1), a structural feature only previously

reported in some HBIs biosynthesised by a further marine diatom, *Haslea ostrearia*.

The main outcome of this chapter has been published in Organic Geochemistry entitled A novel tri-unsaturated highly branched isoprenoid (HBI) alkene from the marine diatom *Navicula salinicola* by (Gao et al., 2020). This represents the first report of a C_{25} HBI in a marine diatom from the *Navicula* genus.

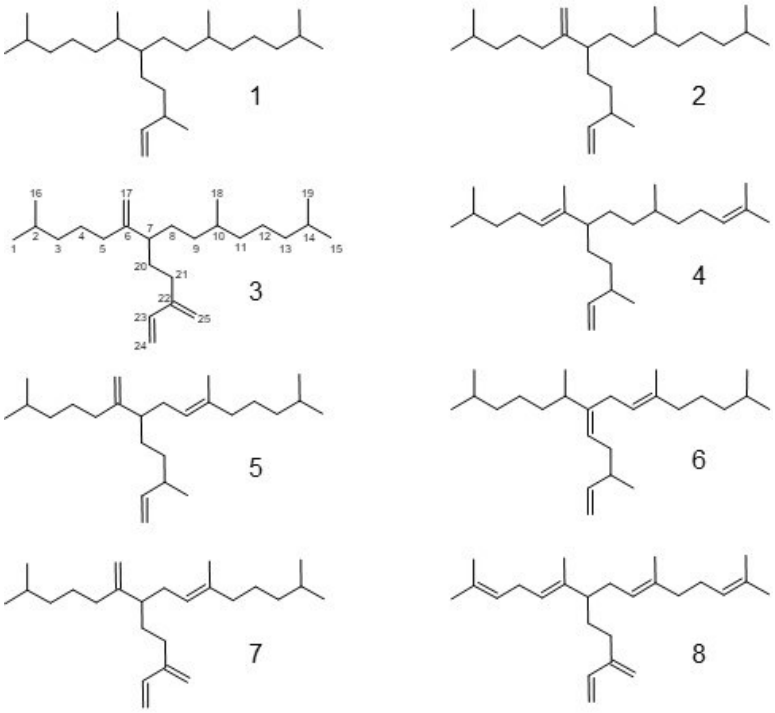

Figure 6-1. Structures of C_{25} HBIs referred to in the text. HBIs are numbered in order of increasing unsaturation.

6.2 Strain information

6.2.1 Sample collection

The benthic diatom *N. salinicola* was collected from a coastal marine environment (M. Kulikovskiy, June 2016 at Nha Trang, Vietnam, 12°13'14.5"N 109°12'18.3"E) and kept as strain BTD1 in the Laboratory of Molecular Taxonomy of Aquatic Plants Institute of Plant Physiology, Russian Academy of Science (RAS).

6.2.2 Sample preparation

Samples of *N. salinicola* were treated with 10% hydrochloric acid to remove carbonates and washed several times using deionized water for 12 hours. Samples were then boiled in concentrated hydrogen peroxide (≈ 37%) to dissolve organic matter. Cleaned frustules were then washed four times with deionized water at 12 hours intervals. After decanting and refilling with up to 100 mL deionized water, the suspension was spread onto coverslips and left to dry at room temperature. Permanent diatom preparations were mounted in Naphrax®. Light microscopic (LM) observations were performed with a Zeiss Axio Scope A1 microscope equipped with an oil immersion objective (× 100, n.a. 1.4, differential interference contrast [DIC]) and Axiocam ERc 5s camera (Zeiss). Valve ultrastructure was examined by means of a JSM-6510LV scanning electron microscope (IBIW, Institute for Biology of Inland Waters RAS, Borok, Russia). For scanning electron microscopy (SEM), parts of the suspensions were fixed on aluminium stubs after air-drying. The stubs were sputter-coated with 50 nm Au in an Eiko IB 3 sputter coater. Samples and slides were also deposited in the public collection of Maxim Kulikovskiy at the Herbarium of the Institute of Plant Physiology Russian Academy of Science, Moscow, Russia.

6.2.3 Strain identification

Identification of *N. salinicola* was made on the basis of the description of Lange-Bertalot (2001) as follows: Valves linear-lanceolate, ends obtusely rounded. Length 14.9-16.2 µm, breadth 3.6-4.4 µm. Raphe filiform, central pore close together, very small and drop-like (Lange-Bertalot, 2001). Distal raphe ends hock-shaped and goes to the mantle. Axial area is very narrow. The central area is small and circular. Striae parallel to slightly radiate, convergent at the ends, 16-18 in 10 µm. Lineolate is about 40 in 10 µm. The presence of lineolate, smooth

valve face outside without hyaline rings shows that this species belongs to typical Navicula taxa, not to Haslea, or other naviculoid taxa. See Figure 6-2 for further details.

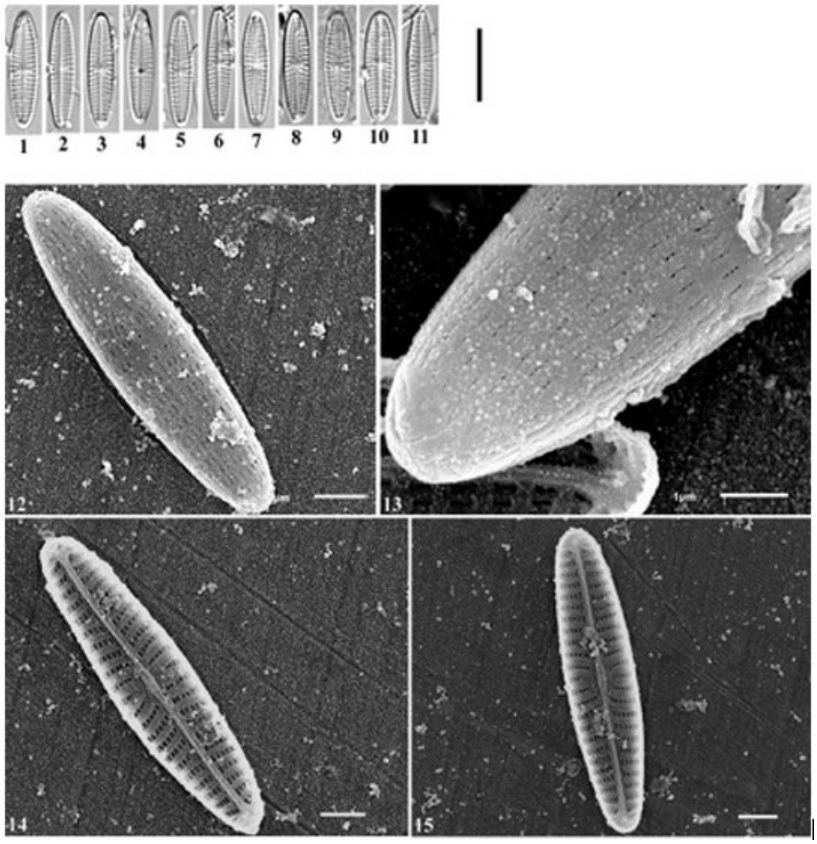

Figure 6-2. *Navicula salinicola* Hustedt. LM, DIC, size diminution series, Scale bar = 10 μm (1–11). SEM, external views (12, 13), internal views (14, 15).

6.3 Experimental

Initially, *N. salinicola* was cultured at 15 °C, 150 μmol m^{-2} s^{-1} continuous light in small flasks (150 mL). Samples were harvested by filtration using MF-Millipore™ membrane filters (25 mm diameter, 0.3 μm pore size) during the exponential and stationary growth phases (Figure 6-3). Large-scale cultures were then set up in several 2 L conical flasks under the same growth conditions. 80 L of such cultures were harvested by centrifugation (4000 rpm, 10 mins) during the stationary growth phase. For the small- and large-scale culture experiments, we used enriched f/2 medium (Guillard & Ryther, 1962), along with the following nutrient concentrations: 2646 μM $NaNO_3$, 318 μM Na_2SiO_3, 108 μM NaH_2PO_4. The filtered and centrifuged biomass was freeze dried and the resulting dry material was extracted via sonication using hexane (3 ml for small-scale cultures; 25 ml for large-scale cultures). The total hexane extract (THE) was then concentrated by removing hexane under a stream of nitrogen and partially purified using column chromatography (SiO_2). The hydrocarbon fraction (hexane) was analysed by GC–MS using an Agilent 7890 gas chromatograph equipped with an HP5MS fused-silica column (30 m; 0.25 μm film thickness; 0.25 mm internal diameter) coupled to an Agilent 5975 series Mass Selective Detector (MSD). NMR data were obtained using a JEOL ECP-400 NMR spectrometer with chemical shifts measured relative to those of CDCl3 (1H: 7.24 ppm; 13C: 77.0 ppm). NMR data were collected on the THE obtained from the large-scale culture. The purity of the newly reported C25:3 HBI in this THE was estimated to be ca. 90% based on its relative peak area (GC–MS; Figure 6-4) and by the relative integration values of H-23 (Figure 6-1) versus the alkenic protons of the co-occurring polyunsaturated linear alkenes (δ = ca. 5.3 ppm) in the 1H NMR spectrum.).

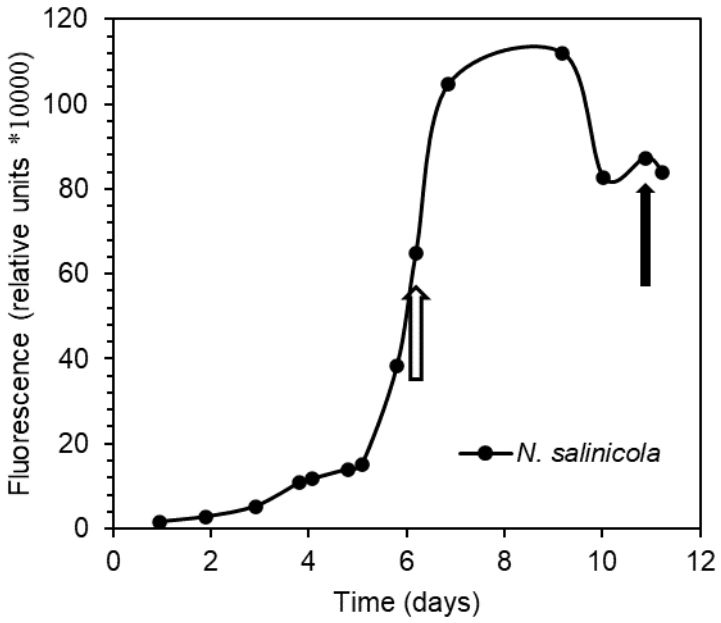

Figure 6-3. Growth curve of the small-scale culture of the marine diatom *N. salinicola*. Cell densities were estimated by measuring in vivo fluorescence between 460 nm to 670 nm using the SpectraMax® iD3 Multi-Mode Microplate Reader. Cultures were harvested during the exponential (empty arrow) and/or stationary (solid arrow) growth phases (n=1).

6.4 Results and discussion

Following extraction of several small-scale cultures of *N. salinicola* from the exponential and stationary growth phases, analysis of partially purified THEs by GC–MS revealed the presence of a suite of closely eluting polyunsaturated linear alkenes (e.g. heneicosa-3,6,9,12,15,18-hexaene; *n*-$C_{21:6}$), trace amounts of a di-unsaturated HBI (**2**; Figure *6-1*) and a further compound exhibiting similar mass spectral properties to a range of C_{25} HBIs characterised previously. However, although the retention index (RI) of this component (RI_{HP5ms} = 2141) did not match that of any previously reported C_{25} HBIs, hydrogenation of an aliquot of one THE resulted in the formation of the parent HBI alkane $C_{25:0}$, thus confirming the C_{25} carbon skeleton. Interestingly, this new HBI was only detected in cultures harvested during the stationary phase and was identified as tri-unsaturated on the basis of its molecular ion ($M^{+\cdot}$ 346; Figure 6-5). At this point, it is not clear why this new HBI and the co-occurring diene **2** were not detected during the exponential growth phase, although we note that some variability in cellular HBI concentrations and distributions have been reported in a small number of previous studies (Brown et al., 2020; Wraige et al., 1997; Wraige et al., 1998; Wraige et al., 1999). From the large-scale culture of *N. salinicola*, we obtained ca. 0.2 mg of the partially purified HBI triene (**3**; Figure 6-1), which enabled full structural characterisation using ^{1}H and ^{13}C NMR spectroscopy. A conjugated diene sub-structure (C22–C25; C23–C24; Figure 6-1) could be readily identified through a particularly characteristic low field resonance in the ^{1}H NMR spectrum due to H-23 ((Allard et al., 2001; Wraige et al., 1997), together with further low field resonances that could be attributed to alkenic methylene protons at C24 and C25 (Table 6-1). The third double bond could also be identified from its methylene protons at C17. Alternative positions for this third double bond at C1–C2 or C14–C15 can be discounted due to the observation of two isopropyl groups in the ^{1}H and ^{13}C NMR spectra (Table 6-1). Further, a double bond at C10–C18 leaves a solitary methyl group at C17 whose ^{13}C chemical shift would be at ca. 15.5 ppm, by comparison with related compounds (e.g. **1**; (Belt et al., 2012). In contrast, isolated methyl groups at C18 in previously characterised HBIs resonate at ca. 19–20 ppm (e.g. 19.8 ppm for HBIs **1** and **2**; Figure *6-1*) (Belt et al., 2012; Johns et al., 1999), consistent with that observed for HBI 3 (i.e. 19.9 ppm; Table 6-1). The 13C NMR spectrum of HBI 3 also contained individual resonances due to the six

magnetically inequivalent alkenic carbon nuclei (Table 6-1) and complete ^{13}C resonance assignments could be proposed by comparison with structurally similar HBIs characterised previously (Figure *6-1*) (Allard et al., 2001; Belt et al., 2012; Belt et al., 1996; Wraige et al., 1997), some of which contain a conjugated diene sub-unit (i.e. **7**–**8**). The GC RI of HBI **3** (RI_{HP5ms} = 2141) is substantially higher than those of some other HBI trienes (e.g. RI_{HP5ms} = 2114 (**4**); 2109 (**5**); 2090 (**6**)) but is consistent with that reported for the structurally related tetraene **7** ($RI_{HP\text{-}5}$ = 2159) (Allard et al., 2001).

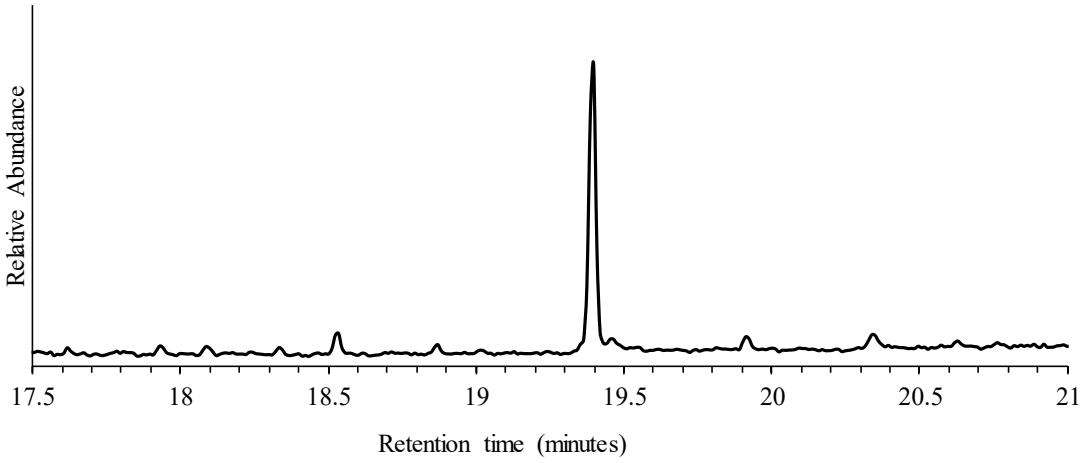

Figure 6-4. Partial GC– MS chromatogram of the THE obtained from the bulk culture of *N. salinicola*.

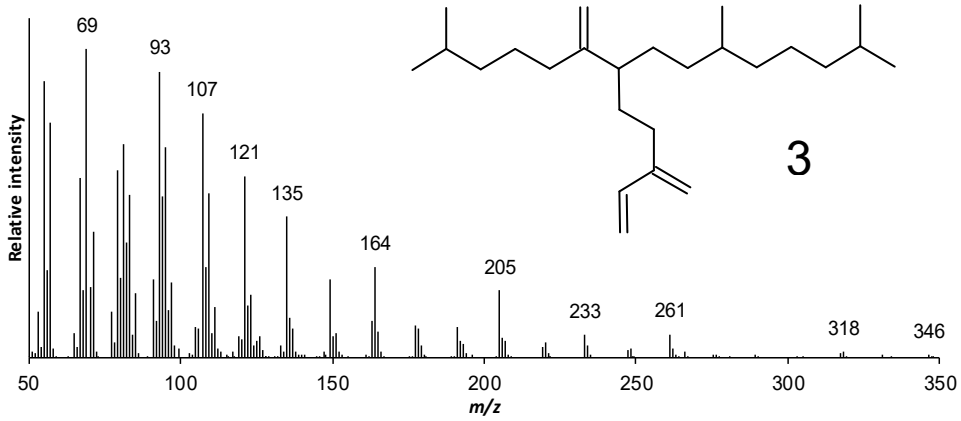

Figure 6-5. Structure and mass spectrum of HBI 3.

Table 6-1. Key NMR data for HBI 3.

	Carbon shift (δ/ppm)	Proton Number	Proton shift (δ/ppm)
1,16*	22.8, 22.7*	1,15,16,19	0.85 (12H, m)
2	28.0	5,7,21	2.05 (5H, m)
3	39.1	17	4.77, 4.72 (2H, 2 x s, br)
4	25.6	18	0.82 (3H, t, J=6.9 Hz)
5	33.0	23	6.33 (1H, dd, J=17.6, 11.0 Hz)
6	152.3	24a	5.01 (1H, d, J=11.0 Hz)
7	47.1	24b	5.16 (1H, d, J=17.6 Hz)
8	29.8	25	4.96 (2H, m, br)
9	34.9		
10	33.0		
11	37.1		
12	24.8		
13	39.4		
14	28.0		
15,19*	22.8, 22.7*		
17	109.0		
18	19.9		
20	29.4		
21	32.0		
22	146.9		
23	139.0		
24	113.1		
25	115.5		

The identification of a C_{25} HBI in *N. salinicola* represents the first example of HBI production within a marine *Navicula* species despite the near-ubiquity of this genus within natural diatom populations. Since the *Navicula* and *Haslea* genera are quite similar, phylogenetically, with the latter well-known as an HBI-producing genus, the new finding is probably not surprising; however, *Navicula* is a far more common genus, potentially making it a more important source of some HBIs in marine sediments. In terms of its structure, the conjugated diene sub-structure (C22–C25; C23-C24; Figure 6-1) is somewhat unusual, although there is some previous precedent for such a feature in other HBIs isolated from a small number of cultures of the marine diatom *Haslea ostrearia* (Allard et al., 2001; Wraige et al., 1997). In fact, HBI **3** is a close structural analogue of HBI **7** identified previously in *H. ostrearia*, albeit as a minor component. Since the retention index of HBI **3** (RI_{HP5ms} = 2141) is similar to two HBI tetraenes identified in some cultures of *H. ostrearia* (*viz.* $RI_{HP\text{-}5}$ = 2143–2146) (Allard et al., 2001), one of which also contained HBI **7**, it possible that HBI **3** may also have been present in the corresponding lipid extracts, but not identified due to co-elution. We are unaware of any geochemical reports of HBI **3** although its characterisation described herein may, in the future, lead to its positive identification in sedimentary archives, an outcome that may potentially add to the use of HBIs as

paleoenvironmental indicators (c.f. HBIs **1** and **2** for the Arctic and Antarctic sea ice; see (Belt, 2018) for a review).

6.5 Conclusions

We report the structural identification of a novel C_{25} HBI biomarker in the marine diatom *N. salinicola*, the first example of HBI production within a marine *Navicula* species, thus expanding the potential number of sources of HBIs in the environment. Further studies into *N. salinicola* and related species may prove valuable in the use of HBIs as palaeoenvironmental proxies.

7 Chapter SEVEN Conclusions and future work

7.1 Conclusions

To investigate the effect of irradiance on hydrogen and carbon isotopic compositions of algal lipids, light-controlled growth experiments of potential HBI-producers *N. salinicola*, *P. intermedium* and *R. setigera* were set up. Cultures were monitored on a daily basis and harvested in the exponential phase and stationary phase respectively.

The growth rate of all three strains increased as the light increased until the maximum growth rate was reached. The yields of fatty acids produced by *P. intermedium* remained proportionate to the irradiance even at the highest irradiance, while the yield of HBIs dropped after reaching the maximum growth rate. In addition, an inversed correlation between the concentration of HBI C25:5 produced by *R. setigera* and light intensity was observed.

For the relative amount of HBIs C25:3 and C25:4 produced by *P. intermedium*, a sharp diminishing of the fraction of C25:3 was observed both in the exponential phase and stationary phase as the light increased. We believe that the ratio of C25:3 versus C25:4 holds the potential to indicate light conditions while in practical application, attention needs to be paid to the biodegradation and shift between HBIs.

The hydrogen isotopic compositions of algal lipids isolated from *P. intermedium* and *R. setigera* showed different directions and magnitude of $^{2}H/^{1}H$ fractionation within and among lipid classes as irradiance increased. A turning point of hydrogen isotopic composition of fatty acids harvested from stationary phase in response to the increase of the light was observed both in *P. intermedium* and *R. setigera*. The $\delta^{2}H$ values first decreased because more ^{2}H-depleted photosynthetic NADPH was produced as light increased. When light continued getting higher and the cell eventually reach the highest growth rate, more ^{2}H-enriched metabolic NADPH was involved to fulfil the increasing yields of fatty acids, hence minimising the $^{2}H/^{1}H$ fractionation. $\delta^{2}H$ values of the isoprenoid lipids from *P. intermedium* were negatively correlated with light. The increasing NADPH and pyruvate produced by photosynthesis in high light conditions were responsible for this larger $^{2}H/^{1}H$ fractionation.

Besides, fatty acids harvested in the stationary phase experienced greater $^{2}H/^{1}H$ fractionation than that from the exponential phase as a result of accumulated photosynthetic NADPH originated lipids. Significant differences in algal lipids produced by two diatom species were observed as well. HBI C25:5 produced by *R. setigera* showed an opposite direction and smaller sensitivity in response to light compared to the HBIs produced by *P. intermedium*.

Carbon isotopic compositions of lipids isolated from *P. intermedium* showed HBIs C25:3 and C25:4 were the most ^{13}C-enriched lipids, fatty acids C14:0, C16:1 and C16:0 and squalene had the intermediate $\delta^{13}C$ values and phytol had the largest ^{13}C depletion. Same fatty acids produced by *R. setigera* showed similar $\delta^{13}C$ values with HBI C25:5.

The $\delta^{13}C$ values of all lipid classes showed a positive correlation with irradiance. A linear correlation between growth rate and carbon isotopic compositions of fatty acids and HBIs was observed both in *P. intermedium* and *R. setigera*. The limitation of DIC exchange and/or carboxylation by growth rate is likely responsible for the $^{13}C/^{12}C$ fractionation during photosynthesis.

Samples harvested from the stationary phase were generally enriched in ^{13}C compared to those from the exponential phase since an increasing amount of ^{13}C-enriched DIC was fixed by RuBisCO when ^{12}C-enriched DIC was used up during the earlier growth phase.

Incorporating published carbon isotopic compositions of different HBIs from polar regions, our data showed similar values but a much wider range and high sensitivity towards varied irradiance, especially in low light conditions. Large differences in carbon isotopic signatures of algal lipids induced by varied irradiance and growth phase may lead to misinterpretations of HBIs as sea ice proxies.

Laboratory culture and field-based studies of hydrogen and carbon isotopic fractionation of algal lipids in response to a variety of environmental conditions such as salinity, temperature have been applied to interpret hydrological and climate models. However, the mechanisms underly the effect of light on hydrogen and carbon isotopic compositions of algal lipids can be of great complexity as light can not only impact the growth rate of cells but also directly control the photosynthesis rate. This study presented the first data set of both hydrogen and

carbon isotopic compositions of algal lipids isolated from laboratory cultured marine diatom under varied light conditions. Systematic changes were observed both in hydrogen and carbon isotopic compositions of algal biomarkers. The results of this study can provide new insights into the fundamental mechanisms responsible for determining the isotopic composition of lipid biomarkers.

More importantly, this study characterises the relationship between hydrogen and carbon isotopic fractionation of the sea ice biomarker HBI(s) and light. This novel work can potentially develop a new method for identifying variable light transmission through sea ice. However, the exact biosynthetic pathway and function of HBIs in different diatom species still need to explore.

7.2 Future work

Initially, the main purpose of this study is to enhance the role of HBI(s) as a sea ice indicator by interpreting their isotope compositions. However, due to the limitation of the length of a Ph.D. project and the effect of COVID-19, we failed to conduct culture experiments under lower temperature conditions to mimic the polar regions, which may lead to a mismatch between our results and environmental samples.

However, systemic differences of hydrogen and carbon isotopic compositions within and among different lipids classes were observed both in room temperature (15°C) and low temperature (8°C). Our results have provided fundamental evidence of how light influent the growth of phytoplankton with regards of its hydrogen and carbon isotopic values on the compound-specific level.

In order to improve the role of HBI(s) toward a quantitative sea ice thickness assessment, more extensive data is a prerequisite. Future work should be more focused including not limited on several points below,

(1) More algal culture experiments are required, especially the stains can produce IP_{25} and $IPSO_{25}$. Ideally low light and low temperature should be applied to growth conditions, these may result in extreme slow growth rate and long growth length though.
(2) Increase the number of varied light levels used in culture experiments, particularly in low light conditions (below 40 μmol m^{-2} s^{-1}). As significant different responses to increasing light has been observed between *P. intermedium* and *R. setigera*, the influence of light can be specie-dependent. The test of other potential HBI-producers will also be required.
(3) Apart from laboratory culture, field studies should collect sea ice thickness data alongside biochemical data from the Arctic and Antarctic sample sites to determine the validity of the novel proxy in real world environments and to determine the influence of diagenesis on HBI isotopic signature. Further, the influence of snow thickness and meltwater ponding on the hydrogen and carbon isotopic compositions requires further analysis, focusing on the inter annual variability of sea ice and snow thickness.

(4) Last but not least, the physiological function and biosynthetic pathway of HBIs requires more solid work such as isotope-labelling and sequencing to reveal.

Once again, sea ice has extremely complicated structure, and light as an essential resource for sea ice ecosystems, was characterised not only by the thickness of the sea ice but also other features such as sea ice type, the formation process and snow cover. Our study provide the evidence of the influence of light on algal growth and provide the possible mechanism in terms of different biosynthetic pathways. However, no attempted being made to correlate irradiance range in laboratory conditions with light in real world in the sea ice. The simulation of sea ice condition in laboratory is required, which may require a longer time scale culture work up to several years. Nepenthes, a better understanding of the mechanism of the phototrophic organisms in response to variable light intensity is vital and will aid our ability to interpret changes to paleo sea ice thickness and infer the state of the wider paleo Arctic climate system.

References

Allard, W. G., Belt, S. T., Massé, G., Naumann, R., Robert, J.-M., & Rowland, S. J. (2001). Tetra-unsaturated sesterterpenoids (Haslenes) from Haslea ostrearia and related species. *Phytochemistry*, *56*, 795-800.

Armand, L., Ferry, A., & Leventer, A. (2017). Advances in palaeo sea ice estimation. In D. N. Thomas (Ed.), *Sea Ice* (Third ed., pp. 600-629). John Wiley & Sons.

Armand, L. K., Crosta, X., Romero, O., & Pichon, J.-J. (2005). The biogeography of major diatom taxa in Southern Ocean sediments. *Palaeogeography, Palaeoclimatology, Palaeoecology*, *223*(1-2), 93-126. https://doi.org/10.1016/j.palaeo.2005.02.015

Armand, L. K., & Leventer, A. (2010). Palaeo sea ice distribution and reconstruction derived from the geological record. In D. N. Thomas & G. S. Dieckmann (Eds.), *Sea Ice* (Second ed., pp. 469-530). Wiley-Blackwell Publishing Ltd, Oxford.

Arrigo, K. R. (2017). Sea ice as a habitat for primary producers. In D. N. Thomas (Ed.), *Sea Ice* (Third ed., pp. 352-369). John Wiley & Sons.

Arrigo, K. R., Mock, T., & Lizotte, M. P. (2010). Primary producers and sea ice. In D. N. Thomas & G. S. Dieckmann (Eds.), *Sea Ice* (Second ed., pp. 293-325). Wiley-Blackwell Publishing Ltd, Oxford.

Bailleul, B., Berne, N., Murik, O., Petroutsos, D., Prihoda, J., Tanaka, A., Villanova, V., Bligny, R., Flori, S., Falconet, D., Krieger-Liszkay, A., Santabarbara, S., Rappaport, F., Joliot, P., Tirichine, L., Falkowski, P. G., Cardol, P., Bowler, C., & Finazzi, G. (2015). Energetic coupling between plastids and mitochondria drives CO2 assimilation in diatoms. *Nature*, *524*(7565), 366-369. https://doi.org/10.1038/nature14599

Barbara, L., Crosta, X., Leventer, A., Schmidt, S., Etourneau, J., Domack, E., & Massé, G. (2016). Environmental responses of the Northeast Antarctic Peninsula to the Holocene climate variability. *Paleoceanography*, *31*(1), 131-147. https://doi.org/10.1002/2015pa002785

Barbara, L., Crosta, X., Massé, G., & Ther, O. (2010). Deglacial environments in eastern Prydz Bay, East Antarctica. *Quaternary Science Reviews*, *29*(19-20), 2731-2740. https://doi.org/10.1016/j.quascirev.2010.06.027

Barbara, L., Crosta, X., Schmidt, S., & Massé, G. (2013). Diatoms and biomarkers evidence for major changes in sea ice conditions prior the instrumental period in Antarctic Peninsula. *Quaternary Science Reviews*, *79*, 99-110. https://doi.org/10.1016/j.quascirev.2013.07.021

Bassham J, Benson A, Calvin M (1950). The path of carbon in photosynthesis. J Biol Chem. 185 (2): 781–7. doi:10.2172/910351.

Belt, S. T. (2018). Source-specific biomarkers as proxies for Arctic and Antarctic sea ice. *Organic Geochemistry*, *125*, 277-298. https://doi.org/10.1016/j.orggeochem.2018.10.002

Belt, S. T., Allard, W. G., Massé, G., Robert, J.-M., & Rowland, S. J. (2000). Highly branched isoprenoids (HBIs): Identification of the most common and abundant sedimentary isomers. *Geochimica et Cosmochimica Acta*, *64*, 3839-3851.

Belt, S. T., Brown, T. A., Cabedo-Sanz, P., & Navarro-Rodriguez, A. (2012). Structural confirmation of the sea ice biomarker IP25 found in Arctic marine sediments.

Environmental Chemistry Letters, *10*(2), 189-192. https://doi.org/10.1007/s10311-011-0344-0

Belt, S. T., Brown, T. A., Smik, L., Tatarek, A., Wiktor, J., Stowasser, G., Assmy, P., Allen, C. S., & Husum, K. (2017). Identification of C25 highly branched isoprenoid (HBI) alkenes in diatoms of the genus Rhizosolenia in polar and sub-polar marine phytoplankton. *Organic Geochemistry*, *110*, 65-72. https://doi.org/10.1016/j.orggeochem.2017.05.007

Belt, S. T., Cooke, D. A., Robert, J.-M., & Rowland, S. (1996). Structural Characterisation of Widespread Polyunsaturated Isoprenoid Biomarkers: A C25 Triene, Tetraene and Pentaene from the Diatom Haslea ostrearia Simonsen. *Tetrahedron Letters*, *37*, 4755-4758.

Belt, S. T., Massé, G., Allard, W. G., Robert, J.-M., & Rowland, S. J. (2001). Identification of a C25 highly branched isoprenoid triene in the freshwater diatom Navicula sclesvicensis. *Organic Geochemistry*, *32*, 1169-1172.

Belt, S. T., Massé, G., Rowland, S. J., Poulin, M., Michel, C., & LeBlanc, B. (2007). A novel chemical fossil of palaeo sea ice: IP25. *Organic Geochemistry*, *38*(1), 16-27. https://doi.org/10.1016/j.orggeochem.2006.09.013

Belt, S. T., Massé, G., Vare, L. L., Rowland, S. J., Poulin, M., Sicre, M.-A., Sampei, M., & Fortier, L. (2008). Distinctive 13C isotopic signature distinguishes a novel sea ice biomarker in Arctic sediments and sediment traps. *Marine Chemistry*, *112*(3-4), 158-167. https://doi.org/10.1016/j.marchem.2008.09.002

Belt, S. T., & Müller, J. (2013). The Arctic sea ice biomarker IP25_ a review of current understanding, recommendations for future research and applications in palaeo sea ice reconstructions. *Quaternary Science Reviews*, *79*, 9-25.

Belt, S. T., Smik, L., Brown, T. A., Kim, J. H., Rowland, S. J., Allen, C. S., Gal, J. K., Shin, K. H., Lee, J. I., & Taylor, K. W. (2016). Source identification and distribution reveals the potential of the geochemical Antarctic sea ice proxy IPSO25. *Nature Communications*, *7*, 12655. https://doi.org/10.1038/ncomms12655

Bidigare, R., Fluegge, A., & Freeman, K. H. (1997). Consistent fractionation of13C in nature and in the laboratory: growth-rate effects in some haptophyte algae. *Global Biogeochemical Cycles*, *11*, 279-292.

Braarud, T. (1979). The temperature range of the non-motile stage ofCoccolithus pelagicusin the North Atlantic region. *British Phycological Journal*, *14*(4), 349-352. https://doi.org/10.1080/00071617900650391

Briner, J. P., McKay, N. P., Axford, Y., Bennike, O., Bradley, R. S., de Vernal, A., Fisher, D., Francus, P., Fréchette, B., Gajewski, K., Jennings, A., Kaufman, D. S., Miller, G., Rouston, C., & Wagner, B. (2016). Holocene climate change in Arctic Canada and Greenland. *Quaternary Science Reviews*, *147*, 340-364. https://doi.org/10.1016/j.quascirev.2016.02.010

Brown, T. A. (2011). Production and preservation of the Arctic sea ice diatom biomarker IP25. *University of Plymouth*, *Ph.D. thesis*.

Brown, T. A., Assmy, P., Hop, H., Wold, A., & Belt, S. T. (2017). Transfer of ice algae carbon to ice-associated amphipods in the high-Arctic pack ice environment. *Journal of Plankton Research*, *39*(4), 664-674. https://doi.org/10.1093/plankt/fbx030

Brown, T. A., & Belt, S. T. (2016). Novel tri- and tetra-unsaturated highly branched isoprenoid (HBI) alkenes from the marine diatom Pleurosigma intermedium. *Organic Geochemistry*, *91*, 120-122. https://doi.org/10.1016/j.orggeochem.2015.11.008

Brown, T. A., Belt, S. T., & Cabedo-Sanz, P. (2014a). Identification of a novel di-unsaturated C25 highly branched isoprenoid in the marine tube-dwelling diatom Berkeleya rutilans. *Environmental Chemistry Letters*, *12*(3), 455-460. https://doi.org/10.1007/s10311-014-0472-4

Brown, T. A., Belt, S. T., Tatarek, A., & Mundy, C. J. (2014b). Source identification of the Arctic sea ice proxy IP25. *Nature Communications*, *5*, 4197. https://doi.org/10.1038/ncomms5197

Brown, T. A., Rad-Menéndez, C., Ray, J. L., Skaar, K. S., Thomas, N., Ruiz-Gonzalez, C., & Leu, E. (2020). Influence of nutrient availability on Arctic sea ice diatom HBI lipid synthesis. *Organic Geochemistry*, *141*, 103977. https://doi.org/10.1016/j.orggeochem.2020.103977

Buchanan, B. B. (2016). The carbon (formerly dark) reactions of photosynthesis. *Photosynth Res*, *128*(2), 215-217. https://doi.org/10.1007/s11120-015-0212-z

Cabedo-Sanz, P., Belt, S. T., Knies, J., & Husum, K. (2013). Identification of contrasting seasonal sea ice conditions during the Younger Dryas. *Quaternary Science Reviews*, *79*, 74-86. https://doi.org/10.1016/j.quascirev.2012.10.028

Calvin, M. (1962). The Path of Carbon in Photosynthesis. *Science*, *135*, 879-889.

Campagne, P., Crosta, X., Houssais, M. N., Swingedouw, D., Schmidt, S., Martin, A., Devred, E., Capo, S., Marieu, V., Closset, I., & Masse, G. (2015). Glacial ice and atmospheric forcing on the Mertz Glacier Polynya over the past 250 years. *Nat Commun*, *6*, 6642. https://doi.org/10.1038/ncomms7642

Campagne, P., Crosta, X., Schmidt, S., Noëlle Houssais, M., Ther, O., & Massé, G. (2016). Sedimentary response to sea ice and atmospheric variability over the instrumental period off Adélie Land, East Antarctica. *Biogeosciences*, *13*(14), 4205-4218. https://doi.org/10.5194/bg-13-4205-2016

Caron, D. A., Gast, R. J., & Garneau, M.-È. (2017). Sea ice as a habitat for micrograzers. In D. N. Thomas (Ed.), *Sea Ice* (Third ed., pp. 370-393). John Wiley & Sons.

Chikaraishi, Y. (2006). Carbon and hydrogen isotopic composition of sterols in natural marine brown and red macroalgae and associated shellfish. *Organic Geochemistry*, *37*(4), 428-436. https://doi.org/10.1016/j.orggeochem.2005.12.006

Chikaraishi, Y. (2014). 13C/12C Signatures in Plants and Algae. In *Treatise on Geochemistry* (pp. 95-123). https://doi.org/10.1016/b978-0-08-095975-7.01008-1

Chikaraishi, Y., & Naraoka, H. (2003). Compound-specific δD–δ13C analyses of n-alkanes extracted from terrestrial and aquatic plants. *Phytochemistry*, *63*(3), 361-371. https://doi.org/10.1016/s0031-9422(02)00749-5

Chikaraishi, Y., Naraoka, H., & Poulson, S. R. (2004a). Hydrogen and carbon isotopic fractionations of lipid biosynthesis among terrestrial (C3, C4 and CAM) and aquatic plants. *Phytochemistry*, *65*(10), 1369-1381. https://doi.org/10.1016/j.phytochem.2004.03.036

Chikaraishi, Y., Suzuki, Y., & Naraoka, H. (2004b). Hydrogen isotopic fractionations during desaturation and elongation associated with polyunsaturated fatty acid biosynthesis in marine macroalgae. *Phytochemistry*, *65*(15), 2293-2300. https://doi.org/10.1016/j.phytochem.2004.06.030

Chivall, D., M'boule, D., Sinke-Schoen, D., Sinninghe Damsté, J. S., Schouten, S., & van der Meer, M. T. (2014). The effects of growth phase and salinity on the hydrogen isotopic composition of alkenones produced by coastal haptophyte algae. *Geochimica et Cosmochimica Acta*, *140*, 381-390.

Collins, L. G., Allen, C. S., Pike, J., Hodgson, D. A., Weckström, K., & Massé, G. (2013). Evaluating highly branched isoprenoid (HBI) biomarkers as a novel Antarctic sea-ice proxy in deep ocean glacial age sediments. *Quaternary Science Reviews*, *79*, 87-98. https://doi.org/10.1016/j.quascirev.2013.02.004

Comiso, J. C. (2006). Abrupt decline in the Arctic winter sea ice cover. *Geophysical Research Letters*, *33*(18), n/a-n/a. https://doi.org/10.1029/2006gl027341

Cormier, M. A., Werner, R. A., Sauer, P. E., Grocke, D. R., Leuenberger, M. C., Wieloch, T., Schleucher, J., & Kahmen, A. (2018). (2) H-fractionations during the biosynthesis of carbohydrates and lipids imprint a metabolic signal on the delta(2) H values of plant organic compounds. *New Phytol*, *218*(2), 479-491. https://doi.org/10.1111/nph.15016

Cronin, T., M., Holtz, T. R., & Whatley, R. C. (1994). Quaternary paleoceanography of the deep Arctic Ocean based on quantitative analysis of Ostracoda. *Marine Geology*, *119*, 305-332.

Cronin, T. M., Gemery, L., Briggs, W. M., Jakobsson, M., Polyak, L., & Brouwers, E. M. (2010). Quaternary Sea-ice history in the Arctic Ocean based on a new Ostracode sea-ice proxy. *Quaternary Science Reviews*, *29*(25-26), 3415-3429. https://doi.org/10.1016/j.quascirev.2010.05.024

Crosta, X., Romero, O., Armand, L. K., & Pichon, J.-J. (2005). The biogeography of major diatom taxa in Southern Ocean sediments: 2. Open ocean related species. *Palaeogeography, Palaeoclimatology, Palaeoecology*, *223*(1-2), 66-92. https://doi.org/10.1016/j.palaeo.2005.03.028

Crosta, X., Sturm, A., Armand, L., & Pichon, J.-J. (2004). Late Quaternary sea ice history in the Indian sector of the Southern Ocean as recorded by diatom assemblages. *Marine Micropaleontology*, *50*(3-4), 209-223. https://doi.org/10.1016/s0377-8398(03)00072-0

Curran, M. A. J., van Ommen, T. D., Morgan, V. I., Phillips, K. L., & Palmer, A. S. (2003). Ice Core Evidence for Antarctic Sea Ice Decline Since the 1950s. *Science*, *302*, 1203-1206.

de la Mare, W. K. (1997). Abruptmid-twentieth-century decline inAntarctic sea-ice extent fromwhaling records. *Nature*, *389*, 57-60.

de Vernal, A., Eynaud, F., Henry, M., Hillaire-Marcel, C., Londeix, L., Mangin, S., Matthiessen, J., Marret, F., Radi, T., Rochon, A., Solignac, S., & Turon, J. L. (2005). Reconstruction of sea-surface conditions at middle to high latitudes of the Northern Hemisphere during the Last Glacial Maximum (LGM) based on dinoflagellate cyst assemblages. *Quaternary Science Reviews*, *24*(7-9), 897-924. https://doi.org/10.1016/j.quascirev.2004.06.014

de Vernal, A., Gersonde, R., Goosse, H., Seidenkrantz, M.-S., & Wolff, E. W. (2013a). Sea ice in the paleoclimate system: the challenge of reconstructing sea ice from proxies – an introduction. *Quaternary Science Reviews*, *79*, 1-8. https://doi.org/10.1016/j.quascirev.2013.08.009

de Vernal, A., Henry, M., Matthiessen, J., Mudie, P. J., Rochon, A., Boessenkool, K. P., Eynaud, F., GrØsfjeld, K., Guiot, J., Hamel, D., Harland, R., Head, M. J., Kunz-Pirrung, M., Levac, E., Loucheur, V., Peyron, O., Pospelova, V., Radi, T., Turon, J.-

L., & Voronina, E. (2001). Dinoflagellate cyst assemblages as tracers of sea-surface conditions in the northern North Atlantic, Arctic and sub-Arctic seas: the new 'n= 677' data base and its application for quantitative palaeoceanographic reconstruction. *Journal of Quaternary Science*, *16*(7), 681-698. https://doi.org/10.1002/jqs.659

de Vernal, A., Hillaire-Marcel, C., Rochon, A., Fréchette, B., Henry, M., Solignac, S., & Bonnet, S. (2013b). Dinocyst-based reconstructions of sea ice cover concentration during the Holocene in the Arctic Ocean, the northern North Atlantic Ocean and its adjacent seas. *Quaternary Science Reviews*, *79*, 111-121. https://doi.org/10.1016/j.quascirev.2013.07.006

de Vernal, A., Rochon, A., Fréchette, B., Henry, M., Radi, T., & Solignac, S. (2013c). Reconstructing past sea ice cover of the Northern Hemisphere from dinocyst assemblages: status of the approach. *Quaternary Science Reviews*, *79*, 122-134. https://doi.org/10.1016/j.quascirev.2013.06.022

Denis, D., Crosta, X., Barbara, L., Massé, G., Renssen, H., Ther, O., & Giraudeau, J. (2010). Sea ice and wind variability during the Holocene in East Antarctica: insight on middle–high latitude coupling. *Quaternary Science Reviews*, *29*(27-28), 3709-3719. https://doi.org/10.1016/j.quascirev.2010.08.007

Dirghangi, S. S., & Pagani, M. (2013). Hydrogen isotope fractionation during lipid biosynthesis by Haloarcula marismortui. *Geochimica et Cosmochimica Acta*, *119*, 381-390. https://doi.org/10.1016/j.gca.2013.05.023

Divine, D. V., & Dick, C. (2006). Historical variability of sea ice edge position in the Nordic Seas. *Journal of Geophysical Research*, *111*(C1). https://doi.org/10.1029/2004jc002851

Englebrecht, A. C., & Sachs, J. P. (2005). Determination of sediment provenance at drift sites using hydrogen isotopes and unsaturation ratios in alkenones. *Geochimica et Cosmochimica Acta*, *69*(17), 4253-4265. https://doi.org/10.1016/j.gca.2005.04.011

Estep, M. F., & Hoering, T. C. (1980). Biogeochemistry of the stable hydrogen isotopes. *Geochimica et Cosmochimica Acta*, *64*, 1197-1206.

Etourneau, J., Collins, L. G., Willmott, V., Kim, J. H., Barbara, L., Leventer, A., Schouten, S., Sinninghe Damsté, J. S., Bianchini, A., Klein, V., Crosta, X., & Massé, G. (2013). Holocene climate variations in the western Antarctic Peninsula: evidence for sea ice extent predominantly controlled by changes in insolation and ENSO variability. *Climate of the Past*, *9*(4), 1431-1446. https://doi.org/10.5194/cp-9-1431-2013

Fahl, K., & Stein, R. (2012). Modern seasonal variability and deglacial/Holocene change of central Arctic Ocean sea-ice cover: New insights from biomarker proxy records. *Earth and Planetary Science Letters*, *351-352*, 123-133. https://doi.org/10.1016/j.epsl.2012.07.009

Fetterer, F., Knowles, K., Meier, W. N., Savoie, M., & Windnagel, A. K. (2017, updated daily). *Sea Ice Index (G02135)* Version 3). https://doi.org/https://doi.org/10.7265/N5K072F8

Francis, J. A., Hunter, E., Key, J. R., & Wang, X. (2005). Clues to variability in Arctic minimum sea ice extent. *Geophysical Research Letters*, *32*(21). https://doi.org/10.1029/2005gl024376

Freeman, K. H., Hayes, J. M., Trendelt, J.-M., & Albrechtt, P. (1990). Evidence from carbon isotope measurements for diverse origins of sedimentary hydrocarbons. *Nature*, *343*, 254.

Gamarra, B., & Kahmen, A. (2015). Concentrations and delta(2)H values of cuticular n-alkanes vary significantly among plant organs, species and habitats in grasses from an alpine and a temperate European grassland. *Oecologia*, *178*(4), 981-998. https://doi.org/10.1007/s00442-015-3278-6

Gao, S., Smik, L., Kulikovskiy, M., Shkurina, N., Gusev, E., Pedentchouk, N., Mock, T., & Belt, S. T. (2020). A novel tri-unsaturated highly branched isoprenoid (HBI) alkene from the marine diatom Navicula salinicola. *Organic Geochemistry*, *146*. https://doi.org/10.1016/j.orggeochem.2020.104050

Garcin, Y., Schwab, V. F., Gleixner, G., Kahmen, A., Todou, G., Séné, O., Onana, J.-M., Achoundong, G., & Sachse, D. (2012). Hydrogen isotope ratios of lacustrine sedimentary n-alkanes as proxies of tropical African hydrology: Insights from a calibration transect across Cameroon. *Geochimica et Cosmochimica Acta*, *79*, 106-126. https://doi.org/10.1016/j.gca.2011.11.039

Gersonde, R., Crosta, X., Abelmann, A., & Armand, L. (2005). Sea-surface temperature and sea ice distribution of the Southern Ocean at the EPILOG Last Glacial Maximum—a circum-Antarctic view based on siliceous microfossil records. *Quaternary Science Reviews*, *24*(7-9), 869-896. https://doi.org/10.1016/j.quascirev.2004.07.015

Gibson, J. A. E., Trull, T., Nichols, P. D., Summons, R. E., & McMinn, A. (1999). Sedimentation of 13C-rich organic matter from Antarctic sea-ice algae: A potential indicator of past sea-ice extent. *Geology*, *27*, 331-334.

Gilbert, A., Silvestre, V., Robins, R. J., & Remaud, G. S. (2009). Accurate Quantitative Isotopic 13C NMR Spectroscopy for the Determination of the Intramolecular Distribution of 13C in Glucose at Natural Abundance. *Analytical Chemistry*, *81*, 8978–8985.

Grigorov, I., Rigual-Hernandez, A. S., Honjo, S., Kemp, A. E. S., & Armand, L. K. (2014). Settling fluxes of diatoms to the interior of the Antarctic circumpolar current along 170°W. *Deep Sea Research Part I: Oceanographic Research Papers*, *93*, 1-13. https://doi.org/10.1016/j.dsr.2014.07.008

Grossi, V., Beker, B., Geenevasen, J. A. J., Schouten, S., Raphel, D., Fontaine, M.-F., & Sinninghe Damsté, J. S. (2004). C25 highly branched isoprenoid alkenes from the marine benthic diatom Pleurosigma strigosum. *Phytochemistry*, *65*(22), 3049-3055. https://doi.org/10.1016/j.phytochem.2004.09.002

Guillard, P. R., & Ryther, J. H. (1962). Studies of marine planktonic diatoms. I. Cyclotella nana Hustedt, and Detonula confervacea (cleve) Gran *Canadian Journal of Microbiology*, *8*, 229-239. https://doi.org/10.1139/m62-029

Gutknecht, J., Bisson, M. A., & Tosteson, F. C. (1977). Diffusion of Carbon Dioxide through Lipid Bilayer Membranes, Effects of Carbonic Anhydrase, Bicarbonate, and Unstirred Layers. *The Journal of General Physiology*, *69*, 779-794.

Guy, R. D., Fogel, M. L., Berry, J. A., & Hoering, T. C. (1987). Isotope fractionation during oxygen production and consumption by plants. In J. Biggin (Ed.), *Progress in photosynthesis research* (Vol. 3, pp. 597-600).

Hart, T. J. (1942). Phytoplankton periodicity in Antarctic surface waters. *Discovery Reports 21*, 261-356.

Hayes, J. M. (1993). Factors controlling 13C contents of sedimentary organic compounds: Principles and evidence. *Marine Geology*, *113*, 111-125.

Hayes, J. M. (2001). Fractionation of the Isotopes of Carbon and Hydrogen in Biosynthetic Processes. *Rev. Mineral Geochem*, *43*, 225-277.

Hayes, J. M., Freeman, K. H., Popp, B. N., & Hoham, C. H. (1990). Compound-specific isotopic analyses: A novel tool for reconstruction of ancient biogeochemical processes. *Advances in Organic Geochemistry*, *16*, 1115-1128.

Hebbeln, D., Henrich, R., & Baumann, K.-H. (1998). Palaeoceanography of the last interglacial/glacial cycle in the polar North Atlantic. *Quaternary Science Reviews*, *17*, 125-153.

Hebbeln, D., & Wefer, G. (1997). Late Quaternary paleoceanography in the Fram Strait. *Paleoceanography*, *12*(1), 65-78. https://doi.org/10.1029/96pa02753

Heinzelmann, S. M., Chivall, D., M'Boule, D., Sinke-Schoen, D., Villanueva, L., Damste, J. S., Schouten, S., & van der Meer, M. T. (2015). Comparison of the effect of salinity on the D/H ratio of fatty acids of heterotrophic and photoautotrophic microorganisms. *FEMS Microbiol Lett*, *362*(10). https://doi.org/10.1093/femsle/fnv065

Horner, R., Ackley, S., Dieckmann, G., Gulliksen, B., Hoshiai, T., Legendre, L., Melnikov, I., Reeburgh, W., Spindler, M., & Sullivan, C. (1992). Ecology of sea ice biota. *Polar Biology*, *12*(3-4). https://doi.org/10.1007/bf00243113

Hou, J., D'Andrea, W. J., & Huang, Y. (2008). Can sedimentary leaf waxes record D/H ratios of continental precipitation? Field, model, and experimental assessments. *Geochimica et Cosmochimica Acta*, *72*(14), 3503-3517. https://doi.org/10.1016/j.gca.2008.04.030

Huang, Y., Shuman, B., Wang, Y., & Webb, T. (2002). Hydrogen isotope ratios of palmitic acid in lacustrine sediments record late Quaternary climate variations. *Geology*, *30*, 1103-1106.

Huang, Y., Shuman, B., Wang, Y., & Webb, T. (2004). Hydrogen isotope ratios of individual lipids in lake sediments as novel tracers of climatic and environmental change: a surface sediment test. *Journal of Paleolimnology*, *31*, 363-375.

Johannessen, O. M., Mlies, M., Bjorgo, E., & Bj0rgo, O. M. J. M. M. E. (1995). The Arctic's shrinking sea ice. *Nature*, *376*, 126-127.

Johns, L., Wraige, E. J., Belt, S. T., Lewis, C. A., Massé, G., Robert, J.-M., & Rowland, S. J. (1999). Identification of a C25 highly branched isoprenoid (HBI) diene in Antarctic sediments, Antarctic sea-ice diatoms and cultured diatoms. *Organic Geochemistry*, *30*, 1471-1475.

Jones, R. L., Whatley, R. C., Cronin, T., M., & Dowsett, H. J. (1999). Reconstructing late Quaternary deep-water masses in the eastern Arctic Ocean using benthonic Ostracoda. *Marine Micropaleontology*, *37*, 251-272.

Justwan, A., & Koç, N. (2008). A diatom based transfer function for reconstructing sea ice concentrations in the North Atlantic. *Marine Micropaleontology*, *66*(3-4), 264-278. https://doi.org/10.1016/j.marmicro.2007.11.001

Kai, Y., Matsumura, H., & Izui, K. (2003). Phosphoenolpyruvate carboxylase: three-dimensional structure and molecular mechanisms. *Archives of Biochemistry and Biophysics*, *414*(2), 170-179. https://doi.org/10.1016/s0003-9861(03)00170-x

Kaiser, J., Belt, S. T., Tomczak, M., Brown, T. A., Wasmund, N., & Arz, H. W. (2016). C25 highly branched isoprenoid alkenes in the Baltic Sea produced by the marine planktonic diatom Pseudosolenia calcar-avis. *Organic Geochemistry*, *93*, 51-58.

Kaiser, M. J., Attrill, M. J., Jennings, S., Thomas, D. N., Barnes, D. K., Brierley, A. S., Hiddink, J. G., Kaartokallio, H., Polunin, N. V. C., & Raffaelli, D. G. (2011). *Marine Ecology: Processes, Systems, and Impacts* (second ed.). Oxfore University Press.

Kaufman, D. S., Axford, Y. L., Henderson, A. C. G., McKay, N. P., Oswald, W. W., Saenger, C., Anderson, R. S., Bailey, H. L., Clegg, B., Gajewski, K., Hu, F. S., Jones, M. C., Massa, C., Routson, C. C., Werner, A., Wooller, M. J., & Yu, Z. (2016). Holocene climate changes in eastern Beringia (NW North America) – A systematic review of multi-proxy evidence. *Quaternary Science Reviews*, *147*, 312-339. https://doi.org/10.1016/j.quascirev.2015.10.021

Kennedy, H., Thomas, D. N., Kattner, G., Haas, C., & Dieckmann, G. S. (2002). Particulate organic matter in Antarctic summer sea ice: concentration and stable isotopic composition. *Marine Ecology Progress Series*, *238*, 1-13.

Killops, S., & Killops, V. (2005). *Introduction to Organic Geochemistry* (second ed.). Blackwell.

Kirst, G. O., & Wiencke, C. (1995). Ecophysiology of polar algae. *Journal of Phycology*, *31*, 181-199.

Köseoğlu, D., Belt, S. T., Smik, L., Yao, H., Panieri, G., & Knies, J. (2018). Complementary biomarker-based methods for characterising Arctic sea ice conditions: A case study comparison between multivariate analysis and the PIP25 index. *Geochimica et Cosmochimica Acta*, *222*, 406-420. https://doi.org/10.1016/j.gca.2017.11.001

Kroth, P. G., Chiovitti, A., Gruber, A., Martin-Jezequel, V., Mock, T., Parker, M. S., Stanley, M. S., Kaplan, A., Caron, L., Weber, T., Maheswari, U., Armbrust, E. V., & Bowler, C. (2008). A model for carbohydrate metabolism in the diatom Phaeodactylum tricornutum deduced from comparative whole genome analysis. *PLoS One*, *3*(1), e1426. https://doi.org/10.1371/journal.pone.0001426

Kwok, R., & Untersteiner, N. (2011). The thinning of Arctic sea ice. *Physics Today*, 36-41.

Ladd, S. N., Nelson, D. B., Bamberger, I., Daber, L. E., Kreuzwieser, J., Kahmen, A., & Werner, C. (2021). Metabolic exchange between pathways for isoprenoid synthesis and implications for biosynthetic hydrogen isotope fractionation. *New Phytol*, *231*(5), 1708-1719. https://doi.org/10.1111/nph.17510

Lalande, C., Nöthig, E.-M., Bauerfeind, E., Hardge, K., Beszczynska-Möller, A., & Fahl, K. (2016). Lateral supply and downward export of particulate matter from upper waters to the seafloor in the deep eastern Fram Strait. *Deep Sea Research Part I: Oceanographic Research Papers*, *114*, 78-89. https://doi.org/10.1016/j.dsr.2016.04.014

Lange-Bertalot, H. (2001). *Navicula Sensu Stricto, 10 Genera Separated from Navicula Sensu Lato, Frustulia* (Vol. 2).

Leu, E., Søreide, J. E., Hessen, D. O., Falk-Petersen, S., & Berge, J. (2011). Consequences of changing sea-ice cover for primary and secondary producers in the European Arctic shelf seas: Timing, quantity, and quality. *Progress in Oceanography*, *90*(1-4), 18-32. https://doi.org/10.1016/j.pocean.2011.02.004

Leu, E., Wiktor, J., Søreide, J. E., Berge, J., & Falk-Petersen, S. (2010). Increased irradiance reduces food quality of sea ice algae. *Marine Ecology Progress Series*, *411*, 49-60. https://doi.org/10.3354/meps08647

Li, C., Sessions, A. L., Kinnaman, F. S., & Valentine, D. L. (2009). Hydrogen-isotopic variability in lipids from Santa Barbara Basin sediments. *Geochimica et Cosmochimica Acta*, *73*, 4803-4823.

Lichtenthaler, H. K. (1999). The 1-Deoxy-D-xylulose5-phosphate pathway of isoprenoid biosynthesis in plants. *Annu. Rev. Plant Physiol. Plant Mol. Biol.*, *50*, 47-65.

Lizotte, M. P. (2001). The Contributions of Sea Ice Algae to Antarctic Marine Primary Production. *American Zoologist*, *41*, 57-73.

Luo, Y.-h., Sternberg, L., Suda, S., Kumazawa, S., & Mitsui, A. (1991). Extremely Low D/H Ratios of Photoproduced Hydrogen by Cyanobacteria. *Plant and Cell Physiology*, *32*, 897-900.

M'boule, D., Chivall, D., Sinke-Schoen, D., Sinninghe Damsté, J. S., Schouten, S., & van der Meer, M. T. (2014). Salinity dependent hydrogen isotope fractionation in alkenones produced by coastal and open ocean haptophyte algae. *Geochimica et Cosmochimica Acta*, *130*, 126-135.

Maclntyre, H. L., & Kana, T. M. (2002). Photoacclimation of photosynthesis irradiacne response curves and photoysnthetic pigments in microalgae and cyanobacteria *Journal of Phycology*, *38*, 17-38.

Maloney, A. E., Shinneman, A. L. C., Hemeon, K., & Sachs, J. P. (2016). Exploring lipid 2H/1H fractionation mechanisms in response to salinity with continuous cultures of the diatom Thalassiosira pseudonana. *Organic Geochemistry*, *101*, 154-165. https://doi.org/10.1016/j.orggeochem.2016.08.015

Massé, G., Belt, S. T., Crosta, X., Schmidt, S., Snape, I., Thomas, D. N., & Rowland, S. J. (2011). Highly branched isoprenoids as proxies for variable sea ice conditions in the Southern Ocean. *Antarctic Science*, *23*(05), 487-498. https://doi.org/10.1017/s0954102011000381

Massé, G., Belt, S. T., & Rowland, S. J. (2004a). Biosynthesis of unusual monocyclic alkenes by the diatom Rhizosolenia setigera (Brightwell). *Phytochemistry*, *65*(8), 1101-1106. https://doi.org/10.1016/j.phytochem.2004.02.019

Massé, G., Belt, S. T., Rowland, S. J., & Rohmer, M. (2004b). Isoprenoid biosynthesis in the diatoms Rhizosolenia setigera (Brightwell) and Haslea ostrearia (Simonsen). *Proceedings of the National Academy of Sciences*, *101*, 4413–4418.

Matsuda, Y., Hara, T., & Colman, B. (2001). Regulation of the induction of bicarbonate uptake by dissolved CO2 in the marine diatom, Phaeodactylum tricornutum. *Plant, cell and environment*, *24*, 611-620.

Mook, W. G., Bommerson, J. C., & Staverman, W. H. (1974). Carbon isotope fractionation between dissolved bicarbonate and gaseous carbon dioxide. *Earth and Planetary Science Letters*, *22*, 169-176.

Müller, J., Wagner, A., Fahl, K., Stein, R., Prange, M., & Lohmann, G. (2011). Towards quantitative sea ice reconstructions in the northern North Atlantic: A combined biomarker and numerical modelling approach. *Earth and Planetary Science Letters*, *306*(3-4), 137-148. https://doi.org/10.1016/j.epsl.2011.04.011

Navarro-Rodriguez, A., Belt, S. T., Knies, J., & Brown, T. A. (2013). Mapping recent sea ice conditions in the Barents Sea using the proxy biomarker IP25: implications for palaeo sea ice reconstructions. *Quaternary Science Reviews*, *79*, 26-39. https://doi.org/10.1016/j.quascirev.2012.11.025

Nelson, D. B., & Sachs, J. P. (2014a). The influence of salinity on D/H fractionation in alkenones from saline and hypersaline lakes in continental North America. *Organic Geochemistry*, *66*, 38-47. https://doi.org/10.1016/j.orggeochem.2013.10.013

Nelson, D. B., & Sachs, J. P. (2014b). The influence of salinity on D/H fractionation in dinosterol and brassicasterol from globally distributed saline and hypersaline lakes. *Geochimica et Cosmochimica Acta*, *133*, 325-339. https://doi.org/10.1016/j.gca.2014.03.007

Nichols, D. S. (2003). Prokaryotes and the input of polyunsaturated fatty acids to the marine food web. *FEMS Microbiology Letters*, *219*(1), 1-7. https://doi.org/10.1016/s0378-1097(02)01200-4

Nichols, P. D., Volkman, J. K., Palmisano, A. C., Smith, G. A., & White, D. C. (1988). Occurrence of an isoprenoid C25 diunsaturated alkene and high neutral lipid content in Antarctic sea-ice diatom communities. *Journal of Phycology*, *24*, 90-96.

Nicolaus, M., Katlein, C., Maslanik, J., & Hendricks, S. (2012). Changes in Arctic sea ice result in increasing light transmittance and absorption. *Geophysical Research Letters*, *39*(24). https://doi.org/10.1029/2012gl053738

O'Leary, M. H. (1981). Carbon isotope fractionation in plants. *Phytochemistry*, *20*, 553-567.

O'Leary, M. H. (1988). Carbon isotopes in photosynthesis. *BioScience*, *38*, 328-336.

Pagani, M. (2014). Biomarker-Based Inferences of Past Climate: The Alkenone pCO2 Proxy. In *Treatise on Geochemistry* (pp. 361-378). https://doi.org/10.1016/b978-0-08-095975-7.01027-5

Perovich, D. K. (1996). *The optical properties of sea ice*. Cold Regions Research & Engineering Laboratory.

Perovich, D. K. (2017). Sea ice and sunlight. In D. N. T. Thomas (Ed.), *Sea Ice* (Third ed., pp. 110-137). John Wiley & Sons.

Polissar, P. J., & Freeman, K. H. (2010). Effects of aridity and vegetation on plant-wax δD in modern lake sediments. *Geochimica et Cosmochimica Acta*, *74*(20), 5785-5797. https://doi.org/10.1016/j.gca.2010.06.018

Polissar, P. J., & D'Andrea, W. J. (2014). Uncertainty in paleohydrologic reconstructions from molecular δD values. *Geochimica et Cosmochimica Acta*, 129, 146-156. https://doi.org/10.1016/j.gca.2013.12.021

Popp, B. N., Laws, E. A., Bidigare, R., Dore, J. E., Hanson, K. L., & Wakeham, S. G. (1998). Effect of phytoplankton cell geometry on carbon isotopic fractionation. *Geochimica et Cosmochimica Acta*, *62*, 69–77.

Rahman, A., & de Vernal, A. (1994). Surface oceanographic changes in the eastern Labrador Sea: nannofossil record of the last 31,000 years. *Marine Geology*, *121*, 247-263.

Raven, J. A., & Geider, R. J. (2003). Adaptation, acclimation and regulation in algal photosynthesis In A. W. D. Larkum, S. Douglas, & J. A. Raven (Eds.), *Photosynthesis of Algae* (pp. 385–412). Kluwer Academic Publishers.

Riaux-Gobin, C., Poulin, M., Dieckmann, G., Labrune, C., & Vétion, G. (2011). Spring phytoplankton onset after the ice break-up and sea-ice signature (Adélie Land, East Antarctica). *Polar Research*, *30*(1). https://doi.org/10.3402/polar.v30i0.5910

Rodríguez-Concepción, M. (2006). Early Steps in Isoprenoid Biosynthesis: Multilevel Regulation of the Supply of Common Precursors in Plant Cells. *Phytochemistry Reviews*, *5*(1), 1-15. https://doi.org/10.1007/s11101-005-3130-4

Rodríguez-Concepción, M., & Boronat, A. (2015). Breaking new ground in the regulation of the early steps of plant isoprenoid biosynthesis. *Curr Opin Plant Biol*, *25*, 17-22. https://doi.org/10.1016/j.pbi.2015.04.001

Roeske, C. A., & O'Leary, M. H. (1984). Carbon Isotope Effects on the Enzyme-Catalyzed Carboxylation of Ribulose Bisphosphate. *Biochemistry*, *23*, 6275-6284.

Rohmer, M., Knani, M. h. K., Simonin, P., Sutter, B., & Sahm, H. (1993). Isoprenoid biosynthesis in bacteria: a novel pathway for the early steps leading to isopentenyl diphosphate. *Biochemical Journal*, *295*, 517-524.

Rontani, J.-F., Belt, S. T., & Amiraux, R. (2018). Biotic and abiotic degradation of the sea ice diatom biomarker IP25 and selected algal sterols in near-surface Arctic sediments. *Organic Geochemistry*, *118*, 73-88. https://doi.org/10.1016/j.orggeochem.2018.01.003

Rosell-Melé, A., & Koç, N. (1997). Paleoclimatic significance of the stratigraphic occurrence of photosynthetic biomarker pigments in the Nordic seas. *Geology*, *25*, 49-52.

Rossmann, A., Butzenlechner, M., & Schmidt, H.-L. (1991). Evidence for a Nonstatistical Carbon Isotope Distribution in Natural Glucose. *Plant Physiology*, *96*, 609-614.

Rowland, S. J., Allard, W. G., Belt, S. T., Massé, G., Robert, J.-M., Blackburn, S., Frampton, D., Revil, A. T., & Volkman, J. K. (2001). Factors influencing the distributions of polyunsaturated terpenoids in the diatom, Rhizosolenia setigera. *Phytochemistry*, *58*, 717–728.

Saba, G. K., Fraser, W. R., Saba, V. S., Iannuzzi, R. A., Coleman, K. E., Doney, S. C., Ducklow, H. W., Martinson, D. G., Miles, T. N., Patterson-Fraser, D. L., Stammerjohn, S. E., Steinberg, D. K., & Schofield, O. M. (2014). Winter and spring controls on the summer food web of the coastal West Antarctic Peninsula. *Nat Commun*, *5*, 4318. https://doi.org/10.1038/ncomms5318

Sachs, J. P. (2014). Hydrogen Isotope Signatures in the Lipids of Phytoplankton. In *Treatise on Geochemistry* (2nd ed., pp. 79-94). https://doi.org/10.1016/b978-0-08-095975-7.01007-x

Sachs, J. P., & Kawka, O. E. (2015). The Influence of Growth Rate on 2H/1H Fractionation in Continuous Cultures of the Coccolithophorid Emiliania huxleyi and the Diatom Thalassiosira pseudonana. *PLoS One*, *10*(11), e0141643. https://doi.org/10.1371/journal.pone.0141643

Sachs, J. P., Maloney, A. E., & Gregersen, J. (2017). Effect of light on 2 H/ 1 H fractionation in lipids from continuous cultures of the diatom Thalassiosira pseudonana. *Geochimica et Cosmochimica Acta*, *209*, 204-215. https://doi.org/10.1016/j.gca.2017.04.008

Sachs, J. P., Maloney, A. E., Gregersen, J., & Paschall, C. (2016). Effect of salinity on 2H/1H fractionation in lipids from continuous cultures of the coccolithophorid Emiliania huxleyi. *Geochimica et Cosmochimica Acta*, *189*, 96-109. https://doi.org/10.1016/j.gca.2016.05.041

Sachs, J. P., & Schwab, V. F. (2011). Hydrogen isotopes in dinosterol from the Chesapeake Bay estuary. *Geochimica et Cosmochimica Acta*, *75*, 444-459.

Sachse, D., Billault, I., Bowen, G. J., Chikaraishi, Y., Dawson, T. E., Feakins, S. J., Freeman, K. H., Magill, C. R., McInerney, F. A., van der Meer, M. T. J., Polissar, P., Robins, R. J., Sachs, J. P., Schmidt, H.-L., Sessions, A. L., White, J. W. C., West, J. B., & Kahmen, A. (2012). Molecular Paleohydrology: Interpreting the Hydrogen-Isotopic Composition of Lipid Biomarkers from Photosynthesizing Organisms. *Annual Review of Earth and Planetary Sciences*, *40*(1), 221-249. https://doi.org/10.1146/annurev-earth-042711-105535

Sachse, D., Radke, J., & Gleixner, G. (2004). Hydrogen isotope ratios of recent lacustrine sedimentary n-alkanes record modern climate variability. *Geochimica et Cosmochimica Acta*, *68*, 4877-4889.

Sachse, D., & Sachs, J. P. (2008). Inverse relationship between D/H fractionation in cyanobacterial lipids and salinity in Christmas Island saline ponds. *Geochimica et Cosmochimica Acta*, *72*(3), 793-806. https://doi.org/10.1016/j.gca.2007.11.022

Samtleben, C., & Schroder, A. (1992). Living coccolithophore communities in the NorwegianGreenland Sea and their record in sediments. *Marine Micropaleontology*, *19*, 333-354.

Sauer, P. E., Eglinton, T. I., Hayes, J. M., Schimmelmann, A., & Sessions, A. L. (2001). Compound-specific D/H ratios of lipid biomarkers from sediments as a proxy for environmental and climatic conditions. *Geochimica et Cosmochimica Acta*, *65*(2), 213-222.

Schimmelmann, A., Qi, H., Coplen, T. B., Brand, W. A., Fong, J., Meier-Augenstein, W., Kemp, H. F., Toman, B., Ackermann, A., Assonov, S., Aerts-Bijma, A. T., Brejcha, R., Chikaraishi, Y., Darwish, T., Elsner, M., Gehre, M., Geilmann, H., Groning, M., Helie, J. F., . . . Werner, R. A. (2016). Organic Reference Materials for Hydrogen, Carbon, and Nitrogen Stable Isotope-Ratio Measurements: Caffeines, n-Alkanes, Fatty Acid Methyl Esters, Glycines, L-Valines, Polyethylenes, and Oils. *Anal Chem*, *88*(8), 4294-4302. https://doi.org/10.1021/acs.analchem.5b04392

Schmidt, H.-L., Werner, R. A., & Eisenreich, W. (2003). Systematics of 2H patterns in natural compounds and its importance for the elucidation of biosynthetic pathways. *Phytochemistry Reviews*, *2*, 61–85.

Schmidt, K., Brown, T. A., Belt, S. T., Ireland, L. C., Taylor, K. W. R., Thorpe, S. E., Ward, P., & Atkinson, A. (2018). Do pelagic grazers benefit from sea ice? Insights from the Antarctic sea ice proxy IPSO<sub>25</sub&gt. *Biogeosciences*, *15*(7), 1987-2006. https://doi.org/10.5194/bg-15-1987-2018

Schouten, S., Breteler, W. C. M. K., Blokker, P., Schogt, N., Rijpstra, W. I. C., & Grice, K. (1998). Biosynthetic effects on the stable carbon isotopic compositions of algal lipids: Implications for deciphering the carbon isotopic biomarker record. *Geochimica et Cosmochimica Acta*, *62*, 1397–1406.

Schouten, S., Ossebaar, J., Schreiber, K., Kienhuis, M. V. M., Langer, G., Benthien, A., & Bijma, J. (2006). The effect of temperature, salinity and growth rate on the stable hydrogen isotopic composition of long chain alkenones produced by Emiliania huxleyi and Gephyrocapsa oceanica. *Biogeosciences*, *3*, 113–119.

Schubert, C. J., & Calvert, S. E. (2001). Nitrogen and carbon isotopic composition of marine and terrestrial organic matter in Arctic Ocean sediments: implications for nutrient utilization and organic matter composition. *Deep-Sea Research I*, *48*, 789-810.

Schwender, J., Seemann, M., Lichtenthaler, H. K., & Rohmer, M. (1996). Biosynthesis of isoprenoids (carotenoids, sterols, prenyl side-chains of chlorophylls and

plastoquinone) via a novel pyruvate/glyceraldehyde 3-phosphate non-mevalonate pathway in the green alga Scenedesmus obliquus. *Biochemical Journal*, *316*, 73–80.

Scott, D. B., Schell, T., Rochon, A., & Blasco, S. (2008). Modern benthic foraminifera in the surface sediments of the Beaufort shelf, slop e and MacKenzie Trough, Beaufort Sea, Canada: taxonomy and summary of surficia l distributions. *Journal of Foraminiferal Research*, *38*, 228-250.

Serreze, M. C., Barrett, A. P., Stroeve, J. C., Kindig, D. N., & Holland, M. M. (2009). The emergence of surface-based Arctic amplification. *The Cryosphere*, *3*, 11-19.

Serreze, M. C., & Barry, R. G. (2011). Processes and impacts of Arctic amplification: A research synthesis. *Global and Planetary Change*, *77*(1-2), 85-96. https://doi.org/10.1016/j.gloplacha.2011.03.004

Sessions, A. L., Burgoyne, T. W., Schimmelmann, A., & Hayes, J. M. (1999). Fractionation of hydrogen isotopes in lipid biosynthesis. *Organic Geochemistry*, *30*, 1193-1200.

Sessions, A. L., Jahnke, L. L., Schimmelmann, A., & Hayes, J. M. (2002). Hydrogen isotope fractionation in lipids of the methane-oxidizing bacterium Methylococcus capsulatus. *Geochimica et Cosmochimica Acta*, *66*, 3955–3969.

Sinninghe Damsté, J. S., Muyzer, G., Abbas, B., Rampe, S. W., Massé, G., Allard, W. G., Belt, S. T., Robert, J.-M., Rowland, S. J., Moldowan, J. M., Barbanti, S. M., Fago, F. J., Denisevich, P., Dahl, J., Trindade, L. A. F., & Stefan, S. (2004). The Rise of the Rhizosolenid Diatoms. *Science*, *304*, 584-587.

Sinninghe Damsté, J. S., Rijpstra, W. I. C., Coolen, M. J. L., Schouten, S., & Volkman, J. K. (2007). Rapid sulfurisation of highly branched isoprenoid (HBI) alkenes in sulfidic Holocene sediments from Ellis Fjord, Antarctica. *Organic Geochemistry*, *38*, 128-139.

Sinninghe Damsté, J. S., Schouten, S., Rijpstra, W. I. C., Hopmans, E. C., Peletier, H., Gieskes, W. W. C., & Geenevasen, J. A. J. (1999). Structural identification of the C25 highly branched isoprenoid pentaene in the marine diatom Rhizosolenia setigera. *Organic Geochemistry*, *30*, 1581-1583.

Sinninghe Damsté, J. S., Schouten, S., Rijpstra, W. I. C., Hopmans, E. C., Peletier, H., Gieskes, W. W. C., & Geenevasen, J. A. J. (2000). Novel polyunsaturated n-alkenes in the marine diatom Rhizosolenia setigera. *European Journal of Biochemistry*, *267*, 5727-5732.

Smik, L., & Belt, S. T. (2017). Distributions of the Arctic sea ice biomarker proxy IP 25 and two phytoplanktonic biomarkers in surface sediments from West Svalbard. *Organic Geochemistry*, *105*, 39-41. https://doi.org/10.1016/j.orggeochem.2017.01.005

Smik, L., Belt, S. T., Lieser, J. L., Armand, L. K., & Leventer, A. (2016). Distributions of highly branched isoprenoid alkenes and other algal lipids in surface waters from East Antarctica: Further insights for biomarker-based paleo sea-ice reconstruction. *Organic Geochemistry*, *95*, 71-80. https://doi.org/10.1016/j.orggeochem.2016.02.011

Smith, S. R., Abbriano, R. M., & Hildebrand, M. (2012). Comparative analysis of diatom genomes reveals substantial differences in the organization of carbon partitioning pathways. *Algal Research*, *1*(1), 2-16. https://doi.org/10.1016/j.algal.2012.04.003

Smith, S. R., Gillard, J. T., Kustka, A. B., McCrow, J. P., Badger, J. H., Zheng, H., New, A. M., Dupont, C. L., Obata, T., Fernie, A. R., & Allen, A. E. (2016). Transcriptional Orchestration of the Global Cellular Response of a Model Pennate Diatom to Diel Light Cycling under Iron Limitation. *PLoS Genet*, *12*(12), e1006490. https://doi.org/10.1371/journal.pgen.1006490

Stoynova, V., Shanahan, T. M., Hughen, K. A., & de Vernal, A. (2013). Insights into Circum-Arctic sea ice variability from molecular geochemistry. *Quaternary Science Reviews*, *79*, 63-73. https://doi.org/10.1016/j.quascirev.2012.10.006

Stroeve, J., Holland, M. M., Meier, W., Scambos, T., & Serreze, M. (2007). Arctic sea ice decline: Faster than forecast. *Geophysical Research Letters*, *34*(9). https://doi.org/10.1029/2007gl029703

Stroeve, J. C., Serreze, M. C., Holland, M. M., Kay, J. E., Malanik, J., & Barrett, A. P. (2012). The Arctic's rapidly shrinking sea ice cover: a research synthesis. *Climatic Change*, *110*(3-4), 1005-1027. https://doi.org/10.1007/s10584-011-0101-1

Stumm, W., & Morgan, J. J. (1995). *Aquatic Chemistry: Chemical Equilibria and Rates in Natural Waters* (3rd ed.). JOHN WILEY & SONS, INC.

Sundqvist, H. S., Kaufman, D. S., McKay, N. P., Balascio, N. L., Briner, J. P., Cwynar, L. C., Sejrup, H. P., Seppä, H., Subetto, D. A., Andrews, J. T., Axford, Y., Bakke, J., Birks, H. J. B., Brooks, S. J., de Vernal, A., Jennings, A. E., Ljungqvist, F. C., Rühland, K. M., Saenger, C., . . . Viau, A. E. (2014). Arctic Holocene proxy climate database – new approaches to assessing geochronological accuracy and encoding climate variables. *Climate of the Past*, *10*(4), 1605-1631. https://doi.org/10.5194/cp-10-1605-2014

Taldenkova, E., Bauch, H., Stepanova, A., Demyankov, S., & Ovsepyan, A. (2005). Last postglacial environmental evolution of the Laptev Sea shelf as reflected in molluscan, ostracodal, and foraminiferal faunas. *Global and Planetary Change*, *48*(1-3), 223-251. https://doi.org/10.1016/j.gloplacha.2004.12.015

Thomas, D. N., & Dieckmann, G. S. (2003). *Sea Ice: An Introduction to its Physics, Chemistry, Biology and Geology*. Wiley-Backwell.

Tynan, C. T., Ainley, D. G., & Ian, S. (2010). Sea Ice: A Critical Habitat for Polar Marine Mammals and Birds. In D. N. Thomas & G. S. Dieckmann (Eds.), *Sea Ice* (Second ed., pp. 395-457). Blackwell Publishing Ltd, Oxford.

van der Meer, M. T. J., Benthien, A., French, K. L., Epping, E., Zondervan, I., Reichart, G.-J., Bijma, J., Sinninghe Damsté, J. S., & Schouten, S. (2015). Large effect of irradiance on hydrogen isotope fractionation of alkenones in Emiliania huxleyi. *Geochimica et Cosmochimica Acta*, *160*, 16-24. https://doi.org/10.1016/j.gca.2015.03.024

van Dongen, B. E., Schouten, S., & Sinninghe Damsté, J. S. (2002). Carbon isotope variability in monosaccharides and lipids of aquatic algae and terrestrial plants. *Marine Ecology Progress Series*, *232*, 83-92.

Vare, L. L., Massé, G., Gregory, T. R., Smart, C. W., & Belt, S. T. (2009). Sea ice variations in the central Canadian Arctic Archipelago during the Holocene. *Quaternary Science Reviews*, *28*(13-14), 1354-1366. https://doi.org/10.1016/j.quascirev.2009.01.013

Vinnikov, K. Y., Robock, A., Stouffer, R. J., Walsh, J. E., Parkinson, C. L., Cavalieri, D. J., Mitchell, J. F. B., Garrett, D., & F., Z. V. (1999). Global Warming and Northern Hemisphere Sea Ice Extent. *Science*, *286*, 1934-1937.

Volkman, J. K., Barrett, S. M., & Dunstan, G. A. (1994). C25 and C30 highly branched isoprenoid alkenes in laboratory cultures of two marine diatoms. *Organic Geochemistry*, *21*.

Walsh, J. E., Fetterer, F., Stewart, J. S., & Chapman, W. L. (2017). A database for depicting Arctic sea ice variations back to 1850. *Geographical Review*, *107*, 89-107.

Wolhowe, M. D., Prahl, F. G., Probert, I., & Maldonade, M. (2009). Growth phase dependent hydrogen isotopic fractionation in alkenone-producing haptophytes. *Biogeosciences*, *6*, 1681–1694.

Wraige, E. J., Belt, S. T., Lewis, C. A., Cooke, D. A., Robert, J.-M., Massé, G., & Rowland, S. J. (1997). Variations in structures and distributions of C25 highly branched isoprenoid (HBI) alkenes in cultures of the diatom, Haslea ostrearia (Simonsen). *Organic Geochemistry*, *27*, 497-505.

Wraige, E. J., Belt, S. T., Massé, G., Robert, J.-M., & Rowland, S. J. (1998). Variations in distributions of C25 highly branched isoprenoid (HBI) alkenes in the diatom, Haslea ostrearia: influence of salinity. *Organic Geochemistry*, *28*, 855-859.

Wraige, E. J., Johns, L., Belt, S. T., Massé, G., Robert, J.-M., & Rowland, S. (1999). Highly branched C14 isoprenoids in axenic cultures of Haslea ostrearia. *Phytochemistry*, *51*, 69-73.

Xiao, X., Fahl, K., Müller, J., & Stein, R. (2015). Sea-ice distribution in the modern Arctic Ocean: Biomarker records from trans-Arctic Ocean surface sediments. *Geochimica et Cosmochimica Acta*, *155*, 16-29. https://doi.org/10.1016/j.gca.2015.01.029

Xiao, X., Fahl, K., & Stein, R. (2013). Biomarker distributions in surface sediments from the Kara and Laptev seas (Arctic Ocean): indicators for organic-carbon sources and sea-ice coverage. *Quaternary Science Reviews*, *79*, 40-52. https://doi.org/10.1016/j.quascirev.2012.11.028

Yakir, D., & DeNiro, M. J. (1990). Oxygen and Hydrogen Isotope Fractionation during Cellulose Metabolism in Lemna gibba L. *Plant Physiology*, *93*, 325-332.

Young, J. N., Heureux, A. M., Sharwood, R. E., Rickaby, R. E., Morel, F. M., & Whitney, S. M. (2016). Large variation in the Rubisco kinetics of diatoms reveals diversity among their carbon-concentrating mechanisms. *J Exp Bot*, *67*(11), 3445-3456. https://doi.org/10.1093/jxb/erw163

Zhang, X., Gillespie, A. L., & Sessions, A. L. (2009a). Large D/H variations in bacterial lipids reflect central metabolic pathways. *Proceedings of the National Academy of Sciences*, *106*, 12580–12586.

Zhang, Z., & Sachs, J. P. (2007). Hydrogen isotope fractionation in freshwater algae: I. Variations among lipids and species. *Organic Geochemistry*, *38*(4), 582-608. https://doi.org/10.1016/j.orggeochem.2006.12.004

Zhang, Z., Sachs, J. P., & Marchetti, A. (2009b). Hydrogen isotope fractionation in freshwater and marine algae: II. Temperature and nitrogen limited growth rate effects. *Organic Geochemistry*, *40*(3), 428-439. https://doi.org/10.1016/j.orggeochem.2008.11.002

Zhou, Y., Grice, K., Stuart-Williams, H., Farquhar, G. D., Hocart, C. H., Lu, H., & Liu, W. (2010). Biosynthetic origin of the saw-toothed profile in delta(13)C and delta(2)H of n-alkanes and systematic isotopic differences between n-, iso- and anteiso-alkanes in leaf waxes of land plants. *Phytochemistry*, *71*(4), 388-403. https://doi.org/10.1016/j.phytochem.2009.11.009

Zhou, Y., Grice, K., Stuart-Williams, H., Hocart, C. H., Gessler, A., & Farquhar, G. D. (2016). Hydrogen isotopic differences between C3 and C4 land plant lipids: consequences of compartmentation in C4 photosynthetic chemistry and C3 photorespiration. *Plant Cell Environ*, *39*(12), 2676-2690. https://doi.org/10.1111/pce.12821